

Don't step back, not even to pick up the pace

*Anonymous*

Para atrás, ni para tomar impulso

*Anónimo*

**University of Alberta**

Design, Deployment, Performance and Assessment of Downhole and Near  
Surface Monitoring Technology for Geological CO<sub>2</sub> Storage

by

Gonzalo Zambrano Narváez

A thesis submitted to the Faculty of Graduate Studies and Research  
in partial fulfillment of the requirements for the degree of

Doctor of Philosophy  
in  
Geotechnical Engineering

Civil and Environmental Engineering

©Gonzalo Zambrano Narváez  
Spring, 2012  
Edmonton, Alberta

Permission is hereby granted to the University of Alberta Libraries to reproduce single copies of this thesis and to lend or sell such copies for private, scholarly or scientific research purposes only. Where the thesis is converted to, or otherwise made available in digital form, the University of Alberta will advise potential users of the thesis of these terms.

The author reserves all other publication and other rights in association with the copyright in the thesis and, except as herein before provided, neither the thesis nor any substantial portion thereof may be printed or otherwise reproduced in any material form whatsoever without the author's prior written permission.

## **Dedication**

To my parents, Gonzalo Sr. and Martha Maria  
to my siblings, Carlos Eduardo and Maria Camila  
and to my wife, Veronica

A mis padres, Gonzalo Sr. y Martha María  
A mis hermano y hermana, Carlos Eduardo and María Camila  
y a mi esposa, Verónica

## **Abstract**

Early carbon storage research and development efforts in Canada and elsewhere began with “value-added” projects such as CO<sub>2</sub>-enhanced oil recovery or CO<sub>2</sub> enhanced coalbed methane, where the increase in production helps to offset the costs of CO<sub>2</sub> and of its potential long-term storage. These projects provide a valuable opportunity to assess appropriate measurement, monitoring, and verification protocols for the geological storage component of carbon capture and geological storage technologies. Measurement, monitoring, and verification operations provide confidence that CO<sub>2</sub> has been injected and stored in an environmentally sound and safe manner. Multiple, integrated monitoring instrumentation systems are being deployed in CO<sub>2</sub> field demonstration research projects around the world and will provide experience that can be used in regulatory regimes for future commercial CO<sub>2</sub> sequestration scale projects. The Pembina field was chosen from several fields within Alberta, Canada, for a geological CO<sub>2</sub> storage monitoring pilot study, in which the injection of CO<sub>2</sub> was combined with EOR. As part of the project, an existing wellbore within the study area was used as a dedicated observation well. The design and initial results during cementing of this observation well were reviewed. The experience of implementing monitoring technologies was analyzed in order to assess existing knowledge for deploying downhole instrumentation used for monitoring and verification of CO<sub>2</sub> movements in the subsurface. Analysis indicates that the observation well allows direct monitoring and measurements at reservoir level of multiple variables through geophysical, geochemical, and geomechanical instrumentation, as well as the opportunity to carry out wellbore integrity studies under "in-situ" conditions. A post-cement job and completion analysis that couples downhole measurements, analytical and numerical simulation was conducted to improve future installations. Downhole pressure gauges captured the dynamics of cement displacement and were key elements during post-cement job review and assessments of future well integrity. This research also

include the performance assessment of the surface tiltmeter array, an indirect-near-surface measurement technology, deployed in CSEMP—a CO<sub>2</sub> enhanced coal-bed methane pilot project located also in the Pembina Field. The experience and analyses gained from the installations provide valuable insight for CO<sub>2</sub> geological storage monitoring and risk/performance assessment.

## **Acknowledgement**

The author would like to acknowledge his gratitude to all those people and organizations that made this work possible. In particular to:

The author is particularly indebted to the supervising Professor, Dr. Rick Chalaturnyk, for his technical guidance, support and encouragement throughout the course of this study. To him the author is grateful.

The author thankfully acknowledges the financial support provided by the Alberta Energy Research Institute (AERI), Western Economic Diversification (WED), Natural Resources Canada (NRCan), Penn West Energy Trust, EnerPlus, Sustainable Development Technology Canada (SDTC) and EnCana.

The author would also like to acknowledge the professional expertise of Hal Soderberg, Peter Lang from Opsens Solutions, Dr. Don Lawton from the University of Calgary, Dr. Steve Talman and Dr. Bill Gunter from AITF, Dr. Jaime Jimenez and of whom focused their considerable skills on a challenging design and deployment surveillance projects.

Consideration is also due to all academic and administrative staff, in particular to Steve Gamble for his help in the laboratory, good sense of humor and willingness to collaborate, and to Hope Walls for her administrative help and sense of humor.

The author would like to thank his friends and colleagues for their assorted efforts during his journey. Santiago Paz for his unconditional help during the first years of this journey, Nathan Deisman for his critical reading and correcting the grammar of a key section of this dissertation.

The author deepest gratitude goes to his family for their unflagging love and support throughout his life; this dissertation is simple impossible without them. Finally, a special thanks to Veronica Niehaus that make these last four years easy and the last 6 months possible with her love and happiness.

## Table of Contents

CHAPTER 1	Introduction.....	1
1.1	Statement of the problem.....	1
1.2	Research objective.....	2
1.3	Scope and methodology.....	3
1.4	Organization of Thesis.....	3
CHAPTER 2	Overview of Monitoring Geological CO <sub>2</sub> Storage.....	5
2.1	Introduction.....	5
2.2	Systematic approach to planning monitoring programs.....	5
2.3	Monitoring techniques.....	7
2.4	Current limitations.....	8
CHAPTER 3	Project Descriptions.....	10
3.1	Introduction.....	10
3.2	Pembina Cardium CO <sub>2</sub> monitoring pilot, a CO <sub>2</sub> -EOR project.....	10
3.3	CO <sub>2</sub> Storage/enhanced methane production (CSEMP) monitoring pilot project.....	13
3.3.1	CSEMP Operational Summary.....	14
CHAPTER 4	Monitoring System Design and Deployment.....	16
4.1	Introduction.....	16
4.2	Integrated instrumentation system in a observation well.....	16
4.2.1	Observation well design.....	17
4.2.2	Methodology.....	19
4.2.3	Installation logs.....	24
4.2.4	Conclusions.....	29
4.3	Application of surface tiltmeter array to CSEMP pilot.....	30
4.3.1	Deployment of surface tiltmeters.....	30
4.3.2	Discussion.....	34

4.3.3	Conclusions.....	34
CHAPTER 5	Monitoring System Performance .....	36
5.1	Observation well .....	36
5.1.1	Cementing.....	36
5.1.2	Wellbore Completion.....	41
5.1.3	Measurements during CO <sub>2</sub> -EOR pilot .....	43
5.1.4	Downhole pressure and temperature log throughout the life of the project 48	
5.1.5	Others events.....	51
5.1.6	Fluid Recovery System .....	52
5.1.7	Conclusions.....	56
5.2	Use of surface tiltmeter array for monitoring in the CSEMP pilot project: interpretation and uncertainties in injecting, mapping, and reservoir monitoring .....	57
5.2.1	Short-term versus long-term measurements.....	57
5.2.2	Results/analysis of induced fracturing and CO <sub>2</sub> injection.....	64
5.2.3	Discussion .....	75
5.2.4	Conclusions and Recommendations .....	75
CHAPTER 6	Cement Placement Around Downhole Monitoring Sensor Housing Systems	78
6.1	Introduction.....	78
6.1.1	Cementing.....	78
6.1.2	Analytical interpretation .....	79
6.1.3	Computational fluid dynamic modelling .....	79
6.2	Cement job analysis and results.....	80
6.2.2	Conclusion .....	89
6.3	Hydraulic transmissivity of micro-annulus path.....	90
6.3.1	Micro-annulus configuration within the borehole.....	90

6.3.2	Hydraulic transmissivity of the micro-annulus path .....	93
6.3.3	Approach.....	95
6.3.4	Results and conclusions .....	95
6.4	Detailed near-well numerical modeling of hydraulic isolation assessment of permanent downhole sensors housing system .....	97
6.4.1	Modelling description and computational method.....	98
6.4.2	Approach.....	102
6.4.3	Preliminary 3D CFD simulation of cement displacement in a wellbore environment .....	103
6.4.4	Wellbore section with one cable along the axis of the tubing.....	109
6.4.5	Sensor housing system and tubing conveyed.....	120
6.4.6	Sensor housing, tubing conveyed with flow deflector fins .....	133
6.4.7	Summary and Conclusions.....	143
CHAPTER 7 CFD Modelling of a Novel Outside Casing Conveyed Low Flow Impedance Sensor Housing System.....		
7.1	Modelling description and computation method .....	146
7.1.1	Geometry and grid .....	146
7.1.2	Mathematical model.....	146
7.1.3	Boundary conditions .....	147
7.1.4	Numerical solution control.....	147
7.1.5	Approach.....	147
7.2	Low flow impedance sensor housing geometry.....	149
7.2.1	Geometry and grid .....	149
7.2.2	Numerical solution control.....	152
7.2.3	Results.....	152
7.2.4	Discussion .....	155
7.3	Flow deflector fins optimization.....	156

7.3.1	Fins at level of the fluid sample port standoff.....	157
7.3.2	Fins at top-end of sensor housing .....	166
7.3.3	Fins located at the upstream from the sensor housing .....	172
7.3.4	Summary and Conclusion on Deflector Fin Designs.....	207
7.4	Analysis of sensor housing and flow deflector fins geometry/configuration ....	208
7.4.1	Geometry and grid .....	208
7.4.2	Numerical solution control.....	211
7.4.3	Results.....	212
7.4.4	Discussion.....	216
7.5	Conclusions.....	221
CHAPTER 8	Conclusions and Recommendations .....	222
8.1	Summary.....	222
8.1.1	Observation well.....	222
8.1.2	Surface tiltmeter array.....	225
8.2	Conclusions.....	226
8.3	Recommendations and future work .....	227
8.3.1	Observation well.....	227
8.3.2	Surface tiltmeter array.....	229
CHAPTER 9	References.....	231
APPENDIX A:	The standard operation procedures used for the CSEMP .....	237
APPENDIX B:	Additional simulation results of model with Type-IV fin.....	243
APPENDIX C:	Patent P1396PC00 - Outside casing conveyed low flow impedance sensor gauge system and method.....	245
APPENDIX D:	Additional simulation results of OPS-ZVG model .....	268

## List of Tables

Table 2.1 Direct and indirect techniques that can be used to monitoring the fate of the sequestered CO <sub>2</sub> (After IPCC [1, 2]).....	9
Table 3.1 Operational injection and production events in CSEMP injection well .....	15
Table 4.1 Observation well basic design variables [13]. .....	20
Table 4.2 Physical positioning of the sensors in the tubing string.....	25
Table 6.1. Fluid rheological properties .....	100

## List of Figures

Figure 2.1 Operational, verification and environmental monitoring levels (after Chalaturnyk and Gunter[9]).....	7
Figure 3.1 Location of the pilot site within the Pembina Field, Alberta, Canada [17]. ....	12
Figure 3.2 Location of injector and shallow monitoring well (MM), and geological cross-section within the project [25]. ....	14
Figure 4.1 Location of the monitoring well 100/07-11-048-09 W5M [3]. ....	17
Figure 4.2 Schematic of well instrumentation configuration and geology [13].....	18
Figure 4.3 Installation schematic of sensor within the borehole [13]. ....	22
Figure 4.4 Installation schematic of fluid recovery system [13]. ....	23
Figure 4.5 Top Left: Spool and instrumentation prepared for transport to well site. Top Right: Unloading and assembling the spools and cable for instrumentation. Bottom Left: All instrumentation and spools ready for running the cables over the sheaves. Bottom Right: View of the cables passing over the sheaves during night-time [16]. ....	24
Figure 4.6 Left: Shark fin protector attached to tubing. Right: View of spools from rig floor. ....	26
Figure 4.7 Steps for cementing the observation well. A. Borehole with instruments in place. B. Circulation of pre-wash fluid. C. Circulation of cement. D. End of cement circulation.....	27
Figure 4.8 Cables passing through the dognut after removal of the blowout preventer (blue).....	29
Figure 4.9 Installation of the wellhead(a) and the completed cable/tubing feed-throughs at the wellhead(b). ....	29
Figure 4.10 Surface tiltmeter(a), typical installation setup(b), Surface setup of Tilt-site Ep07(c) and layout of tilt-sites for CSEMP(d). ....	32
Figure 4.11 Two different ground deformation models derived from the same tilt data. In order to distinguish between these two possible solutions, an additional tiltmeter would be required between the middle and furthest right tiltmeters. In	

general, tiltmeter density must be designed to pick up the smallest scale surface deformation that could be associated with the events being monitored. ....	33
Figure 4.12 Tiltmeter site plan for monitoring of micro-pilot Phase I (small volumes of CO <sub>2</sub> injected) and pilot Phase II (large volumes of CO <sub>2</sub> injected).....	34
Figure 5.1 Steps in the cementation of the OW. ....	37
Figure 5.2 Recorded pressure and temperature during the cementing stages of the OW completion [3].....	38
Figure 5.3 Equivalent density and normalized temperature during the cementing stages of the OW completion [3]. ....	40
Figure 5.4 Recorded pressure and temperature between the end of the cementing job and the completion of the well. ....	41
Figure 5.5 Equivalent density and normalized temperature between the end of the cementing job and the completion of the well.....	42
Figure 5.6 Pressure records from all instruments deployed during the entire process.....	42
Figure 5.7 Temperature records from all instruments deployed during the entire installation program. ....	43
Figure 5.8 Pressure reading from wellhead, 1302m KB and 1611m KB pressure gauges. ....	44
Figure 5.9 Recorded pressure and temperature reading from Injector 102/10-11 and OW. ....	45
Figure 5.10 Recorded pressure and temperature of a deep sensor and shallow sensor from May 2005 to September 2005.....	47
Figure 5.11 Downhole pressure response of OW and production index with time. ....	47
Figure 5.12 Schematic description of the zones found in Figure 5.10 and Figure 5.11....	48
Figure 5.13 2005 downhole pressure and temperature logs.....	49
Figure 5.14 2006 downhole pressure and temperature logs.....	49
Figure 5.15 2007 downhole pressure and temperature logs.....	50
Figure 5.16 2008 downhole pressure and temperature logs.....	50

Figure 5.17 Recorded pressure and temperature of a sensor at 1303 m during the pressure recovery test on September 1, 2005.....	51
Figure 5.18 Recorded pressure and temperature for both gauges during pressure recovery tests.....	52
Figure 5.19 Sample Handling Schematic.....	53
Figure 5.20 Typical aqueous composition of producer and OW water samples [3].....	54
Figure 5.21 FRS#2 bubble tube interpretation [3]. .....	56
Figure 5.22 Recorded raw tilt data in months (Site EP14 in Figure 5.27).....	61
Figure 5.23 Recorded raw tilt data in days (Site EP14 in Figure 5.27). .....	61
Figure 5.24 Recorded raw tilt data in hours(Site EP14 in Figure 5.27).....	62
Figure 5.25 Monthly tilt data from Site EP06 - June, 2006. Major changes in tilt correlates with rainy days.....	63
Figure 5.26 Interpretation of log results from Injector 102/7-28-46-W5M (Figure 5.27).65	
Figure 5.27 Map view showing the azimuth for the fracture treatment.....	66
Figure 5.28 (a) Observed and theoretical tilt vectors for the best-fit fracture system and (b) surface deformation for the 102/7-28-46-7W5 Frac treatment (418.5 m to 427.0 m).....	67
Figure 5.29 Offset well tiltmeter tool movement over the course of the fracture treatment [43]. .....	68
Figure 5.30 Surface deformation during CO <sub>2</sub> injection [45].....	69
Figure 5.31 Surface deformation before CO <sub>2</sub> injection (September 4-8, 2006) [46].....	70
Figure 5.32 Surface deformation after post-processing of data during CO <sub>2</sub> injection (September 8-12, 2006) [46]. .....	71
Figure 5.33 Mapped surface deformation during the first CO <sub>2</sub> injection, up to where weather apparently began to affect the tiltmeter data [47]. .....	72
Figure 5.34 Mapped surface deformation during the first CO <sub>2</sub> injection, including the last 12 hours where weather apparently began to affect the tiltmeter data [47].....	72

Figure 5.35 Deformation during the down period between CO <sub>2</sub> injections. Note that weather effects are still considered very significant during this period.....	73
Figure 5.36 Deformation during the first part of the second CO <sub>2</sub> injection (injecting at 35 tonnes/day) [47].....	73
Figure 5.37 Deformation during the injection Phase II (injection rate: 45 tonnes/day) [47]. .....	74
Figure 5.38 Deformation during the injection Phase II (injection rate: 35 tonnes/day) [47]. .....	74
Figure 6.1 Recorded pressure and temperature during cement operation.....	80
Figure 6.2 Steps in the cementation of the observation well from an analytical solution [13]. .....	82
Figure 6.3 Reported and simulated data during cement circulation.....	84
Figure 6.4 ECD at bottom hole below reservoir pressure (blue line). .....	85
Figure 6.5 The BHP (read line) drops from a) 18MPa at 43.7 minutes to b) 17 MPa at 47.4 minutes of circulation. ....	86
Figure 6.6 History match of downhole pressure data [13].....	88
Figure 6.7 Effect of heavier preflush fluids on the annular pressure [13]. ....	89
Figure 6.8 Illustration of (a) geometry of eccentric tubing, (b) and resultant velocity profile. ....	91
Figure 6.9 Schematic of the micro-annular path behind tubing and cables. ....	93
Figure 6.10 Schematic of unwrapping a micro-annulus section. ....	95
Figure 6.11 Analytical results of micro-annulus configurations at a fix flow. ....	96
Figure 6.12 Flow Chart of CFD Simulations [70]. ....	98
Figure 6.13 Preliminary CFD mesh for a wellbore section. ....	99
Figure 6.14 Streamlines of flow through annulus area of a wellbore section.....	101
Figure 6.15. 3D view of the borehole with details of instrumentation. ....	103
Figure 6.16 Mesh of a 5m section of borehole using computational fluid dynamics simulation. ....	104

Figure 6.17 Multiphase flow graphical CFD solution in different time steps. The cement slurry (red) is displacing the preflush-water fluid (blue) within tubing/casing annular area. ....	106
Figure 6.18 Location of monitoring points along the axis and cross section.....	107
Figure 6.19 Recorded reading on monitoring points. ....	108
Figure 6.20 The configuration of the borehole cross-section with the tubing and cable. ....	109
Figure 6.21 3D geometrical configuration of the tubing and cable within the 2 m of a borehole section.....	110
Figure 6.22. Mesh for the 3D axis-symmetrical model of one cable aligned with the tubing and borehole section.....	111
Figure 6.23 VOF simulation results for the axis-symmetrical model of one cable aligned with the tubing and borehole section. Output at times $t = 0.44, 0.88, 1.32, 1.76, 2.20$ and $3.08$ s, after the cement slurry enters to annulus. Each snapshot shows cement slurry volume fraction and ISVF = 0.90 (orange).....	113
Figure 6.24 VOF simulation results for the axis-symmetrical model of one cable aligned with the tubing and borehole section. Output at times $t = 10.21, 20.25, 40.33$ and $89.00$ s, while the cement slurry is displacing through the annulus. Each snapshot shows cement slurry volume fraction and ISVF = 0.90 (orange)....	114
Figure 6.25 Surface area of the ISVF 90 % (integral quantity) – flow time results for the axis-symmetrical model of one cable aligned with the tubing and borehole section.....	115
Figure 6.26 VOF simulation results for the axis-symmetrical model of one cable aligned with the tubing and borehole section. Output at times $t = 89.00$ s, while the cement slurry is displacing through the annulus. The snapshot shows ISVF = 0.90 and velocity profiles of inlet and outlet faces. ....	116
Figure 6.27 VOF simulation results for the axis-symmetrical model of one cable aligned with the tubing and borehole section. Output at times $t = 89.00$ s, while the cement slurry is displacing through the annulus. The snapshot shows cement slurry velocities on a cross-section of the model.....	116

Figure 6.28 VOF simulation results for the axis-symmetrical model of one cable aligned with the tubing and borehole section. Output at time $t = 90.00$ s, while the cement slurry is displacing through the annulus. The snapshot shows cement slurry volume fraction and ISVF = 0.90.....	117
Figure 6.29 VOF simulation results for the axis-symmetrical model of one cable aligned with the tubing and borehole section. Output at time $t = 90.00$ s, while the cement slurry is displacing through the annulus. The snapshot shows the annular distribution of the ISVF with value of 0.90.....	118
Figure 6.30 Mesh for the preliminary 3D model of one cable aligned diagonal with the tubing and borehole section. (a) Outlet, (b) Inlet, (c) isometric view of the model, (d) Cross-section of cable alignment, and (e) velocity profile of cross-section of the model, output time = .0022 s.....	119
Figure 6.31 Sensor housing system: (a) as-is CAD drawing, (b) preliminary 3D drawings.....	121
Figure 6.32 3D geometrical configuration of the sensor housing and tubing conveyed within the 1.7 m of borehole section. ....	122
Figure 6.33 Sketch of Mesh for the axis-symmetric 3D sensor housing model duplicate from the Pembina Cardium CO <sub>2</sub> monitoring observation well.....	123
Figure 6.34 VOF simulation results for the axis-symmetrical model of one sensor housing standoff installed at the Pembina Cardium CO <sub>2</sub> pilot. Output at times $t = 0.08, 0.16, 0.32, 0.64, 1.28$ and $2.10$ s, while the cement slurry is displacing through the annulus. Each snapshot shows cement slurry volume fraction , ISVF = 0.90, and annular velocity streamlines. ....	125
Figure 6.35 VOF simulation results for the axis-symmetrical model of one sensor housing standoff installed at the Pembina Cardium CO <sub>2</sub> pilot. Output at times $t = 3.50$ s, while the cement slurry is displacing through the annulus. Each snapshot shows cement slurry volume fraction, ISVF = 0.90 (light orange), and annular velocity streamlines. ....	126
Figure 6.36 VOF simulation results for the axis-symmetrical model of one sensor housing standoff installed at the Pembina Cardium CO <sub>2</sub> pilot. Output at times $t = 0.08, 0.16, 0.32, 0.64, 0.82, 0.99, 1.13, 1.31, 1.39, 1.51, 1.90, 2.10, 2.32, 2.41$	

and 3.50 s, while the cement slurry is displacing through the annulus. Each snapshot shows cement slurry volume fraction and ISVF = 0.90 (orange). ... 127

Figure 6.37 Summary surface area of the ISVF-90% and ISVF-95% (integral quantities) – flow time results for different grid spacing meshes for the axi-symmetrical models of one sensor housing standoff on the tubing conveyed and borehole section. (a) 44,269 nodes mesh, (b) 123,315 nodes mesh, and (c) 134,212 nodes mesh..... 129

Figure 6.38 VOF simulation results for the axis-symmetrical model of one sensor housing installed at the Pembina Cardium CO<sub>2</sub> pilot. Output at times t = 0.60, 0.82 and 0.99 s, while the cement slurry is displacing through the annulus. The snapshot shows the annular distribution of the ISVF with value of 0.90. .... 130

Figure 6.39 VOF simulation results for the axis-symmetrical model of one sensor housing installed at the Pembina Cardium CO<sub>2</sub> pilot. Output at times t = 3.50 s, while the cement slurry is displacing through the annulus. The snapshot shows the annular distribution of the ISVF with value of 0.90. .... 131

Figure 6.40 Summary of VOF simulation results for the 3D model of the sensor housing standoff, tubing conveyed and borehole sections. Output at time t = 0.64 (a), 0.82 (b), 0.99 (c) and 3.50 (d) s, while the cement slurry is displacing through the annulus. Each snapshot shows the annular distribution of ISVF with value of 0.90..... 132

Figure 6.41 3D geometrical boundary conditions of the borehole and tubing conveyed with the sensor housing and five flow deflector fins. .... 134

Figure 6.42 Geometry of the conceptual sensor housing and five flow deflector fins. . 135

Figure 6.43 Sketch of Mesh of the conceptual 3D sensor housing system with five flow deflector fins. .... 135

Figure 6.44 VOF simulation results for the 3D model of the sensor housing with five flow deflector fins, tubing conveyed and borehole section of 2.2 m length. Output at time t = 4.00 s, while the cement slurry is displacing through the annulus. The snapshots show cement slurry velocity streamlines. .... 137

Figure 6.45 VOF simulation results for the 3D model of the sensor housing with five flow deflector fins, tubing conveyed and borehole section of 2.2 m length. Output at

time  $t = 1.08, 1.34, 1.44, 1.52, 1.60, 1.69, 1.78, 1.88, 1.98, 2.09, 2.20, 2.39$  and  $4.00$  s, while the cement slurry is displacing through the annulus. Each snapshot shows cement slurry volume fraction,  $ISVF = 0.90$ , and velocity streamlines. .... 138

Figure 6.46 Surface area of  $ISVF 90\%$  and  $ISVF 95\%$  (integral quantities) – flow time results for the 3D model of the sensor housing with five flow deflector fins, tubing conveyed and borehole section of  $2.2$  m length. .... 140

Figure 6.47 VOF simulation results for the 3D model of the sensor housing with five flow deflector fins, tubing conveyed and borehole section of  $2.2$  m length. Output at time  $t = 4.00$  s, while the cement slurry is displacing through the annulus. The snapshot shows the annular distribution of  $ISVF$  with value of  $0.90$ . .... 141

Figure 6.48. Summary of VOF simulation results for the 3D model of the sensor housing with four flow deflector fins, tubing conveyed and borehole sections. Output at time  $t =$  (a),  $0.00$  (b),  $1.55$  (c) and  $2.47$  (d)  $4.00$  s, while the cement slurry is displacing through the annulus. Each snapshot shows the annular distribution of  $ISVF$  with value of  $0.90$ . .... 142

Figure 6.49 Surface area of  $ISVF 90\%$  (integral quantity) – flow time results for the 3D model of the sensor housing with four flow deflector fins, tubing conveyed and borehole section of  $2.2$  m length. .... 143

Figure 6.50 Summary of VOF simulation results of the three models of the tubing conveyed and borehole sections with: (a) the sensor housing standoff; and (b) one cable aligned parallel to tubing with  $1$  mm gap; (c) the sensor housing with five flow deflector fins. Output at time  $t = 89.00$  (a),  $3.5$  (b) and  $4.00$  (c) s, while the cement slurry is displacing through the annulus. Each snapshot shows the annular distribution of  $ISVF$  with value of  $0.90$ . .... 145

Figure 7.1 3D geometrical configuration of the novel sensor housing and the casing conveyed within the  $2$  m of a borehole section. .... 150

Figure 7.2 Sketch of the novel sensor housing with some dimensions. .... 151

Figure 7.3 Mesh for the 3D model of (a) the novel sensor housing system and the casing conveyed (b) within the  $2$  m of a borehole section. .... 152

Figure 7.4 VOF simulation results for the 3D model of the novel sensor housing and the casing conveyed within the borehole section of 2.00 m length. Output at time $t = 0.437, 0.583, 0.875, 1.021, 1.075, 1.166, 1.312, 1.458, 1.604, 2.015, 2.302, 2.732, 3.170, 4.046$ and 6.000 s, while the cement slurry is displacing through the annulus. Each snapshot shows cement slurry volume fraction, ISVF = 0.90, and velocity streamlines. ....	153
Figure 7.5 Surface area of the ISVF = 90, 95 and 98 percent (integral quantities) – flow time results for the 3D model of the novel sensor housing and the casing conveyed within the borehole section of 2.00 m length. ....	154
Figure 7.6 VOF simulation results for the 3D model of the novel sensor housing and the casing conveyed within the borehole section of 2.00 m length. Output at time $t = 3.17$ s, while the cement slurry is displacing through the annulus. These snapshots show the annular distribution of the ISVF with value of 0.95. ....	155
Figure 7.7 3D geometrical configuration of the low flow impedance sensor housing with three flow deflector fins located upstream of the sensor housing.....	157
Figure 7.8 Illustration of the three upstream flow deflector fins and the novel sensor housing: a) side view b) cross-section.....	157
Figure 7.9 Sketch of the three flow deflector fins located at the level of the fluid sample port standoff.....	158
Figure 7.10 Mesh for the 3D model of (a) the novel sensor housing system and the casing conveyed with three upstream flow deflector fins (b) within the 2.50 m of a borehole section.....	159
Figure 7.11 VOF simulation results for the 3D model of the novel sensor housing and the casing conveyed with three upstream flow deflector fins within the borehole section of 2.50 m length. Output at time $t = 0.450, 0.600, 0.900, 1.050, 1.200, 1.500, 1.650, 1.940, 2.085, 2.235, 2.285, 2.685$ and 3.900 s, while the cement slurry is displacing through the annulus. Each snapshot shows cement slurry volume fraction, ISVF = 0.90, and velocity streamlines. ....	160
Figure 7.12 Surface area of the ISVF = 90, 95 and 98 percent (integral quantities) – flow time results for the 3D model of the novel sensor housing and the casing	

conveyed with three upstream flow deflector fins within the borehole section of 2.00 m length. ....	162
Figure 7.13 VOF simulation results for the 3D model of the novel sensor housing and the casing conveyed with three upstream flow deflector fins within the borehole section of 5.00 m length. Output at time $t = 3.90$ s, while the cement slurry is displacing through the annulus. These snapshots show the annular distribution of the ISVF with value of 0.95. ....	163
Figure 7.14 VOF simulation results for the 3D model of the novel sensor housing and the casing conveyed with three upstream flow deflector fins within the borehole section of 2.00 m length. Output at time $t = 1.20, 1.35, 1.50, 1.65, 1.80$ and $2.90$ s, while the cement slurry is displacing through the annulus. Each snapshot shows cement slurry volume fraction, $ISVF = 0.90$ , and velocity streamlines. ....	165
Figure 7.15 3D geometrical configuration of low flow impedance sensor housing with three flow deflector fins downstream of sensor housing. ....	166
Figure 7.16 Mesh for the 3D model of (a) the novel sensor housing and the casing conveyed with three downstream flow deflector fins (b) within the 5.00 m of a borehole section. ....	167
Figure 7.17 VOF simulation results for the 3D model of the novel sensor housing and the casing conveyed with three downstream flow deflector fins within the borehole section of 5.00 m length. Output at time $t = 1.039, 1.288, 1.521, 1.774, 2.009, 2.141, 2.493, 2.689, 3.179, 4.199, 5.234, 6.270, 7.050, 8.090$ and $9.130$ s, while the cement slurry is displacing through the annulus. Each snapshot shows cement slurry volume fraction, $ISVF = 0.90$ , and velocity streamlines. ....	168
Figure 7.18 Surface area of the $ISVF = 90, 95$ and $98$ percent (integral quantities) – flow time results for the 3D model of the novel sensor housing and the casing conveyed with three downstream flow deflector fins within the borehole section of 5.00 m length. ....	169
Figure 7.19 VOF simulation results for the 3D model of the novel sensor housing and the casing conveyed with three downstream flow deflector fins within the borehole section of 5.00 m length. Output at time $t = 9.91$ s, while the cement slurry is	

displacing through the annulus. These snapshots show the annular distribution of the ISVF with value of 0.98. ....	170
Figure 7.20 3D geometrical configuration of the low flow impedance sensor housing with four flow deflector fins (Type-I) located at 483 mm upstream of the sensor housing sample port within the borehole section of 5.00 m length. ....	172
Figure 7.21 Sketch of: (a) the cross-section; (b) the isometric view; (c) and the side view of four flow deflector Type-I fins located at 483 mm from the fluid sample port standoff. ....	173
Figure 7.22 Mesh of (a) 3D model of the novel sensor housing and the casing conveyed with four flow deflector fins (Type-I) located at 483 mm upstream of the fluid sample port standoff (b) within the 5.00 m of a borehole section. ....	174
Figure 7.23 VOF simulation results for the 3D model of the novel sensor housing and the casing conveyed with four flow deflector fins (Type-I) located at 483 mm upstream of the sensor housing within the borehole section of 5.00 m length. Output at time $t = 0.259, 0.453, 0.569, 0.722, 0.943, 1.181, 1.389, 1.616, 1.874, 2.085, 2.274, 2.530, 2.783, 4.075$ and $10.00$ s, while the cement slurry is displacing through the annulus. Each snapshot shows cement slurry volume fraction, $ISVF = 0.90$ , and velocity streamlines. ....	175
Figure 7.24 Surface area of the $ISVF = 90, 95$ and $98$ percent (integral quantities) – flow time results for the 3D model of the novel sensor housing and the casing conveyed with four flow deflector fins (Type-I) located at 483 mm upstream of the sensor housing within the borehole section of 5.00 m length. ....	176
Figure 7.25 VOF simulation results for the 3D model of the novel sensor housing and the casing conveyed with four flow deflector fins (Type-I) located at 483 mm upstream of the sensor housing within the borehole section of 5.00 m length. Output at time $t = 10.00$ s, while the cement slurry is displacing through the annulus. These snapshots show the annular distribution of the ISVF with value of 0.98. ....	178
Figure 7.26 3D geometrical configuration of the low flow impedance sensor housing with four flow deflector fins (Type-II) located at the upstream of the sensor housing. ....	179

Figure 7.27 Illustration of the four upstream flow deflector fins (Type-II) and the novel sensor housing: (a) side view (b) cross-sectional view.....	179
Figure 7.28 Sketch of: (a) the cross-section; (b) the isometric view; (c) and the side views of four flow deflector Type-II fins located at 483 mm from the fluid sample port standoff.....	180
Figure 7.29 Mesh for the 3D model of (a) the novel sensor housing and the casing conveyed with four flow deflector fins (Type-II) located at 483.0 mm upstream of the sensor housing (b) within the 2.50 m of a borehole section. ....	181
Figure 7.30 VOF simulation results for the 3D model of sensor housing with four flow deflector fins (Type-II). Output at time $t = 0.299, 0.426, 0.534, 0.642, 0.751, 0.862, 0.972, 1.194, 1.275, 1.338, 1.436, 1.549, 1.600, 1.772$ and 4.000 s, while the cement slurry is displacing through the annulus. Each snapshot shows cement slurry volume fraction, ISVF = 0.90, and velocity streamlines. ....	183
Figure 7.31 Surface area of the ISVF = 90, 95 and 98 percent (integral quantities) – flow time results for the 3D model of the novel sensor housing and the casing conveyed with four flow deflector fins (Type-II) located at 483.0 mm upstream of the sensor housing within the borehole section of 5.00 m length. ....	184
Figure 7.32 VOF simulation results for the 3D model of the novel sensor housing and the casing conveyed with four flow deflector fins (Type-II) located at 483.0 mm upstream of the sensor housing within the borehole section of 2.50 m length. Output at time $t = 4.00$ s, while the cement slurry is displacing through the annulus. These snapshots show the annular distribution of the ISVF with value of 0.98.....	185
Figure 7.33 VOF simulation results for the 3D model of the novel sensor housing and the casing conveyed with four flow deflector fins (Type-II) located at 483.0 mm upstream of the sensor housing within the borehole section of 2.50 m length. Output at time $t = 1.338$ and 1.436 s, while the cement slurry is displacing through the annulus. Each snapshot shows cement slurry volume fraction, ISVF = 0.90, and velocity streamlines.....	186
Figure 7.34 VOF simulation results for the 3D model of the novel sensor housing and the casing conveyed with four flow deflector fins (Type-II) located at 483.0 mm upstream of the sensor housing within the borehole section of 2.50 m length.	

Output at time $t = 0.426$ and $0.534$ s, while the cement slurry is displacing through the annulus. Each snapshot shows cement slurry volume fraction and $ISVF = 0.90$ . .....	187
Figure 7.35 3D geometrical configuration of the low flow impedance sensor housing with four flow deflector fins (Type-III) located at 420 mm upstream of the sensor housing. ....	189
Figure 7.36 Illustration of four upstream flow deflector fins (Type-III) and the novel sensor housing. ....	189
Figure 7.37 Sketch of: (a) the cross-section; (b) the isometric view; (c) and the side view of four flow deflector Type-III fins located at 420 mm from the fluid sample port standoff.....	190
Figure 7.38 Mesh for the 3D model of (a) the novel sensor housing and the casing conveyed with four flow deflector fins (Type-III) located at 420 mm upstream of the sensor housing (b) within the 5.00 m of a borehole section. ....	191
Figure 7.39 VOF simulation results for the 3D model of the novel sensor housing and the casing conveyed with four flow deflector fins (Type-III) located at 420 mm upstream of the sensor housing within the borehole section of 5.00 m length. Output at time $t = 0.203, 0.593, 1.001, 1.205, 1.409, 1.613, 2.021, 2.225, 2.429, 2.837, 4.060, 4.876, 5.080, 7.119$ and $10.000$ s, while the cement slurry is displacing through the annulus. Each snapshot shows cement slurry volume fraction, $ISVF = 0.90$ , and velocity streamlines. ....	192
Figure 7.40 Surface area of the $ISVF = 90, 95$ and $98$ percent (integral quantities) – flow time results for the 3D model of the novel sensor housing and the casing conveyed with four flow deflector fins (Type-III) located at 420 mm upstream of the sensor housing within the borehole section of 5.00 m length. ....	194
Figure 7.41 Surface area of the $ISVF = 90, 95$ and $98$ percent (integral quantities) – flow time results for the 3D model of the novel sensor housing and the casing conveyed with four flow deflector fins (Type-III) located at 420 mm upstream of the sensor housing within the borehole section of 5.00 m length. These snapshots show the annular distribution of $ISVF$ with value of $0.98$ . ....	195

Figure 7.42 VOF simulation results for the 3D model of the novel sensor housing and the casing conveyed with four flow deflector fins (Type-III) located at 420 mm upstream of the sensor housing within the borehole section of 5.00 m length. Output at time $t = 0.407$ and $10.000$ s, while the cement slurry is displacing through the annulus. Each snapshot shows cement slurry volume fraction, ISVF = 0.90, and velocity streamlines.....	196
Figure 7.43 3D geometrical configuration of the low flow impedance sensor housing with four flow deflector fins (Type-IV) located at 420.0 mm from the fluid sample port standoff.....	197
Figure 7.44 Illustration of four upstream flow deflector fins (Type-IV) and the novel sensor housing. ....	198
Figure 7.45 Sketch of: (a) the cross-section; (b) the isometric view; (c) and the side view of four flow deflector Type-IV fins located at 420.0 mm from the fluid sample port standoff.....	199
Figure 7.46 Mesh for the 3D model of (a) the novel sensor housing system and the casing conveyed with four flow deflector fins (Type-IV) located at 420.0 mm upstream of sensor housing (b) within the 5.00 m of a borehole section. ....	200
Figure 7.47 VOF simulation results for the 3D model of the novel sensor housing and the casing conveyed with four flow deflector fins (Type-IV) located at 420.0 mm upstream of the sensor housing within the borehole section of 5.00 m length. Output at time $t = 0.143, 0.287, 0.431, 0.575, 0.719, 0.863, 1.151, 1.438, 1.725, 2.013, 2.575, 2.863, 3.871, 7.039$ and $10.000$ s, while the cement slurry is displacing through the annulus. Each snapshot shows cement slurry volume fraction, ISVF = 0.90, and velocity streamlines. ....	201
Figure 7.48 Surface area of the ISVF = 90, 95 and 98 percent (integral quantities) – flow time results for the 3D model of the novel sensor housing and the casing conveyed with four flow deflector fins (Type-IV) located at 420.0 mm upstream of the sensor housing within the borehole section of 5.00 m length. ....	203
Figure 7.49 VOF simulation results for the 3D model of the novel sensor housing and the casing conveyed with four flow deflector fins (Type-IV) located at 420.0 mm upstream of the sensor housing within the borehole section of 2.50 m length.	

Output at time $t = 4.00$ s, while the cement slurry is displacing through the annulus. These snapshots show the annular distribution of the ISVF with value of 0.98.....	204
Figure 7.50 VOF simulation results for the 3D model of the novel sensor housing and the casing conveyed with four flow deflector fins (Type-IV) located at 420.0 mm of upstream of the sensor housing within the borehole section of 5.00 m length. Output at time $t = 0.287$ and 10.00 s, while the cement slurry is displacing through the annulus. Each snapshot shows cement slurry volume fraction, ISVF = 0.90, and velocity streamlines.....	205
Figure 7.51 VOF steady state simulation results for the 3D model of the novel sensor housing and the casing conveyed with four flow deflector fins (Type-IV) located: (a) at 420.0 mm and (b) 127.0 mm from the upstream of the sensor housing within the borehole section of 5.00 m length. Each snapshot shows the velocity streamlines.....	206
Figure 7.52 3D geometrical configuration of the low flow impedance sensor housing with two sets of four flow deflector fins (Type-IV) located at 127.0 mm down- and up- stream of the sensor housing.....	209
Figure 7.53 Sketch of: (a) the cross-section; (b) the isometric view; (c) and the side view of two set of four flow deflector Type-IV fins located at 127.0 mm from the fluid sample port standoff.....	210
Figure 7.54 Mesh for the 3D model of (a) the novel sensor housing system and the casing conveyed with two sets of four flow deflector fins (Type-IV) each located at 127.0 mm down and up stream of sensor housing (b) within the 5.00 m of a borehole section.....	211
Figure 7.55 VOF simulation results for the 3D model of the novel sensor housing and the casing conveyed with two sets of four flow deflector fins (Type-IV) each located at 127.0 mm of the down- and up- stream of the sensor housing within the borehole section of 5.00 m length. Output at time $t = 0.719, 0.839, 0.959, 1.079, 1.199, 1.319, 1.439, 1.799, 2.122, 2.48, 2.600, 2.840, 3.080, 6.078, 10.000$ s, while the cement slurry is displacing through the annulus. Each snapshot shows cement slurry volume fraction, ISVF = 0.90, and velocity streamlines.....	213

Figure 7.56 Surface area of the ISVF = 90, 95 and 98 percent (integral quantities) – flow time results for the 3D model of the novel sensor housing and the casing conveyed with two sets of four flow deflector fins (Type-IV) each located at 127.0 mm from the down- and up- stream of the sensor housing within the borehole section of 5.00 m length.....	215
Figure 7.57 VOF simulation results for the 3D model of the novel sensor housing and the casing conveyed with two sets of four flow deflector fins (Type-IV) each located at 127.0 mm from the down- and up- stream of the sensor housing within the borehole section of 5.00 m length. Output at time t =10.00 s, while the cement slurry is displacing through the annulus. These snapshots show the annular distribution of the ISVF with value of 0.98.....	216
Figure 7.58 VOF simulation results for the 3D model of the novel sensor housing and the casing conveyed with two sets of four flow deflector fins (Type-IV) each located at 127.0 mm from the down and up stream of sensor housing within the borehole section of 5.00 m length. Output at time t = 0.839 and 10.000 s, while the cement slurry is displacing through the annulus. Each snapshot shows cement slurry volume fraction, ISVF = 0.90, and velocity streamlines. ....	217
Figure 7.59 Rheological prosperities of cement slurry and fresh-water spacer fluids....	218
Figure 7.60 VOF simulation results for the 3D model of the novel sensor housing and the casing conveyed with two sets of four flow deflector fins (Type-IV) each located at 127.0 mm of down and up stream of sensor housing within the borehole section of 5.00 m length. Output at time t = 0.120 and 9.798 s, while the cement slurry is displacing through the annulus. Each snapshot shows cement slurry volume fraction and the velocity profile of a sampling plane in grey color map.....	219

## CHAPTER 1 Introduction

### 1.1 Statement of the problem

In September 2005, the Intergovernmental Panel on Climate Change (IPCC) published a report [1, 2] on carbon capture and storage (CCS) and concluded that injecting carbon dioxide (CO<sub>2</sub>) into subsurface geological formations represents a viable method of mitigating greenhouse gas emissions to the atmosphere [3]. CO<sub>2</sub> injection in subsurface formations is not a new technology; however, it is acknowledged that technical issues related to geological storage of CO<sub>2</sub> as a viable method for managing greenhouse gas emissions have not been fully resolved and that outstanding issues must be addressed before the technology can be accepted by policy makers and the public for wide scale implementation [4]. There are several options for geological storage of CO<sub>2</sub>, including: depleted oil and gas reservoirs, deep saline aquifers, as a bi-product CO<sub>2</sub>-flood enhanced oil recovery (CO<sub>2</sub>-EOR) operations and/or enhanced coalbed methane (ECBM) recovery. Early research and develop (R&D) of geological storage in Canada has generally begun with “value-added” projects such as CO<sub>2</sub>-EOR, where the CCS is associated with production of a hydrocarbon resource which helps offset of CO<sub>2</sub> storage costs. These R&D projects provide a valuable opportunity to assess appropriate measurement, monitoring and verification protocols for the geological storage component of CCS technologies.

There are four levels of CO<sub>2</sub> trapping mechanisms: 1) stratigraphic/hydrogeologic; 2) residual gas; 3) solubility and 4) mineral, each with different time scales of reaction and spatial distribution. It is expected that injected CO<sub>2</sub> will be in a supercritical state for long periods of time (centuries to millennia) before it fully dissolves in the formation fluids. In CO<sub>2</sub>-EOR operations, a large percent of CO<sub>2</sub> will be trapped by dissolution in the oil-water system, leaving a small percent of CO<sub>2</sub> in a free phase. Deep coal seams appear attractive because CO<sub>2</sub> seems to be trapped either physically in the coal matrix or by chemical absorption on the coal surface for hundred years before it fully adsorbs [5-7]. The primary purpose of CO<sub>2</sub> enhance coalbed methane R&D pilot projects is to demonstrate that CO<sub>2</sub> storage in coals is viable as a GHG reduction mechanism, and that an additional benefit is enhanced production of methane. The concept has already been demonstrated by the Alberta Research Council [Alberta Innovates Technology Future] in

micro-pilots at Fenn-Big Valley, Alberta in Mannville coals and in the Qinshui Basin, China.

The measurement, monitoring and verification (MMV) elements of a CO<sub>2</sub> geological storage project will provide assurances that CO<sub>2</sub> has been injected and will be geological stored in an environmentally sound and safe manner. The stakeholders (industry, the financial community, regulators, the nearby communities, the public and civil society, and consumers) will require the confidence that the demonstration projects are effectively regulated to ensure the safety and security of CO<sub>2</sub> geological storage [8]. The government and operator need to be confident that the sites are behaving in a consistent and predictable manner and that the predicted behaviour of the site is acceptable. This will require a judgment that measurements and predictions of storage site behaviour (*e.g. pressure and temperature measurement in above/at the container domain*) are adequate and competent, and that the risk posed by the site is acceptable [9]. Within MMV activities, downhole monitoring technologies (*e.g. integrated observation well*) will provide direct and indirect measurements of the fate of geologically stored CO<sub>2</sub>. Approval of early full-scale geological storage projects is likely to stipulate a level of monitoring that goes beyond current practice. Identification of cost-effective technologies and methodologies will assist industry in moving forward with commercial scale projects while satisfying the desire for performance monitoring.

The University of Alberta, in partnership with Canadian and international organizations, has been studying geological storage of CO<sub>2</sub>, including operational, verification, and environmental monitoring concepts. Two field projects that relate directly to these issues are the Penn West Energy Trust CO<sub>2</sub>-EOR Pilot Project and EnerPlus CSEMP. Field studies like this will help to understand and assess the accuracy and reliability of downhole measurements.

## **1.2 Research objective**

Over the last decade, significant advances in downhole monitoring have been made mostly associated with the effort towards “intelligent wells” and fiber optic systems. While these technologies are sophisticated, their applications in geological storage projects are cost prohibitive. It is certain that for both value-added (*e.g.*, CO<sub>2</sub>-EOR) and non-value-added (*e.g.* saline aquifers) storage projects, monitoring to detect the subsurface fate of injection greenhouse gases will be a regulatory requirement. While

these regulations for CCS have not yet been formally adopted in Alberta or Canada, it is anticipated they will require installation of observation wells, which are not common in practice and not well understood. However, observation well integrity performance downhole is a major issue for long-term CCS storage sites.

The objective of this research program is to provide a fundamental understanding of the design and deployment of monitoring technologies used for measurement and verification in CO<sub>2</sub> geological storage projects. This research will cover both downhole and near surface monitoring technologies and focuses on hydromechanical issues surrounding design and deployment of geological monitoring technology for CO<sub>2</sub> storage projects.

### **1.3 Scope and methodology**

The scope of this research does not include economic assessment of technologies, nor does it involve large-scale engineering design. It will focus on design, deployment and assessment of performance and hydraulic integrity of downhole and near-surface monitoring technologies using two CO<sub>2</sub> geological storage pilot projects.

The research objective will be achieved by identifying a suite of technologies, development and field deployment of monitoring technologies data collection and numerical modelling. To achieve the research objective, the following research tasks will be undertaken:

1. Overview of downhole monitoring technologies for CO<sub>2</sub> geological storage, including design and deployment of two field projects;
2. Assessment of instrumentation performance, using two case histories; and
3. Analytical and numerical simulations post-assessment of installation efficiency, technique, and well hydraulic integrity.

### **1.4 Organization of Thesis**

The overview of monitoring geological CO<sub>2</sub> storage is presented in Chapter 2. It describes the systematic approach to planning monitoring programs, and lists the monitoring techniques identified for CO<sub>2</sub> geological storage applications.

Chapter 3 describes the two field monitoring projects: (1) Pembina Cardium CO<sub>2</sub> monitoring pilot, a CO<sub>2</sub>-EOR project; and (2) EnerPlus CSEMP, an enhanced coal bed methane project. The core of this research focuses on deep downhole monitoring technologies, which was case of the observation well installed at Pembina Cardium CO<sub>2</sub>

monitoring pilot. Also, this study includes a near-surface downhole reservoir monitoring technology that used a surface tiltmeter array to map the CO<sub>2</sub> and coal swelling, possible the first of its kind, at the CSEMP pilot project

Chapter 4 details the monitoring system design and deployment implemented in the two field projects. Following Chapter 4, Chapter 5 studies the performance of these monitoring systems.

Chapter 6 presents the results of analytical and numerical modelling of cement placement around the deep downhole monitoring sensor housing systems that was deployed in the observation well for the Pembina Cardium CO<sub>2</sub> monitoring pilot project.

Chapter 7 assesses the flow mechanics efficiency of new sensor housing geometries within a borehole during cement placement via computational fluid dynamics techniques.

Chapter 8 presents the conclusions and recommendations for future research

## **CHAPTER 2 Overview of Monitoring Geological CO<sub>2</sub> Storage**

### **2.1 Introduction**

MMV operations provide confidence that CO<sub>2</sub> has been injected and stored in an environmentally sound and safe manner. However, current subsurface monitoring technologies being deployed in CO<sub>2</sub> storage projects will not be capable of addressing all issues related to the long term permanence of CO<sub>2</sub> storage due to issues with scales of resolution (i.e. 3D seismic), spatial resolution (i.e. fluid pressure measured at a point versus reservoir pressure) and temporal resolution (i.e. short term operational measurements versus long term site closure measurements). Multiple integrated monitoring instrumentation systems are being deployed in CO<sub>2</sub> field demonstration research projects around the world and will provide experience that can be used in regulatory regimes for future commercial CO<sub>2</sub> sequestration scale projects. The intent of this section is to present main elements involved in monitoring a geological CO<sub>2</sub> storage project, including a systematic approach and monitoring time frames concept that was introduced by Chalaturnyk et al. [10]. The monitoring program combined with evaluation of the monitoring results form the key components of a monitored decision approach for verifying the integrity of the geological storage project. Monitoring in a geological CO<sub>2</sub> sequestration project is needed for a wide range of purposes, which define the type, frequency and duration of monitoring techniques. A monitoring program can be divided into three distinct classes [10]: 1) operational monitoring; 2) verification monitoring; and 3) environmental monitoring. In the planning of a monitoring program at a specific site for each of these classes, the project conditions must be defined, the mechanisms that control the fluid flow must be predicted, technical questions must be identified, the selection of monitoring systems and their location must be made, and the frequency of monitoring must be planned.

### **2.2 Systematic approach to planning monitoring programs**

Verification of CO<sub>2</sub> storage is critically important because the public must be assured (convinced) that the gases have been removed permanently from the atmosphere and that risks due to leakage are minimized and managed. Geological storage of CO<sub>2</sub> is an attractive option for Canada since a large percentage of the CO<sub>2</sub> emissions come from fixed-point sources such as power plants and petroleum processing facilities. If these

emissions are captured and delivered to a geological storage site, they will not be released into the atmosphere. However, merely injecting CO<sub>2</sub> into a reservoir does not guarantee that CO<sub>2</sub> emissions will stay there. The CO<sub>2</sub> may leak back to the surface or into valuable aquifers through a variety of mechanisms. Integrated seismic imaging and geochemical sampling and analysis programs are technologies that can document the motion of the injected CO<sub>2</sub> and detect leakage from the storage horizon [11].

To address these issues, monitoring of fluid/plume travel is considered at three levels, operational (i.e. in the reservoir), verification (i.e. surrounding the reservoir) and environmental (i.e. at shallow depths and the atmosphere). Figure 2.1 illustrates the progression from operational monitoring through to environmental monitoring [10, 11]:

1. Operation Monitoring – monitoring that is normally done as part of hydrocarbon recovery/storage operation and focuses on movement of fluid between wells for specific oil or gas reservoir. Measurements are made of pressure, temperatures flow rate and compositions at injection and production wells. To optimize operation, models are used to both predict and history match the measured flow rate, pressure, temperature and compositions;
2. Scientific or Verification Monitoring – measurements need to be made to track the migration of fluid or a plume in the reservoir or to determine if the plume is leaking out of the reservoir through the caprock into aquifers. This level of monitoring is not normally carried out, and would be instigated only for a high risk project or if interpretation of data collected during operational monitoring suggested unexpected flow behavior of the fluid in the reservoir; and
3. Environmental Monitoring – Additional monitoring aimed at safeguarding against health, safety and environment risks due to seepage of fluid from the reservoir into the potable water zone or the atmosphere. If verification monitoring was being done and a leak through the caprock was detected, then environmental monitoring should be done. This level of monitoring may be carried out, in the absence of any leakage monitoring through the caprock being undertaken to ensure containment integrity and no long term environmental effects are manifested.

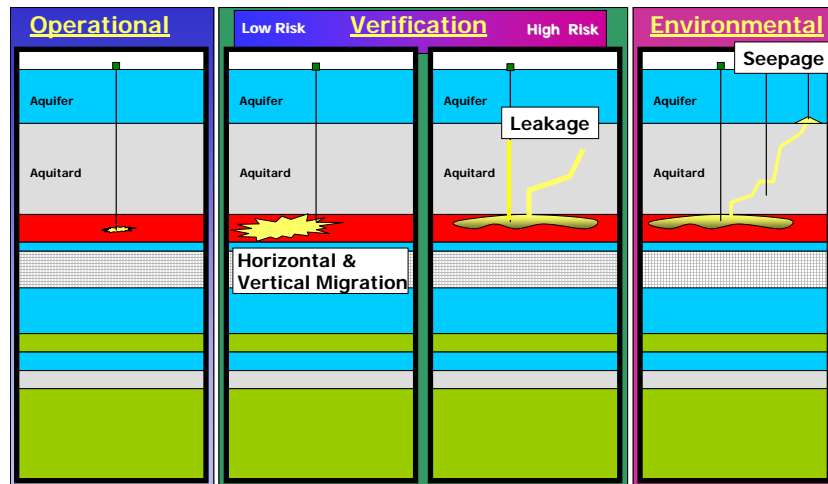


Figure 2.1 Operational, verification and environmental monitoring levels (after Chalaturnyk and Gunter[10])

### 2.3 Monitoring techniques

The 2005 report published by the IPCC summarizes a number of monitoring techniques for CO<sub>2</sub> geological storage. Much of the monitoring technology described below was developed for application in the oil and gas industry. As a result of various research and development projects associated with CCS projects, new technology has been developed specially for monitoring the fate of the sequestered CO<sub>2</sub>; although, much remains to be learned about monitoring of coal formations. Table 2.1 summarizes these techniques and can be divided into direct (engineering and geochemical) and indirect (geophysical and geodetic) methods. The engineering techniques are focused at the reservoir and the wells. Geochemical techniques can be applied in wells (e.g. at reservoir level) and the surface system. Seismic measurements are focused at the reservoir and overburden levels. Geodetic techniques monitor the surface system [2, 12].

There are a number of steps involved in designing a systematic approach to planning monitoring programs including: defining project conditions; predicting mechanisms that control behavior; addressing technical questions; selecting monitoring parameters and identifying their role in answering technical questions; determining the magnitude of expected change in parameters; selecting instrumentation and monitoring approaches/systems; selecting instrument or monitoring locations; and determining timeframes and depth for monitoring [10]. A combination of monitoring techniques can

be used in order to use the advantages of each method individually that consider spatial coverage, resolution and monitoring aspects.

## **2.4 Current limitations**

Many current field CO<sub>2</sub> geological storage projects have implemented MMV programs on a site-specific basis without long-term time frames of required monitoring of CO<sub>2</sub> permanence, which means in most cases, that MMV will cease upon completion of pilot/full scale project. This also has consequences on monitoring informing the assessment of long-term wellbore integrity, which is seen as one of the main issues for long-term performance for CCS storage sites [13]. Most CCS projects worldwide have successfully adopted standards and technologies from the oil and gas industry for storage well design. However the design of observation wells for long timeframes is not common and their long-term performance is not well understood. Consequently, additional fundamental studies on the design of downhole instrumentation deployment and their design for long-term measurements are required. Many of the direct monitoring techniques suggested by the IPCC, as described in Table 1, require downhole deployment technologies that are deployed in dedicated observation wells.

Table 2.1 Direct and indirect techniques that can be used to monitoring the fate of the sequestered CO<sub>2</sub> (After IPPC [1, 2]).

Measurement technique	Measurement parameters	Example applications
Introduced and natural tracers	Travel time, Partitioning of CO <sub>2</sub> into brine or oil and Identification sources of CO <sub>2</sub> .	Tracing movement of CO <sub>2</sub> in the storages formation , Quantifying solubility trapping and Tracing leakage.
Water composition	CO <sub>2</sub> , HCO <sub>3</sub> <sup>-</sup> , CO <sub>3</sub> <sup>2-</sup> , Major ions, Traces elements and Salinity.	Quantifying solubility and mineral trapping , Quantifying CO <sub>2</sub> - water-rock interactions and Detecting leakage into shallow groundwater aquifers.
Subsurface pressure	Formation pressure, Annulus pressure and Ground aquifer pressure.	Control of formulation pressure below fracture gradient , Wellbore and injection tubing condition and Leakage out of the storage formation.
Well logs	Brine salinity, Sonic velocity and CO <sub>2</sub> saturation.	Tracking CO <sub>2</sub> movement in and above storage formation, tracking migration of brine into shallow aquifers and Calibrating seismic velocities for 3D seismic surveys.
Time-lapse 3D seismic imaging	P and S wave velocity, Reflection horizons and Seismic amplitude attenuation.	Tracking CO <sub>2</sub> movement in and above storage formation.
Vertical seismic profiling and crosswell seismic imaging	P and S wave velocity, Reflection horizons and Seismic amplitude attenuation.	Detecting detailed distribution of CO <sub>2</sub> in the storage formation and detecting leakage through faults and fractures.
Passive seismic monitoring	Location, magnitude and source characteristics of seismic events.	Development of microfractures in formation or caprock and CO <sub>2</sub> migration pathways.
Electrical and electromagnetic techniques	Formation conductivity and Electromagnetic induction	Tracking movement of CO <sub>2</sub> in and above the storage formation and Detecting migration of brine into shallow aquifers
Time-lapse gravity measurements	Density changes caused by fluid displacement	Detect CO <sub>2</sub> movement in or above storage formation and CO <sub>2</sub> mass balance in the subsurface
Land surface deformation	Tilt, Vertical and horizontal displacement using interferometry and GPS	Detect geomechanical effects on storage formation and caprock and Located CO <sub>2</sub> migration pathways
Visible and infrared imaging from satellite or planes	Hyperspectral imaging of land surface	Detect vegetative stress
CO <sub>2</sub> land surface flux monitoring using flux chamber or eddy covariance	CO <sub>2</sub> fluxes between the land surface and atmosphere	Detect, locate and quantify CO <sub>2</sub> releases
Soil gas sampling	Soil gas composition Isotopic analysis of CO <sub>2</sub>	Detect elevated levels of CO <sub>2</sub> , Identify source of elevated soil gas CO <sub>2</sub> and Evaluate ecosystem impacts.

## **CHAPTER 3 Project Descriptions**

### **3.1 Introduction**

Early carbon storage research and development efforts in Canada and elsewhere began with “value-added” projects such as CO<sub>2</sub>-enhanced oil recovery (EOR), where the increase in production helps to offset the costs of CO<sub>2</sub> and of its potential long-term storage. These projects provide a valuable opportunity to assess appropriate measurement, monitoring, and verification (MMV) protocols for the geological storage component of carbon capture and geological storage (CCS) technologies [14].

The Province of Alberta, Canada, is committed to developing its oil and gas resources situated in the Alberta Sedimentary Basin in a responsible manner to minimize impacts on the environment. One of Alberta’s major platforms for reducing CO<sub>2</sub> emissions from large point-source final emitters is CCS. In order to accelerate the uptake of this option, industry incentives have been put in place. Early examples of these incentive programs include: a request by the Alberta Energy Research Institute (AERI) that a monitoring program be established in conjunction with the Pembina Cardium CO<sub>2</sub> Monitoring Pilot that had been approved to receive a CO<sub>2</sub> royalty credit; and a CO<sub>2</sub> enhanced coal-bed methane pilot project that was initiated by an industry/government consortium in the Pembina Field of Alberta to test the CO<sub>2</sub> storage and enhanced methane production (CSEMP) in the Cretaceous aged Ardley Coal Zone.

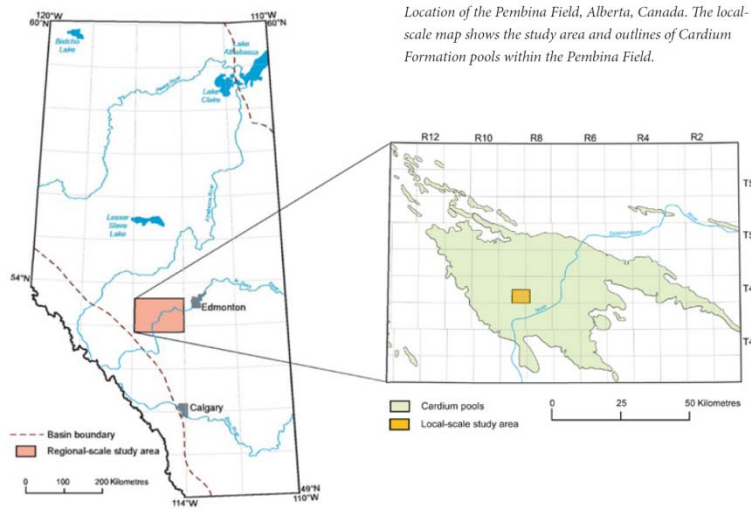
### **3.2 Pembina Cardium CO<sub>2</sub> monitoring pilot, a CO<sub>2</sub>-EOR project**

The CO<sub>2</sub>-EOR pilot project, located in the Pembina Field’s Cardium Formation (Figure 3.1), operated between March 2005 and May 2008. During this period, approximately 66,000 tonnes of CO<sub>2</sub> was injected at rates varying from 35 to 100 tonnes/day. Over the first two years of the project, total CO<sub>2</sub> injection as a percentage of pilot area pore volume reached 18 % [15].

The Pembina oil field covers an area of about 140,000 km<sup>2</sup> (140 townships) and is composed of several producing zones ranging from Devonian to Tertiary aged formations. The four reservoir units comprising the Cardium Formation reach a maximum cumulative thickness of about 20 m and occur at depths ranging from 1,600 m in the northeast to 1,650 m in the southwest of the pilot site area. At the injection site, each of the sandstone units is 3 m thick. The thicknesses of the intervening shale units are

1 m (between the upper and middle sandstone units) and 5 m (between the middle and lower sandstones). Average core porosity and permeability range from 8% and 31 md in the conglomerate to 16 % and 21 md in the middle and upper sandstone units, respectively. As well, permeability may exceed one Darcy in individual beds of the conglomerate. Average permeability in the lower sandstone is 10 md, half that of the upper and middle sandstone units. The reservoir temperature is 50°C, and average reservoir pressure after secondary water flood recovery was approximately 19 MPa. The EOR pilot consisted of two CO<sub>2</sub> injectors and six producers, completed in all four units [16, 17].

This CO<sub>2</sub> storage and monitoring project developed with the CO<sub>2</sub>-EOR pilot focused on two areas. The first area involved mapping and assessing the condition of the existing wells, and assessing geology and hydrogeology at the regional, local, and site scales with a view to defining potential leakage paths and the CO<sub>2</sub> storage capacity of the reservoir [16]. The second area monitored the movement of CO<sub>2</sub> in the reservoir and surrounding overburden formations using seismic, pressure, temperature, and produced fluid signatures both at and above the reservoir.



Well distribution and well types in the study area.

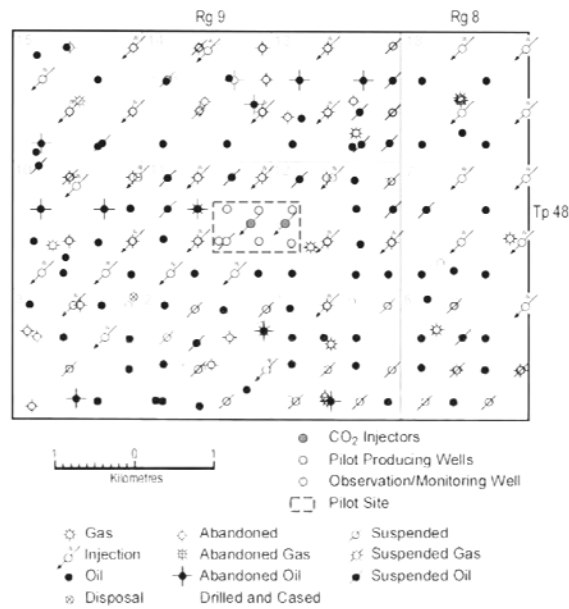


Figure 3.1 Location of the pilot site within the Pembina Field, Alberta, Canada [18].

### **3.3 CO<sub>2</sub> Storage/enhanced methane production (CSEMP) monitoring pilot project**

The CO<sub>2</sub> Storage and Enhanced Methane Production (CSEMP) micro-pilot/pilot project involved the injection of CO<sub>2</sub> into a coal formation located at a depth of approximately 400 m in the Silkstone and Mynheer members of the Ardley coal in the Western Canadian Sedimentary Basin, Pembina area, southwest of Edmonton, Alberta, Canada (Figure 3.2). The Ardley coal occurs in the Scollard Formation and is overlain by the thick fluvial sandstones of the Tertiary Paskapoo Formation. At this site, the coal is over 8 m thick, high volatile B bituminous in rank, and has a permeability between 1 and 5 mD. The primary purpose of the micro-pilot/pilot was to demonstrate that CO<sub>2</sub> storage in Ardley coals is viable as a greenhouse gas reduction mechanism, and that an additional benefit is enhanced production of methane [19]. This has already been demonstrated by the Alberta Research Council in micro-pilots at Fenn-Big Valley, Alberta, in Mannville coals [20] and in the Qinshui Basin, China, [21] in Shanxi coals which has led to a set of recommended practices for field testing for enhanced coal-bed methane [22-24].

In parallel, the CSEMP project had a comprehensive reservoir surveillance program consisting of environmental monitoring, verification monitoring and operational monitoring components [10]. For environmental monitoring, three shallow (100 meter deep) water wells were drilled in a triangle formation around the CO<sub>2</sub> injector (monitoring pressure and compositional changes), and atmospheric ground laser surveys are done periodically (to monitor methane and CO<sub>2</sub> anomalies). In verification monitoring, seismic surveys (both vertical seismic profile, 2D and 3D [25]) were conducted over time, continuous tiltmeter data were collected, and pressure and temperature data were recorded in the water sands above the coal at two depths. In operational monitoring, flowrates, gas composition, pressures and temperatures were continuously monitored downhole and in the coal during injection, soak and production in and from the Ardley coal.

The research undertaken in this thesis examines the application of tiltmeters, an indirect monitoring technique, including interpretation of the recorded data, and its validation for the CSEMP pilot project during the hydraulic fracturing and CO<sub>2</sub> injection events.

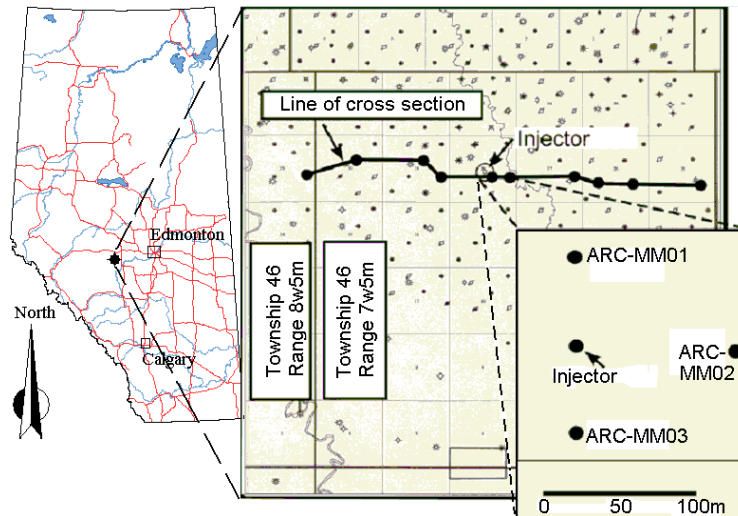


Figure 3.2 Location of injector and shallow monitoring well (MM), and geological cross-section within the project [26].

### 3.3.1 CSEMP Operational Summary

The CSEMP micro-pilot test program consisted of initial drilling and completion of the EnerPlus injection well 102/7-28-46-7 W5Mer in the South Buck Lake area of Alberta (Figure 3.2). Following completion, the following operations were conducted: short water injection/fall-off test, coal seam fracture stimulation, ten day production/build-up test, short-term Phase I CO<sub>2</sub> (180 tonnes) micro-pilot injection/fall-off test followed by a two week production/build-up test, N<sub>2</sub> (24,000 m<sup>3</sup>) tracer test, and medium-term Phase II CO<sub>2</sub> (854 tonnes) pilot injection/fall-off test. It was felt that the tiltmeters would respond to deformation caused by the short-term fracturing event and to the long-term CO<sub>2</sub> injection period. Table 3.1 presents the main seven events that occurred at the injection well of the CSEMP pilot. The detailed operational summary is found in Mavor and Faltinson [27].

Table 3.1 Operational injection and production events in CSEMP injection well

<b>Event</b>	<b>Date</b>
Water injection	May 2006
Fracture job	June 5, 2006
Primary production	June 24 to July 5, 2006
CO <sub>2</sub> injection pulse	August 29, 2006
Micro-pilot CO <sub>2</sub> injection – Phase I	September 8 to 12, 2006
CO <sub>2</sub> production	March, 2007
Pilot N <sub>2</sub> tracer	June 25, 2007
Pilot CO <sub>2</sub> injection- Phase II	June 28 to July 20, 2007

## **CHAPTER 4 Monitoring System Design and Deployment**

### **4.1 Introduction**

As an element of the monitoring program for CO<sub>2</sub> geological storage, this section details the design, deployment and early history of two case studies: (1) the highly instrumented observation well (OW) installed as part of the Pembina Cardium CO<sub>2</sub> monitoring pilot, a CO<sub>2</sub>-EOR project; and (2) the application of a surface tiltmeter array to the CSEMP pilot.

The core of this research focuses on the Pembina Cardium case study that involved deployment of downhole monitoring technologies in an observation well, which was used for monitoring and verification of CO<sub>2</sub> movement in the subsurface. Similarly, the CSEMP case study presents the application of near-surface monitoring technology, and is limited to discussing the advantages and limitations of the surface tiltmeter array on CO<sub>2</sub> geological storage applications.

### **4.2 Integrated instrumentation system in a observation well**

The multidisciplinary Pembina Cardium CO<sub>2</sub> monitoring pilot, a CO<sub>2</sub>-EOR project, included geological characterization, geochemical fluid sampling, geophysical monitoring, reservoir monitoring, reservoir simulations of CO<sub>2</sub> movement and shallow subsurface and atmospheric monitoring programs [3]. As part of this program, Penn West Energy Trust provided an existing wellbore, located 35 m away from a newly drilled production well within the CO<sub>2</sub>-EOR pilot area, to be used as a dedicated vertical observation well (OW) and to assess existing technologies for deploying downhole monitoring instrumentation. The well (100/07-11-048-09 W5M) was instrumented with downhole pressure and temperature sensors, geophones, and fluid sampling devices. Figure 4.1 shows the location of the OW relative to the location of the injection and production wells. The wellbore has allowed direct monitoring and measurements of many parameters and properties at the reservoir level utilizing geophysical, geochemical, and geomechanical instrumentation. As well as the opportunity to carry out wellbore integrity studies under "in-situ" conditions[14].

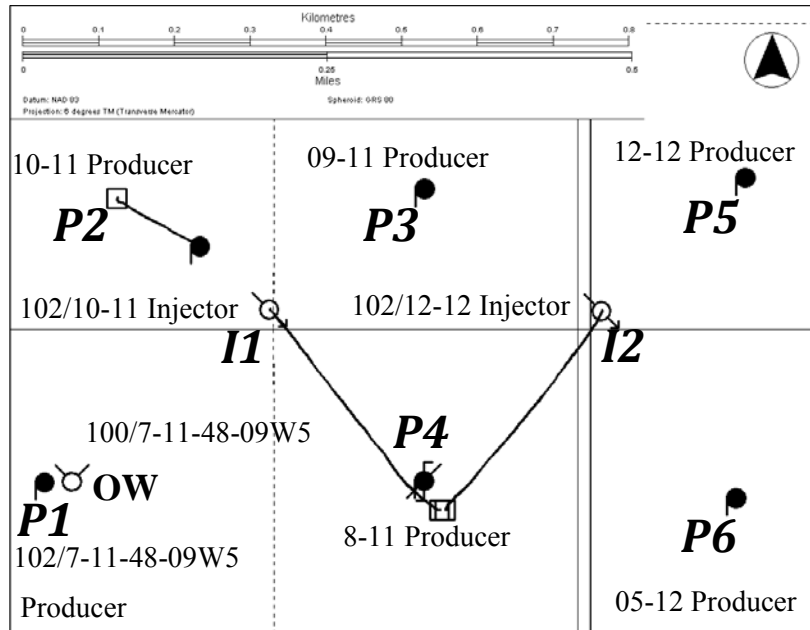
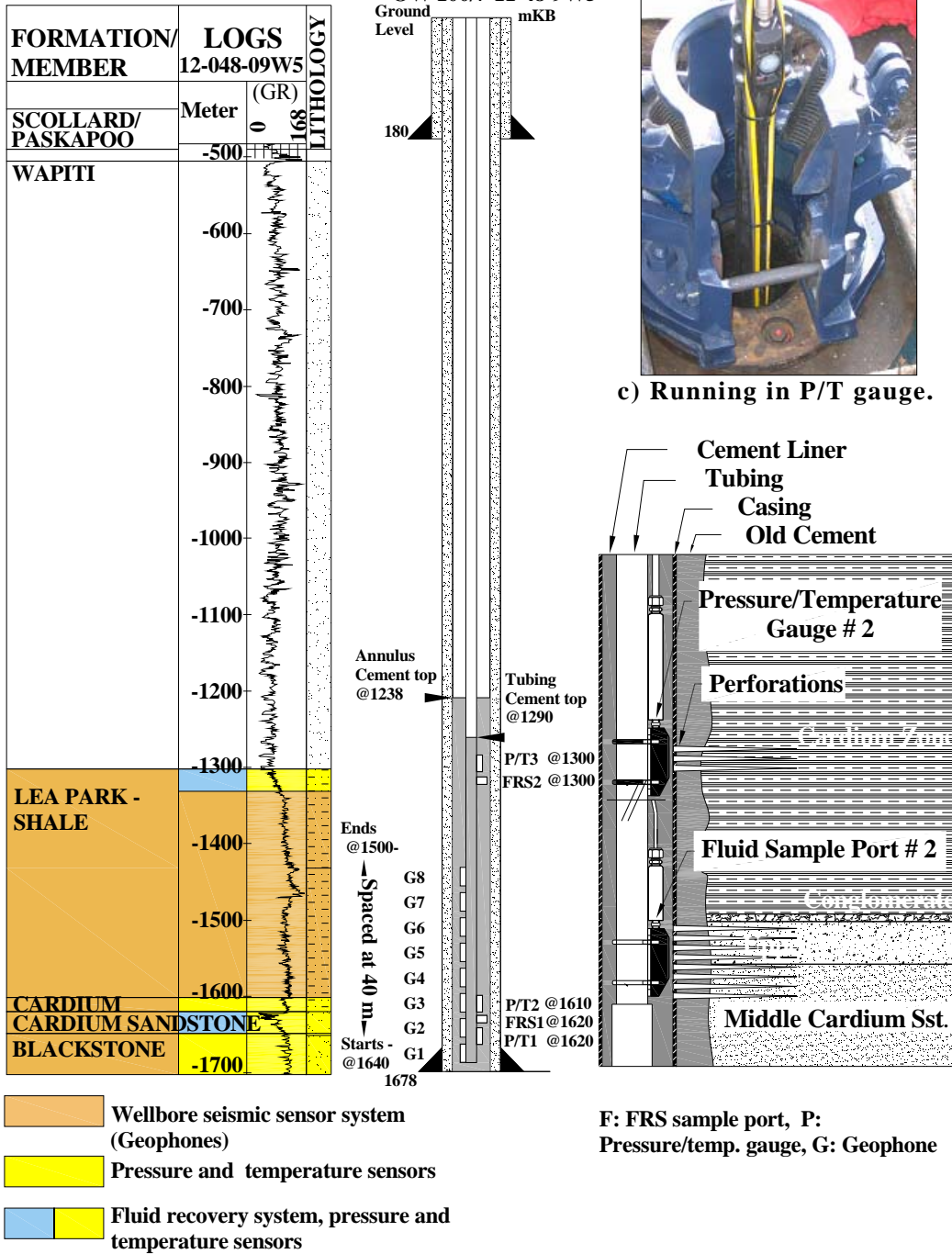


Figure 4.1 Location of the monitoring well 100/07-11-048-09 W5M [3].

#### 4.2.1 Observation well design

The instrumentation was attached to the production tubing (60.3 mm in diameter) and was installed inside production casing (139.7 mm in diameter). One primary sensor and one redundant vibrating wire pressure/temperature (P/T) sensor were installed at each of three depths 1620 m, 1610 m and 1301 m, for a total of six P/T sensors. Fluid recovery sampling ports were installed at depths of 1622 m and 1301 m. Eight geophones were installed at depths of 1640 m, 1,620 m, 1600 m, 1580 m, 1560 m, 1540 m, 1520 m, and 1500 m. The instrumentation was then tested and cemented in place for the life of the project. Figure 4.2 illustrates the completion geometry of the observation well in relation to the geological formations within the pilot area. The installation depths of the P/T sensors and the fluid recovery sampling ports match the pre-existing perforation depths of the production casing. These jet spiral perforations were completed in 1972, 1975 and 2005 with density values of 13 shots/m and 17 shots/m for the Cardium Formation and Lea Park Formation, respectively. The jet spiral shots were perforated every 60 degrees, penetrating 10 cm deep through the casing, cement and formation. The density, distribution and penetration range of these perforations permitted a hydraulic connection between the P/T sensors or fluid sample port and the formations.

Completion Configuration for  
OW 100/7-11-48-9W5



a) Wellbore log and completion configuration. b) Configuration details.

Figure 4.2 Schematic of well instrumentation configuration and geology [14].

Given the small annular clearance, special attention had to be paid to the protection of each element of the instrumentation package to ensure the successful deployment of the instrument string. Consequently, detailed protocols were used for installation, and strict quality assurance and quality control (QA/QC) were implemented for the processes and tools [28].

#### **4.2.2 Methodology**

The design of instrumentation configurations for observation wells can be complex, with as many as five factors to consider in the design: (1) selection of instrument type; (2) selection of monitoring locations; (3) annular geometry; (4) deployment of instruments; and (5) cementing operations. In addition, care and attention are required during the installation of the instrumentation systems due to the high risk of damage to sensors, cables, or tubing. This section presents the first four design variables of the downhole equipment and the OW at the Penn West project. The description of the cementing operations is presented in Chapter 5 followed by the methodology used for the post-cement interpretation that is presented in Chapter 6.

##### **4.2.2.1 Downhole Equipment**

For the anticipated measurement, monitoring, and verification program timeframes in CCS projects, observation wells must be designed to provide reliable data over timeframes of decades [1]. Five main factors were considered in design and installation to meet these criteria. The first was the selection of reliable sensors, recognizing that a small percentage of sensors may fail prematurely due to manufacturing defects. The second was the successful deployment of the instrumentation string into the borehole. In this case study, instrumentation was attached to production tubing and by running inside production casing, helped to reduce installation damage. In some instances, instrumentation is placed on the exterior of the casing and deployed in open borehole which introduces additional challenges related to well trajectory, drilling history, well conditions, and mud type that must be considered to reduce the risk of damage during installation. The third factor for consideration in this project was damage from abrasion or impact against the inner diameter (ID) of the casing while the instrumentation string was being lowered into the well, which increased the risk of sensor or cable damage. For instrumentation systems that run on tubing inside cased wells, additional challenges may arise due to limited annular clearances, increasing with the number of sensors and the

number of cables run to the surface. The fourth factor relates to pre-installation assembly activities, transportation to site, and on-site work, where appropriate workflows are necessary to avoid sensor and cable damage before the instrumentation system enters the well. Installation logistics around the well service rig become important when managing several cables that must converge at the same location on the rig floor. As a result, the installation process must be carefully controlled. With the considerations mentioned above, the basic design variables for the OW at the Penn West project are provided in Table 4.1. The fifth factor relates to planning and execution of the cementing operation, where the rheological properties of the circulated fluids and the control of the pumping and circulation rates are important to encased and sealed the downhole instrumentation.

*Table 4.1 Observation well basic design variables [14].*

Design Variable	Value
No. of pressure/temperature measurement locations	3
No. of geophones	8
No. of downhole fluid sampling locations	2
Depth of well	1648 m (5406 ft)
Production casing:	OD: 139.7 mm (5.5 in.) ID: 124.3 mm (4.89 in.) Weight: 25.3 kg/m (17 lb/ft)
Production tubing:	OD: 60.3 mm (2.375 in.) ID: 50.7 mm (1.99 in.) Weight: 7.0 kg/m (4.7 lb/ft)
Well deviation	Vertical
Initial bottomhole pressure measure on May 8, 2003	Approximately 18 MPa
Initial bottomhole temperature	Approximately 50 Celsius
Well type:	Sweet (no H <sub>2</sub> S)

#### **4.2.2.2 High Sensitivity Geophones**

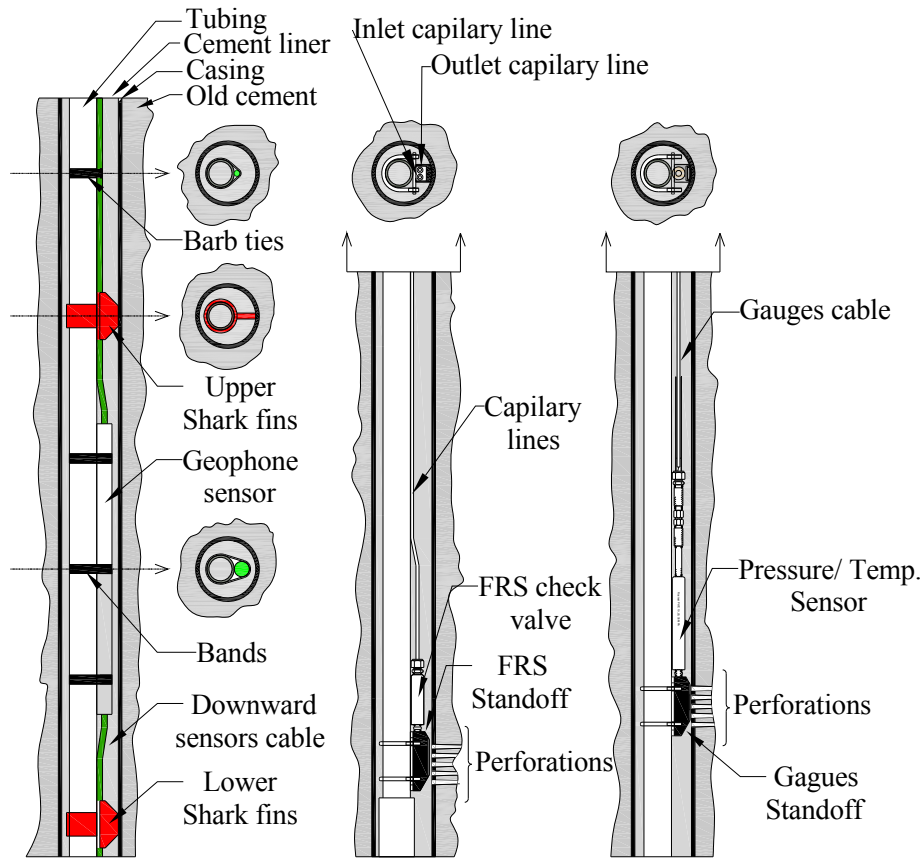
Three-component geophone assemblies (x, y, and z) fabricated from 316 ELC stainless steel were used to collect passive seismic data as well as collect vertical seismic profiling (VSP) data during surface seismic surveys. Results from the VSP surveys was analyzed by Coueslan [29] Each assembly had six moving coil geophones per axial component, with a sensitivity of  $69.69 \pm 1.0$  V/m/s, a natural frequency of 24 Hz, and a spurious frequency of more than 310 Hz. The proposed configuration had two sets of four inline geophone sensors. Figure 4.3(a) illustrates a single geophone sensor attached to the tubing string. Each geophone manufactured by Weir-Jones Group was enclosed within a cylindrical stainless steel housing of 31 mm (1.22 in.) in diameter and 0.8 m (31.5 in.) in length that was sealed to withstand wellbore fluid pressure up to 30 MPa (4350 psi) and

operating temperatures from -45 °C to 100 °C. A maximum of four geophone housings could be linked together on a single, 24-conductor (12 pair) 28 awg stranded copper electrical cable (three pairs per geophone). The cables were jacketed for safety with yellow urethane and one overall aluminized mylar shield.

Aside from the tubing in which the geophone was housed, there was mechanical protection from shock-loads and abrasion. Also, the diameter of the geophone was larger than the annular clearance between the tubing and casing; therefore, an additional form of mechanical protection was required. As shown in Figure 4.3(a), ‘shark fins’ were clamped to the tubing string on either side of every geophone and effectively pushed the tubing away from the inside of the casing and thus generated sufficient clearance for the sensor.

#### ***4.2.2.3 Pressure/Temperature Sensors***

A single gauge carrier system was used for discrete point pressure and temperature measurements. Since the assembly would be permanently cemented in-place, the sensor selected for this application was a vibrating wire piezometer manufactured by RocTest, due to its robustness, lack of integrated circuits, and excellent long-term stability [30] (Figure 4.3(b)). This system consists of a vibrating wire-sensing element enclosed in a protective carrier that clamps rigidly to the tubing string, with the downhole inlet located against the ID of the casing. The electrical cable associated with the sensors consists of two twisted shielded pairs protected by a polyethylene jacket. The gauges have a maximum absolute working pressure of 35 MPa (5,070 psi) with an accuracy of  $\pm 0.5$  % full scale (F.S.) and an operating temperature range from -40°C to 65°C with thermal drift of  $\pm 0.1$  % F.S./°C. During deployment, the carrier provides mechanical protection by pushing the tubing off center.



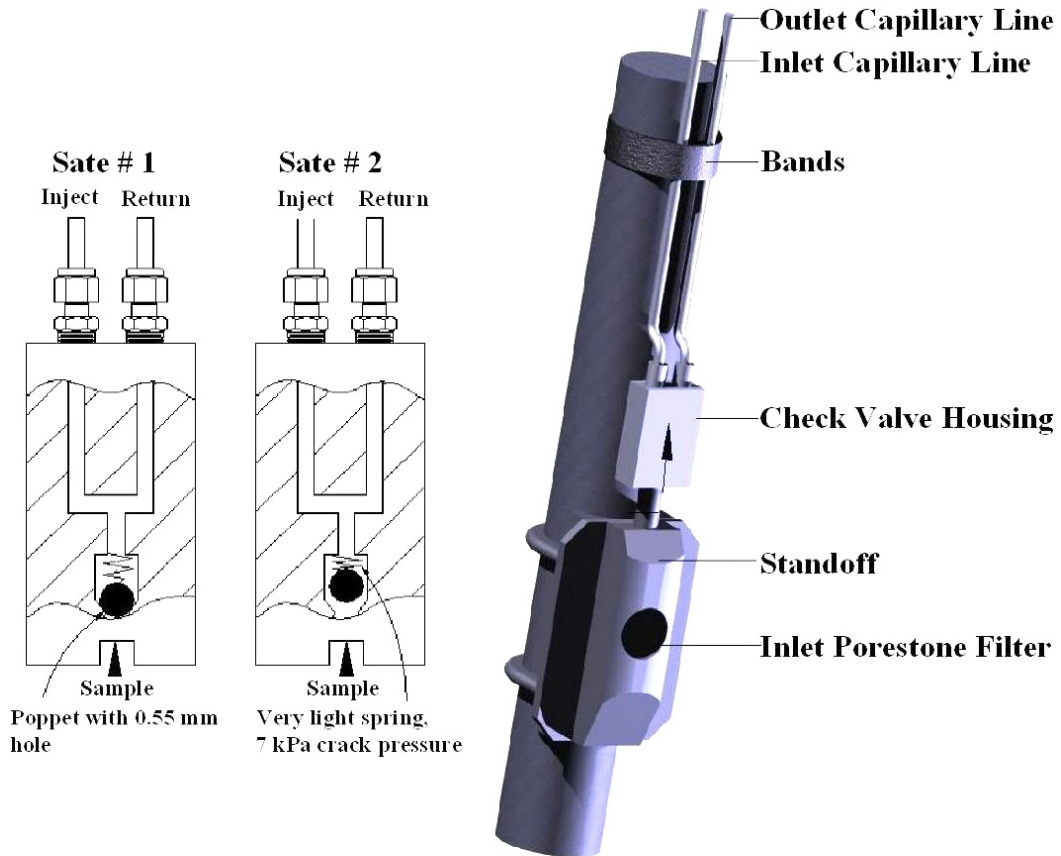
a) Geophone sensor with shark fins      b) Pressure/temperature sensor housing      c) Fluid recovery device

Figure 4.3 Installation schematic of sensor within the borehole [14].

#### 4.2.2.4 Fluid recovery system

The fluid recovery system (FRS), developed at the University of Alberta, is a downhole device specially designed to allow reservoir fluids to be sampled and brought to the surface under "in-situ" conditions within permanent or fully cemented observation wells. FRS uses a configuration that incorporates a shuttle valve located at the sampling interval. Each sampling valve is connected to the surface by two stainless steel tubing lines (6.35 mm in diameter) that are connected to a fluid recovery control panel.

The FRS housing is very similar in size and shape to the pressure sensor carrier (Figure 4.3 (c)) and can be clamped anywhere along the tubing string. The FRS housing was installed as close to the casing perforations as possible to enhance hydraulic communication with the reservoir. Figure 4.4(a) illustrates the hydraulic operation of the valve. The details of its operation and configuration are presented in Chapter 5.



**a) Hydraulic schematic of the FRS check valve**

**b) Configuration of FRS Port**

*Figure 4.4 Installation schematic of fluid recovery system [14].*

### 4.2.3 Installation logs

The following section provides a summarized account of events prior to and during the deployment and completion of the OW to provide the reader with a sense of the activities that are undertaken when designing and installing a dedicated observation well.



*Figure 4.5 Top Left: Spool and instrumentation prepared for transport to well site. Top Right: Unloading and assembling the spools and cable for instrumentation. Bottom Left: All instrumentation and spools ready for running the cables over the sheaves. Bottom Right: View of the cables passing over the sheaves during night-time [17].*

#### 4.2.3.1.1 February 22, 2005

06:00 - Arrive at the University of Alberta to load vehicles. Pressure sensors and geophones are loaded onto a one-ton truck and secured to deck.

08:00 - Ironhorse Pumpjack Services Ltd. arrives at the University of Alberta to load the spools containing stainless steel tubing, centralizers and A-frames for spools.

12:00 - Arrive at the well site, unload the spools, and set up for installation the next day (see Figure 4.5).

After geophone spools were set up, the management of these sensors was turned over to the University of Calgary to check their operation and to prepare for monitoring during installation. All sensors were functioning properly at this time. It was noticed that the heat-shrink tubing installed on the cable end of one sensor was cracked. No repair was attempted at this time.

17:00 - After securing the tools and equipment, left the well site and returned to Edmonton.

#### 4.2.3.1.2 February 23, 2005

07:00 - Arrive on site to complete a walk-around on lease and begin set up for installation. Sheaves were attached to rails near monkey boards. Magnum wireline unit on site to confirm the plug back total depth at 1647.9 meters below Kelly Bushing (m KB).

13:00 - Start running in. First geophone installed at 5.77 m above end (1640 m KB). The targeted depth for each sensor is presented in Table 4.2.

*Table 4.2 Physical positioning of the sensors in the tubing string.*

Sensor Description	Targeted Depth (m KB)	Attached to joint No.	Distance from Bottom of Joint (m)
Geophone No. 1	1640	1	5.77
PT No. 5146	1623	3	3.36
FRS No. 2	1622	3	4.36
PT No. 5147	1621	3	5.36
Geophone No. 2	1620	3	6.36
PT No. 5148	1611	4	5.65
PT No. 5149	1610	4	6.65
Geophone No. 3	1600	5	6.96
Geophone No. 4	1580	7	3.35
Geophone No. 5	1560	9	4.37
Geophone No. 6	1540	11	5.32
Geophone No. 7	1520	13	6.25
Geophone No 8	1500	15	4.16
PT No. 5150	1302	36	3.25
FRS No. 1	1301	36	4.25
PT No 5151	1300	36	5.25
PT = Pressure-temperature sensor		FRS = Fluid recovery system	

Shark fins (see Figure 4.6) were installed above and below each geophone, as well as mid-joint for every joint that did not have a centralizer attached. Cable protectors were used on couplings.



Figure 4.6 Left: Shark fin protector attached to tubing. Right: View of spools from rig floor.

Used centralizers on every collar after the 17<sup>th</sup> joint, then switched back to cable protectors on Joint No. 36. Installed last sensor at 1301 m KB. From Joint No. 37 onward, centralizers were used on each collar.

20:00 - Crew change. The night crew ran in 51 joints without problems. An error was found in tally tag depth: 1644.28 m KB; it should have been 1653.4 m KB. Corrections were made. FEP tape was used to repair the cracked heat-shrink tubing on one of the sensor ends. Rubber mastic tape was wrapped around the FEP to provide a second layer of sealing.

#### 4.2.3.1.3 February 24, 2005

08:00 - Day crew comes on duty. Continued running in tubing. Day crew installed 41 joints for a total of 92 joints. Tubing was losing weight due to friction from centralizers; the weight dropped to 3500 daN running in and 9000 daN pulling up.

20:00 - Crew change. Continued running in tubing. Concern with the centralizers is alleviated due to increasing string weight. Night crew runs in 55 joints for a total of 147 joints.

#### 4.2.3.1.4 February 25, 2005

08:00 - Day crew came on with only 24 joints left to run. Continued running in tubing. Installed three pup joints below Joint No. 172 (at 2.45 m, 2.46 m and 1.22 m). Ran in 2.5 m pup joint and land collar at same depth as tubing mandrel (commonly referred to as tubing hanger or a dognut). Cable integrity checked, and the measurements were normal.

14:30 - Ultraline wireline unit logged at 1300 m KB – 1302 m KB. Good correlation. Marker pup picked up at 1294.7 m. Therefore, fluid sample port was landed at 1302 m KB. The log showed bottom at 1641.6 m KB. Sensors locations were according to the installation program.

16:30 - Pull up on tubing and remove landing pup. Installed dognut, string cables and stainless steel tubing through holes. Lowered string down and landed dognut. The new dognut landed 5 cm higher than the old one.

19:30 – Begin overnight well monitoring.

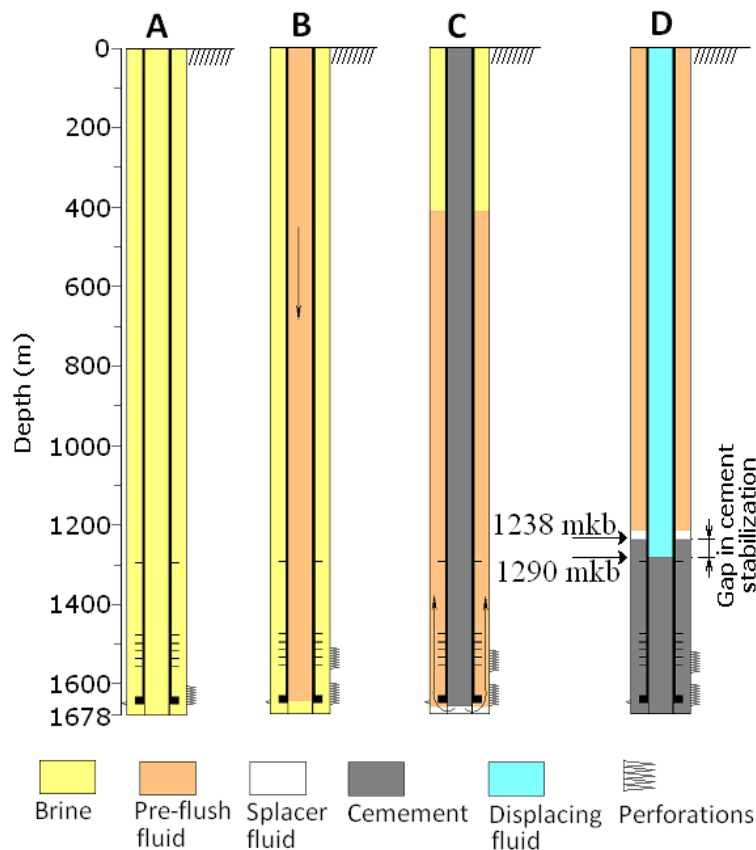


Figure 4.7 Steps for cementing the observation well. A. Borehole with instruments in place. B. Circulation of pre-wash fluid. C. Circulation of cement. D. End of cement circulation.

#### 4.2.3.1.5 February 26, 2005

08:00 - Crew on site to hook up the data logger to pressure sensors.

11:00 - Start pumping inhibited water followed by cement slurry. The steps for cementing the OW are shown in Figure 4.7.

12:06 – Cementing completed. Fluid started flowing after completion of cementing job reaching 10 litres per minute at approximately 13:00. After two hours, the flow decreased to 7 litres per minute. At this time, the annular blowout preventer was shut in. Bag pressure was increased to 9,000 kPa to stop flow. Flow slows to 1 litre per minute. Pressure built up to 1,000 kPa. Pressure sensors increase pressure equal to well pressure, indicating communication between all of sensors. With bag closed, all sensors continue to function properly.

18:30 - Rig crew is released. Annular leakage slows to 0.5 litres per minute. Pressure increases to 1,550 kPa.

#### 4.2.3.1.6 February 27, 2005

08:30 - Arrived on site, packed equipment, and set up the data logger to take readings every 5 minutes.

12:00 – Returned to Edmonton.

#### 4.2.3.1.7 March 1, 2005

08:30 - Annular blowout preventer was opened and raised up. Then, a wellhead was installed (Figure 4.8 and Figure 4.9). All cables were pulled through and laid out on lease. Instrumentation was checked: four pressure sensors had failed. Several sensors on geophone cable 1 showed shorts to shield. Review of the logged data showed that these sensors stopped working at approximately 20:30 on February 28, 2005. Discussions with the rig crew confirmed that this was during the time when brine was pumped and circulated into the well (a hole was punched in the tubing at roughly 18:30 that same evening). The “uphole” tubing pressure during circulation was believed to have reached approximately 10 MPa.

Cables were cleaned and pulled through the spool, wellhead and bonnet along with stainless steel tubing. Roughly 8 feet of cable was pushed back into the spool. The stainless steel tubing feed-throughs were tightened down. Cables were pulled through another feed-through.

16:00 - Epoxy was mixed, applied, and heated. Packed equipment and waited on site for epoxy to cure.

24:00 - Heater was dismantled and feed-through was completed.

4.2.3.1.8 March 2, 2005

16:00 - Left site and returned to Edmonton.



Figure 4.8 Cables passing through the dognut after removal of the blowout preventer (blue).

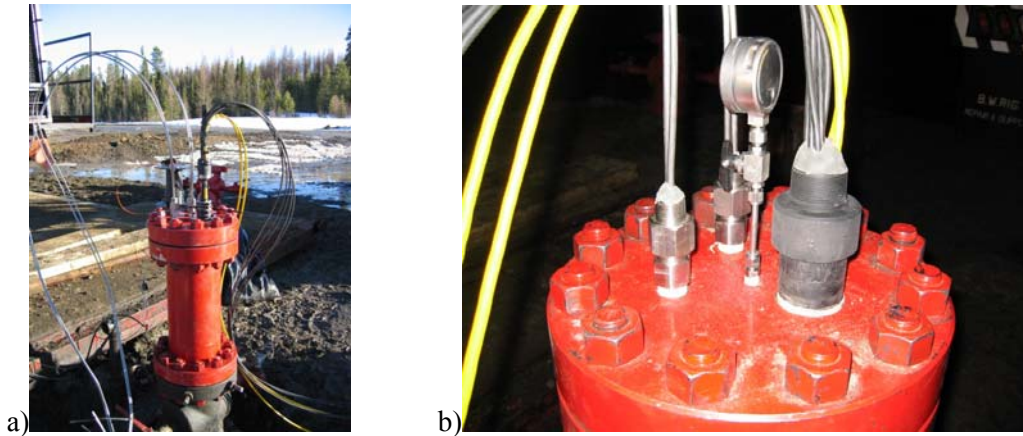


Figure 4.9 Installation of the wellhead(a) and the completed cable/tubing feed-throughs at the wellhead(b).

#### 4.2.4 Conclusions

The deployment of the instrumentation in the monitoring well was successful, although the cement job failed with constant leakage of reservoir fluid occurring afterwards. A post-failure assessment that examines the causes of this failure are presented in Chapter 5. The problem was solved by perforating the tubing and injecting a dense brine. However, during this process four pressure sensors and two temperature sensors were

lost. Serendipitously, the cementing failure has led to valuable lessons for robust designs for observation wells and has led to development of a patent pending design.

### **4.3 Application of surface tiltmeter array to CSEMP pilot**

A surface tiltmeter array is an indirect measurement technique used for fracture mapping (short term) and reservoir monitoring systems on waterflood/steamflood/EOR processes (long term). The primary functions of these arrays are to quickly detect out-of-zone fracture growth at the injection wells before the mechanical integrity of wellbores may be compromised. In addition to monitoring fracture growth, tiltmeter arrays are ideally suited for the long-term measurement of subsidence or dilation caused by production or injection activities for oil and gas applications. The long-term application of the surface tiltmeter array in the CSEMP project focused on the long-term deformation caused by the increase in pore pressure and swelling of the coal as a result of CO<sub>2</sub> injection. There are many case studies that report on the use of surface tiltmeter arrays on long-term production scenarios for the oil and gas sector, where the expected surface deformations are on the order of centimeters. Because part of the CSEMP pilot was an application of CO<sub>2</sub> geological storage, the injection pressure cannot fracture the containment, and the expected surface deformations were on the order of a millimeter.

The IPCC [1] listed tiltmeters as an indirect technique that can be used to monitor CO<sub>2</sub> storage projects. At the time of the CSEMP project, there were no peer-reviewed publications of case studies that deployed tiltmeters for monitoring CO<sub>2</sub> migration, CSEMP presented an opportunity to understand how the surface tiltmeter array are normally designed and deployed, and the advantages and limitations when using tiltmeters in a CCS pilot project.

#### **4.3.1 Deployment of surface tiltmeters**

A comprehensive tiltmeter monitoring program was carried out in CSEMP. Sixteen tiltmeters manufactured by Pinnacle were deployed in January 2006 at the site. Data was collected manually with software called Tilt Talk and provided by Pinnacle. The baseline data were downloaded the day before the fracture treatment and after the fracture treatment. Monthly field trips were scheduled to collect data for interpretation.

#### **4.3.1.1 Tilt-sites**

The tilt-site consists of a surface tiltmeters with 15 m cables, 5 W solar panels and rechargeable batteries (Figure 4.10(a)). The sensing element at the core of each tiltmeter is a pair of orthogonal bubble levels, in which electrodes detect movements of the air bubble within a conductive fluid as the fluid seeks the lowest spot in the sensor. It can resolve tilt to as little as one billionth of a radian (500 nano degrees).

The surface of the Earth naturally moves miniscule amounts every day due to thermal fluctuations (heating and cooling of the earth), solid earth tides (due to the Earth's rotation with respect to the sun and moon, similar to ocean tides), and cultural noise – any surface movement that causes the ground to deform (traffic, cattle, storage tanks, pump units, flow lines, etc.) Therefore, surface tiltmeters are deployed below the surface to avoid the “noise” due to thermal fluctuations and cultural noise on the surface. Each surface tool was installed at a depth of 6 m (Figure 4.10 (b) and (c)). The standard operation procedures for surface tiltmeter site drilling and abandonment implemented on CSEMP are presented in Appendix A.

The surface tiltmeter tools are installed in an array on the ground surface, as illustrated in Figure 4.10(d). The number of tools in an array depends on the depth of the fracture and surface considerations. The array usually consists of between 12 to 40 surface sites/tools. Pinnacle designs long-term monitoring arrays for the oil and gas industry with radii of 75% - 150% of injection depth plus the expected horizontal extent of fluid invasion. The tilt signal from each surface tool is used to form a tilt deformation pattern resulting from a hydraulic fracture or CO<sub>2</sub> injection.

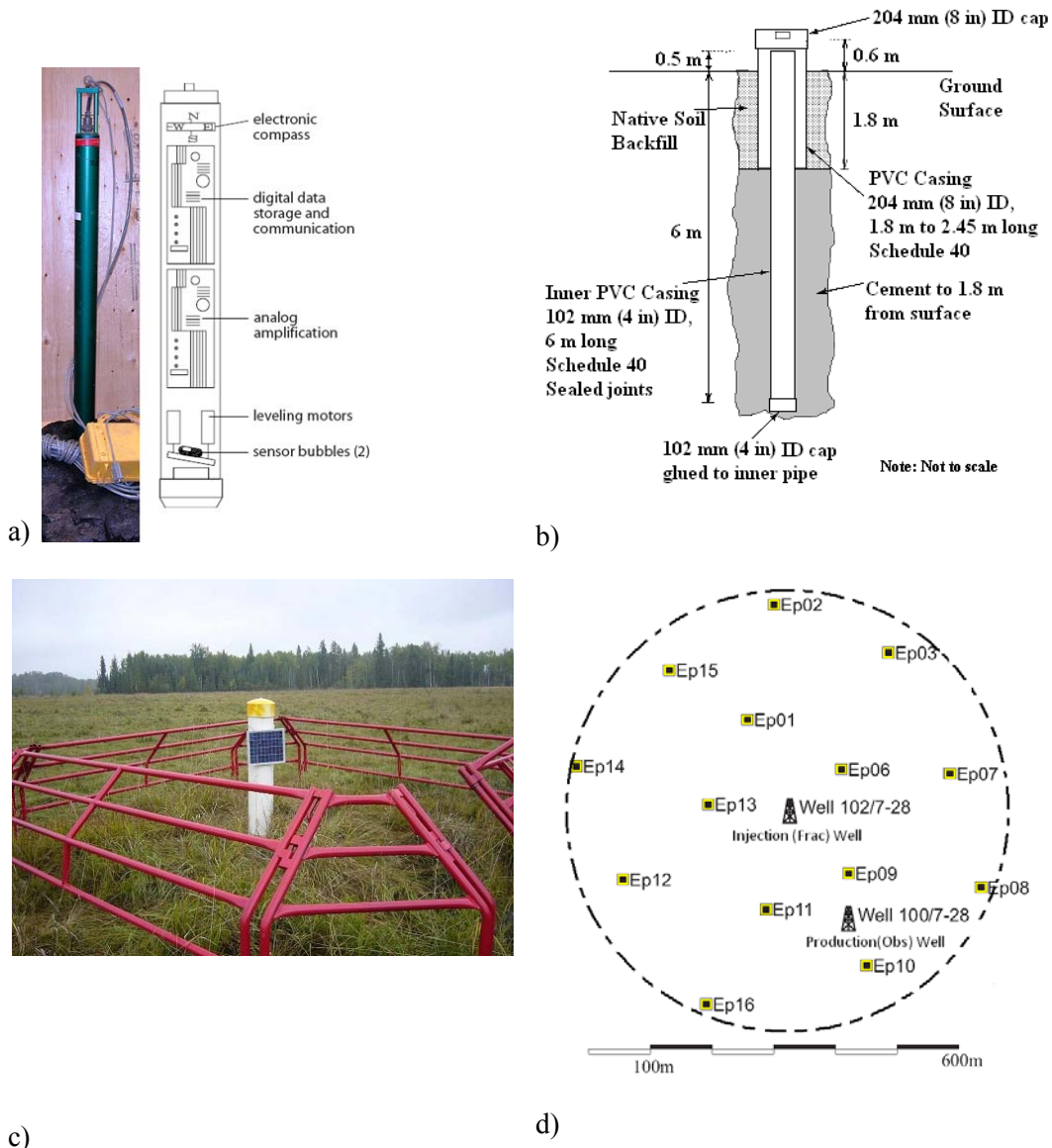
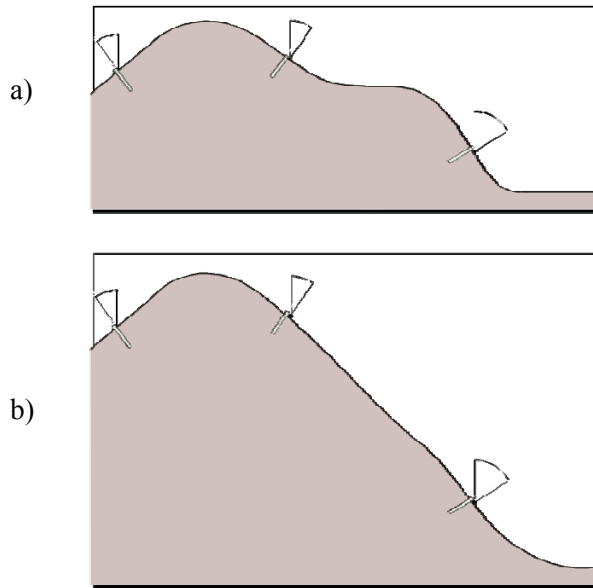


Figure 4.10 Surface tiltmeter(a), typical installation setup(b), Surface setup of Tilt-site Ep07(c) and layout of tilt-sites for CSEMP(d).

The surface tiltmeter array of 16 tiltmeters was used in the Phase I (See Chapter 3) of the pilot project for fracture mapping analysis and monitoring of the micro-pilot CO<sub>2</sub> injection test. Both the density of the tiltmeters in the array and the size of the array must be sufficient to allow accurate depiction of the deformation. Figure 4.11 shows how the ground surface deformation may be incorrectly determined when too few tiltmeters are used.



*Figure 4.11 Two different ground deformation models derived from the same tilt data. In order to distinguish between these two possible solutions, an additional tiltmeter would be required between the middle and furthest right tiltmeters. In general, tiltmeter density must be designed to pick up the smallest scale surface deformation that could be associated with the events being monitored.*

For the CSEMP project, Pinnacle used their internal design guidelines to develop the surface tiltmeter array presented in Figure 4.12. In addition, the option of ten extra tiltmeters was recommended by Pinnacle for monitoring the large volumes and extended spread of CO<sub>2</sub> during the multi-well pilot phase (Phase II) CO<sub>2</sub> injection. Figure 4.12 presents the surface tiltmeter array site plan for the monitoring of the micro-pilot Phase and the larger volume injection of CO<sub>2</sub> during the pilot phase. A total surface tiltmeter array radius of 538 m was required to monitor a 200 m spread of CO<sub>2</sub> during the pilot (Phase II) as compared to an approximately 358 m array radius for monitoring the hydraulic fracture operation. It was assumed that the smaller array distance of 358 m would be suitable for the micro-pilot as the spread of CO<sub>2</sub> from the injection well would be much smaller (i.e. on the order of 20 m to 30 m radius), similar to the hydraulic fracture.

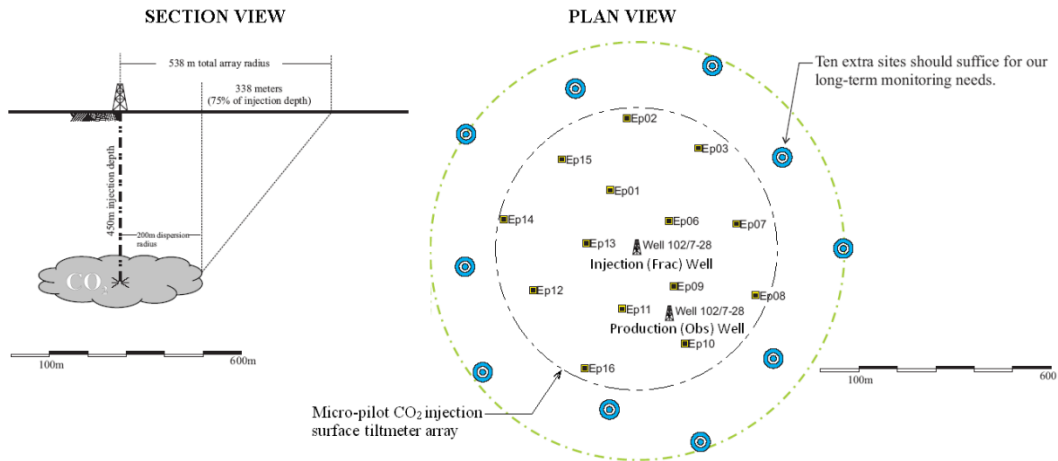


Figure 4.12 Tiltmeter site plan for monitoring of micro-pilot Phase I (small volumes of CO<sub>2</sub> injected) and pilot Phase II (large volumes of CO<sub>2</sub> injected).

#### 4.3.2 Discussion

During the design phase of the CSEMP case study, no preliminary site evaluation was conducted to define whether the standard of practice for deploying the surface tiltmeter array was suitable for this case study. The recommended installation depth of 6 m for each tiltmeter was selected as the standard of practice because at this depth there is small annual variation of  $\pm 1.389$  °C [31]. However, the impact of these conditions could not be assessed because these tiltmeters did not have a temperature calibration on the range of the ground annual temperature variations.

The loading and unloading due to frost-heave or wetting-drying cycles were other variables that were identified by the IPCC [1], which were not considered for the design and deployment of this technology. Because the expected long-term surface deformation for this case study was within the millimetre range, this small fluctuation of annual temperature and loading-unloading cycles could have had an impact on the readings and subsequently on the data interpretation outcomes. The assessment of the performance of the surface tiltmeter array deployed in the CSEMP site is presented in Chapter 5.

#### 4.3.3 Conclusions

The deployment of the surface tiltmeter array was successful, but the standard of practice used to design and install arrays does not include a pre-evaluation of the site conditions. The surface tiltmeter array installed at the CSEMP pilot site was designed and deployed

with standards used for oil and gas operational sites where large surface deformations are expected; however, the primary purpose of the CSEMP pilot was to demonstrate that CO<sub>2</sub> storage in Ardley coals is viable as a greenhouse gas reduction mechanism; thus, small surface deformations were expected.

## CHAPTER 5 Monitoring System Performance

This chapter provides an analysis of the early performance history of both the Pembina Cardium Project (PCP) and the CSEMP project. Analysis in the PCP project focuses on how effectively the cementing operations encased and sealed the downhole instrumentation. For the CSEMP project the tiltmeter monitoring system was assessed, including interpretation of the recorded data and its validation for the CSEMP pilot project during hydraulic fracturing and CO<sub>2</sub> injection.

### 5.1 Observation well

The presence of permanent downhole instrumentation allows the monitoring of pressure and temperature variations that occur during cementing operations. This monitoring capability provides valuable data to better understand potential problems and risks during the cementing and abandonment of conventional wells in addition to the cementing of the instrumentation or monitoring of wells. As fate would have it, the cementing operations on the observation well (OW) did not proceed as designed and a channel was created in the cement annulus. Utilizing the data obtained from the downhole instrumentation, the following sections discuss the cementing operations, including the cement circulation pressures and presents an argument for the cause of a channel in the cement. These circulation pressures are discussed in more detail subsequently [3, 14].

#### 5.1.1 Cementing

The cementing program for the OW was design by B.J. Services (now a subsidiary of Baker Hughes). Figure 5.1 shows schematically the steps during the cementing of the instrumentation well. All fluids during the cementing operation are pumped down the tubing and up the annulus between the tubing and casing. The cased well was filled with brine having a density of 1.3 g/cm<sup>3</sup> during the installation of the instrumentation system (Figure 5.1 (a)). Once the instruments were deployed at their final depth, a prewash fluid having a density of 1.0 g/cm<sup>3</sup> was circulated (Figure 5.1 (b)). The prewash fluid contains a surfactant to help clean the walls of the casing and tubing to aid in steel-cement bonding and to minimize cement contamination by wellbore fluids. Downhole static bottomhole pressure measurements in wells within the pilot area indicated that the expected reservoir pressure at 1640 m deep would be approximately 18.5 MPa. To prevent the influx of reservoir fluids into the well, the density of the completion fluids

(prewash and cement) should be large enough to balance the reservoir pressure and prevent any uncontrolled migration of native fluids into the wellbore.

Special CO<sub>2</sub> resistant cement slurry having a density of 1.76 g/cm<sup>3</sup> was pumped immediately behind the prewash fluid (Figure 5.1 (c)). Once the prescribed volume of cement was pumped into the tubing, it was followed immediately with water that was used as displacing fluid to complete the circulation of the specified cement volume. For this OW, the cement volume was computed based on a final cement “top” (the final depth of the cement top) at a depth of 1200 m. In general, a higher density of cement will result in a temporary differential height of cement between the tubing/casing annulus and the tubing. Once cement circulation stops, however, this differential height will equilibrate, and the cement tops will be at the same depth. For this OW, equalization did not occur, and as illustrated in Figure 5.1 (d), the cement in the tubing/casing annulus remained higher (shallower depth) than the cement top inside the tubing. The final depth of the cement in the tubing/casing annulus was 1238 m and in the tubing was 1290 m.

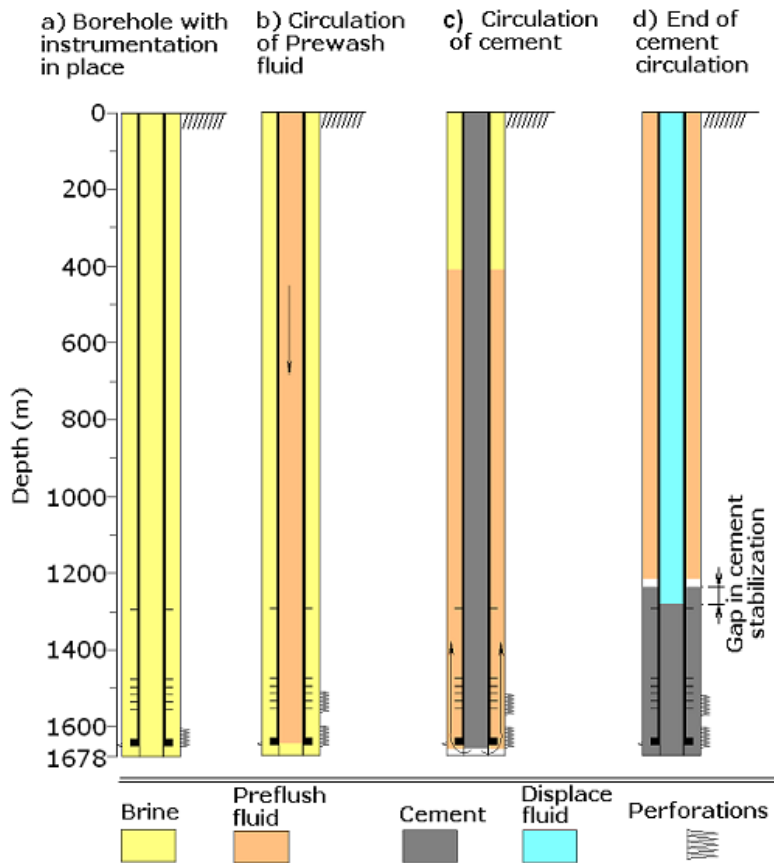


Figure 5.1 Steps in the cementation of the OW.

### 5.1.1.1 Pressure and temperature observations during cementing operations

Figure 5.2 provides seven hours' worth of data showing downhole pressures and temperatures during the cementing operation.

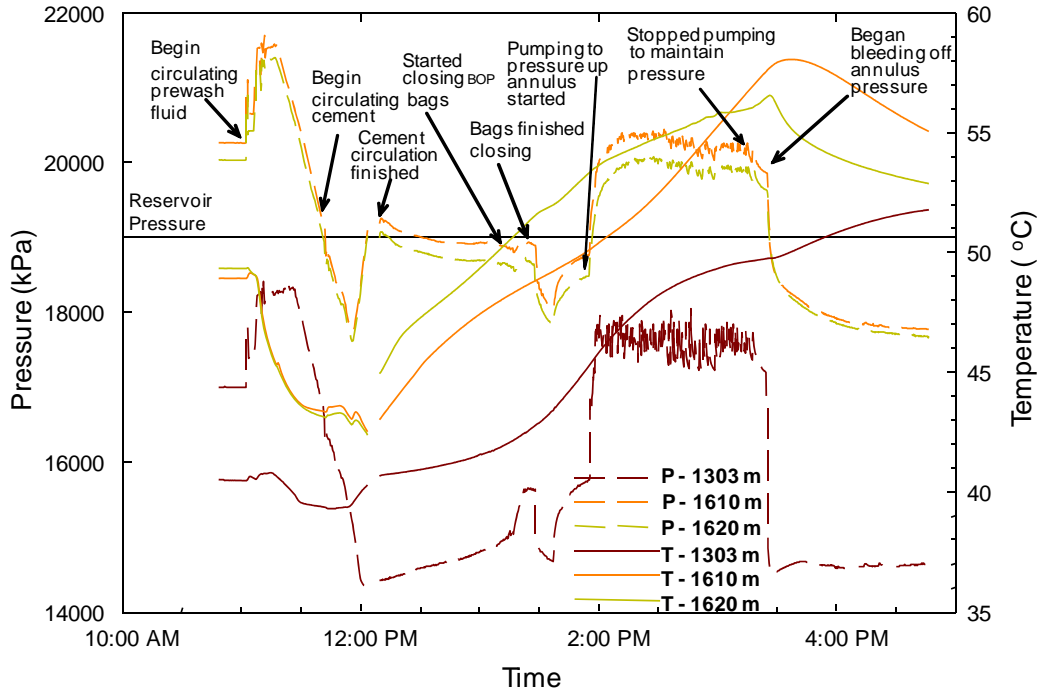


Figure 5.2 Recorded pressure and temperature during the cementing stages of the OW completion [3].

The downhole pressures increased dramatically when circulation of the prewash fluid began at 11:18 am due to initial requirement to circulate the denser brine completion fluids out of the borehole. Once the prewash fluid was the dominant fluid in the wellbore, the pressures began to decrease, reflecting the change in prewash fluid density versus brine density. Note the concomitant decrease in bottomhole temperature as the colder prewash fluids began to circulate by the downhole gauges. Cement circulation began at approximately 11:45 am, and once the cement circulated up the tubing/casing annulus past the gauges, the downhole pressures increased as the gauges sensed the denser cement slurry. Note that the temperature also began to rise almost at the same time indicating minimal lag in the cement hydration temperatures. Once cement circulation concludes, it is followed by a slow leak-off period as the cement fluid pressures equilibrate with the reservoir pressure.

At approximately 1:15 pm, it was apparent that a fluid channel had formed in the tubing/casing cement annulus. The remainder of the pressure fluctuations shown in Figure 5.2 following 1:15 pm is associated with wellhead pressure control activities to assess the extent of the fluid channel.

Fluid started flowing after completion of the cementing operation, reaching approximately 10 L/min. After about one or two hours, the flow decreased to 7 L/min. At this time, the annular blowout preventer (BOP) bag, a large rubber doughnut that is mechanically squeezed inward to seal the annular space between the casing and the tubing [32], was shut in. Bag pressure was increased to 9 MPa to stop the flow, and the flow slowed to 1 L/min. This increase in the annular pressure led to an instantaneous response of the borehole (see Figure 5.2 and Figure 5.3). The response was more dramatic at the 1300 m-deep sensors, which indicates a poorer cement job at this level.

Since the cementing operation involved fluids of various densities, normalizing the downhole pressures to the density or unit weight of brine provides additional insight into the dynamics that are occurring downhole.

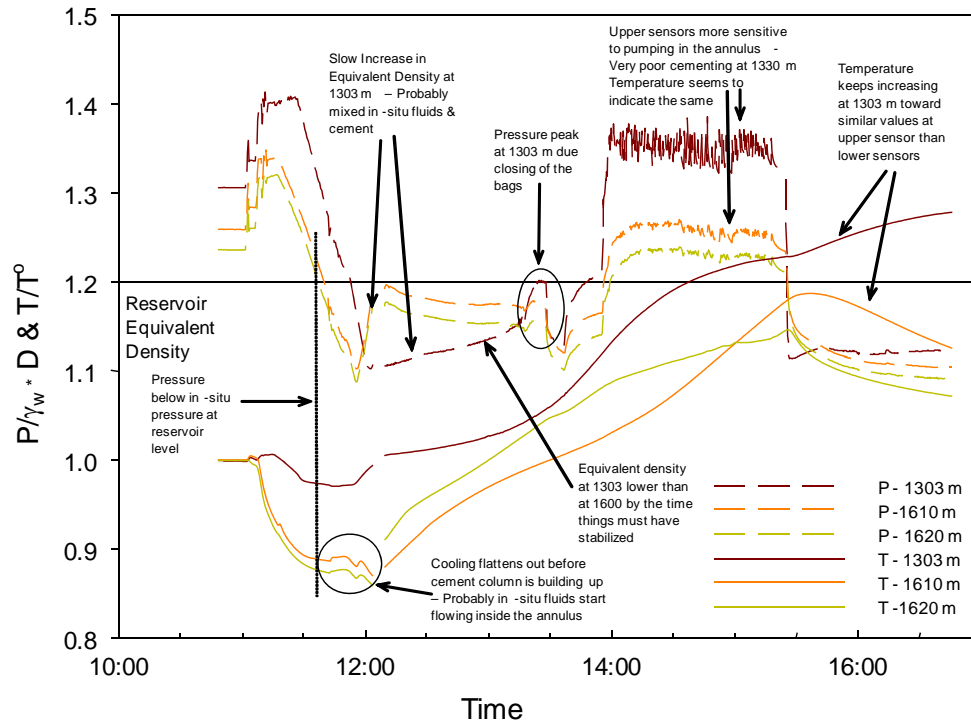


Figure 5.3 Equivalent density and normalized temperature during the cementing stages of the OW completion [3].

Figure 5.3 shows the pressures normalized to brine density in order to obtain an equivalent density during the process, and normalized temperatures (normalized to the initial temperature at each sensor depth). One explanation for the development of the fluid channel in the cement is that the decrease in bottomhole pressure below the reservoir pressure resulted in fluids flowing into the tubing/casing annulus during the cement operations. This is noted in Figure 5.3 at approximately 11:35 am. Supporting this hypothesis is the reduction in the rate of cooling initiated by the circulation of cooler prewash fluids, which resulted from warmer reservoir fluids flowing into the wellbore almost at the same time the cement circulation pressure fell below the reservoir pressure (at 11:35 am, Figure 5.3). A second equally plausible scenario for the development of the fluid channel is the poor prewash fluid displacement efficiency by the cement as a result of the high density of sensor assemblies, sensor cables and stainless steel tubing used for the fluid recovery system. Computational fluid dynamics simulations were conducted to assess this scenario and are presented in Chapter 6.

### 5.1.2 Wellbore Completion

In order to “weight-up” (increase the fluid density in the well), a field decision was made to “punch” a hole in the tubing (using a tubing punch) just above the cement top in the annulus between the tubing and the casing. Following the creation of the hole, dense brine would be injected to increase the annular fluid density leading to cessation of annular flow by balancing the bottomhole pressure in the reservoir. Discussions with the rig crew indicated that the hole was punched at roughly 6:30 pm on February 28, 2005, and that brine was pumped and circulated at 8:30 pm at a pressure that may have reached 10 MPa (based on information from the rig crew) at the wellhead. Analysis of the recorded data shows that pressure in the annulus was released at noon on February 28, 2005, with an instantaneous response of both pressure and temperature sensors. Injection of the brine was clearly seen as both pressure and temperature gauges showed a dramatic and erratic change at around 8:30 pm the same day. Only two pressure gauges survived: one at 1303 m and another at 1610 m (Figure 5.4 to Figure 5.7). Temperature gauges that were with the pressure gauges, at 1303 m and 1610 m also survived the process. Two others at 1610 m and 1620 m showed post-injection readings, but they were erratic, so it seems they were damaged. Likewise, several sensors on geophone cable 1 showed shorts to the shield, indicating that were damaged as well.

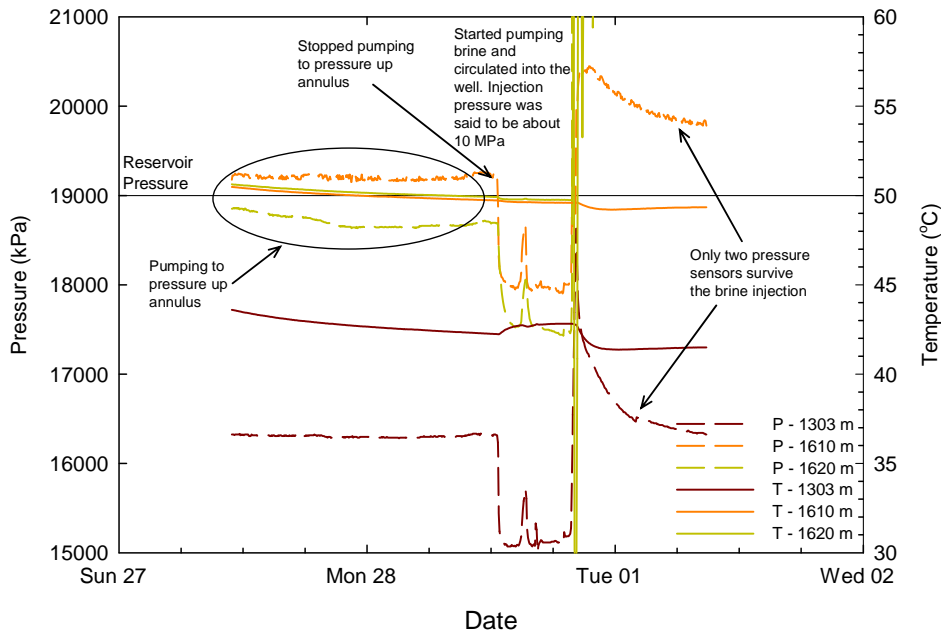


Figure 5.4 Recorded pressure and temperature between the end of the cementing job and the completion of the well.

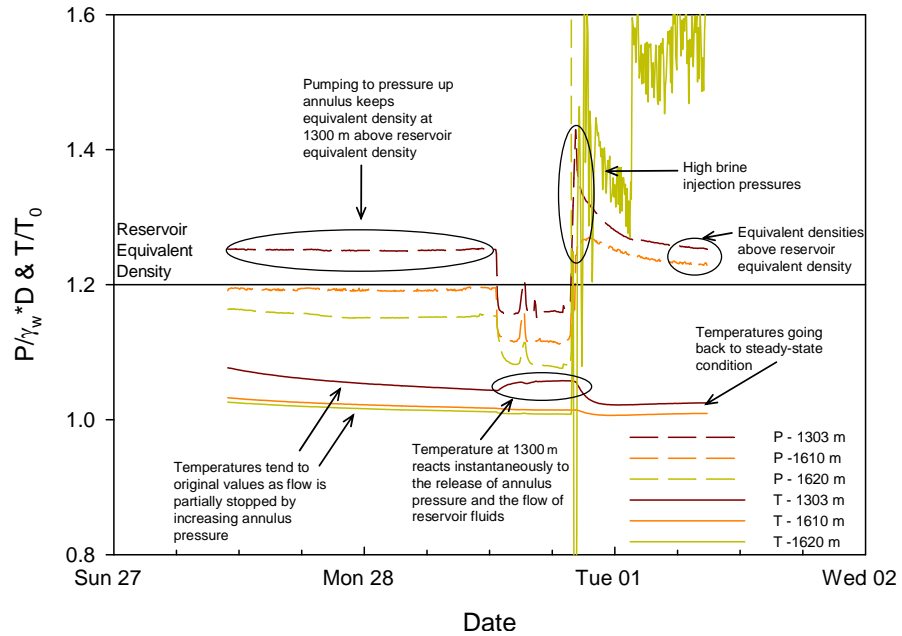


Figure 5.5 Equivalent density and normalized temperature between the end of the cementing job and the completion of the well.

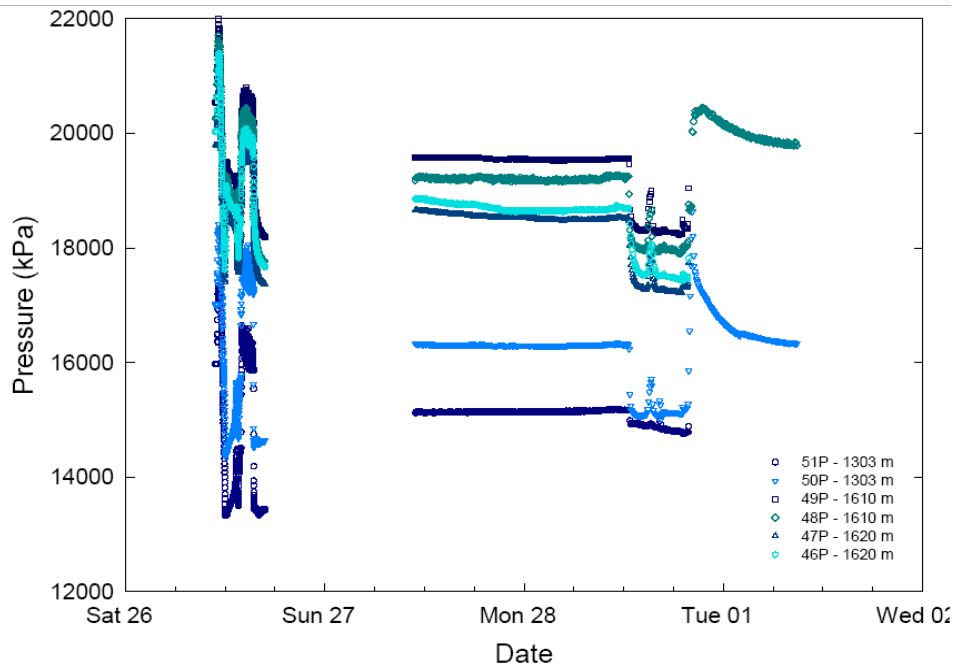


Figure 5.6 Pressure records from all instruments deployed during the entire process.

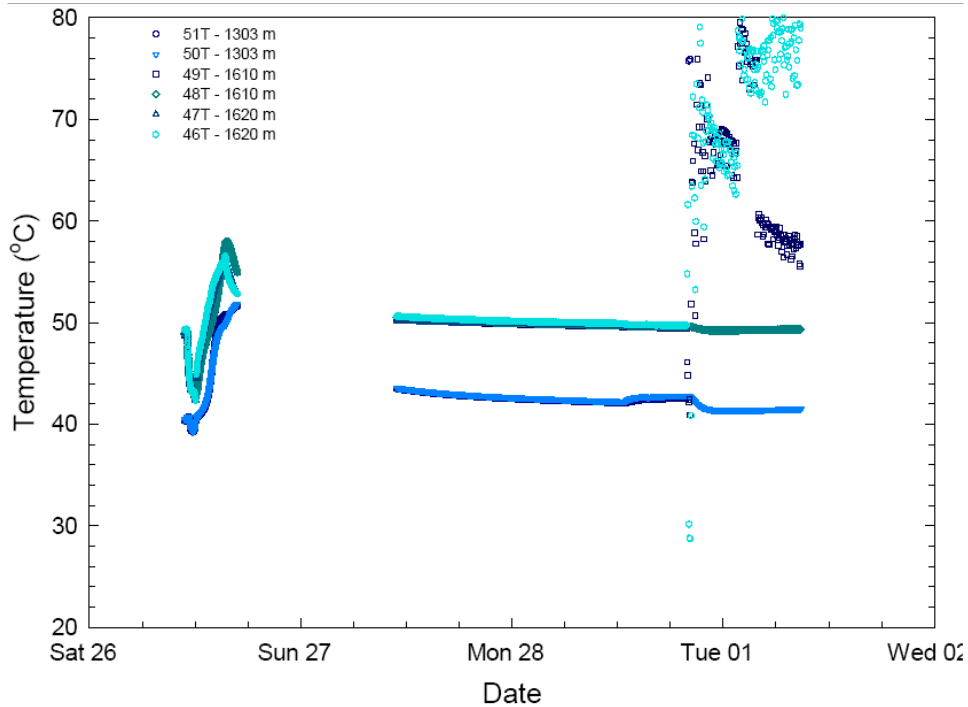


Figure 5.7 Temperature records from all instruments deployed during the entire installation program.

### 5.1.3 Measurements during CO<sub>2</sub>-EOR pilot

The downhole pressure/temperature gauges have also yielded valuable performance measurements during CO<sub>2</sub> injection into the Pembina Cardium Formation.

Figure 5.8 presents a typical pressure log from the wellhead, 1303 m KB (shallow), and 1611m KB (deep) sensors. From this figure, it is observed that the wellhead and bottomhole pressure gauges are connected through a saturated fluid media, and the differential pressure between these two sensors is due to the hydrostatic pressure of the fluid column at 1611m KB. An interpretation of the downhole pressure/temperature data during the first month of operation of the Pembina Cardium CO<sub>2</sub>-EOR monitoring pilot project is provided in Figure 5.8.

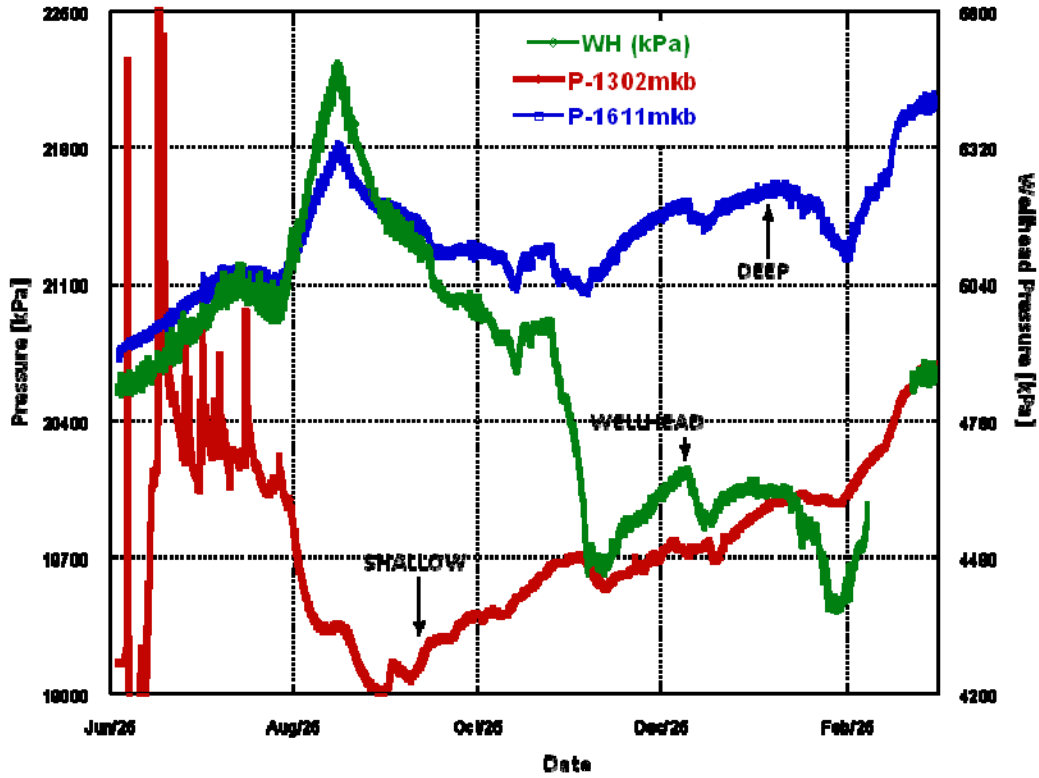


Figure 5.8 Pressure reading from wellhead, 1302m KB and 1611m KB pressure gauges.

In addition to pressure/temperature data from the OW, a pressure/temperature gauge was deployed in the deviator injector 102/10-11, which its bottomhole target depth drove pressure to the producer 102/7-11 and the OW zone. Figure 5.9 presents the recorded injector 102/10-11 and OW pressure/temperature readings. This information was used to understand the response of the OW throughout the production stages and to history matching with a reservoir-model software.

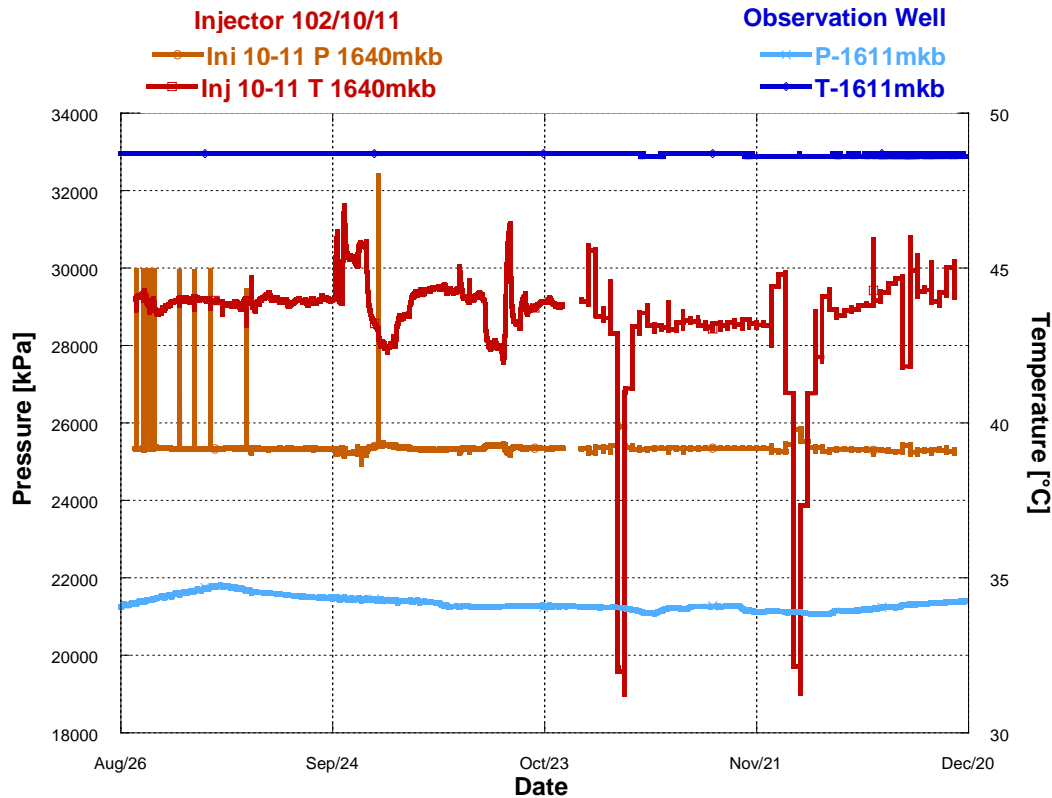


Figure 5.9 Recorded pressure and temperature reading from Injector 102/10-11 and OW.

### 5.1.3.1 Early interpretation of downhole pressure/temperature

Zambrano and Chalaturnyk [3] presented an early interpretation of the downhole pressure/temperature data for a five-month period from the OW. Figure 5.10 shows the profiles of one deep (1610 m) and one shallow (1303 m) pressure and temperature sensor during the first five months of the CO<sub>2</sub>-EOR project. This data shows pressure depletion occurring due to the startup of the production well approximately 35 m away. Using information obtained from a weekly operator’s report, average CO<sub>2</sub> concentrations over this five-month period are shown in Figure 5.10 and Figure 5.11 and have been used to identify six zones that display consistent behaviour.

Major operating events occurring at the injection and production wells within the CO<sub>2</sub>-EOR pilot were captured in the pressure/temperature responses of the downhole sensors. In most cases, the time lag between the response of the deep and shallow sensors was minor. The following brief descriptions explain the fluid phase behavior within the first four zones that gave rise to the recorded pressure/temperature response.

Zone I - As pumping began in the nearby production well, a steady reduction in pressure readings occurred with minimal pressure fluctuations due to the low percentage of CO<sub>2</sub>. It was observed that there was an approximate 13-day time lag between the response of the deep sensor and the shallow sensor.

Zone II – The instability of pressure readings early in this zone indicate that the first CO<sub>2</sub> front arrived at the OW. It is postulated that fluctuating pressure readings are due to the presence of gas phase in near-well region. Operator's records indicate 10% CO<sub>2</sub> in the production well.

Zone III – Near the end of Zone II and throughout Zone III, the CO<sub>2</sub> percentage increases to approximately 55%. Pressure/temperature (PT) readings are more sensitive to the change in production rate due to the supercritical fluid surrounding the sensor. Vertical migration of CO<sub>2</sub> occurred because the percentage of CO<sub>2</sub> was increasing; the vertical permeability in the well was high due to the fluid channel in the cement annulus. Fluid migration led to increased pressures in the upper zones, as measured in the PT 1302 m KB sensor. The velocity of migration and pressure build-up into the upper zones was proportional to the percentage of the CO<sub>2</sub> front. Continued production in the production well was reflected in the constant decrease in bottomhole pressure (BHP) as recorded by the deep sensor. However, once the BHP became lower than the upper zone pressure, vertical CO<sub>2</sub> migration through the fluid channel stopped, and the migrated gas was trapped. PT readings stabilized with receding vertical gas migration. The build-up pressure in the upper zone continued as a result of migration of the trapped CO<sub>2</sub> due to buoyancy.

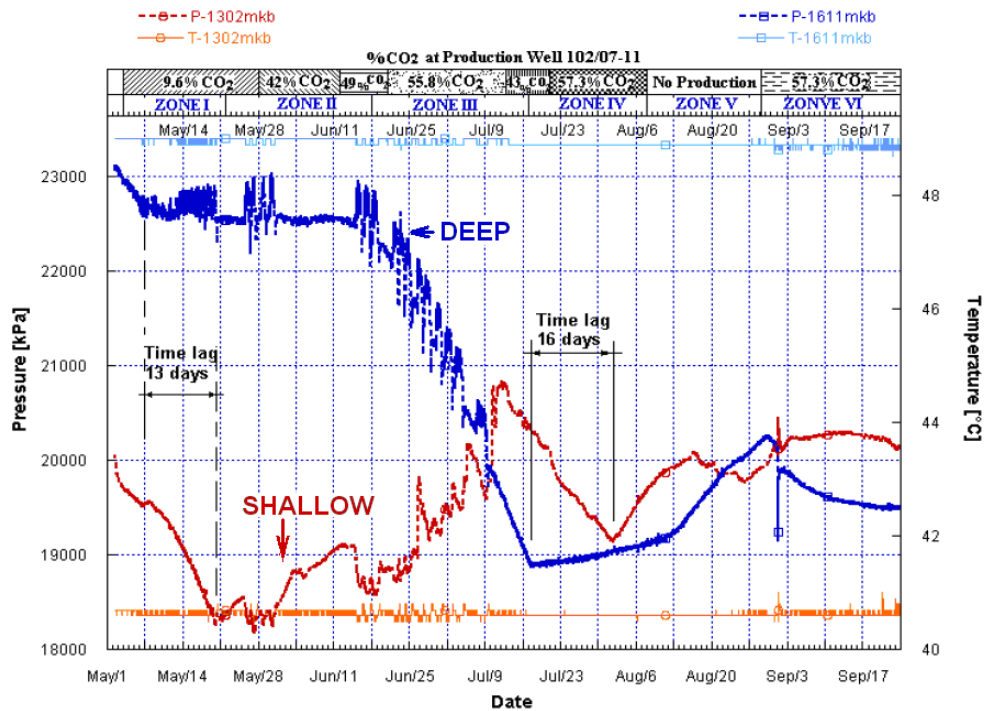


Figure 5.10 Recorded pressure and temperature of a deep sensor and shallow sensor from May 2005 to September 2005.

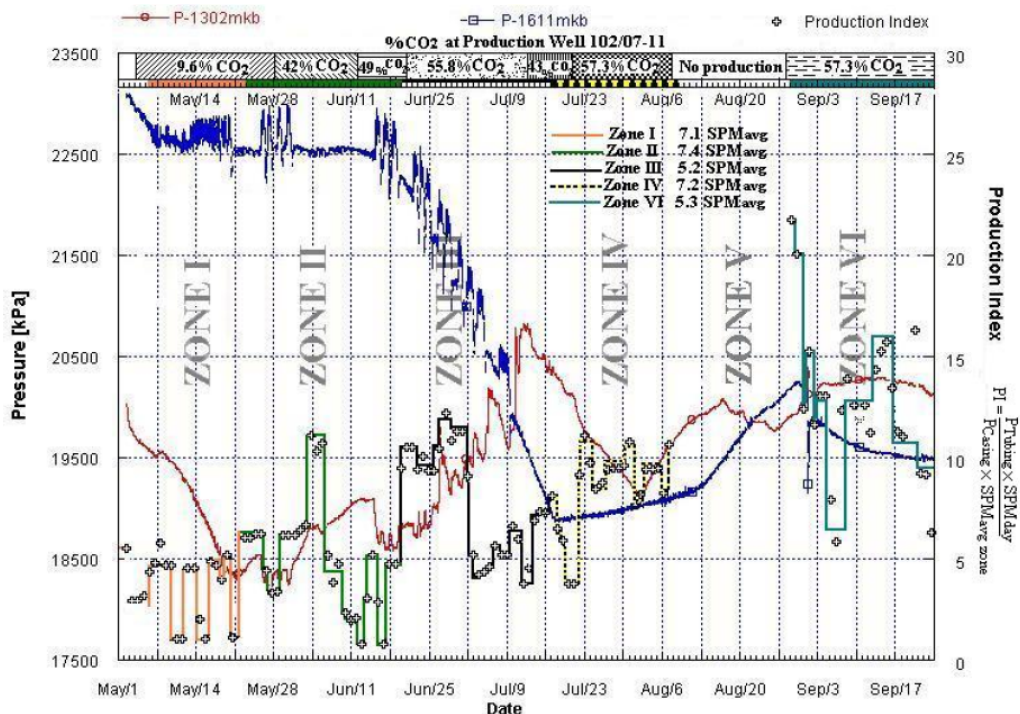


Figure 5.11 Downhole pressure response of OW and production index with time.

Zone IV - The percentage of CO<sub>2</sub> in the front increased to approximately 57%. The trapped CO<sub>2</sub> was diluted into the brine, reducing its density gradually with time. The PT

1302 m KB sensor recorded the pressure reduction of the brine column. There was possible downward vertical migration of fluid and CO<sub>2</sub>. The rate of production was more stable than previous zones. Time lag between the bottom and upper PT sensors was 16 days.

A schematic description of the above-mentioned zones is presented in Figure 5.12. The phase behaviour of the fluids both within and surrounding the OW led to complex pressure/temperature responses within the OW. The presence of the fluid channel in the tubing/cement annulus provided a flow path for reservoir fluids, which further complicated the recorded pressure/temperature behaviour.

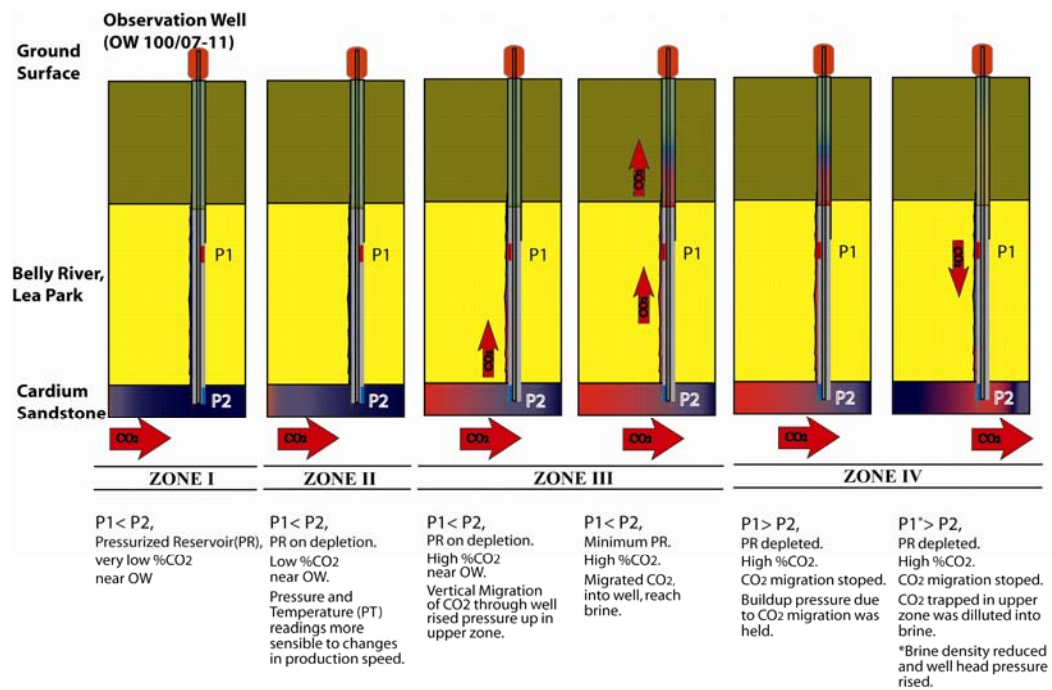


Figure 5.12 Schematic description of the zones found in Figure 5.10 and Figure 5.11.

#### 5.1.4 Downhole pressure and temperature log throughout the life of the project

The pressure/temperature data was downloaded and collected remotely via cell phone-modem and reported online via a website. Figure 5.13 to Figure 5.16 present the recorded downhole pressure/temperature data throughout the life of the project. Although, reservoir simulation modelling was not in the scope of these, the downhole pressure and temperature measurements were used by Lim et al.[15] to history matching their models on this pilot project.

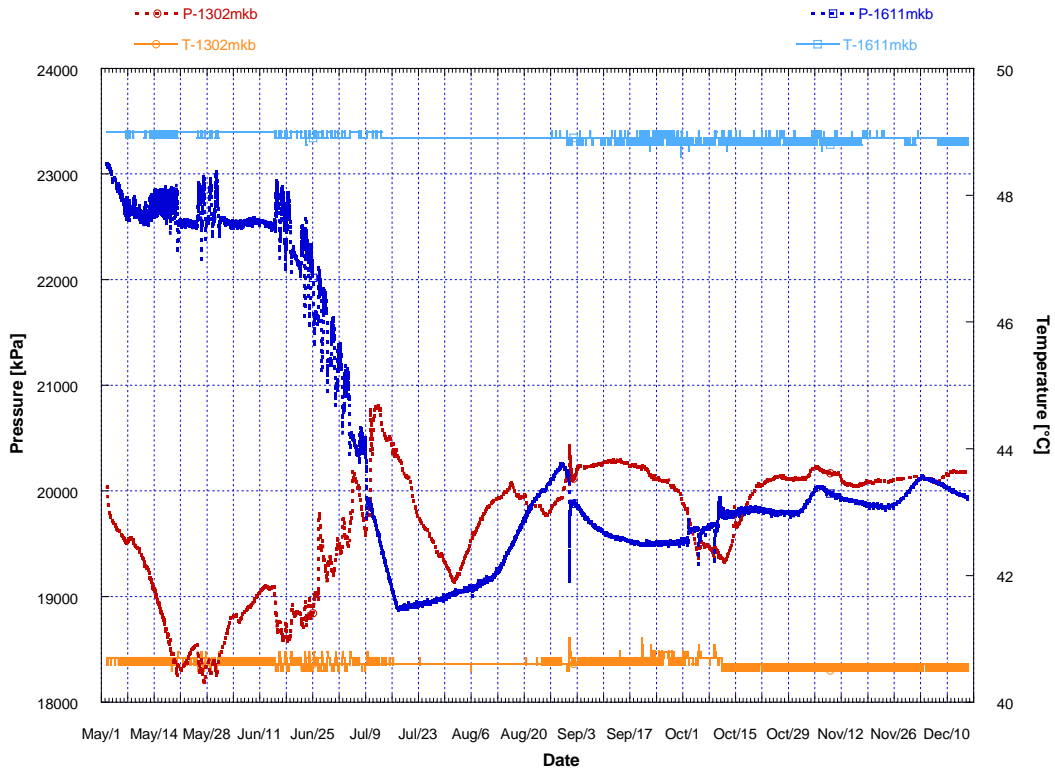


Figure 5.13 2005 downhole pressure and temperature logs.

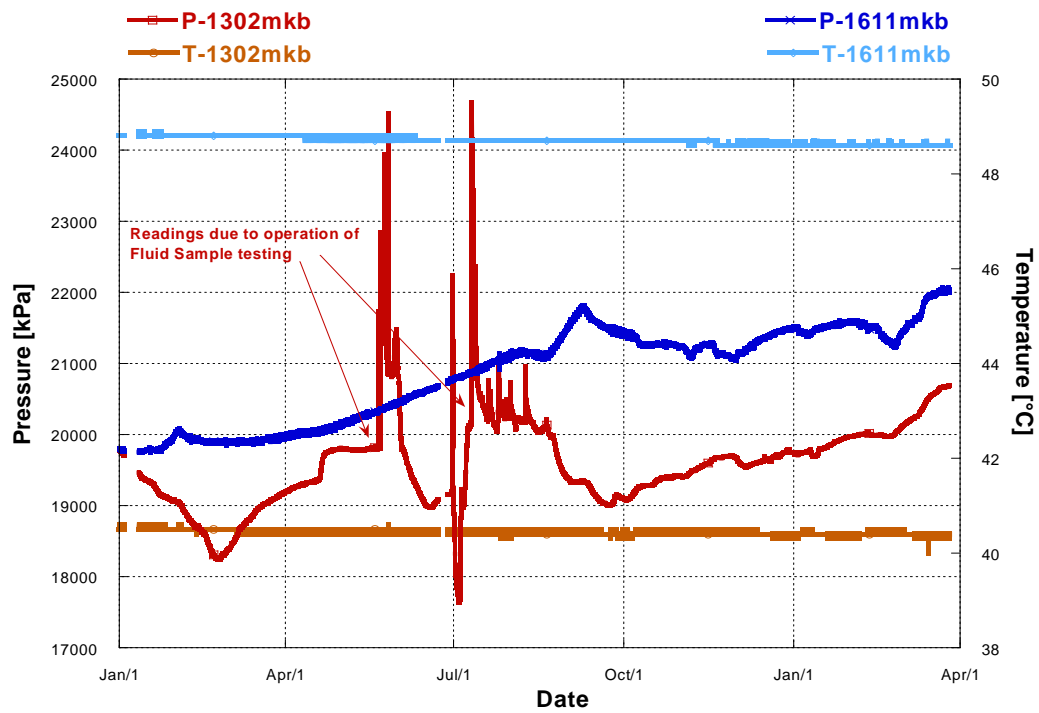


Figure 5.14 2006 downhole pressure and temperature logs.

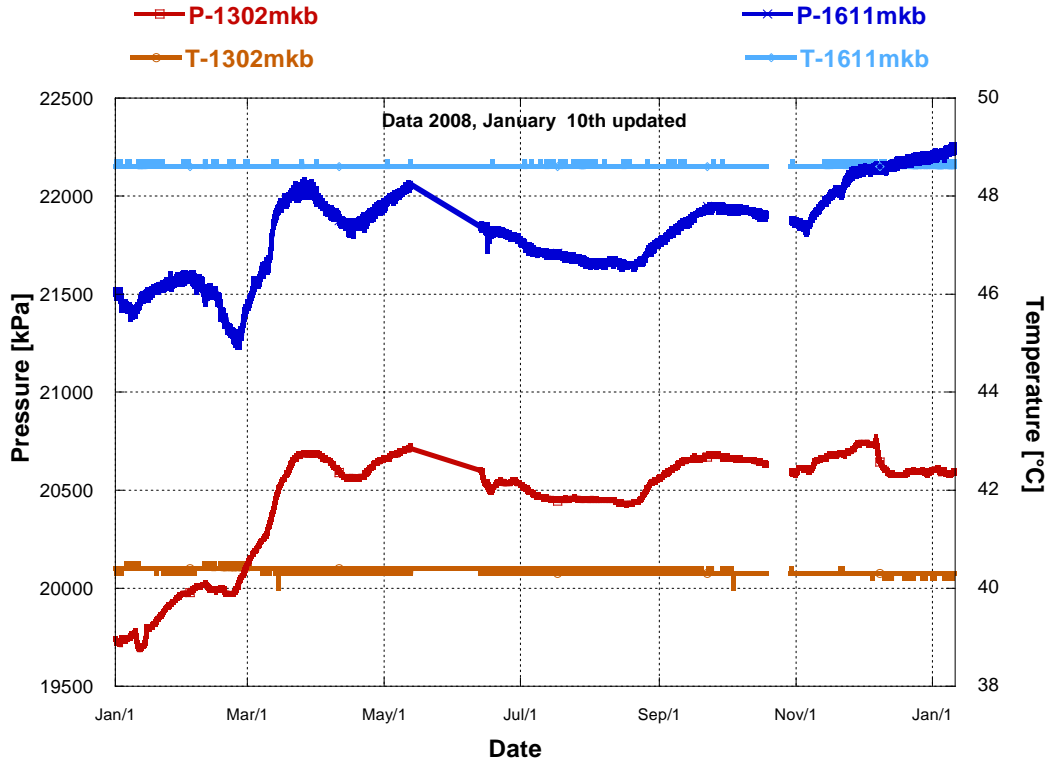


Figure 5.15 2007 downhole pressure and temperature logs.

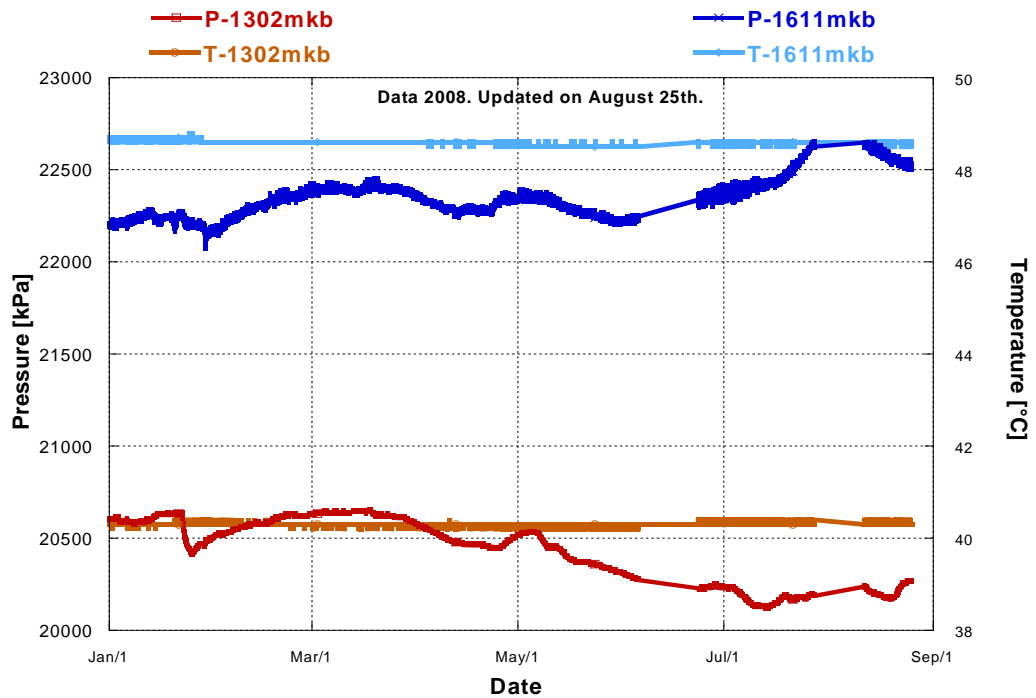


Figure 5.16 2008 downhole pressure and temperature logs.

### 5.1.5 Others events

From the internal field reports, pressure was observed to increase with time at the wellhead. The reason for this pressure gradient was the dilution of CO<sub>2</sub> into brine and then the reduction of its density. On August 26, 2005, gas-oil leakage through the PT sensor cables was detected. To solve this problem, a new cable sealing of the wellhead had to be performed. On September 1, 2005, the wellhead was pressurized to 4400 kPa (640 psi), and a pressure recovery test was conducted on the OW to evaluate the procedure to fix the leakage. Migration of CO<sub>2</sub> reduced the time of the test to 40 minutes, recovering 0.25 m<sup>3</sup> of yellowish liquid mixture. The results of this test revealed the communication from an upper zone through the annulus to a depth where the PT 1302 m KB sensor is located (Figure 5.17 and Figure 5.18). The wellhead pressure after the test is approximately 4500 kPa, and the injection of heavy brine with a low pump rate is thus required to kill the well without damaging the operating sensors.

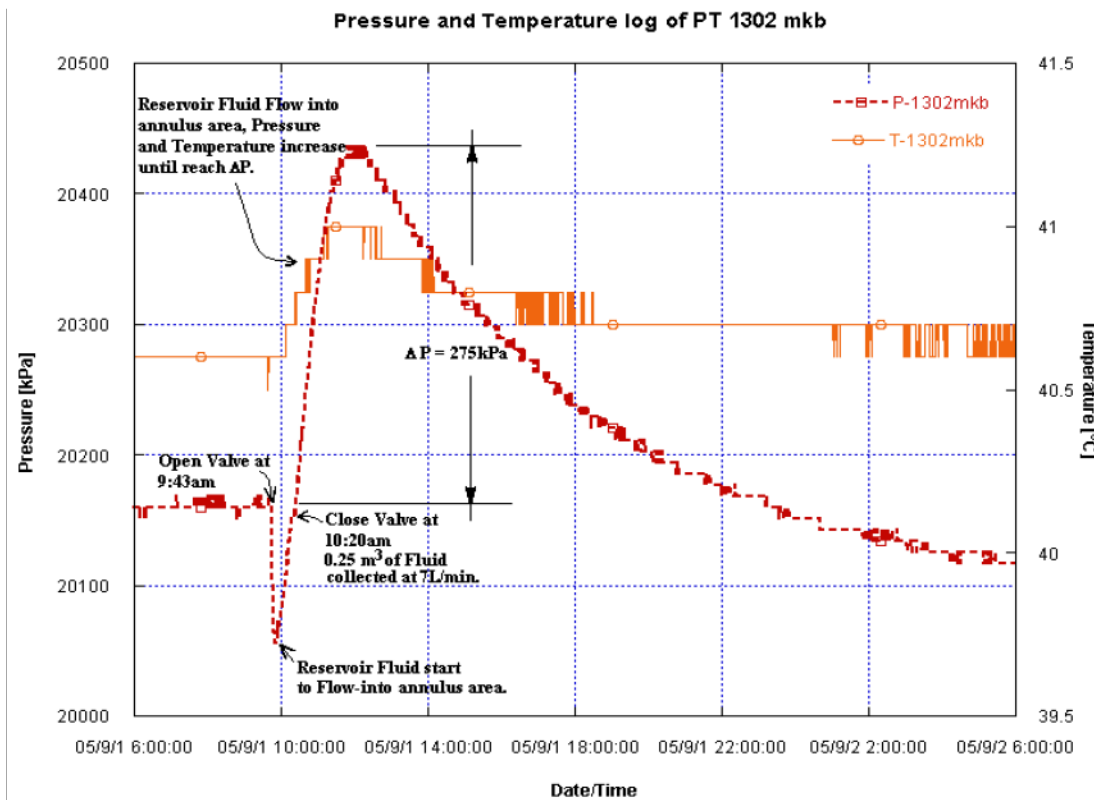


Figure 5.17 Recorded pressure and temperature of a sensor at 1303 m during the pressure recovery test on September 1, 2005.

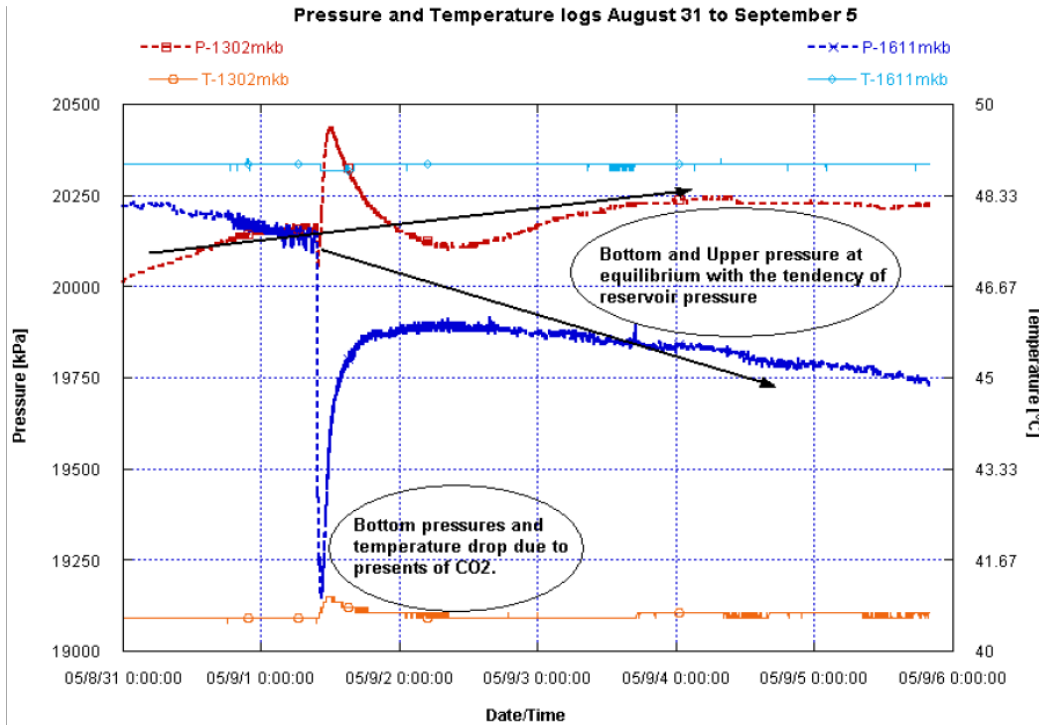


Figure 5.18 Recorded pressure and temperature for both gauges during pressure recovery tests.

### 5.1.6 Fluid Recovery System

The fluid recovery system (FRS) installed within the OW consists of two downhole fluid ports at different horizons and a fluid recovery control panel, as illustrated in Figure 5.19. The reason for installing permanent, downhole fluid sampling ports was to assess the feasibility of acquiring reservoir fluids under reservoir pressure conditions. Fluid samples under pressure at surface level will be acquired and their composition will be analyzed for comparison with fluid samples taken at ambient conditions at offset production wells. This comparison will aid in assessing whether depressurization effects affect ambient condition fluid samples and in assessing the cost-benefit of downhole pressurized fluid samples. One additional advantage of the FRS design is its use as a “bubble” tube pressure sensor to confirm the BHP of the pressure gauges permanently installed within the OW [3].

The site has two 2.30 m x 2.3 m x 2.45 m insulated sheds mounted on skids located adjacent to the OW with one of the sheds dedicated to the FRS. Approximately 8 m of the 6.35 mm (1/4 in) diameter stainless steel tubing exits the OW wellhead for each downhole sample port. Each end of the FRS samplers is configured with a ball valve

attached to the FRS panel control. The FRS#2 port is located in the Cardium reservoir, and the FRS#1 port is adjacent to the Lee Park Shale Formation.

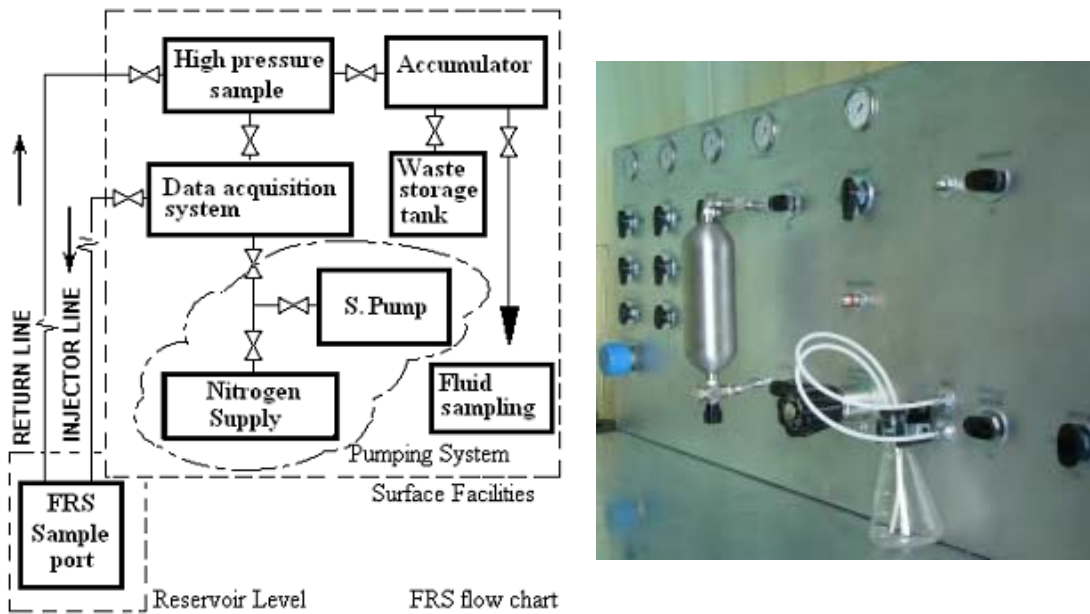


Figure 5.19 Sample Handling Schematic.

### 5.1.6.1 Preliminary interpretation of aqueous sample

During fieldwork conducted from June 2006 to September 2006, 40 L of reservoir fluid was recovered with a 1:4 ratio of water to oil phase. The aqueous samples were sent to three different laboratories for geochemical analysis. Figure 5.20 shows the analysis of several major dissolved ions as a function of time along with the produced water chemistry<sup>1</sup>. The plot shows the water analyses from the production well from June and July 2006, and from the OW from June to September 2006. The data presents the typical producer and OW aqueous sample composition, which is governed by the different concentrations of Cl, Na and Ca.

As a historical reference, Figure 5.20 also presents the composition of formation and produced water samples<sup>2</sup> from the 1950s of wells located close to the pilot area. A comparison with analyses of producer water samples from others areas of the field had shown that the salinity persistence effect observed in the pilot area generally occurs in the Pembina reservoir [33].

<sup>1</sup> The laboratory results presented are from three laboratories: University of Calgary (UofC), University of Alberta (UofA) and Baker Petrolite.

<sup>2</sup> Analysis from AEUB.

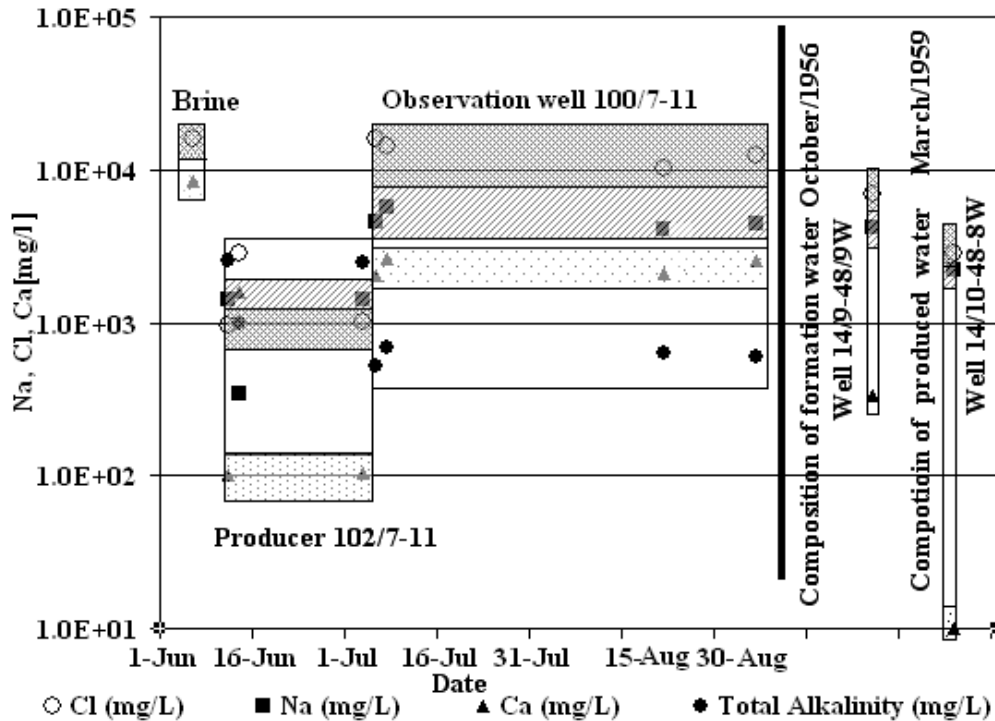


Figure 5.20 Typical aqueous composition of producer and OW water samples [3].

This data also shows that there is very little change in the composition of the water taken from the producer water between June and July 2006. The water samples are dominated by NaCl and bicarbonate, and there is very little  $\text{Ca}^{+2}$  by comparison. The water samples taken from the OW in June 2006 is of comparable concentration, but the  $\text{Ca}^{+2}$ ,  $\text{Cl}^{-1}$ , and  $\text{Mg}^{+2}$  concentrations are higher ( $\text{Mg}^{+2}$  concentration was really high – almost off the graph), and the  $\text{Na}^{+}$  concentration and alkalinity are lower. The July 2006 OW water samples are much more concentrated, but more normal in that  $\text{Ca}^{+2}$  concentration was less than that of Na; however, the alkalinity remained very low. It is difficult to understand what may be driving the composition in this matter. If we assume that there was contamination with brine<sup>3</sup>, then the June 2006 sample makes sense. However, it is difficult to increase the Na values above the  $\text{Ca}^{+2}$  values, unless some formation fluid (which has a high Na:Ca value) is mixed in with the brine. Even then, the  $\text{Na}^{+}$  concentration cannot surpass the concentration in the reservoir, or as seen in the production well. Much of the produced water chemistry seems to be influenced by ion exchange, which could possibly explain some of these results as well. The August 22, 2006, and September 6, 2006, samples are similar to the July 2006 results, except they

<sup>3</sup> Completions and Workovers Report # 11, February 23, 2005, stated  $\text{CaCl}_2$ .

seem to decrease concentration, which is positive sign of stabilization in the disturbed borehole area. Continued fluid sample collection and analysis will aid in understanding early fluid chemistry interpretation.

#### **5.1.6.2 Bubble-tube test interpretation**

The BHP can be obtained from the capillary line or bubble tube using nitrogen ( $N_2$ ) as follows: pressure up tubing with  $N_2$ , accurately measures wellhead pressure and determines gas gradient for pressurized  $N_2$ . Nitrogen gas is inert, relatively inexpensive, and generally, easy to obtain. Unlike many other gases, such as  $CO_2$ ,  $N_2$  will not go through a phase change in the range of pressures and temperatures typically encountered in reservoirs [34, 35].

Figure 5.21 shows an estimate of the BHP with the surface pressure response of FRS#2's capillary line during a bubble tube test. The gas gradient for  $N_2$ , corrected for a surface ambient temperature and bottomhole temperatures of 41 °C (106 °F) at 1302 m KB or 49 °C (120 °F) at 1622 m KB, was added to the stabilized surface pressure. Gas gradient was calculated using the thermophysical properties of fluids at isobaric conditions. Because the diameter of the capillary outlet in the FRS sample port is one order of magnitude smaller than the main capillary line, the early pressure signal was largely affected. With this instrument, the early data pressure response curve was due to the configuration of the instrumentation and not the BHP of the well [36].

Also, Figure 5.21 shows the field comparisons of the downhole vibrating-wire pressure gauges located at 1611 m KB and the capillary (bubble tube) pressure sensors of the FRS located at 1622 m KB, confirming  $N_2$  gradient accuracy within  $\pm 100$  kPa ( $\pm 14.5$  psi). The effect of the sample port diameter is evident in the amount of time needed to reach equilibrium. While this may not be of adequate sensitivity for a well test analysis, it is certainly acceptable for long-term well monitoring.

### BHP can be obtained from a capillary line or bubble tube

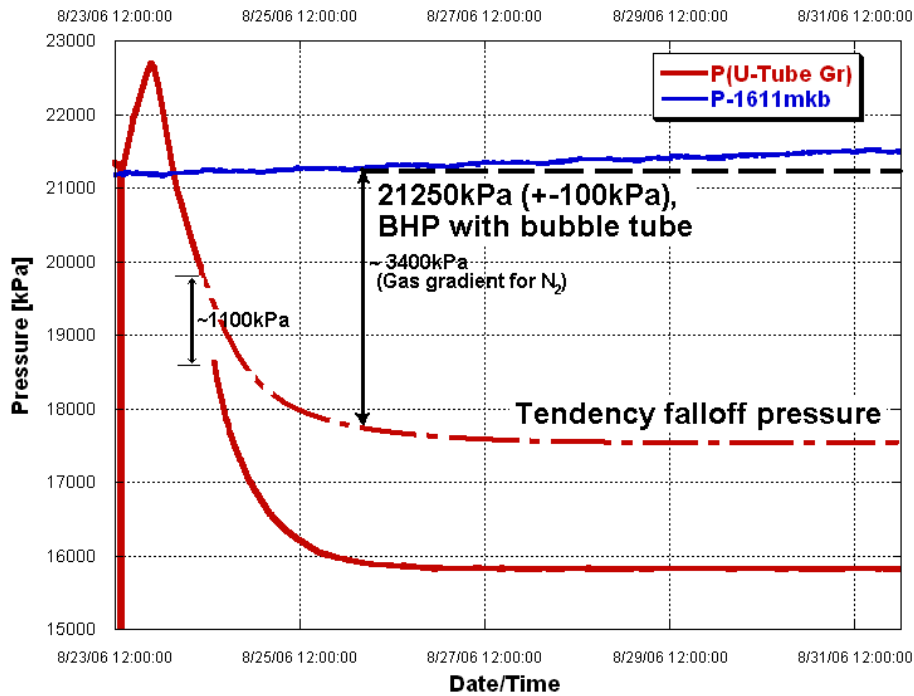


Figure 5.21 FRS#2 bubble tube interpretation [3].

#### 5.1.7 Conclusions

The OW at the Pembina Cardium CO<sub>2</sub> Monitoring Pilot, a CO<sub>2</sub>-EOR project, has enabled direct monitoring and measurements at the reservoir level for a variety of parameters and properties through geophysical, geochemical, and geomechanical instrumentation.

A detailed analysis of each aspect of OW completion, cementing behavior, annular flow behavior, and its impact on the integrity of downhole systems will provide valuable insight for current projects and the professional community considering the increased deployment of sophisticated multi-instrument strings in CO<sub>2</sub> storage field demonstration projects.

The application of the innovate FRS, permanently cemented at different depths, has proven to be effective technology for geochemical monitoring at economic cost. One additional advantage of the FRS design is its use as a “bubble” tube pressure sensor that can be used to confirm the BHP of the pressure gauges permanently installed within the OW.

## **5.2 Use of surface tiltmeter array for monitoring in the CSEMP pilot project: interpretation and uncertainties in injecting, mapping, and reservoir monitoring**

A surface tiltmeter array of 16 tiltmeters was deployed at the CSEMP site to monitor surface deformation due to short-term hydraulic fracturing and longer-term injection of CO<sub>2</sub> in Ardley coals 400 m deep in the Pembina area of the Western Canadian Sedimentary Basin southwest of Edmonton, Alberta, Canada. To measure the dimensions of the induced fracture, an additional vertical string of tiltmeters was deployed in a production well approximately 200 m offset from the injector. A maximum surface deformation of 0.05 mm was interpreted from the tiltmeters during the hydraulic fracture operation. Interpretation of surface deformation from longer-term injection of CO<sub>2</sub> was more complex because of long-term external noise including earth tides, rainfall, and temperature. These effects, which could be as large or even larger than the deep-induced event, had to be subtracted from the tiltmeter signal to determine the surface deformation due to the deep injection of CO<sub>2</sub>. The most difficult noise to assess was the heavy rain events that affected the water table and consequently also affected the readings from the tiltmeters located at 6 m deep. A maximum ground deformation of approximately 2 mm was interpreted by Pinnacle from the tiltmeters due to injection of approximately 1000 tonnes of CO<sub>2</sub> into the coal. Some recommendations for similar future applications are also made.

This section presents the tiltmeter monitoring assessment, including interpretation of the recorded data, and its validation for the CSEMP pilot project during the hydraulic fracturing and CO<sub>2</sub> injection events. The scope of this section is to assess the performance of the surface tiltmeter array on CSEMP and to discuss the advantages and limitations of this type of technology for measurement, monitoring and verification (MMV) activities for CO<sub>2</sub> geological storage.

### **5.2.1 Short-term versus long-term measurements**

There is one fundamental difference between fracture mapping with tiltmeters and reservoir monitoring with tiltmeters – the time scales of the two processes are very different. The time of the fracture event is measured in minutes (short term) while the CO<sub>2</sub> injection is measured in days, months, or years (long term). The analysis of the tiltmeter measurements for both cases look at the induced tilt over time to map how the

surface has changed. However, fracture mapping events have a definite duration, which is generally much longer than short-term noise sources, such as traffic, and shorter than long-term signals associated with seasonal changes or site and instrument drift. This duration allows the fracture signals to be extracted quite easily even in the presence of significant amounts of noise. For reservoir monitoring, only the very short term noise sources are easily removed from the data while the longer term ambient or background noise remains in measured data since long-term noise cannot easily be distinguished from deformation due to the reservoir processes that are being investigated.

An assessment was conducted on the impact of the trend or drift in the surface displacement due to the four days of CO<sub>2</sub> micro-pilot injection. A similar period of time with minimum noise and no surface operation was chosen for comparison. The only surface displacements expected were due to earth tides, which are normally cycled with maximum surface displacements of approximately 0.06 mm. However, during this quiet period not only earth tides were observed, but also an additional large trend or drift was observed. Detailed information on the methodology used to interpret these issues is presented in the results and analysis section of this chapter.

#### ***5.2.1.1 Time scale effects***

The high sensitivity of the array of tiltmeters allows the recording of earth tides, seasonal earth movements, rain events, heavy snow events, and the secondary effects of instrument installation. As discussed above, tiltmeter arrays have proven effective in monitoring a short-term application, like induced fracturing, because most of the external events occur on a different time scale than the fracturing event. During the analysis of hydraulic fractures, movements on time scales that differ from the event in question are generally straightforward to filter.

During the analysis of long-term events, data filtering of background, unrelated events not associated with reservoir processes become more difficult because the events are of equal magnitudes. Data filtering must be done carefully to ensure information associated with a subsurface-initiated deformation response, which has propagated to the surface, is not inadvertently removed from the data. The tiltmeter tool motion due to near-surface effects, including ground water level changes and thermal effects, may remain in the data and affect the tilt interpretation. Consequently, if the tiltmeter array were dense enough, it would theoretically be possible to filter out motion that fails to affect nearby tools in a

coherent manner consistent with deformation sourced at or near the injection depth. However, this type of filtering is not developed to a point of sufficient robustness. Furthermore, the CSEMP project deployed a relatively sparse tiltmeter array which did not allow this filtering technique to be used. On the other hand, earth tides effects did not seriously compete in magnitude with induced reservoir surface displacements, and could be filtered from the measured data due to their rhythmic nature and their smaller rate of deformation.

As a result, long-term data are typically handled differently than short-term data. For short-term injection scenarios, dislocation models using either rectangular dislocations in homogeneous half spaces [37], elliptical models in homogeneous spaces [38], rectangular dislocations in layered half spaces [39, 40], or distributed strain solutions [41] can be applied to find the dislocation parameters that best fit the measured tilt. For longer-term injections, where a few dislocations growing smoothly over the entire analysis period are unlikely to provide a satisfactory match to the measurements, a different method of interpretation is needed.

One potential method for interpreting long-term measurements is to utilize the raw surface tilt measurements, which represents the change in surface displacement gradient, to subdivide the data into spatial and temporal subsets. Integrating this data permits tracking surface elevation changes, which alone is a valuable monitoring technique. Another benefit of using surface displacement gradients to confirm the magnitude and direction of surface movements is that these measurements are independent from the selection of geomechanical reservoir properties [42, 43].

The tiltmeter tools used in CSEMP record raw tilt in microradians ( $\mu\text{R}$ ) in the X and Y directions, voltage (V) of the battery supply, and downhole temperature ( $^{\circ}\text{C}$ ), including the fixed orientation of installation. The voltage and temperature are used to evaluate the integrity of the sensors. Average voltage readings of 13.5 V and the smooth transition of downhole temperature, no greater than  $1^{\circ}\text{C}$  per month, were normal CSEMP tiltmeter readings. Figure 5.22, Figure 5.23 and Figure 5.24 show an example of the resolution of the raw-tilt data of CSEMP at different time scales that includes the time during which the hydraulic fracture operation was conducted on June 5, 2006. Figure 5.22, Figure 5.23 and Figure 5.24 illustrate three sets of raw-tilt data from one tilt station for time scale periods of months, days, and hours, respectively. It can be observed that there is one order of magnitude difference between tilt data ( $\mu\text{R}$ ) for short-term events (Figure 5.24 -

hours), intermediate-term events (Figure 5.23 - days), and long-term events (Figure 5.22 - months). This highlights that at different time scales the induced tilt magnitude and trend are not the same. For example these figures show that the maximum induced differential x-tilt on a short-term event is 0.35  $\mu\text{R}$  (Figure 5.24), 7  $\mu\text{R}$  (Figure 5.23) for intermediate term is, and over 60  $\mu\text{R}$  (Figure 5.22) for long-term event. For the short-term hydraulic fracture operation, it can be seen that a rapid change in tilt occurred compared to the baseline signal. However, for the long-term surface tiltmeter applications, the differential induced tilt data due to reservoir operations were larger, similar or less than the maximum differential tilt measurement of the baseline readings over the same time period. For CSEMP, the expected surface deformations for the long term were of similar magnitude to the baseline deformations due to long-term near-surface effects, which complicates the analysis.

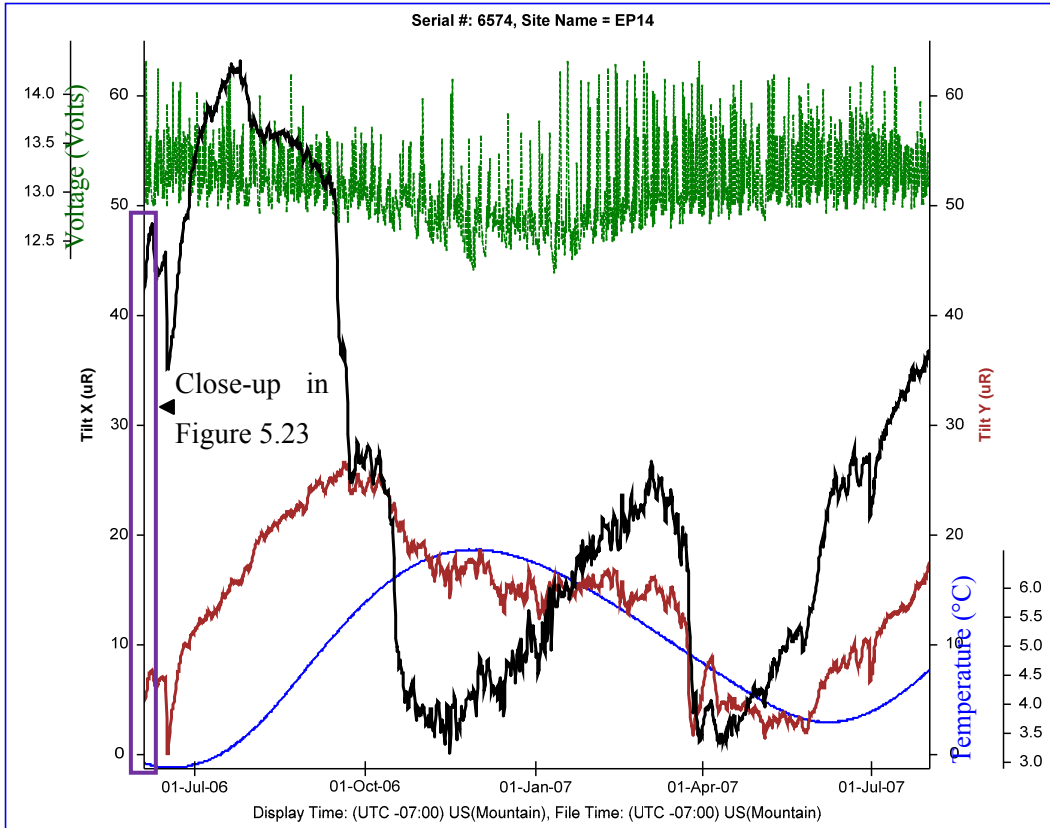


Figure 5.22 Recorded raw tilt data in months (Site EP14 in Figure 5.27).

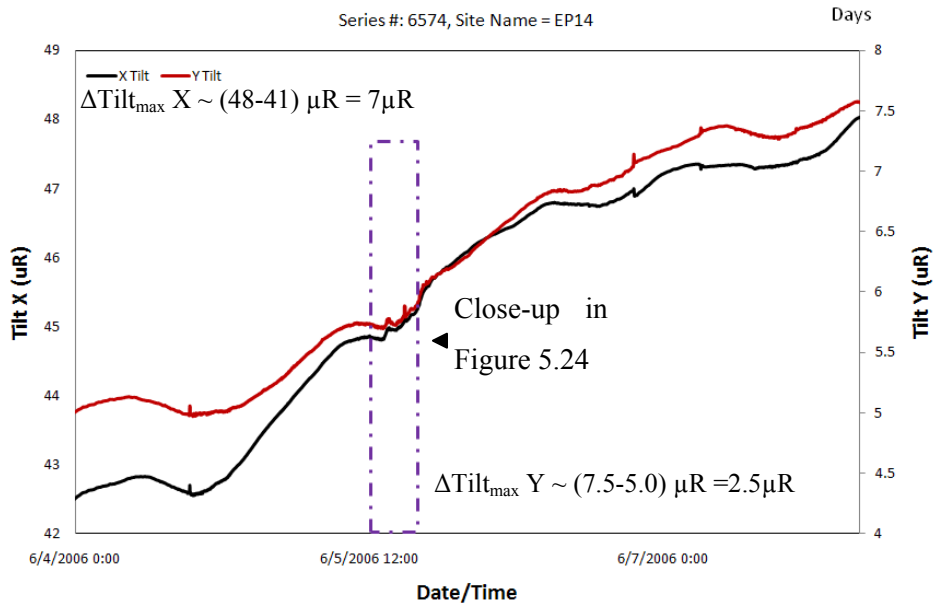


Figure 5.23 Recorded raw tilt data in days (Site EP14 in Figure 5.27).

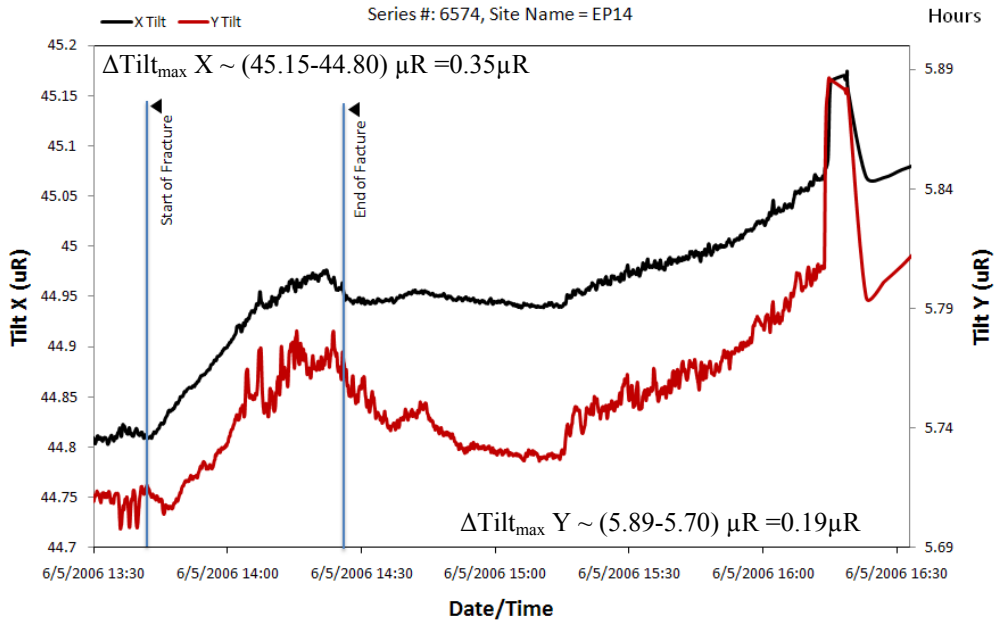


Figure 5.24 Recorded raw tilt data in hours(Site EP14 in Figure 5.27).

### 5.2.1.2 Rain and temperature effect.

The installation geometry of the tiltmeters is designed to prevent the direct ingress of water into the main borehole containing the tiltmeter tool. The ground water level outside the tiltmeter casing will fluctuate through the weather seasons. Rain infiltration leading to changes in the water table will result in volumetric deformation within the soil and may lead to tilt measurements that are unrelated to reservoir processes. Since ground water is subject to flow and elevation changes in the ground, standing and moving ground water in the area originated by rain can cause instruments to deflect depending on the soil composition surrounding the tiltmeter locations. Figure 5.25 presents examples of data affected by rainstorms.

Figure 5.25 depicts the complete tilt data from site EP06 (Figure 5.27) for June 2006, showing the changes on tilt data (movement) observed on June 8-9 and 15-16 that correlates with days with considerable precipitation observed at the closest (approximately 30 km away) weather station that reported a total of 41 mm and 22 mm of rain for June 8 and 15, respectively. Similar changes in tilt data were observed in all tiltmeters.

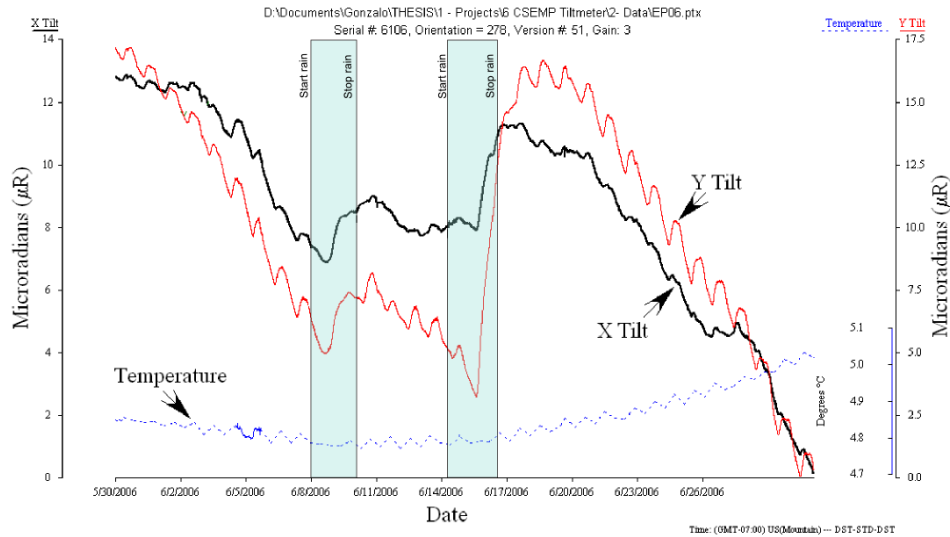


Figure 5.25 Monthly tilt data from Site EP06 - June, 2006. Major changes in tilt correlates with rainy days.

For systems installed specifically to be isolated from environmental effects, these apparent weather-correlated motions at these sites were larger than expected. The exact reasons for the deflections are unclear, but the sensitivity to weather may be related to the particular soil type, an issue with the site construction, or groundwater level changes in the area. The results suggest that a modified installation designing such as greater burial depth of the tiltmeters, isolating them from near surface motion is required if the objective is long term reservoir monitoring.

Each tiltmeter records downhole temperature. The annual temperature variation of CSEMP tiltmeter locations from 2006 to 2007 was  $\pm 2$  °C (Figure 5.22). Annual ground profile temperature variations depend on the soil type, ground water table flux and precipitation/snowing. The author could not quantify the effect of this temperature variation on the long-term tilt readings because at the time of the study Pinnacle did not have a calibration of temperature for the tiltmeter tools. This suggests that a calibration of the tools in this temperature range is needed to understand and document the effect of temperature on tilt reading for a future research.

For long-term monitoring purposes, the periods with heavy precipitation could be filtered or ignored due to the fact that the time frame of occurrence of these events is relatively short (usually 1-2 days) when compared to the time period of monitoring (weeks to months). Given the sensitivities demonstrated within the CSEMP project, it is highly recommended that local weather stations be installed in conjunction with tiltmeter arrays deployed for long-term reservoir monitoring projects (i.e., CO<sub>2</sub> geological storage).

## **5.2.2 Results/analysis of induced fracturing and CO<sub>2</sub> injection**

### **5.2.2.1 Fracture tilt mapping**

While not the focus of this research, a summary of the hydraulic fracture geometry interpretation using the tiltmeter measurements is provided to allow comparisons with the long-term reservoir monitoring results. The results of the fracture interpretation were generated by Pinnacle Services [44].

The injection well was stimulated for coalbed methane (CBM) production using a single-stage hydraulic fracture treatment. Approximately 352 tonnes of KCl water and 12 tonnes of hydraulic fracture sand were injected during the fracture operation through the perforations in the well casing from 418.5 m to 427.0 m. The objectives of the fracture mapping were: 1) to determine fracture coverage in the pay zone along the vertical wellbore; 2) and to measure fracture geometry (height, length and azimuth).

Baseline data was collected for the surface tiltmeter array for several weeks prior to the beginning of the project, and was downloaded just prior to the hydraulic fracture. The injection well at CSEMP was fractured on June 5, 2006. To improve the interpretation of hydraulic fracture dimensions, an additional string of 13 borehole tiltmeters was installed temporarily in the production well (100/7-28-46-7W5M), which served as an observation well and was located 200 m from the “Frac” well as illustrated in Figure 5.27. During the hydraulic fracture stimulation, data was collected and displayed in real-time from the borehole tiltmeter array and recorded in memory in the surface tiltmeter array. Following the treatment, all surface-recorded data were retrieved and combined with the downhole data for use in computing the size and direction of the induced hydraulic fracture.

The data were analyzed using a homogeneous half-space dislocation solution, developed by Okada [37]. While uniform layers have essentially no impact on the dislocation orientation determined from surface tiltmeter measurements, strong layer contrasts can influence downhole tiltmeter measurements enough to impact the analysis. A study completed for the Gas Research Institute [45] determined that the effects of strong layer contrasts are generally negligible unless the layer modulus contrasts exceed a factor of four. Even then, the most significant effects are only noticeable very close to the layer interfaces. The layers present in the CSEMP pilot were not considered sufficiently high in contrast or thick enough to warrant the complexity of a layered model calculation. Figure 5.26 presents some log results from the “Frac” well (102/7-28-46-7W5Mer).

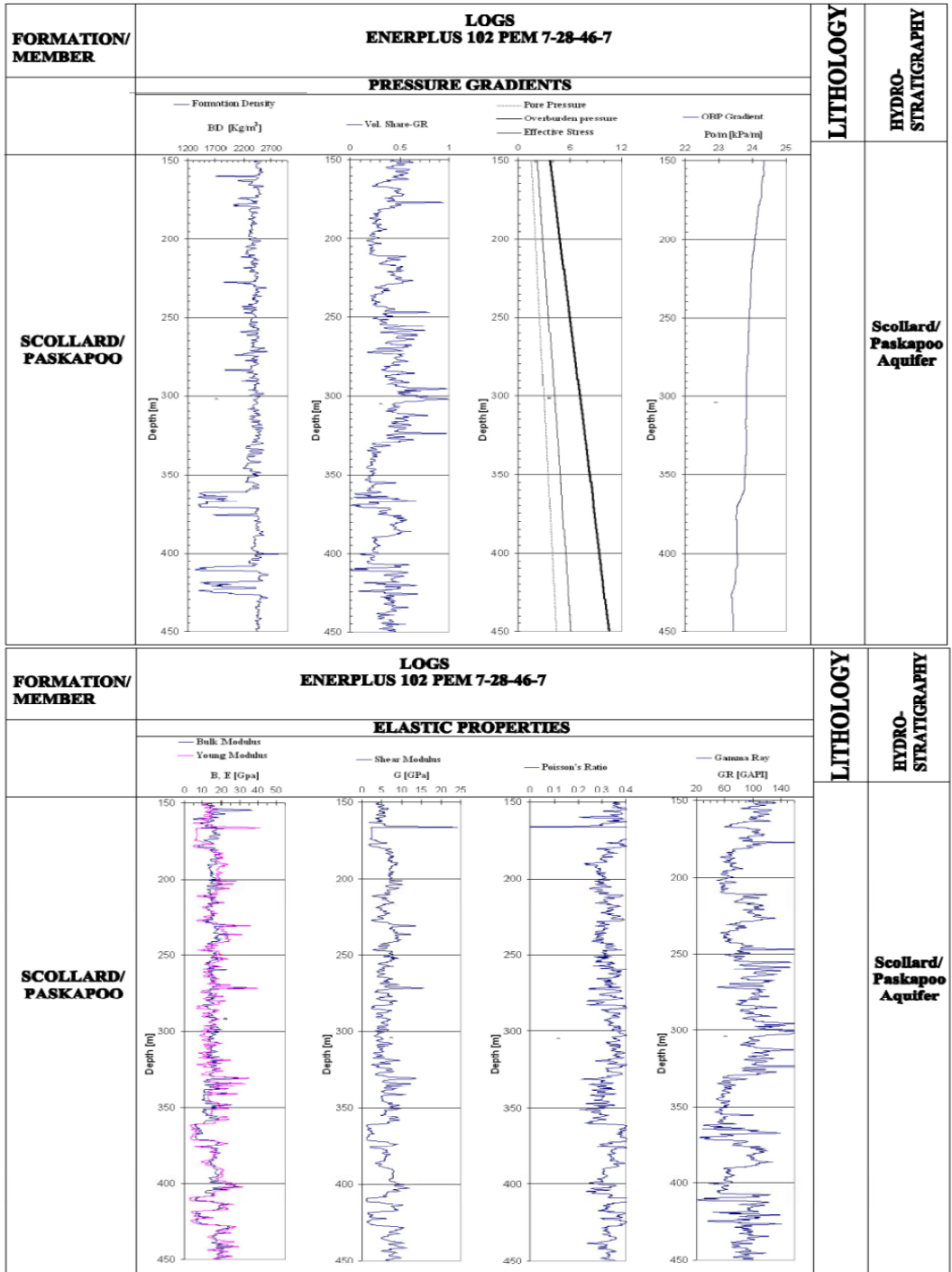


Figure 5.26 Interpretation of log results from Injector 102/7-28-46-W5M (Figure 5.27).

From the downhole and surface tiltmeter array, the azimuth of the fracture was computed to be N50°E with a dip of 86° to the SE. These results are shown in Figure 5.27. This fracture was 88% vertical with the horizontal component(s) representing 12% of the fracture volume. The maximum surface deformation was 0.05 mm. The fracture length was  $\geq 150$  m, while the fracture height was 40 m centered at a depth of 430 m.

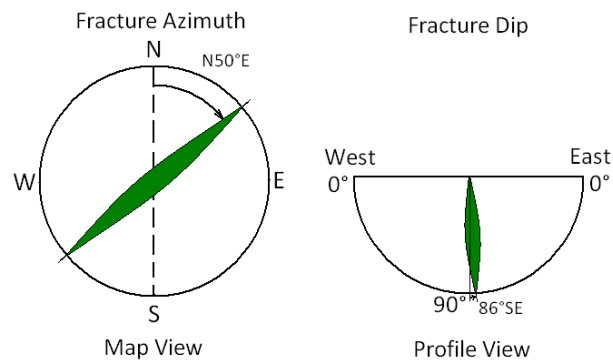
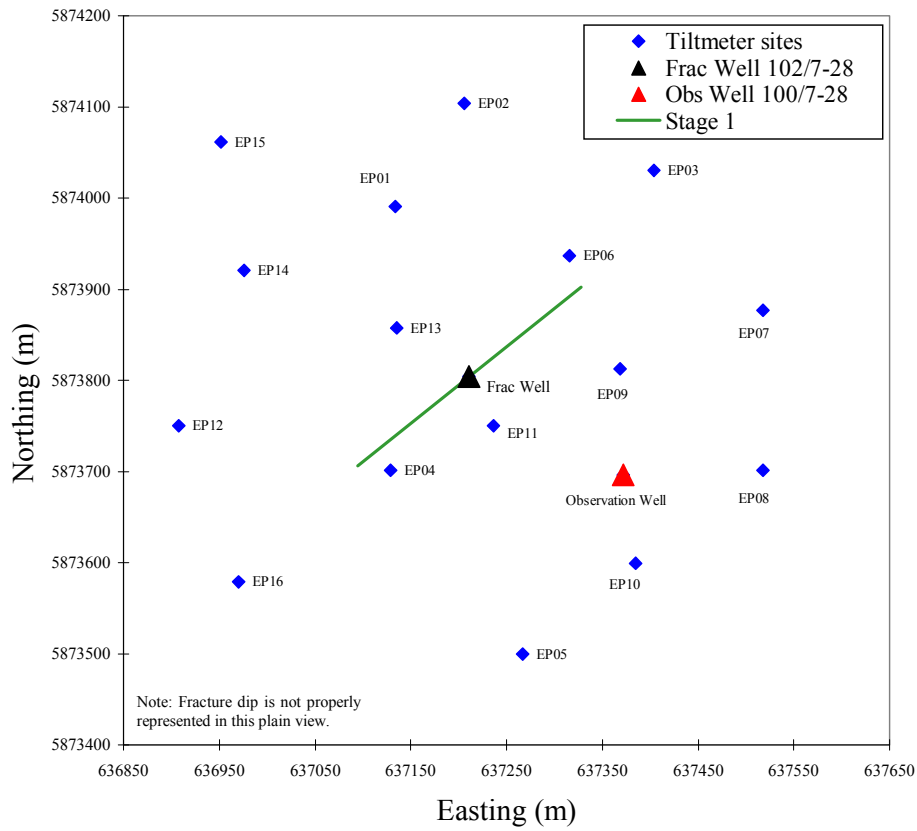


Figure 5.27 Map view showing the azimuth for the fracture treatment.

Figure 5.28 shows tilt vectors and surface deformation from the hydraulic fracture operation. Figure 5.28 (a) shows measured and theoretical tilt vectors for the surface deformation. Each vector is constituted with dip (tilt magnitude) and dip-direction obtained between two times ( $t_2 - t_1$ ). The theoretical tilt vectors are extracted from the ground displacement closed-form solution relative to the measured tilt vector. This model uses the internal fracture deformation due to shear and tensile faults in a half-space derived by Okada [37]. Figure 5.28 (b) presents the best-fit surface deformation surface

that also illustrates the orientation of the fracture. The downhole tiltmeter array provided additional data to help constrain interpretations of fracture height and length as illustrated in Figure 5.29. The fracture length was estimated to be  $\geq 150$  meters, while the fracture height was estimated to be 40 meters, centered at 430 meters.

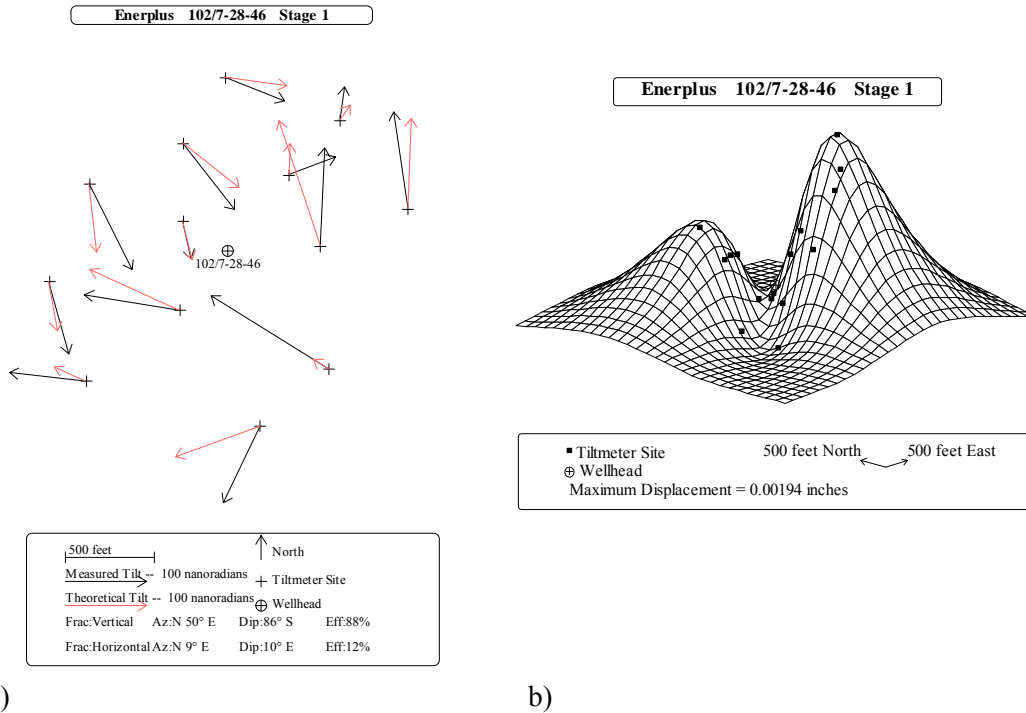


Figure 5.28 (a) Observed and theoretical tilt vectors for the best-fit fracture system and (b) surface deformation for the 102/7-28-46-7W5 Frac treatment (418.5 m to 427.0 m).

Uncertainty for the fracture orientation was determined through a Monte-Carlo analysis. In this analysis, the uncertainty in measurement for each tiltmeter site is determined by extracting data from a time period of the same duration as the fracture treatment, during a time when no actual treatment occurred. The measurement uncertainty is a vector added to the actual measurement, in a random direction for each site, and a new best-fit fracture system is calculated. The procedure is repeated for a large set of different perturbations of the measured data, and the uncertainty is calculated as the standard deviation of the solution set from all the runs. For this treatment, the calculated uncertainty was less than  $2^\circ$  in both azimuth and dip directions.

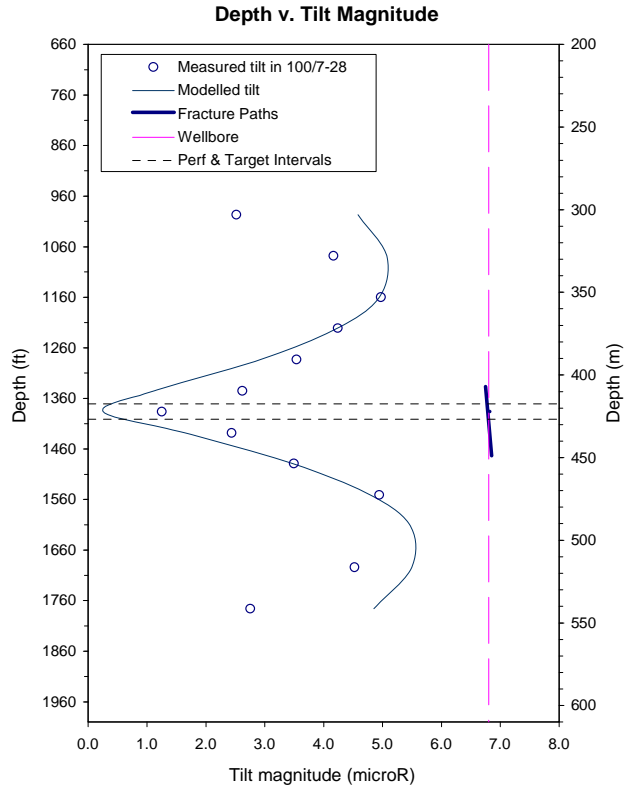


Figure 5.29 Offset well tiltmeter tool movement over the course of the fracture treatment [44].

Uncertainty for the fracture dimensions is calculated through a different method. The signal to noise ratio for downhole tiltmeters is typically much larger than for surface tiltmeters, so the dominant factor in determining the uncertainty of the solution is not the determination of the measured tilt, but the ability of the relatively simple dislocation model to fit the measurements. For the dimension measurements obtained by the downhole tiltmeters, uncertainty is determined by running the model over a wide range of parameters and determining the outer limits of parameters that could reasonably fit the measured data. For this treatment, the analysis showed that there is little sensitivity to the fracture half-length once the length extended beyond 150 m, and the fracture height could reasonably fit the measurements if it falls within 10 m of the optimal solution of 40 m.

### 5.2.2.2 Phase I – CO<sub>2</sub> micro-pilot injection monitoring

A continuous CO<sub>2</sub> injection test was performed on well 102/7-28-46-7W5M from September 8 -12, 2006. Recall that the primary focus for surface tiltmeter measurements during Phase I CO<sub>2</sub> injection was to detect any changes to the fracture and/or swelling of the coal matrix. The downhole tiltmeter string was removed from the observation well

and was not available for the long-term monitoring program. Cumulative deformation (relative) observed in time frames generated with tilt data (15 minutes increments) during the micro-pilot CO<sub>2</sub> injection shows two distinct uplifts (Figure 5.31): one to the NW and the second to the SE of the well. This produces a trough, which is oriented to the fracture azimuth mapped during the main fracture treatment. The maximum cumulative deformation observed in Figure 5.30 over a four-day period (September 8 -12, 2006) is approximately 0.7 mm. This interpretation correctly depicts the cumulative ground deformation due to CO<sub>2</sub> injection, earth tides, temperature changes and rainfall. The last three events must be filtered out to determine the magnitude of the deformation due to the CO<sub>2</sub> injection into the Ardley coal.

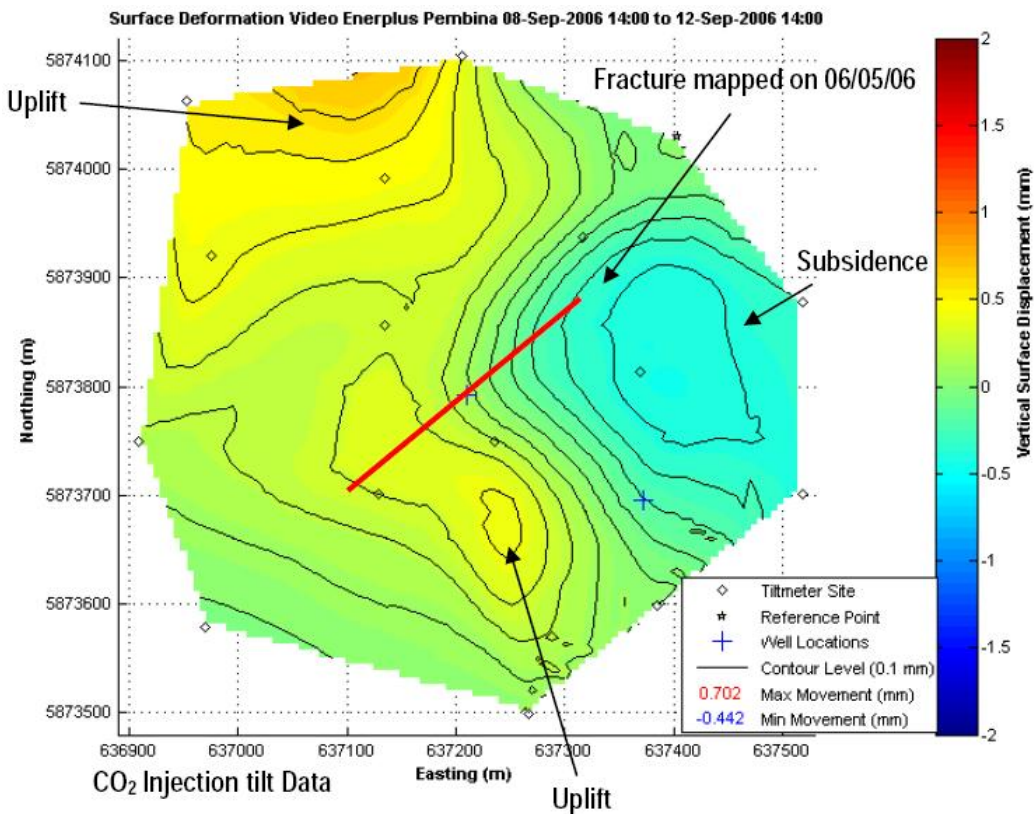


Figure 5.30 Surface deformation during CO<sub>2</sub> injection [46].

To have a better understanding of the drifts, intrinsic movements, and random noise affecting the instruments, an image of cumulative deformation (relative to site EP03) was generated with background tilt data before the CO<sub>2</sub> injection between September 4, 2006 and September 8, 2006. Figure 5.31 shows the deformation over the same amount of time (four days) as the CO<sub>2</sub> injection, but over a period when no fluid was injected.

There are some similarities on the trend of surface deformation in the image presented in Figure 5.31 when compared to the image generated during the CO<sub>2</sub> injection (Figure 5.30); however, the magnitude of the maximum and minimum values of deformation is clearly smaller than the values under CO<sub>2</sub> injection. The maximum cumulative deformation observed in Figure 5.31 is approximately 0.4 mm.

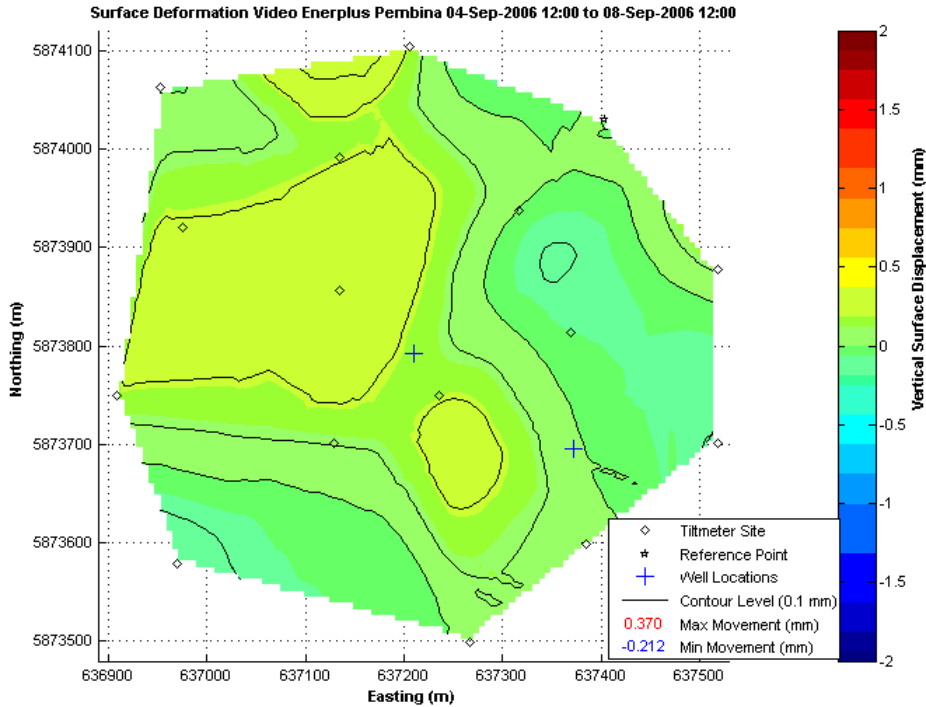


Figure 5.31 Surface deformation before CO<sub>2</sub> injection (September 4-8, 2006) [47].

Because the trend observed in the data before (Figure 5.31) the CO<sub>2</sub> injection has some similarities to the trend during the CO<sub>2</sub> injection, the values of relative deformation of background data were subtracted from the values of relative deformation during the CO<sub>2</sub> injection. In other words, the background motion prior to the CO<sub>2</sub> injection was assumed to continue throughout the injection.

The resultant grid that is assumed to have minimum background deformation effects was calculated, and the resultant image is shown in Figure 5.32. The maximum cumulative deformation observed in Figure 5.32 is approximately 0.5 mm, which is still one order of magnitude higher than during the fracture job deformation; and is attributed as a result of the deformation from the injection of 180 tonnes of CO<sub>2</sub> in the micro-pilot phase.

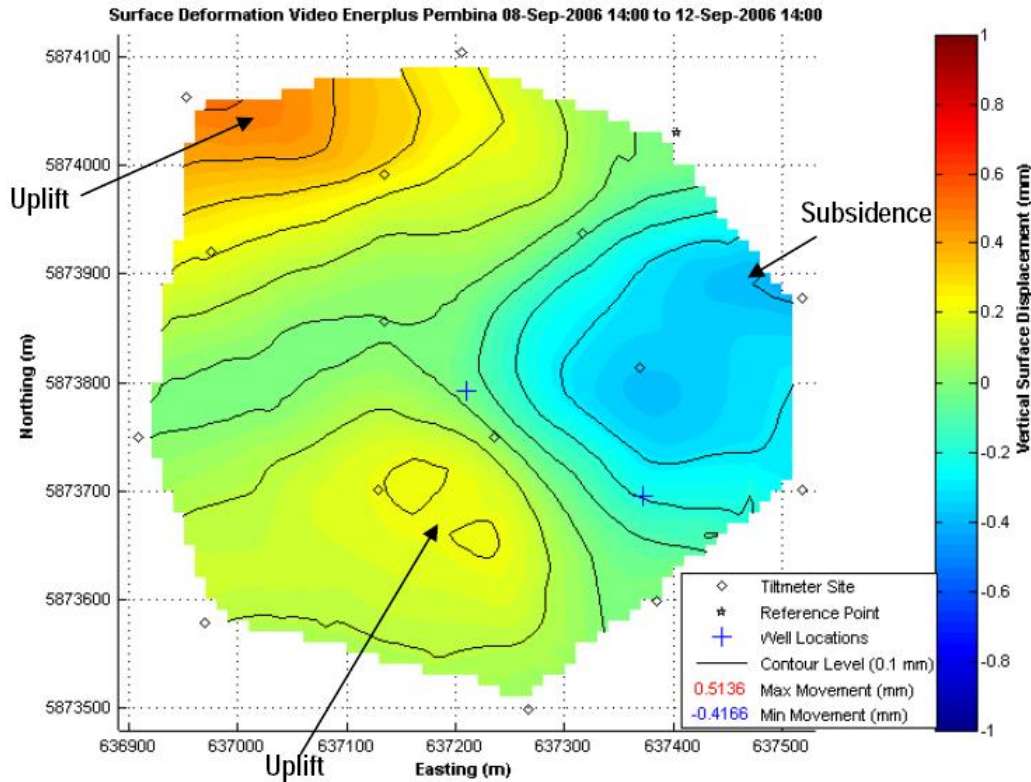


Figure 5.32 Surface deformation after post-processing of data during CO<sub>2</sub> injection (September 8-12, 2006) [47].

### 5.2.2.3 Phase II - CO<sub>2</sub> pilot injection monitoring

It was predicted that during the duration of the micro-pilot CO<sub>2</sub> injection (4 days), swelling was probably affected by the time frame of CO<sub>2</sub> absorption that tended to smear the deformation out over a larger area. However, the surface tiltmeter array was also exposed to 19 days of CO<sub>2</sub> injection with an approximate total volume of 854 tonnes in the longer pilot test. In this case, diffusion would be less of an issue.

The deformation created during the first increment of 65 tonnes of CO<sub>2</sub> injected in Phase II can be analyzed separately. Deformation in a north-south direction is observed with a maximum total vertical displacement (tvd) of + 0.15 mm during the first day of injection (June 28-29, 2007, Figure 5.33).

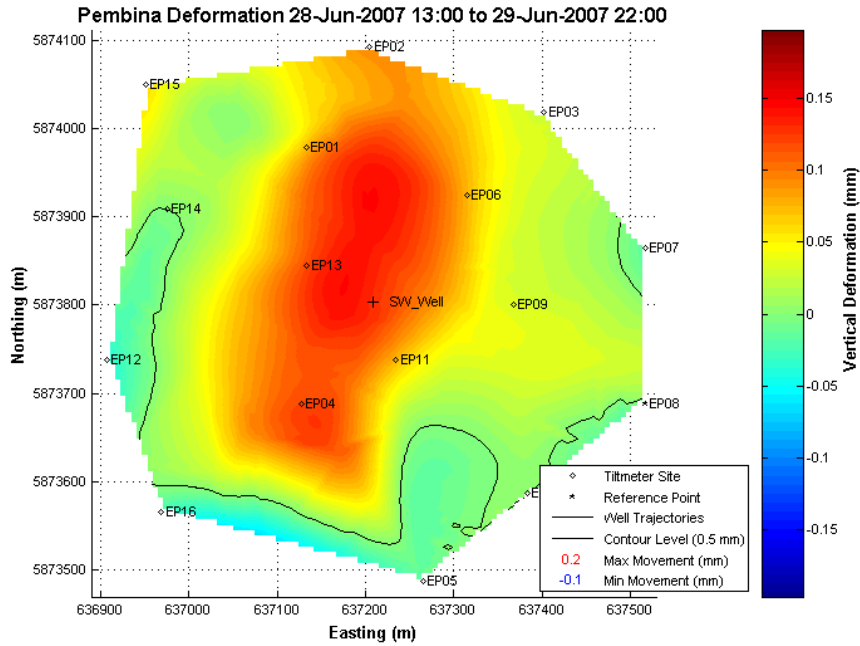


Figure 5.33 Mapped surface deformation during the first CO<sub>2</sub> injection, up to where weather apparently began to affect the tiltmeter data [48].

However, during the rainstorm and continued CO<sub>2</sub> injection, the tvd decreased to -1 mm (June 28-30, 2007, Figure 5.34).

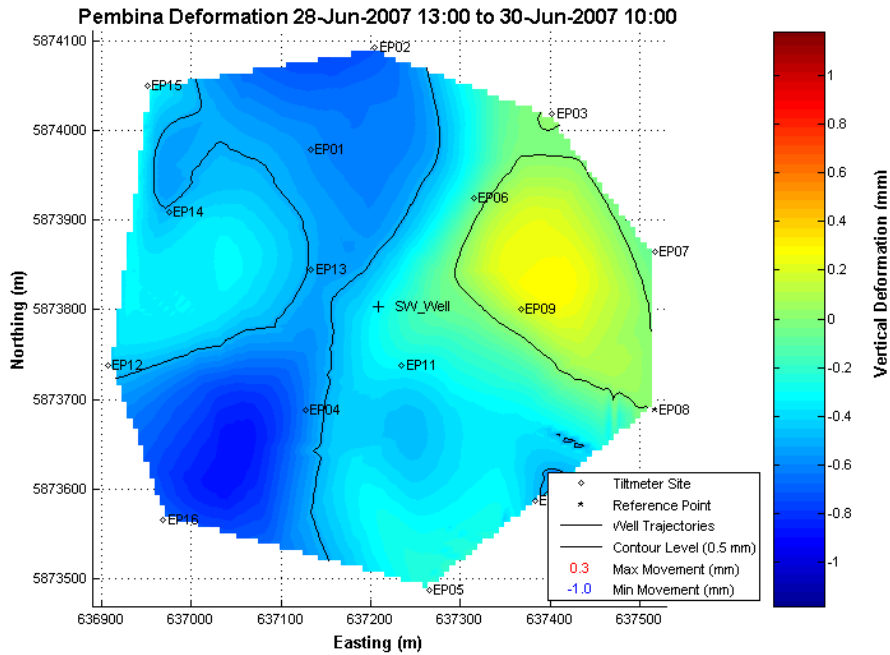


Figure 5.34 Mapped surface deformation during the first CO<sub>2</sub> injection, including the last 12 hours where weather apparently began to affect the tiltmeter data [48].

After a period when a lightning strike resulted in CO<sub>2</sub> not being injected, the true vertical depth (tvd) decreased further to -0.4 mm (June 30-July 3, 2007, Figure 5.35).

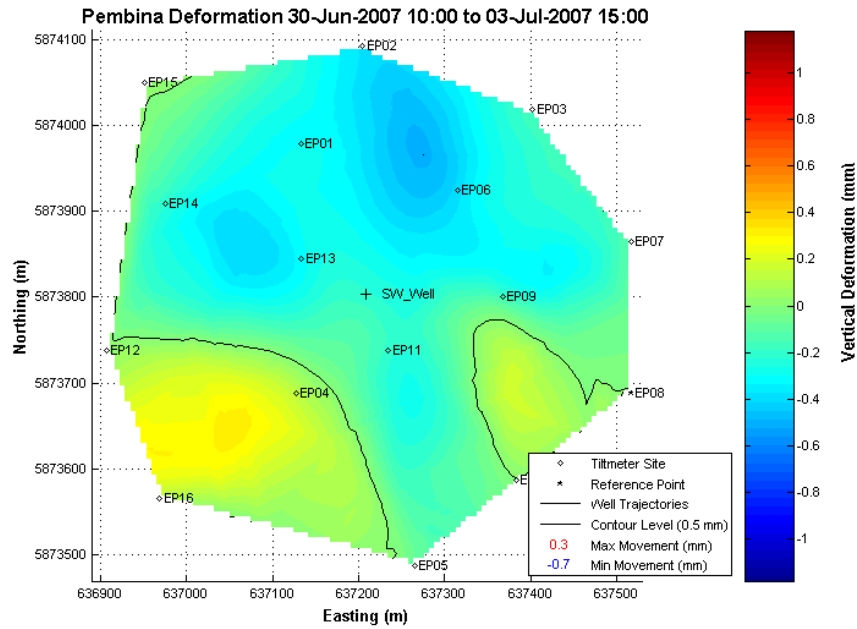


Figure 5.35 Deformation during the down period between CO<sub>2</sub> injections. Note that weather effects are still considered very significant during this period.

After one day of injecting CO<sub>2</sub> again, a tvd of +0.3 mm was observed (July 3-4, 2007, Figure 5.36).

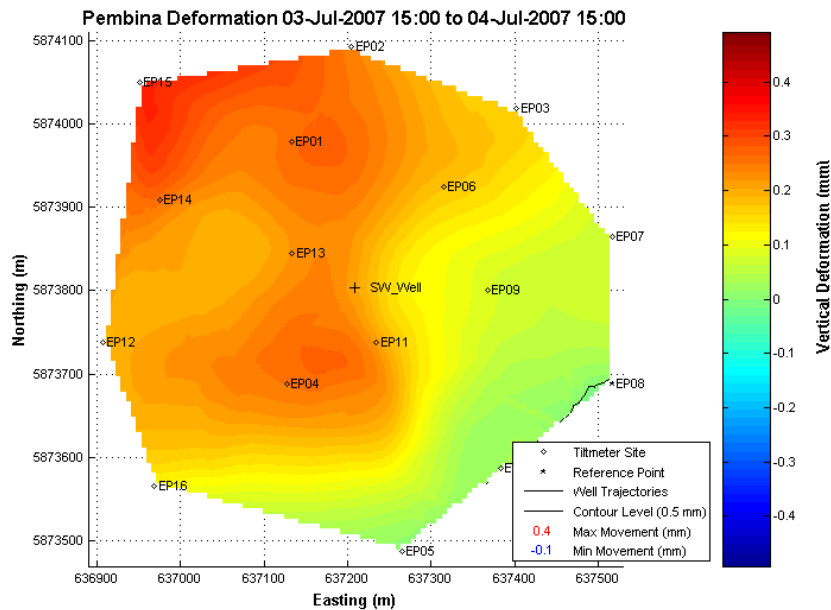


Figure 5.36 Deformation during the first part of the second CO<sub>2</sub> injection (injecting at 35 tonnes/day) [48].

After eight days of CO<sub>2</sub> injection (July 4 -12, 2007), a tvd of +1.2 mm was observed (Figure 5.37).

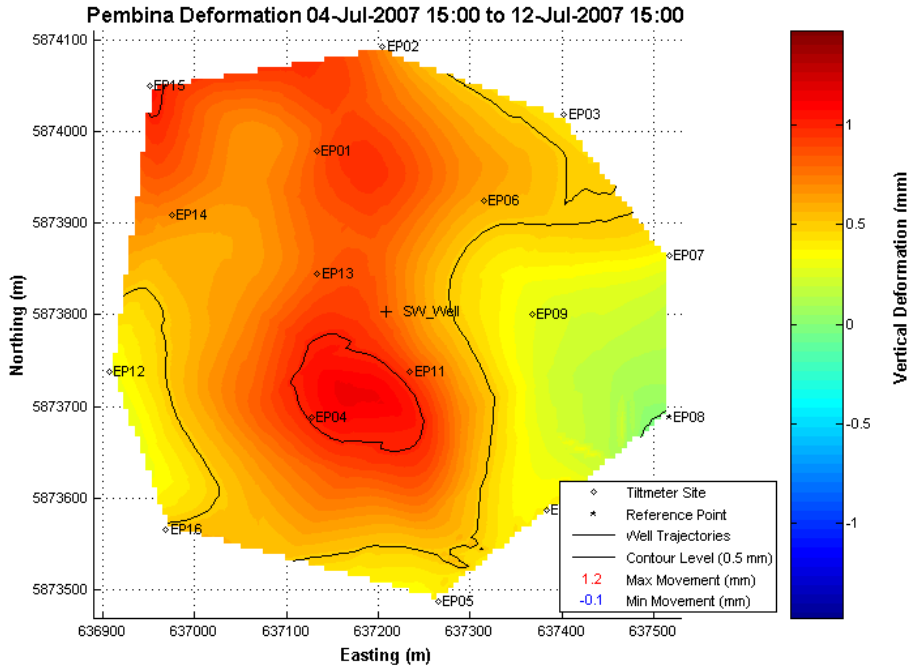


Figure 5.37 Deformation during the injection Phase II (injection rate: 45 tonnes/day) [48].

After eight more days of injection, a tvd of + 0.7 mm was observed (July 12-20, 2007, Figure 5.38).

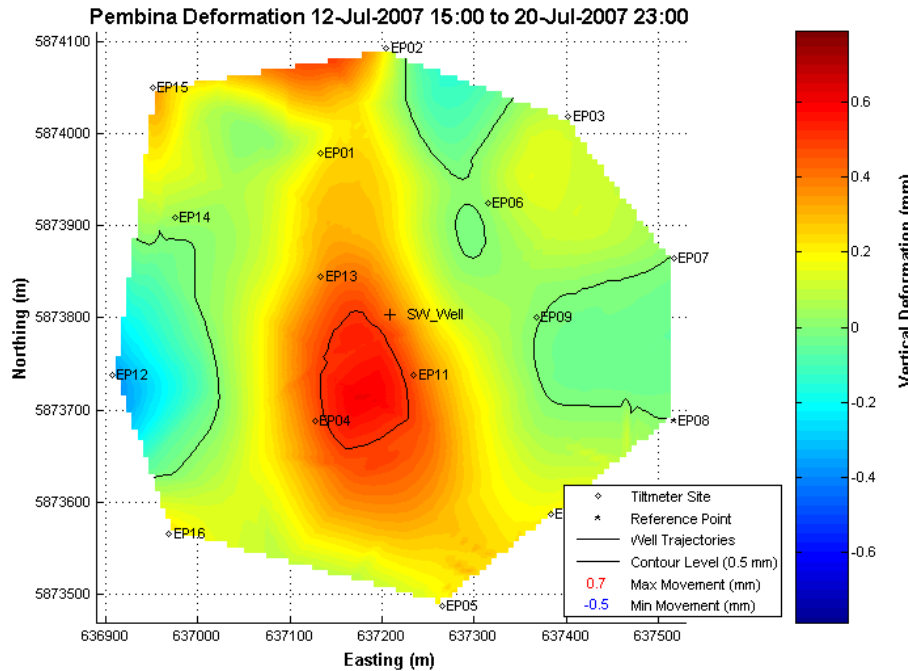


Figure 5.38 Deformation during the injection Phase II (injection rate: 35 tonnes/day) [48].

From Figure 5.34 and Figure 5.35, it is observed that during precipitation periods, a loading effect is captured by the surface tiltmeter array signature that may possibly be due to the heavier wet soil. It is not clear that this issue is due to a specific problem at this location, the installation techniques used, something inherent in the tiltmeter tool or its application. Although the error introduced by rain was accounted (recorded in Figure 5.34 and Figure 5.35) for in the calculation, other surface events may have affected this value. During the injection stages, the surface tiltmeter array captured the positive total vertical displacement of the surface deformation. For the total 850 tonnes of injected CO<sub>2</sub>, a positive maximum deformation of approximately 2 mm was estimated after ignoring the effects of the rain.

### **5.2.3 Discussion**

Surface tiltmeters are sensitive to reservoir deformations from CO<sub>2</sub> injection as shown here by tiltmeter measurements, but surface processes also impact the instrument responses. Many surface effects are cyclical and elastic in nature allowing the desired reservoir signal trends to show through when measurement periods are appropriately chosen. If an injection interval corresponds closely to a period of heavy rain and ice thaw, then the desired signal would be lost in extraneous sources. If the injection and measurement period are long enough for the temporary signal spike to return back to the baseline, then the signal may often be extracted. The analysis depends upon the total change in tilt from one time to another. Deformation that occurs in between those two measurement points, as long as it is elastic and has time to return to the baseline, has no impact on the results.

### **5.2.4 Conclusions and Recommendations**

Tiltmeter technology for short-term (hours) applications as a fracture diagnostic tool has been successfully applied in the oil and gas industry since 1996. Fracture mapping is much longer than short-term noise (e.g., traffic) and shorter than long-term external effects associated with seasonal changes or site and instrumentation drift. This characteristic allows the fracture signals to be extracted even in the presence of significant amounts of noise. The results of the fracture mapping, using surface tiltmeter array and downhole tiltmeters, for the hydraulic fracture operation in CSEMP was successful.

This long term surface tiltmeter array reservoir monitoring (months) application, possibly the first of its kind (at least at the time of the CSEMP pilot) to interpret the deformation of coal from tiltmeters due to CO<sub>2</sub> injection, could capture a positive maximum deformation of approximately 2 mm after injecting 850 tonnes of CO<sub>2</sub> in the Ardley coals at a depth of 400 m. Extensive examination of the tilt signature was conducted to extract the reservoir response during the CO<sub>2</sub> injection. It is expected that for a surface deformation greater than 5 mm the signature of reservoir response can overcome the external effects in long-term reservoir monitoring.

The most obvious result from the reservoir monitoring analysis at CSEMP is that there is a large amount of movement in the tiltmeter tools that is not related to the injection, which complicates the analysis. The author considers that for the layout and installation configuration adopted at CSEMP, this technology cannot be used as an indirect measurement of CO<sub>2</sub> migration. The tools have potential, but more research and development is required to overcome the installation issues and the effect of the ambient variables that are unique for each site.

Compared to hydraulic fracturing, images of surface deformation during CO<sub>2</sub> injection are strongly affected by sensor motion due to sources other than the CO<sub>2</sub> injection, including rainfall and possible temperature effects. Constructing deeper sites and using a denser tiltmeter array could substantially mitigate these effects. During analysis of hydraulic fracture treatments, sensor motion on time scales shorter and longer than the treatment are removed, minimizing effects of temperature, rainfall, sensor drift, etc. Since the time scale of the reservoir motion due to the longer term CO<sub>2</sub> injection cannot be predicted beforehand (for instance, the injected fluid may move to a shallower depth partway through injection, causing a drastic change in signals), the temperature- and rainfall- induced motion cannot currently be distinguished from reservoir-sourced motion and is not removed when interpretations are made for long-term injection. The following recommendations are made to improve the sensitivity of surface tiltmeter arrays for long-term applications in CO<sub>2</sub> enhanced coal-bed methane projects:

1. Dramatic elevation changes evident in Figure 5.34 and Figure 5.35 are likely to be largely due to weather-related effects on the tiltmeter sites. It is highly recommended that a local weather monitoring station be installed in conjunction with tiltmeter arrays deployed for long-term reservoir monitoring projects.

2. Temperature calibration for expected ground temperature variations is highly recommended for long-term surface tiltmeter applications.
3. For long-term application of MMV activities for CO<sub>2</sub> geological storage, a modified installation design such as great burial depth of the tiltmeter is required. For reservoir monitoring at the Pembina, tiltmeter sites at a depth of 6 m were found to be inadequate. Twelve metres deep is recommended to limit the site movement due to rainfall, temperature changes, and other environmental effects. Additional research is required for this issue.
4. Increase the number of tilt sites by using a denser array, to ensure all changes in the surface shape are captured by the tiltmeters.
5. Adding GPS to the array provides a reference position that is stable over long periods (more than 30 days) and is not subject to drift. For any monitoring that will occur over a period of several months or more, adding GPS will improve the results.
6. Expose the tools to longer periods of CO<sub>2</sub> injection and production to characterize and verify the operation of the tools and array.
7. There is some potential to filter the tiltmeter data to remove effects that are not likely to be sourced from at or near the injection depth. This option is currently being developed.

## **CHAPTER 6 Cement Placement Around Downhole Monitoring Sensor Housing Systems**

### **6.1 Introduction**

Detailed analyses of the OW were completed over the tenure of the Pembina Cardium CO<sub>2</sub> Monitoring Project, including completion job, cement behaviour, annular flow behaviour and integrity of downhole systems long-term pressure/temperature history. Synthesis and integration of these analyses helps to inform recommendations on the deployment of downhole technology in OWs used for monitoring and verification of CO<sub>2</sub> movement in the subsurface. Post-cement placement modeling was conducted that couples real-time data and analytical, and numerical simulations was conducted to enhance the planning, and operations of cement placement around deep downhole monitoring tools, and to identify difficulties of cement placement. The analytical simulation provides an assessment of the pressure boundary conditions along the wellbore profile at the metre scale, and the numerical simulation assesses the impact, at the millimetre scale, of the geometry of the downhole monitoring tools during the cement placement.

#### **6.1.1 Cementing**

For this monitoring well, cementing all sensors in place was necessary to ensure hydraulic isolation between pressure monitoring and fluid sampling points and to minimize acoustic impedance between the geophone sensors and the formation. To further improve the acoustic coupling of the geophones to the formation, cement was retained within the tubing string [49-51]. Once the assembly had been fully installed and prior to cement placement, each sensor was tested to verify its operation.

During cementing, the control of the pumping and circulation rates are important to minimize the shear forces generated with a high circulation rate that could potentially damage sensors and cables. Although not implemented in this project, real time downhole pressure and temperature measurements made available to the cementing contractor would provide significant data on the progress of the cementing operation. For the present case study, detailed information on the cement placement obtained from the cement job field logs, and the downhole pressure and temperature results are used to

assess the issues of cement placement around complex downhole instrumentation assemblies.

### **6.1.2 Analytical interpretation**

The analytical evaluation of the cementing operation of the OW at the Pembina Cardium CO<sub>2</sub> monitoring pilot focused on two elements: (1) the cementing phase during the operation; and (2) the hydraulic transmissivity of the channel or flow path developed the cementing operation.

The first study of the post-cement job evaluation coupled real-time downhole pressure and temperature measurements with an analytical assessment of fluid circulation using CEMPRO5<sup>TM</sup>, a commercial software for cement displacement simulations. The 1D analytical solution incorporated in CEMPRO5<sup>TM</sup> is the result of integrating flow equations across sections with the frictional pressure drop along the section [32, 52]. The boundary conditions for the simulations are fluid density, fluid rheology, pumping rate, and well configuration (casing sizes, and the internal and external diameters of the tubing at various depths). The program calculates the dynamic pressure and outlet flow rate during cement slurry placement process, and bottomhole equivalent circulation density.

Two important constraints must be considered in post-cement placement analysis. These are: (1) the equivalent circulation density (ECD), which is used to evaluate possible hole collapse, fluid invasion, or fracturing of the formation, and (2) the flow rate at each depth interval to determine the possible creation of micro-annuli at any given annular geometry [52].

The second analytical study focuses on the evaluation of the hydraulic transmissivity of the channel or flow path, which was constrained by a measured wellhead fluid flow rate of 10 L/min.

### **6.1.3 Computational fluid dynamic modelling**

It was initially intended to model the full-size wellbore, but the large scale ratio ( $10^5$ ) between the length and the diameter of the wellbore and the significant computer power and computational time required for this scale of modelling limited the extent of this research. Therefore, the use of computation fluid dynamics (CFD) on this research focuses only on small sections of borehole, and the hydraulic isolation assessment of permanent downhole sensors installations.

## 6.2 Cement job analysis and results

The early observations during the cement circulation are presented in this section, focusing on the response of the deepest pressure and temperature gauge (1610 m). Figure 6.1 illustrates the downhole pressure and temperature measurements from one shallow gauge (1303 m) and one deep gauge (1610 m) during the 60 minutes of the cementing operation. In this process, the tubing and sensors were cemented into the wellbore by pumping a sequence of fluids (preflush water, spacer, cement slurry, and cement displacement fluid). All fluids during the cementing operation were circulated down the tubing and up the annulus between the tubing and casing. Details of the cement operations and downhole recorded pressure and temperature data are presented in §5.1.

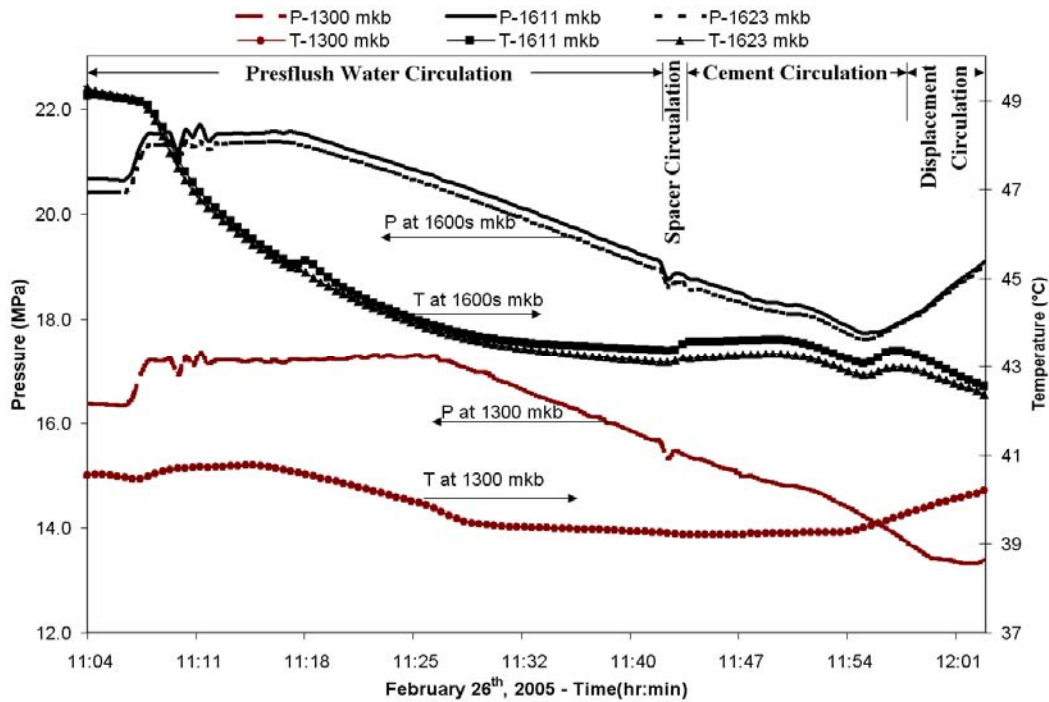


Figure 6.1 Recorded pressure and temperature during cement operation.

Figure 6.2 shows the steps analyzed for the cementing operation. The target depth of the cement top was 1200 m, cementing all sensors within the last 400 m of the cased well, which was initially filled with brine having a density of  $1.3 \text{ g/cm}^3$  (Figure 6.2(a)). Once the instruments had been deployed to their final depth and confirmed to all be operational, a preflush fluid [ $11.0 \text{ m}^3$  of water (density equal to  $1.0 \text{ g/cm}^3$ ) with  $2.0 \text{ L/m}^3$  of a corrosion inhibitor] was pumped at an average flow rate of  $0.3 \text{ m}^3/\text{min}$  (Figure

6.2(b)). The corrosion inhibitor was added to aid in casing and tubing cleaning and steel cement bonding. After the preflush fluid, a 0.2 m<sup>3</sup> fresh-water spacer was circulated at an average flow rate of 0.2 m<sup>3</sup>/min to minimize cement contamination by wellbore fluids (Figure 6.2(c)). The spacer was followed by 4.8 m<sup>3</sup> of CO<sub>2</sub>-resistant cement slurry (density: 1.76 g/cm<sup>3</sup>), with rheological parameters: power law index,  $n = 0.9839$ , consistency,  $K = 0.0619 \text{ Pa s}^{(0.9839)}$ , and pumped at an average flow rate of 0.35 m<sup>3</sup>/min (Figure 6.2(d)). Cement displacement was performed at 0.31 m<sup>3</sup>/min until the cement top was reached.

The cement volume was computed based on a final cement top of 1200 m deep. In general, the higher cement density results in a temporary differential of cement height between the tubing/casing annulus and the tubing. Once cement circulation stops, however, this differential height equilibrates and the cement tops are at the same depth. As illustrated in Figure 6.2(e), that did not occur for this OW. The cement in the tubing/casing annulus remained higher (i.e., at a shallower depth) than the cement top inside the tubing. The final depth of the cement was 1238 m in the tubing/casing annulus and 1290 m in the tubing [3].

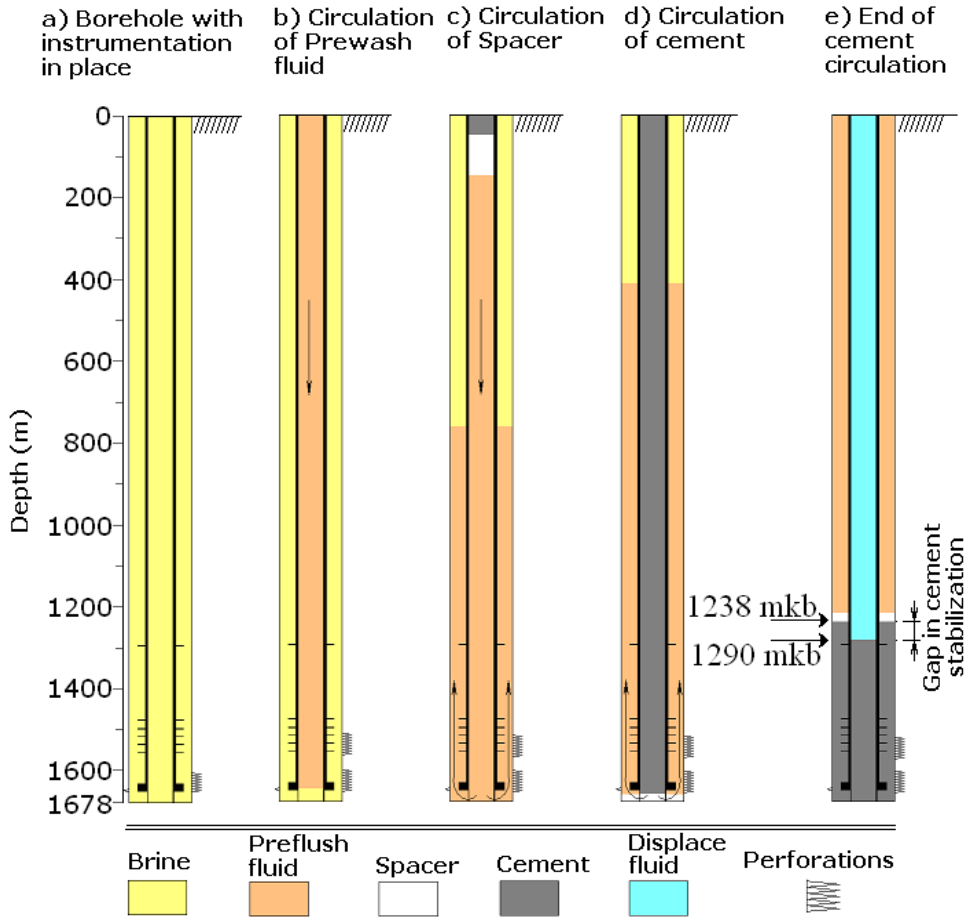


Figure 6.2 Steps in the cementation of the observation well from an analytical solution [14].

### 6.2.1.1 Simulated results

To improve our understanding of the cementing process for highly instrumented wells, a post-analysis of the cement operation was performed using CEMPRO5<sup>TM</sup>. The analysis focuses on the pressure and temperature signature profile along the wellbore, and is divided into two sections: (1) the preflush circulation; and (2) the spacer and cement circulation. The analytical solution for the 1D numerical problem attempts to capture the complex 3D numerical problem through correlations. This analytical process is used in most commercial simulators [52, 53], which should match actual operation conditions, and ideally, simulations' results should match field data. However, unforeseen pressure signatures required an explanation. Different factors result in unforeseen pressure signatures, including well influx (migration of native fluid), pumping steps, and multiphase flow and rheology of fluids, which can be modeled by using the CEMPRO5<sup>TM</sup> approach [52, 54]. The scope of this section is not to analyze small differences

between the simulator and the field data, but to focus the analysis on the major events such as the shut-in period, fluid changeover, and variations in pressure trends.

Downhole static bottomhole pressure (BHP) measurements in wells within the pilot area indicated that the expected reservoir pressure at 1640 m deep would be approximately 18 MPa [15]. To prevent the influx of reservoir fluids into the well, the density of the completion fluids (prewash and cement) should always remain larger than the reservoir pressure.

#### 6.2.1.1.1 Preflush circulation

Figure 6.3 shows the measured and simulated results for the pressure profiles at 1610 m deep, and pump rate as a function of circulation time for the complete cement circulation process. During the first 11 min of this process, the prewash-water circulated inside the tubing and displaced the heavier brine through the annular tubing/casing area. The downhole pressure measurements slightly increase in slope is indicative of frictional flow losses as brine flows up the annulus between the tubing and casing. The simulated pressure was modestly higher than the gauge measurements, the largest difference being 70 kPa (10 psi). After the preflush water front began to circulate at the tubing shoe, annular pressure gradually decreased because the heavier brine column of the annular space was being displaced against gravity by lighter preflush water. The simulated pressure at the end of the preflush step was lower than the actual pressure measurements by 150 kPa (22 psi). This small difference could be attributed to the assumptions of the analytical solution, and that solution's failure to account for viscous fingering of the brine into the preflush water.

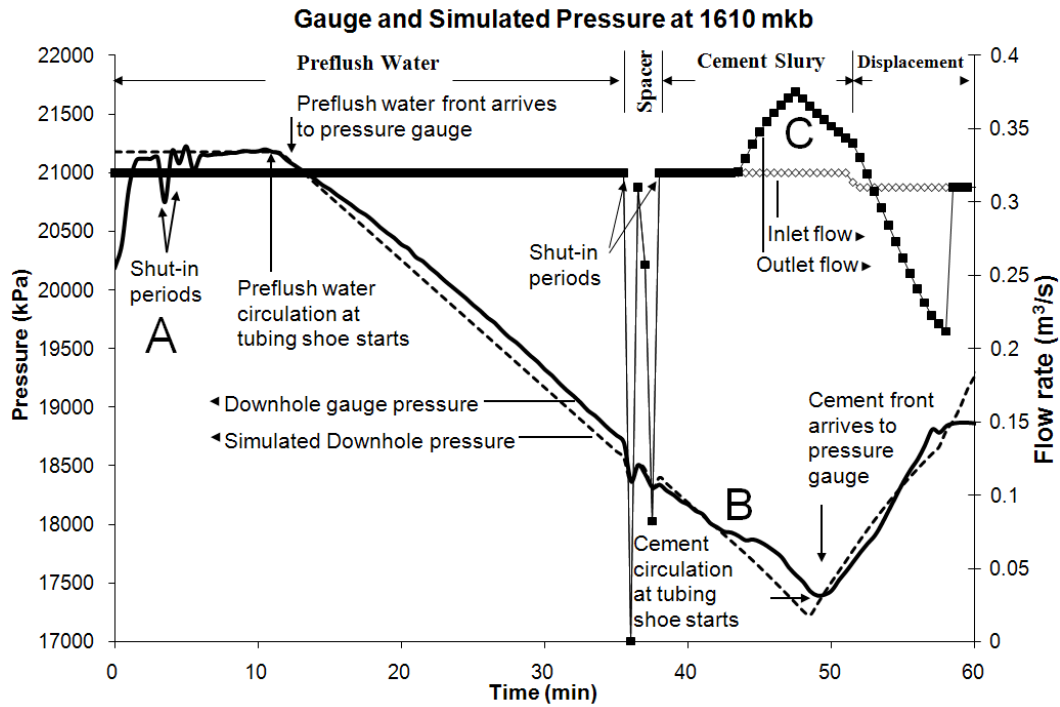


Figure 6.3 Reported and simulated data during cement circulation.

Another point to consider during the preflush water step is Event A in Figure 6.3 in which the pump rates collected from the field operation inlet flow were average measurements, and some shut-in periods events were not included. However, these events are incorporated into the model to history match the downhole pressure data (Figure 6.6).

#### 6.2.1.1.2 Spacer and cement circulation

The change of circulation fluid from preflush water to spacer, and then to cement slurry, generated shut-in periods at each changeover. These periods were matched by the simulated pressure profile, which was still declining because the column of less dense preflush water was filling all the annular tubing/casing space (Figure 6.3). After four minutes of cement circulation (43 minutes since the circulation operation started – Event B), the downhole pressure started to follow a different trend, as per the solid line in Figure 6.3. Meanwhile, the ECD (Figure 6.4) at the bottomhole fell below the reservoir pressure, indicating that the unexpected pressure trend at minute 43 was the result of migration of reservoir fluid into the borehole. Figure 6.5 shows the annular pressure before and after the cement slurry front entered the tubing shoe. When the preflush water dominated the annular tubing/casing space, the annular pressure immediately decreased

and fell below the reservoir pressure (ECD of 1.12). The BHP (red line) dropped from 18MPa at 43.7 min (Figure 6.5(a)) to 17 MPa at 47.4 min (Figure 6.5(b)) of circulation.

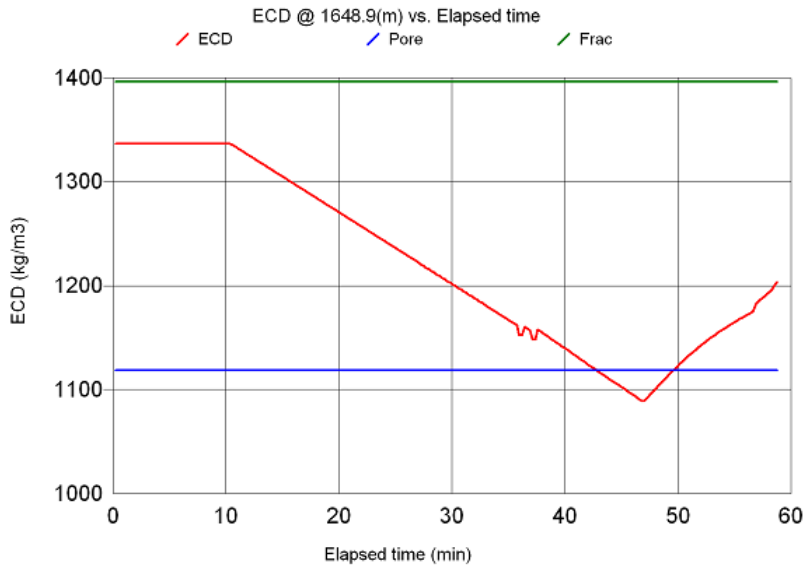
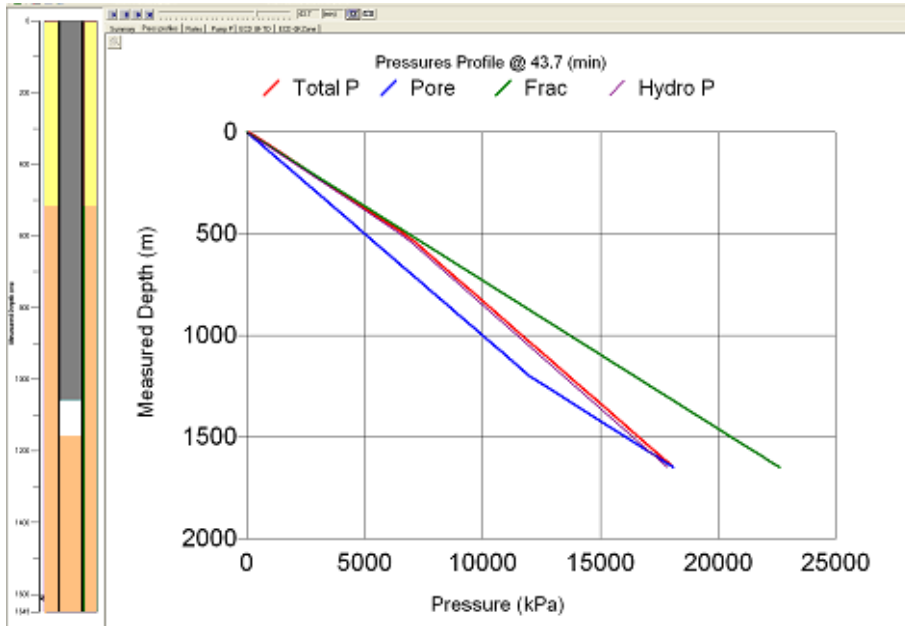
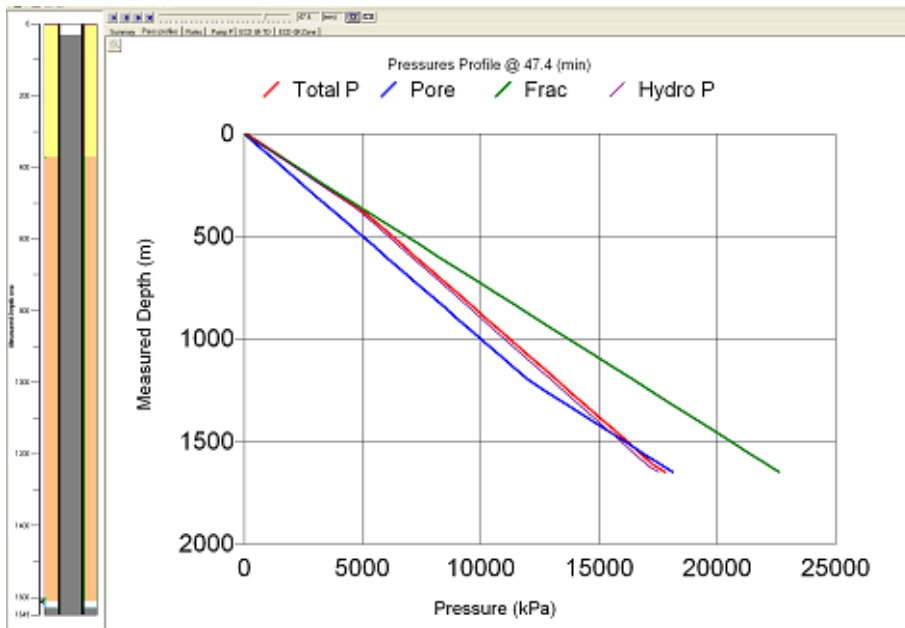


Figure 6.4 ECD at bottom hole below reservoir pressure (blue line).

Wellbore downhole influx is a complex process, and the simulated annular pressure responses for this event are not captured in the model. However, they provide a wellbore pressure profile that explains the difference from the actual pressure measurements. Therefore, the ability of downhole pressure gauges to capture important dynamic events is key for a post-cement job review and future well integrity assessment.



a) Annular pressure profile at 43.7 minutes of the circulation operation.



b) Annular pressure profile at 47.4 minutes of the circulation operation.

Figure 6.5 The BHP (read line) drops from a) 18MPa at 43.7 minutes to b) 17 MPa at 47.4 minutes of circulation.

Another point to be considered is the analysis of free-fall phenomenon, described by Beirut [55]. This occurred while the heaviest fluid (cement slurry) was being pumped down the tubing (Figure 6.3 - Event C). The imbalance of forces caused the cement column in the tubing to fall faster than the cement was being pumped in, as outlet flow

rate increased at this stage. This rate reached a maximum value and then slowed as the heavy cement slurry front moved through the tubing/casing shoe and the lighter displacement fluid was pumped behind it. From the point of view of production and borehole stability, this phenomenon could increase friction pressures, and therefore annular pressures, to the point of causing losses of circulation during the cement job. However, observation wells are not meant to be in production, and borehole stability is not critical for pre-cased wells if the annular pressure is above the pore pressure profile.

#### **6.2.1.2 History matching**

The initial comparisons and observations between downhole pressure measurements and simulated pressure used average pump rates. To filter the events that are affected by pump rates and to corroborate the early observations, the simulation was history matched by changing the pump inlet flow rate (Figure 6.6).

There are two events that are not pump rate-dependent. The first is the fingering phenomenon between the heavy brine and the light preflush water, which means that the preflush water has been contaminated by the heavier brine. The second and most important is the influx of native reservoir fluid into the borehole after the annular pressure is reduced below the reservoir pressure. The common element of these two events is the light preflush water, which does not effectively displace heavy fluid, causing a decrease in annular pressure when the volume of light preflush water dominates the annular tubing/casing space. The last point is critical for an overpressured reservoir (such as in this case study), which causes an influx of reservoir fluids into a well that, in turn, could lead to the formation of a micro-annulus and potential fluid leakage path, which was the case in this monitoring well. At the conclusion of cementing, a flow to surface of approximately 10 L/min was measured. To “kill” the well (i.e., stop the flow), a downhole tubing punch was used to create access between the tubing and tubing-casing annulus above the top cement. High density brine was circulated in the well to stop flow and allow the well to be converted to a monitoring well. Issues surrounding this operation and the subsequent surveillance records obtained in the monitoring well are discussed in Chapter 5.

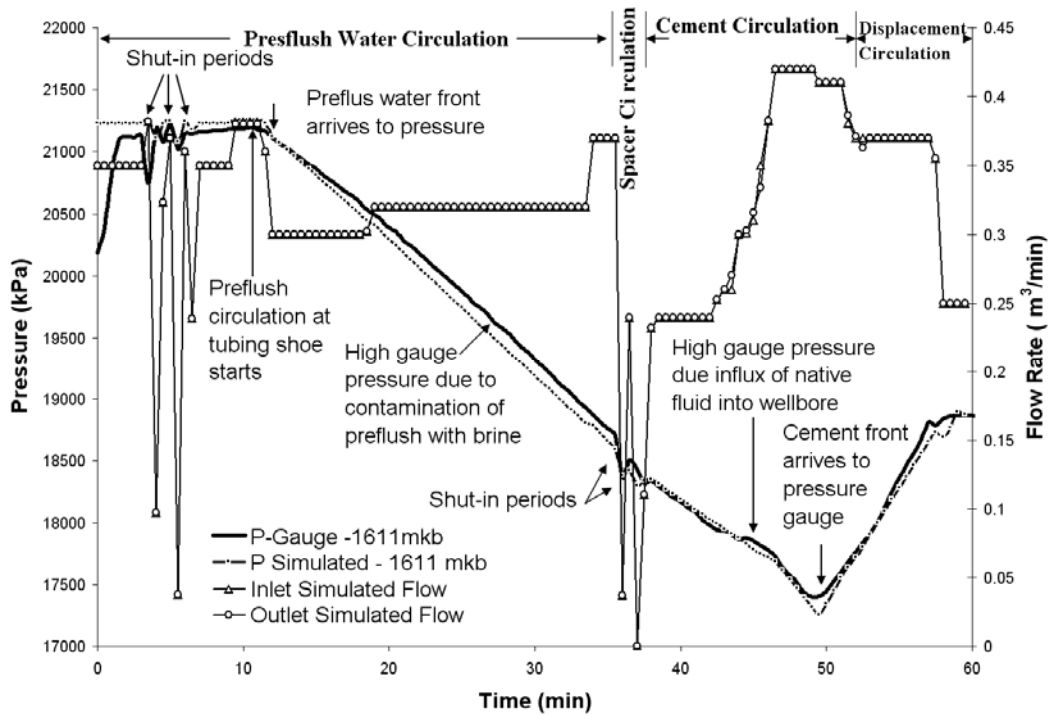


Figure 6.6 History match of downhole pressure data [14].

### 6.2.1.3 Effect of heavier preflush fluid and recommendations

Many of the observation wells with an integrated multi-instrumentation system are deployed with tubing hanging inside of pre-cased boreholes. Pre-cased boreholes are used to guarantee zonal isolation during primary cement operations where cement is placed between the casing and formation. However, the main objective of a cement operation for this type of observation well is to hydraulically isolate the response of each sensor within the borehole. To obtain this zone isolation, cement slurry placement is constrained by two distinct envelopes — the cement circulation envelope, and the cement displacement efficiency envelope.

For each depth, the cement circulation envelope determines the minimum pore pressure profile and the maximum fracture pressure profile during the placement to avoid influx or fracturing. The cement displacement efficiency envelope is constrained by the flow rate at each depth, which helps to avoid cement channeling or contamination for a given wellbore geometry. Figure 6.7 shows five simulations with different preflush fluids. Simulation (a) used water as a preflush fluid, and in subsequent simulations, the preflush fluid was made to be 5 %, 10 %, 15%, and 20 % denser than water, respectively. To

prevent the invasion of the well by native fluid, the preflush fluid should be dense enough to balance the reservoir pressure and prevent any influx into the wellbore.

It is recommended to include cement circulation simulation reports as part of the pre-cement placement design phase for observation wells. This will help to highlight potential problems in design and execution, as well as solutions for the same.

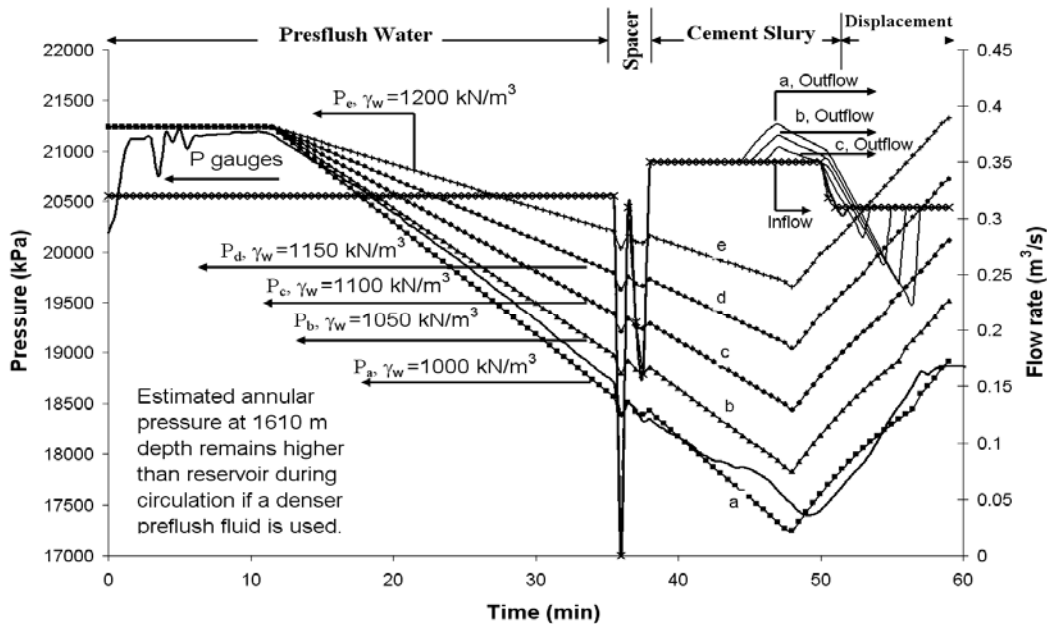


Figure 6.7 Effect of heavier preflush fluids on the annular pressure [14].

## 6.2.2 Conclusion

The experience with the observation well at the Pembina Cardium CO<sub>2</sub> monitoring pilot project provides valuable insight regarding measurement, monitoring, and verification protocols around the deployment of sophisticated multi-instrument strings in field demonstration projects of CO<sub>2</sub> geological storage. The case study of this observation well has addressed issues of direct monitoring and measurement of large varieties of parameters and properties at the reservoir level.

Sensor bodies used to diagnose cement displacement do not have a large effect on the pressure response during cement circulation. Density, volumes, and flow rate have a large impact on circulation pressures. Downhole pressure gauges capture the dynamics of cement displacement. They are key to a post-cement job review and future well integrity assessment. They provide direct diagnosis of boundary conditions of cement displacement operations.

### **6.3 Hydraulic transmissivity of micro-annulus path**

In the previous analytical evaluation provided in §6.2, it was concluded that native fluid invasion at the reservoir level occurred during the cementing operation. Reservoir fluid influx into the well during cementing is detrimental for the completion process because reservoir fluid can mix with the cement slurry phase, which becomes contaminated and later does not harden when the circulation stops, creating a micro-annulus path in the cement column. It is possible to identify and locate the source of the leak by logging (e.g. ultrasonic cement evaluation logs) or other mechanical means [32, 56]. However, for this case study it was impossible to deploy a downhole logging tool because cement was (also) placed behind the tubing, as described in Chapter 5. This section presents an evaluation of the hydraulic transmissivity of the micro-annulus path, including the configuration needed for a wellhead fluid flow of 10 L/min.

There are three important variables for this analysis: (1) the large wellhead fluid flow, (2) the presence of cables and capillary lines through the axial length of the primary cemented geometry, and (3) the well influx during cementing. The first variable is the larger wellhead fluid flow that ranged from 10L/min to 7L/min indicates the presence of a fully developed channel through the entire cement column. This communication from bottomhole (1650 m) to near top cement (1200 m) was confirmed with the downhole pressure and temperature measurements during the completion operation, as describe in Chapter 5. The second variable is the configuration of wellbore cross-section that prevails along the axis of the primary cemented geometry, which mainly constitutes casing, tubing, cables and capillary lines. The study of this configuration during cement circulation could help to identify possible channel location. The third variable, well influx that affects the quality of the cement displaced, could narrow the hypothesis of the possible location of the micro-annulus path of the OW.

#### **6.3.1 Micro-annulus configuration within the borehole**

The location of this micro-annulus path is proportional to the areas of poor quality cement resulted from inadequate displacement efficiency. From the flow prospective two elements impact the efficiency of cement displacement. These are: (1) the level of eccentricity of the tubing, which can be controlled with the use of centralizers [32, 57, 58] and (2) the rheology of displaced fluids [32, 59]. During post-analysis, these elements were reviewed to determine the possible location of micro-annulus as a hypothesis.

On the OW, centralizer devices were installed to reduce eccentricity generated due to well trajectory or sensor body configuration. The percent of standoff (SF%) is a term used to measure eccentricity [32, 59, 60], for perfect concentric cases SF% is 100, and it is defined as:

$$SF\% = \frac{\delta}{R_{casing} - R_{tubing}} \times 100 \text{ percent} \quad \text{Equation 6.1}$$

where  $\delta$  is the minimum separation of the wall of the casing and the tubing,  $R_{casing}$  is the radius of the casing and  $R_{tubing}$  radius of the tubing.

Cement displacement efficiency is affected if the annular cross-section velocity is not uniform. This could occur when the tubing is eccentric and the distance between the casing wall and tubing are not uniform in cross-section [32, 59, 61-63]. Figure 6.8 illustrates how the flow profile is affected in eccentric configurations. As described in Chapter 4, the wellbore configuration near each sensor/gauge has multiple elements that protect the sensors to reduce the risk of installation damage. These wellbore configuration sections could result in a SF% of 40% and without any correction the entire tubing could have the same low level of eccentricity. This was critical on the design and installation stages of the OW; therefore, centralizers were installed at every collar (9.5 m interval) during the first 300 m of the cement column, increasing the SF% to 90% (reducing eccentricity).

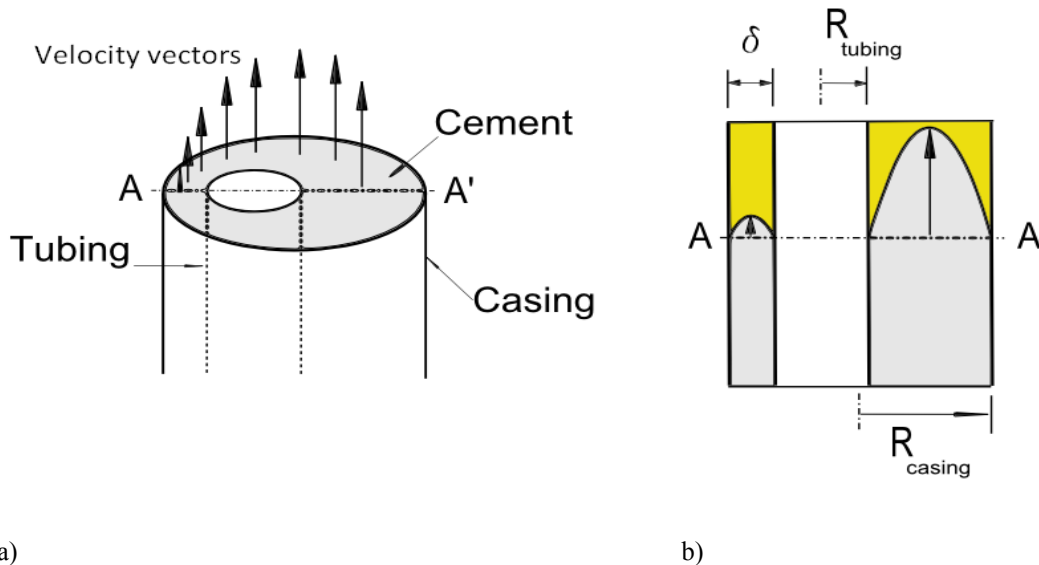


Figure 6.8 Illustration of (a) geometry of eccentric tubing, (b) and resultant velocity profile.

After ruling out tubing eccentricity, the analysis focused on the eccentricity of the 12 cables and capillary lines. These elements ran from the bottom hole to the surface completion of the well. They were secured on the side of the tubing to reduce risk of installation damage (Figure 6.9). This means that the micro-annulus space between the production tubing and cables could store a mixture of native fluid that invaded the borehole during circulations and cement slurry. This mixture was never displaced because the velocities near the tubing walls are low or near zero in the absence of slippage. Figure 6.9 shows the configuration of the tubing, cables, capillary lines, and micro-annulus. The possible cross-section area of the micro-annulus path is defined by a mean aperture ( $h$ ) and a perimeter ( $w$ ) of the section of the tubing where these elements were tied down. The following section studies the hydraulic transmissivity of this micro-annulus space and evaluates the possible dimensions that could match the wellhead flow of 7 L/m to 10 L/min.

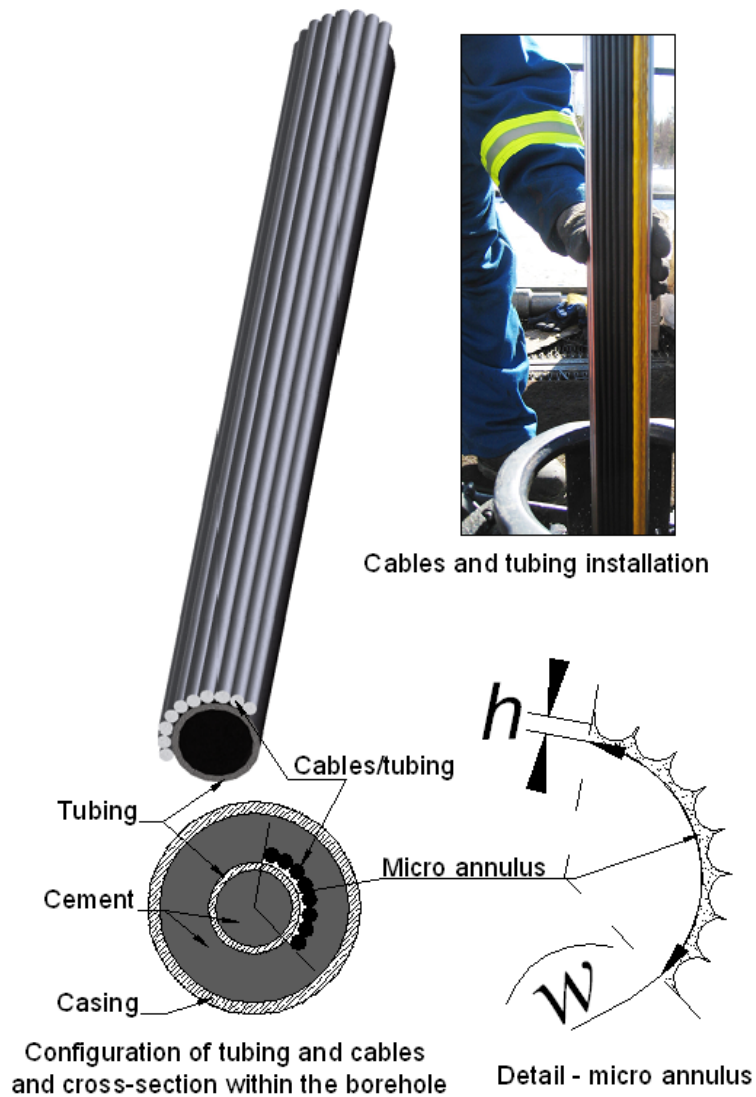


Figure 6.9 Schematic of the micro-annular path behind tubing and cables.

### 6.3.2 Hydraulic transmissivity of the micro-annulus path

As presented before, the most probable location of this micro-annulus path is behind cables and capillary lines which are located through all the length of the OW. The objective of this section is to evaluate the hydraulic transmissivity of the micro-annulus path, which can be assessed with a simple conceptual model of flow between parallel walls separated by uniform mean aperture  $h$ . The derivation of this model assumes parabolic velocity profile between the walls. This model often used to assess motion of fluid on a rock fracture is [64, 65] :

$$u_x = -\frac{1}{2\mu} \frac{\partial p}{\partial x} [(h/2)^2 - z^2], \quad u_y = 0, \quad u_z = 0, \quad \text{Equation 6.2}$$

where  $\partial p/\partial x$  is the pressure gradient aligned to x-axis,  $\mu$  is the fluid viscosity,  $z$  is the direction normal to the aperture, with the aperture walls located at  $z = \pm h/2$ ,  $u_x$  is the velocity aligned with the pressure gradient,  $u_y$  and  $u_z$  are orthogonal velocities and normal to the pressure gradient.

The total volumetric flux is found integrating the above velocity:

$$Q_x = w \int_{-h/2}^{+h/2} u_x dz = -\frac{w}{2\mu} \frac{\partial p}{\partial x} \int_{-h/2}^{+h/2} [(h/2)^2 - z^2] dz = -\frac{wh^3}{12\mu} \frac{\partial p}{\partial x} \quad \text{Equation 6.3}$$

where  $w$  is the depth of the micro-annulus path in the y direction (Figure 6.10). The term  $T = wh^3/12$  is known as fracture transmissivity [57].

The above model was used to assess the extent of the cement column leakage path because the rock fracture has similar conditions to the micro-annulus path in the cement column, where the fluid flow takes place mainly through micro-annulus path rather than through the porous media of the cement column. Figure 6.10 illustrates the unwrapped narrow annular space of the micro-annulus, which matches the conceptual model of flow between parallel walls.

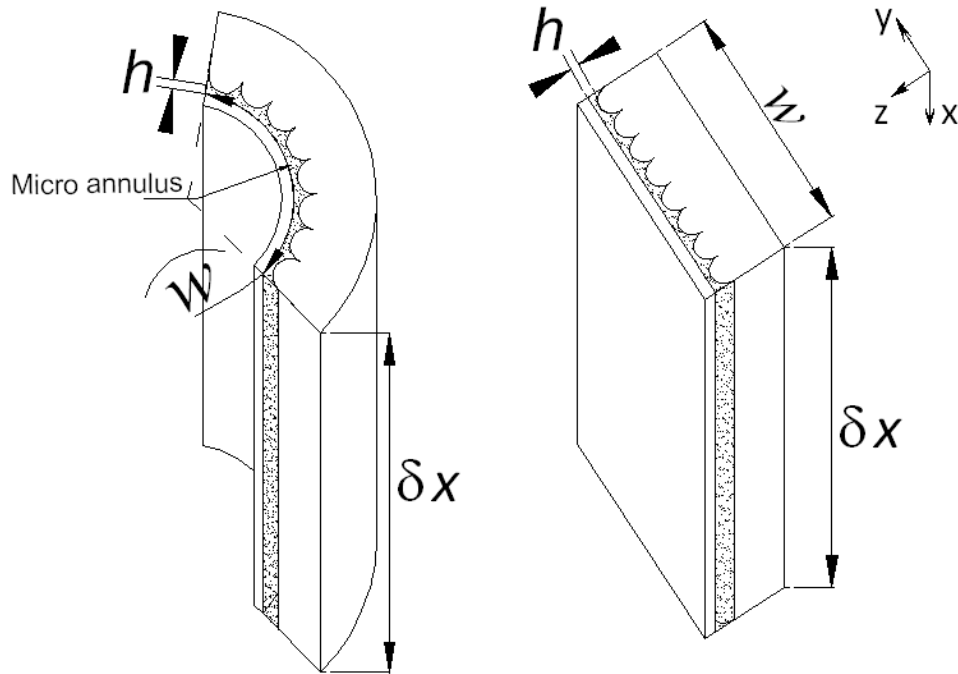


Figure 6.10 Schematic of unwrapping a micro-annulus section.

### 6.3.3 Approach

A sensitivity analysis was conducted in order to evaluate multiple possible configurations of the micro-annulus path. The conceptual model was used to history match the volumetric flux of the wellhead of 10 L/min by changing the length of the micro-annulus path and the number the cables of 1 cm nominal diameter that fit on the arch section  $w$ .

Although there is strong evidence to suggest that native reservoir fluid invasion occurred during cement circulation, which would have likely contained hydrocarbons, this analytical approach used the brine rheological properties only for the fluid that was flowing through the aperture (micro-annulus).

### 6.3.4 Results and conclusions

The curves presented on Figure 6.11 are the multiple solutions for a given aperture, number of cables and length of micro-annulus path. The blue points are the solutions that match the location or length micro-annulus path and number of cables within the cement column of the observation well. From this figure concluded that a micro-annulus path between cables/capillary lines and tubing is highly possible, and it is mainly constituted by 8 cables/capillary-lines with an annular aperture that range from 0.8 mm to 1.6 mm.

The following section presents additional numerical flow simulation that assessed the impact, at the millimeter scale, of the geometry of the downhole sensor housing system during the cement placement.

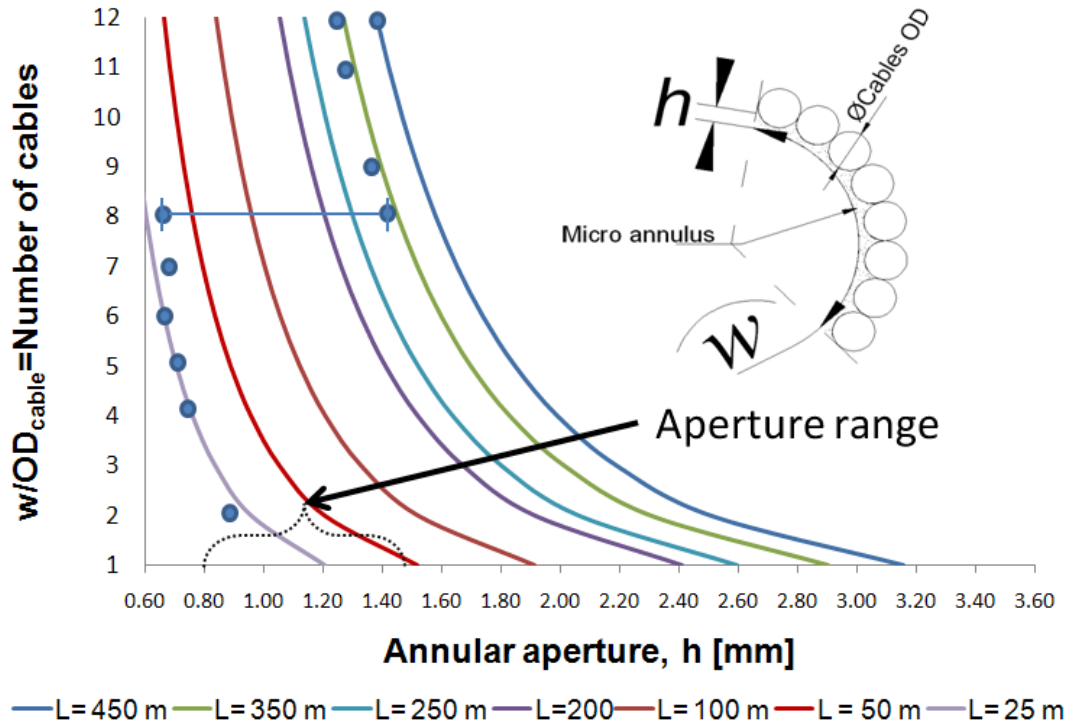


Figure 6.11 Analytical results of micro-annulus configurations at a fix flow.

#### **6.4 Detailed near-well numerical modeling of hydraulic isolation assessment of permanent downhole sensors housing system**

While flow pattern transitions in multi-phase flow of cement placement around complex annular geometries are not well understood, advancements in both measurement techniques and numerical simulations are helping to increase the understanding of multi-phase flow in downhole sensor housing systems. The approach used to determine the parameters affecting the wellbore environment during cement circulation is presented in this section. This method utilizes computational fluid dynamics (CFD) modeling. The use of CFD models has proven to be successful in many areas of fluid flow [66-70]. The effectiveness of CFD was determined by simulating results of similar scales from an experiment reported in literature [66]. These simulations of the wellbore environment allow the velocity and pressure gradients and the turbidity in multiphase flow systems (mud, spacer and cement) to be visualized.

The scope of this section is to use CFD techniques to assess the hydraulic isolation of the sensor housing system deployed in the OW at the Pembina Cardium CO<sub>2</sub> monitoring pilot. The scale of resolution of this study focuses on the millimeter and centimeter of borehole sections that were not greater than 5 m in length, simulating short cement circulation periods of less than 20 s. The maximum size of borehole section (5 m) was set by the computer capacity available and the standard length of the tubing/casing used for this type of installation by industry.

The transient simulation presented in this section did not include the reservoir fluid invasion because the spatial and time scale of this event was likely occurred over distances greater than 5 m or times greater than 20 s. In addition, the boundary conditions of this event are generally unknown making it difficult to model.

The models presented in this section include a preliminary CFD model of the complete section of a downhole sensor housings system, and three CFD models of different elements of the sensor housing system. A total of four simulations are presented in this section, requiring approximately 1,540 hours of computation time. These CFD simulations were conducted on a workstation and a computer cluster.

## 6.4.1 Modelling description and computational method

### 6.4.1.1 Introduction

Computational fluid dynamics (CFD) simulations were conducted to assess the impact of the geometry of the downhole monitoring systems during the cement placement, using the volume of fluid (VOF) two-phase model. A commercial CFD software package (ANSYS CFX/Fluent) was used for the simulations.

CFD works by dividing the region of interest, the inside of an annulus area of the wellbore, into a large number of cells or control volumes (the mesh or grid). In each of these cells, the partial differential equations describing the fluid flow (the Navier-Stokes equations) are rewritten as algebraic equations that relate the pressure, velocity, temperature and other variables, such as species concentrations, to the values in the neighboring cells. These equations are then solved numerically yielding a complete picture of the flow down to the resolution of the grid.

This section presents a brief description of the CFD commercial code that was used in this analysis. ANSYS CFX/Fluent software is a world-class CFD simulation package that provides a full range of engineering simulation solutions. The technology in CFX/Fluent includes: Advanced coupled multigrid linear solver technology, unmatched meshing flexibility, parallel efficiency and pre and post-processing capabilities.

The multiphase model in the ANSYS CFX/Fluent solves separate transport equations for velocity, temperature and mass fractions etc. for each fluid, with inter-phase connections through drag, heat and mass transfer. In addition to the coupled solver for the velocity and pressure fields for single-phase flows, velocities of all phases and pressure are also solved together in a fully coupled manner to make the calculation of multiphase flows fast and robust. Figure 6.12 shows the steps of a CFD simulation.

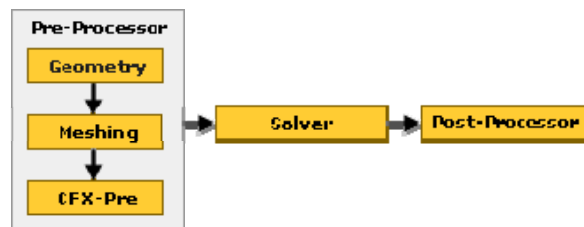


Figure 6.12 Flow Chart of CFD Simulations [71].

The following provides a general description of the geometry and grid, mathematical model, boundary conditions and numerical solution controls used in the models of this study. Detailed information for each model is provided in the result sections of this Chapter.

#### 6.4.1.2 Geometry and grid

The first stage in any CFD model is to create a geometry that represents the object being modeled. The detail 3D geometry of the wellbore section was drawn and assembled in CAD (Autodesk Inventor). Grid data was processed by the Workbench interface of CFX/Fluent. The geometrical discretization of the downhole sensor housing systems was generated with structured hexahedral and unstructured tetrahedral cells.

From this point, a mesh was generated which created the cells or control volumes. A preliminary mesh of the wellbore section with downhole sensor housing elements is presented in Figure 6.13. Once the mesh was completed, the model input values were specified and the software then solved the equations of state for each cell until an acceptable convergence was achieved. This could be a time consuming process, but fast-optimized codes could exploit parallel processing.

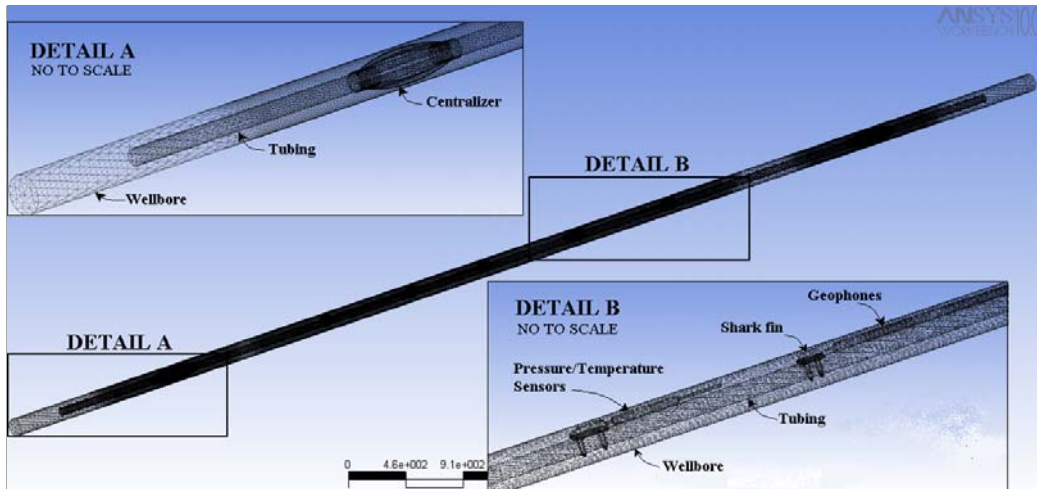


Figure 6.13 Preliminary CFD mesh for a wellbore section.

### 6.4.1.3 *Mathematical model*

The two-phase transient simulations presented here were based on standard laminar flow and volume of fluid (VOF) method, which tracked the interface between the phases by continuously tracing the volume fraction of each phase within each volume cell at every time step. The interface between the phases was estimated with this information [72, 73]. The time dependent term scheme used was the first order implicit. The pressure-velocity coupling was calculated through the PISO scheme. Least squared cell based gradient, PRESTO! pressure, second order upwind momentum, geo-reconstruct volume fraction and quadratic upwind interpolation (QUICK) energy were used as spatial discretization settings. Because fluids were moving against gravitational forces, the formulation of implicit body force was used.

### 6.4.1.4 *Boundary conditions and fluid properties*

The initial step involved in the completion of an observation well is to displace the drilling mud or brine that surrounds the formation of the openhole or pre-cased well, respectively, to place cement. This provided the initial boundary conditions for the detailed wellbore modeling presented on these studies.

All of the surfaces were set at zero-slip walls, except for the inlet, which was set as a uniform constant velocity of 0.737 m/s and the outlet, which was set as a transient pressure that increased every time step, using a user defined function (UDF). The pressure gradient as a function of time was estimated from the downhole pressure measurements collected during cement placement.

In this study, the CFD simulator solved the Navier-Stokes equations of a power law fluid and a Newtonian fluid, which correspond to the cement slurry and fresh-water spacer, respectively. Table 6.1 presents the rheological properties of the non-Newtonian and Newtonian fluids, which were similar to the ones used in the observation well 100/07-11-48-09W5M [74].

Table 6.1. Fluid rheological properties

Fluid Properties	CO <sub>2</sub> cement slurry	Fresh-water spacer
n	0.9839	
K	0.0619 Pa s <sup>(n)</sup>	
Density	1.76 g/cm <sup>3</sup>	1 g/cm <sup>3</sup>

#### 6.4.1.5 Numerical solution control

The code was run on a workstation and a computer cluster of sixteen nodes, depending on the complexity and number of elements of the models two to four nodes were used for these CFD simulations. Because the models were dominated by convection, the minimum time step used in the simulations was a function of the grid size in particular the minimum volume cell, and it is defined as [75, 76]:

$$\Delta t = \frac{V_{cell,min}^{1/3}}{U} \quad \text{Equation 6.4}$$

where  $V_{cell, min}$  is the minimum grid cell volume, and  $U$  is the inlet velocity.

The number of iterations were adjusted to reduce the scaled residual errors below an acceptable value in each time step  $10^{-5}$  (five orders of magnitude). These residuals are 3D fields associated with conservation laws of mass, momentum and energy, They indicate how far the present approximate solution is away from exact cancelation of flux balances in each cell [76]. Initializing the transient calculation with the steady state solution was needed to develop the velocity and pressure profiles within the models.

After the models were solved, the results were analyzed both numerically and graphically. ANSYS CFX /Fluent provides a powerful, comprehensive set of post-processing tools to create visualization ranging from simple 2-D graphs to 3-D representations of particle tracks, vectors and gradients. Preliminary post-processing result of a wellbore approach is presented in Figure 6.14.

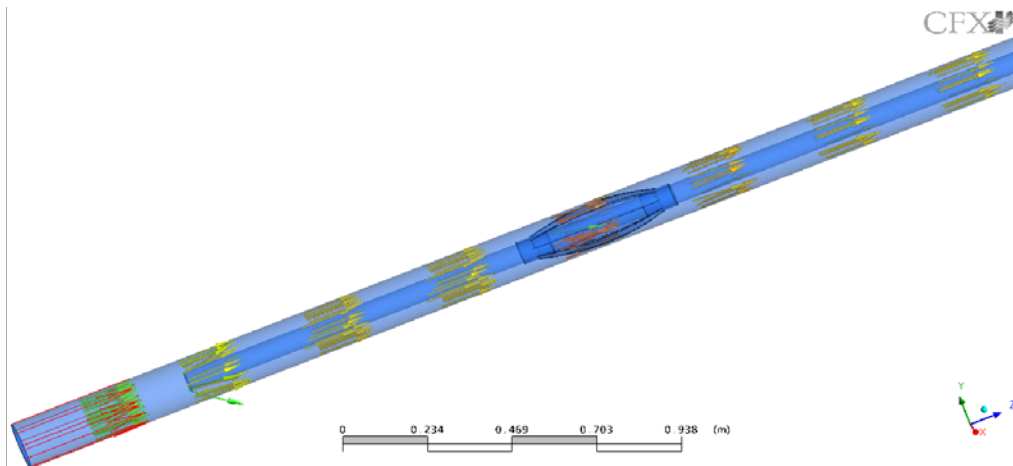


Figure 6.14 Streamlines of flow through annulus area of a wellbore section.

### **6.4.2 Approach**

The permanent downhole reservoir surveillance systems generally consist of sensors that are lowered into a well and cemented in place at specific elevations to make contact with the geological formation of interest, often for the sake of measuring in-situ pressure and temperature. These sensors are packaged in steel housings that are welded or clamped to the outside of the casing or tubing, and designed primarily for mechanical protection of the delicate sensor. This way, the sensor is carried downhole with the casing or tubing string. Sensor signals are conveyed to surface by cable banded alongside the casing or tubing. In many installations, more than one sensor is lowered into the same well, with each designed to measure physical phenomena within a zone of interest. Often, this will result in multiple sensor cables being run to surface, along the casing or tubing.

In these types of installations, prevention of hydraulic communication between two or more zones of interest is essential for monitoring, measurement and verification (MMV) activities because this ensures confirmation of the movement of CO<sub>2</sub> within a geological unit near each sensor. The sensors are therefore cemented in place within the wellbore along with the casing or tubing, and it is the cement that acts as a barrier for migration of in-situ fluids from zone to zone. This was not achieved at the OW; therefore, the following approach that used CFD techniques was conducted to understand how the cement slurry was placed in the complex annular configuration of the OW.

The approach comprised on one preliminary CFD model of a duplicate wellbore section of the downhole sensor housing system and three wellbore sections with different elements. These last three models were: (1) a wellbore section with one cable along the axis of the tubing; (2) a sensor housing and tubing conveyed; and (3) a sensor housing, tubing conveyed with flow deflector fins. The preliminary results of the duplicate wellbore section model were used to understand how all the main elements of the sensor housing system affected the flow dynamics and the cement displacement efficiency. The sensor housing and cables were the main elements of this system; therefore, two CFD models of wellbore section with each of these elements were conducted to assess how these geometries affected the cement displacement efficiency. A third model focused on a conceptual enhanced sensor housing geometry that could reduce the annular flow impedance caused by the sensor housing body. The descriptions, results, discussions and conclusions of these models are presented on the following sections.

### 6.4.3 Preliminary 3D CFD simulation of cement displacement in a wellbore environment

This section presents a preliminary CFD model with a midsize gridding of the sophisticated geometry of 5 m section of a borehole from the OW. The simulation was conducted on a workstation with Microsoft Windows XP 64, Intel Xeon (3.4 GHz) and 8 GB of memory. The time step used in the unsteady calculation was set to  $5.78 \times 10^{-5}$  s. A total of 15 s of flow time was simulated, requiring approximately 72 hours of computation time. The objective of this preliminary analysis was to identify the effect that the sensor configuration geometry had on the cement displacement process. This was reflected on two monitoring points that recorded the evolution of volume fraction and velocity.

#### 6.4.3.1 Geometry definition.

Figure 6.15 depicts an isometric view of this preliminary model, which includes a pressure gauge and a fluid recovery sample port with cables and capillary lines.

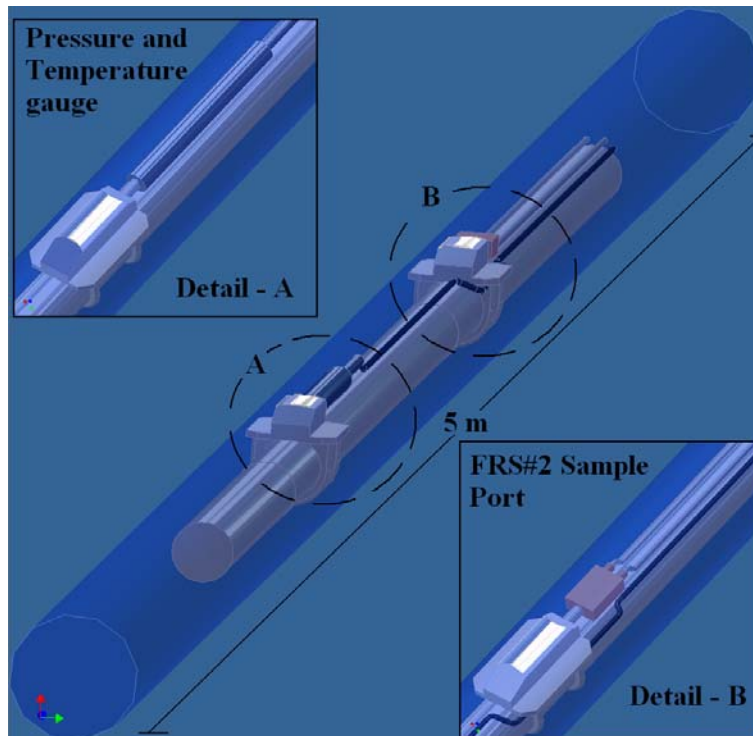


Figure 6.15. 3D view of the borehole with details of instrumentation.

### 6.4.3.2 Grid generation.

The highly detailed, three dimensional drawing and slenderness of the borehole geometry section required a considerable number of nodes. A medium fine mesh with 476,225 nodes and 2,487,157 elements was used for this preliminary analysis. Figure 6.16 presents the mesh of the model.

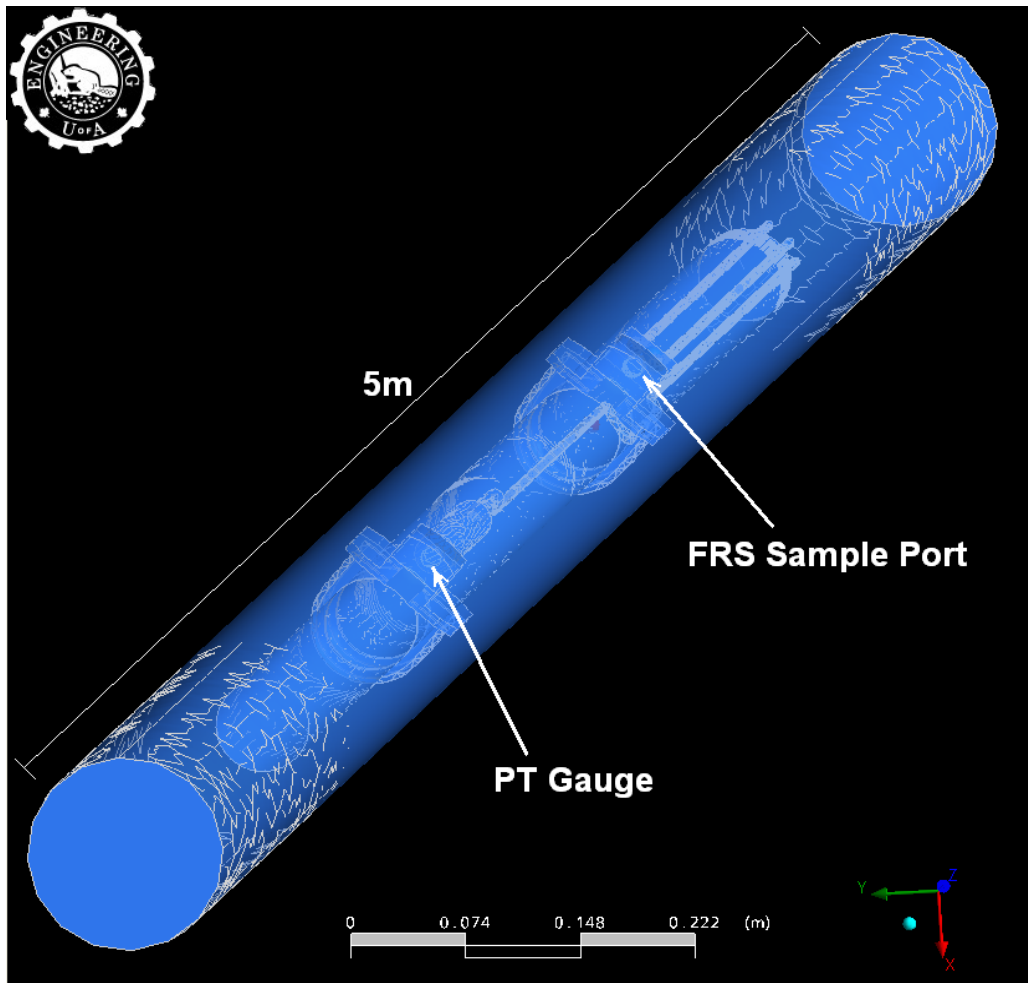


Figure 6.16 Mesh of a 5m section of borehole using computational fluid dynamics simulation.

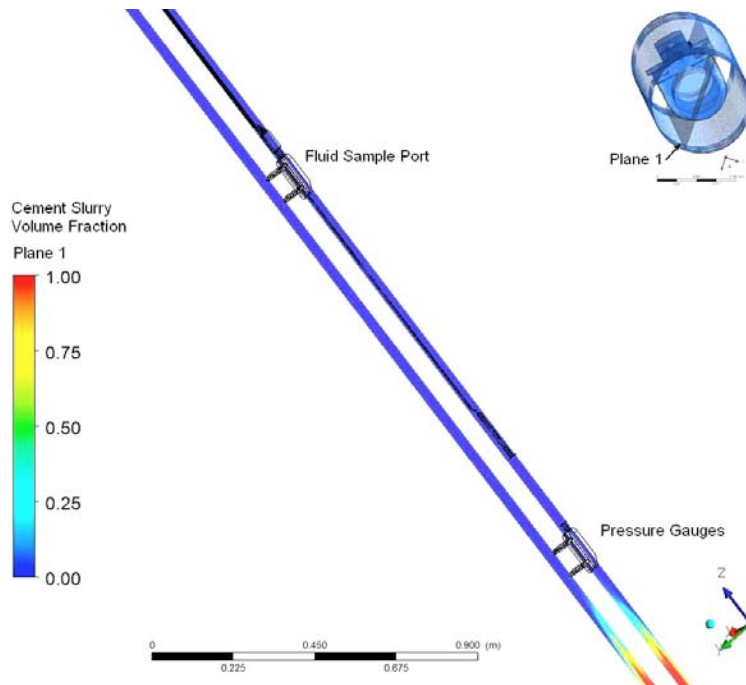
### 6.4.3.3 Boundary condition

For this preliminary approach the boundary conditions were simplified by setting the inlet as a constant bulk mass flow inlet and the outlet as constant pressure outlet. The inlet bulk mass flow was 14.5 kg/min, and the total pressure outlet was 20 MPa. The reference temperature was set to a value of 48 °C, which corresponds to a reservoir conditions.

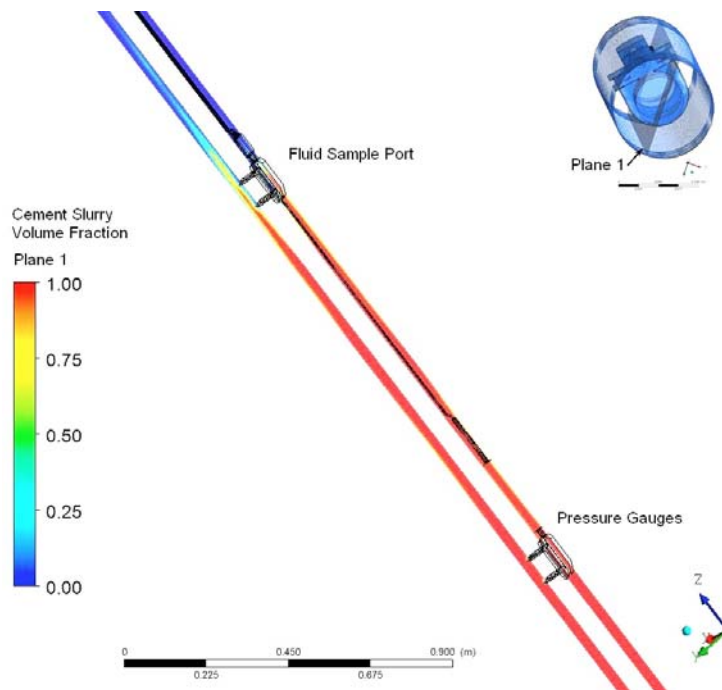
#### **6.4.3.4 Results and discussion**

Figure 6.17 presents some graphical CFD solutions of the multiphase flow, where the red and blue fluids represent the phases of the cement slurry and fresh-water spacer, respectively.

During the first 2.9 s of circulations, the face of the cement slurry was displacing within an annular space without the sensor bodies, the cables or the capillary lines; as a result, the cement slurry was uniformly moving upward displacing the fresh-water spacer (Figure 6.17 (a)). On the other hand, after 3.9 s of circulations the front face of the cement slurry had passed through two sensor bodies, a cable and two capillary lines, and some fingering on the cement displacement was observed (Figure 6.17 (b)). The sensor bodies, cables and capillary lines that were located on the same side of the borehole are causing significant flow impedance. This, in turn, could result in poor quality cement displacement efficiency.



a)  $t = 0.29$  s



b)  $t = 3.9$  s

Figure 6.17 Multiphase flow graphical CFD solution in different time steps. The cement slurry (red) is displacing the preflush-water fluid (blue) within tubing/casing annular area.

The early results presented on this chapter suggest that a micro-annulus path within the cement column was located near the cables and/or capillary lines that were strapped to the tubing along its axis. Figure 6.18 illustrates two monitoring points that were located at the same depth and same radial distance from the tubing, one (blue) near cables and the

other (red) without near cables. They were used to compare the effect that sensor elements configuration have on the cement displacement efficiency.

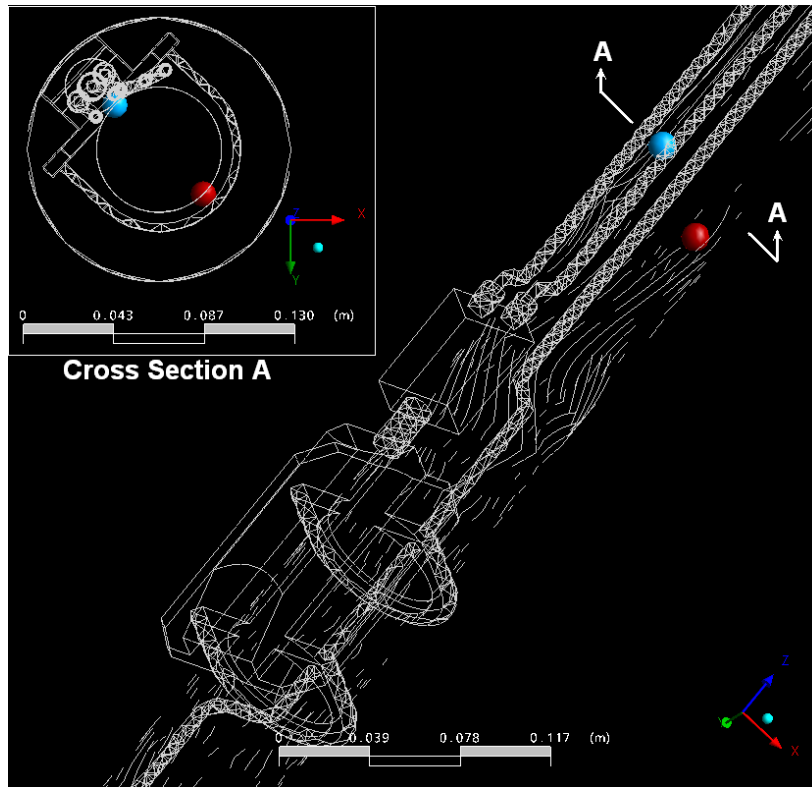


Figure 6.18 Location of monitoring points along the axis and cross section.

Figure 6.19 presents the values of the monitoring points, which corresponds to the cement displacement velocity and volume fraction near cables and tubing (blue point) and near tubing (red point) during 15 s of flow. It is observed that the velocity near cables is half that of the velocity for the location without cables. Therefore, the cement displacement efficiency, as measured by the volume fraction of cement, decreased, never reaching 100 per cent near cables

Although, these results are preliminary, they show how the presence of instruments could affect cement placement, and in turn, the propensity of the well to leak fluid to the surface. Understanding these complex downhole sensor-housing systems with computational fluid dynamics simulators can provide a powerful framework for a new system design with minimum annular flow impedance.

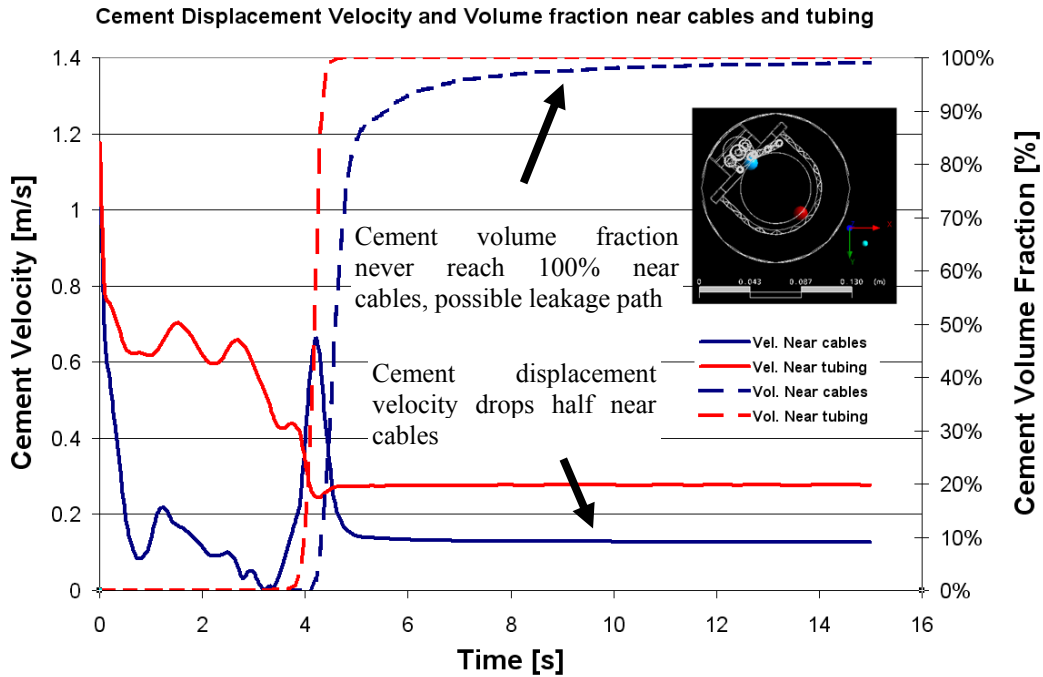


Figure 6.19 Recorded reading on monitoring points.

#### 6.4.3.5 Preliminary conclusions

This study has showed that the presence of sensor housings and cables, all attached to the outside of the tubing or casing, could result in heterogeneous cement flow around these components. Low cement displacement velocities and poor sweep efficiency could result in the formation of a channel, or micro-annulus, that can hydraulically connect two or more zones where sensor were installed, or even to surface

#### 6.4.4 Wellbore section with one cable along the axis of the tubing

The installation of integrated multiple sensors in an observation well is the preferable option for geological CO<sub>2</sub> storages because it maximizes the utility of a single wellbore. The signal cables from sensor gauges and/or capillary lines from fluid sample ports run from downhole depths to the surface, to convey the sensor measurements or to recover downhole fluid samples. It is standard practice that cables and capillary lines are installed along the axis of the tubing for pre-cased wells or outside of the casing of openhole wells to reduce the risk of damaging or losing them during the installation. Figure 6.20 shows a cross section of the observation well configuration with a concentric tubing (60.3 mm in diameter) and one cable (8.0 mm in diameter) with 1 mm gap between them. The magnitude of a gap of one millimeter was chosen based on early analytical results of hydraulic transmissivity of micro-annulus path of Section 6.3, which concludes that the micro-annulus gap could range from 0.8 mm to 1.6 mm depending on the number of cables/capillary lines and the vertical length of the micro path.

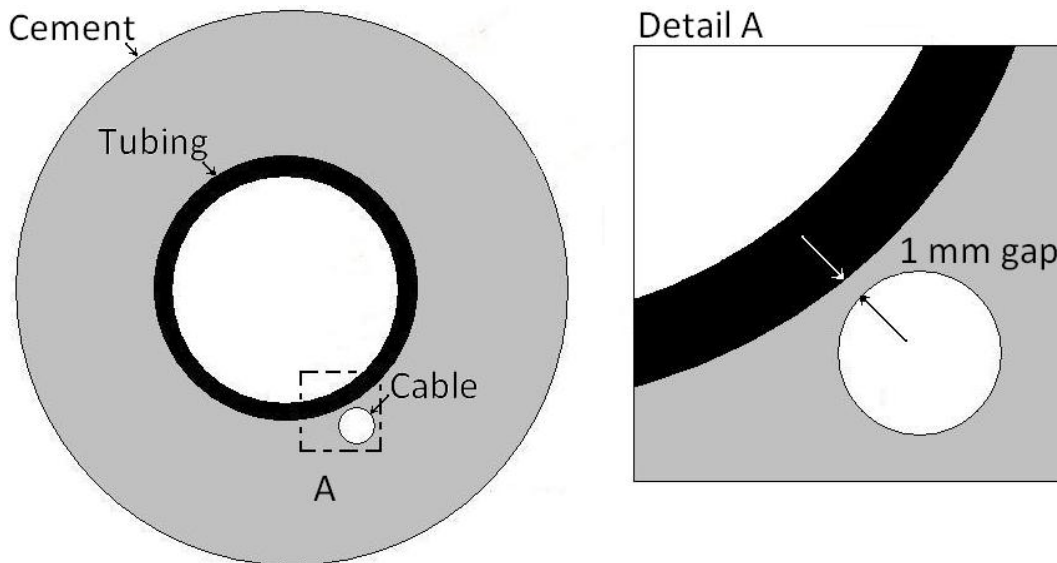


Figure 6.20 The configuration of the borehole cross-section with the tubing and cable.

The preliminary model of a borehole segment, which was a duplicate of a segment installed at Penn West and presented in the previous section, included cables, capillary lines, sensor housings and complex configuration of these elements within the annular space. This model was simplified to study the effect of one cable, but the complexity degree of the discretization and resolutions (0.25 mm) was higher than the previous

models by one order of magnitude. This section studies the cement displacement efficiency of a 2 m long borehole, tubing and cable segment. Figure 6.20 and 6.22 illustrate the cross-section and 3D configuration of the model, respectively. The axis-symmetry condition of this model was used to reduce its volume in half and save some computational time.

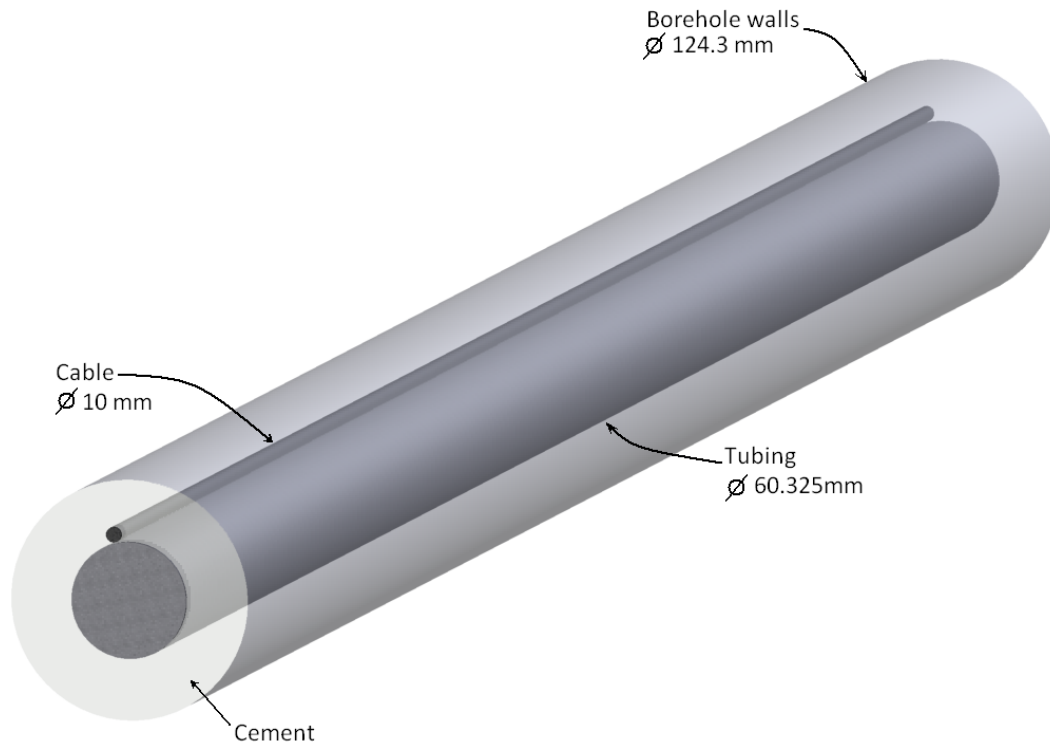


Figure 6.21 3D geometrical configuration of the tubing and cable within the 2 m of a borehole section.

#### 6.4.4.1 Geometry and grid

A geometrical discretization of the 3D axis-symmetrical model was made for the computational fluid dynamics analysis. Structured hexahedral cells were generated to define the model. A view of the generated grid can be seen in Figure 6.22, including the detail of the gap of 1 mm between cable and tubing. This gap of 1 mm was discretized in four cells on the cross-section of this model. This fraction of millimeter resolution resulted in small time steps and significant large computation time for the remaining of CFD simulations presented in this and the following sections.

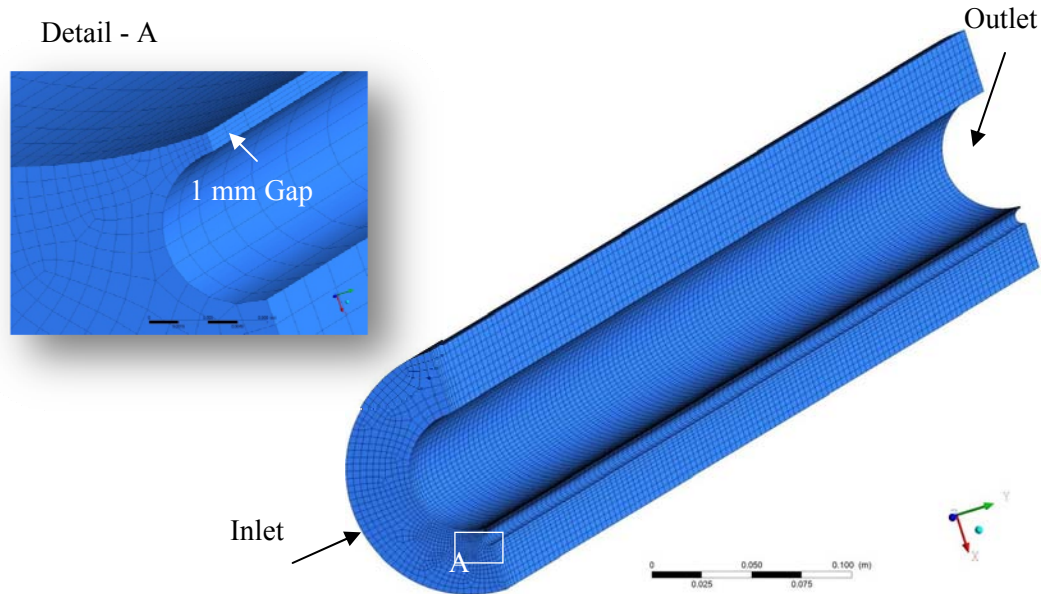


Figure 6.22. Mesh for the 3D axis-symmetrical model of one cable aligned with the tubing and borehole section.

#### 6.4.4.2 Numerical solution control

The simulation was conducted on a computer cluster of 16 nodes with OS-Linux, dual processor AMD Opteron (2.4 GHz) and 27 GB total RAM. Based on the size of this model and the computer cluster capacity, two out of the sixteen nodes were dedicated to this simulation. The time step used in the unsteady calculation was set to  $9.08 \times 10^{-4}$  s, according to Equation 6.4 (page 101). A total of 89 s of flow time was simulated, requiring approximately 676 hours (26 days) of computation time. A mesh with 105,455 nodes and 95,760 elements was used on this analysis.

Intensive grid size dependence tests were carried out with several grid spacing, monitoring the profile variation and an integral quantity from one grid to the other. This was completed to ensure that grid refinement was not generating non-realistic flow artifacts in the simulations. The integral quantities are variables that must take into account the whole solution (i.e., pressure, temperature, velocity, fluid rheology, time, etc). The integral quantity selected for this model and the remaining models was the iso-surface<sup>4</sup> area of the cement slurry volume fraction with value of 0.90, which represents the area within the annular space around the downhole components (tubing conveyed, sensor cable and casing) where there was cement of poor quality (high permeable). These regions are also referred to as “inadequate cement slurry volume fraction” (ISVF) for

<sup>4</sup>The iso-surface is a surface within the model that has a constant value for an specified variable

values of volume fraction less than the unit. The integral quantity value selected for these models was reasonably equal between the several grid spacing meshes, which was expected for structural meshes.

#### **6.4.4.3 Results**

Figure 6.23 and Figure 6.24 show the simulation results of the unsteady displacement of cement displacing fresh-water spacer. The cement slurry volume fraction is presented in a color map format, from which the color “orange” corresponds to the iso-surface with cement slurry volume fraction with value of 0.90 (ISVF-90%).

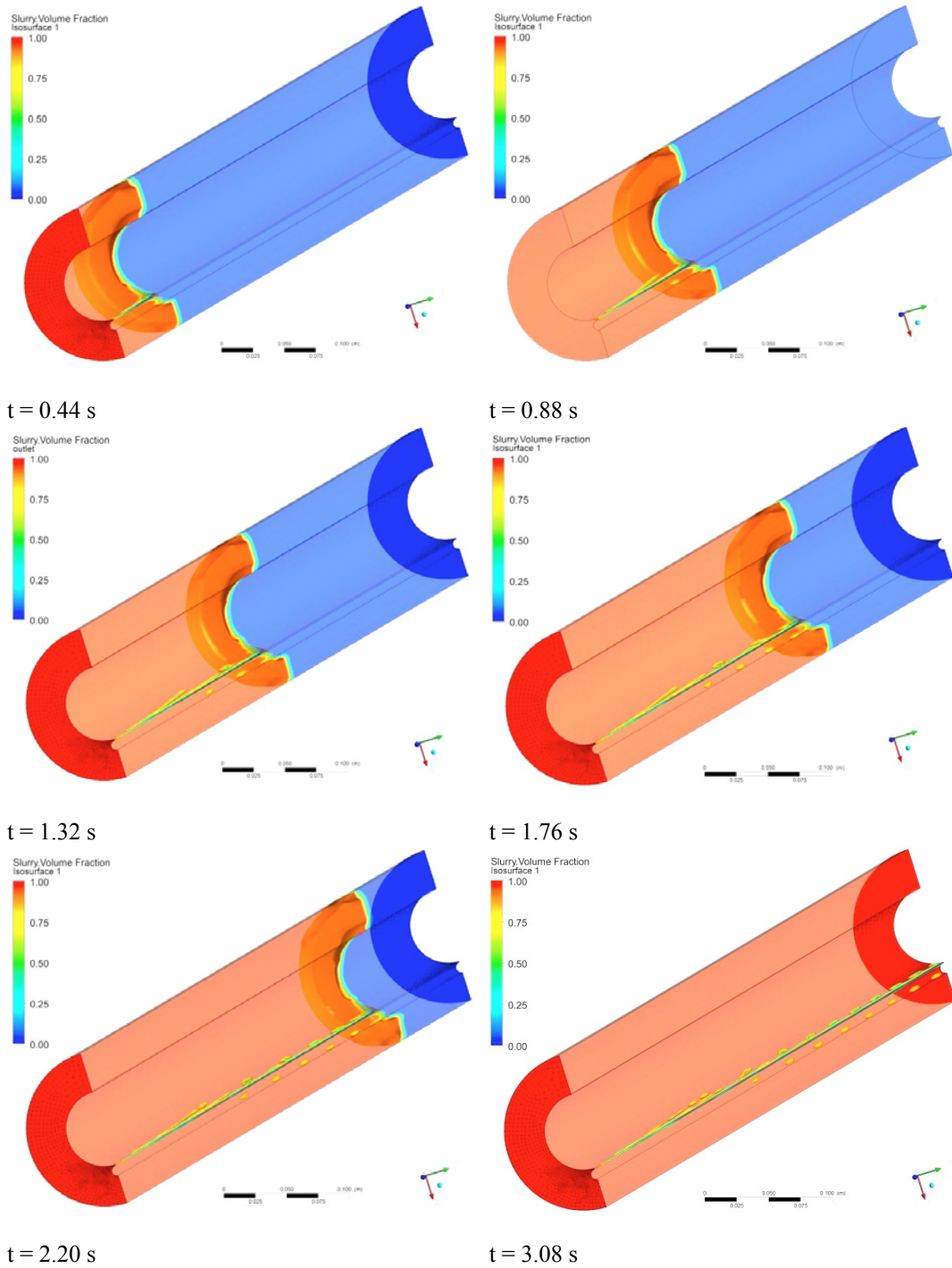


Figure 6.23 VOF simulation results for the axis-symmetrical model of one cable aligned with the tubing and borehole section. Output at times  $t = 0.44, 0.88, 1.32, 1.76, 2.20$  and  $3.08$  s, after the cement slurry enters to annulus. Each snapshot shows cement slurry volume fraction and ISVF = 0.90 (orange).

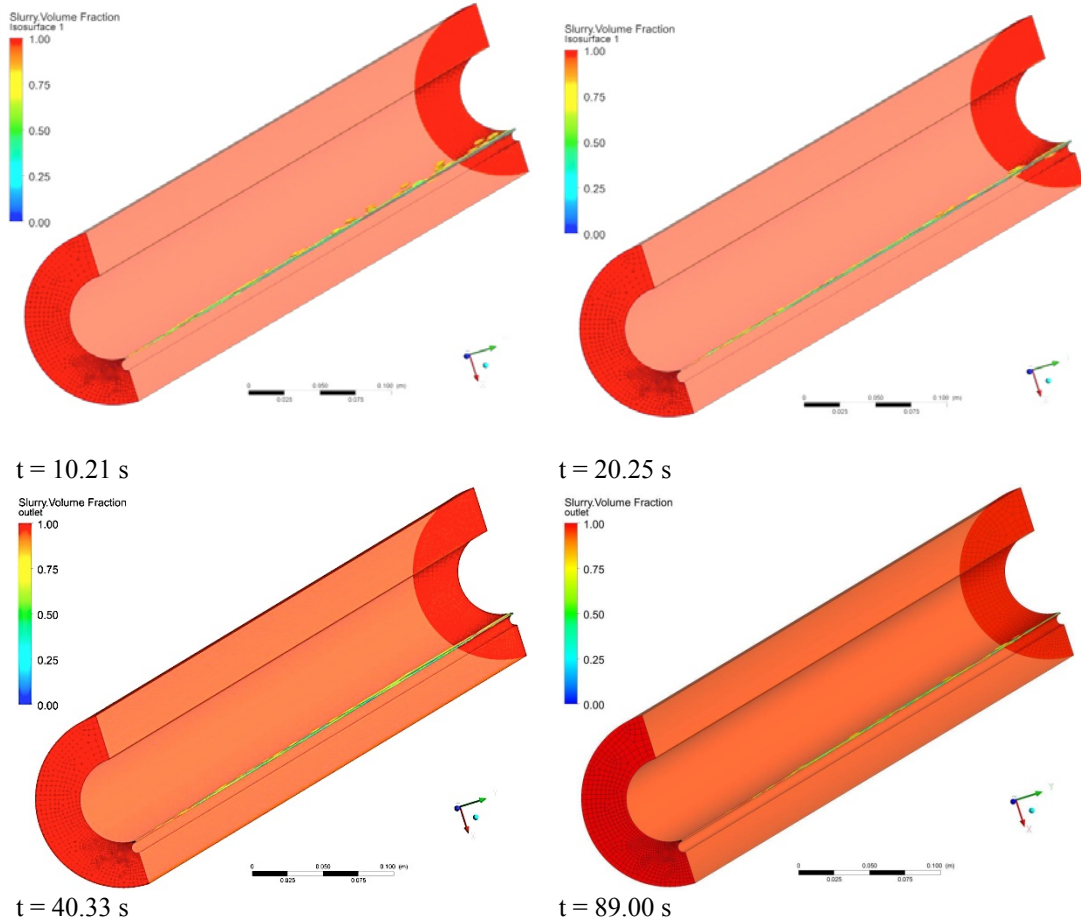


Figure 6.24 VOF simulation results for the axis-symmetrical model of one cable aligned with the tubing and borehole section. Output at times  $t = 10.21, 20.25, 40.33$  and  $89.00$  s, while the cement slurry is displacing through the annulus. Each snapshot shows cement slurry volume fraction and ISVF = 0.90 (orange).

Throughout the entire simulations it was observed that the cement phase displaced most of the freshwater spacer phase except for the gap between the production tubing and the cable. The time to displace the fresh-water spacer by the cement slurry from the inlet to the outlet was 3.00 s (Figure 6.23), but the simulated time was stopped at 89.00 s (Figure 6.24). The main reason for the additional 86 s was because elements like cables are not a local point of flow impedance. They are presented from the bottom hole/inlet to the surface/outlet (or through the entire cement column). Studying the effect for longer circulation times was needed to assess the effect that these elements have when they are installed parallel and close to the tubing.

Figure 6.25 shows the evolutions of the integral quantity through the 89 s of the simulation. The peak value of the area of the iso-surface with volume fraction with value of 0.90 (ISVF-90%) was  $0.0340 \text{ m}^2$ , and it was reached at 3.00 s when the cement slurry

displaced the majority of the fresh-water-spacer phase. The post-peak shown a significant reduction of ISVF-90% in short period time, and it was followed by a creep trend with a residual value of  $0.0308 \text{ m}^2$ . Considering the 3D geometry of the model the final residual ISVF-90% values was  $6.15 \times 10^{-3} \text{ m}^2$  (twice the axi-symetry area of  $3.08 \times 10^{-3} \text{ m}^2$ ) at simulated time of 89.00 s.

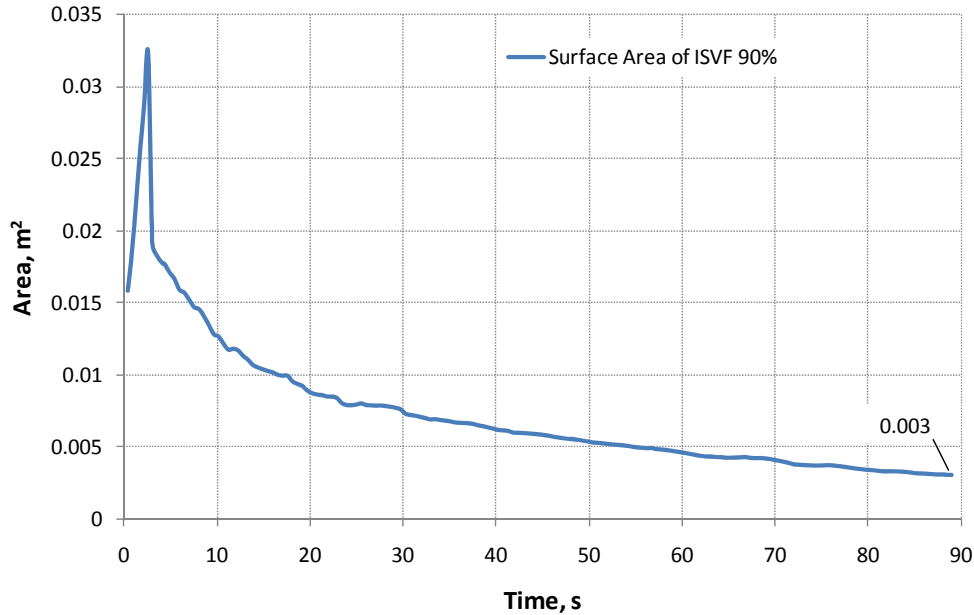


Figure 6.25 Surface area of the ISVF 90 % (integral quantity) – flow time results for the axis-symmetrical model of one cable aligned with the tubing and borehole section.

The inlet and outlet profile velocity and ISVF-90% results of the final time step are presented on Figure 6.26. It is important to notice that the velocity profile of inlet and outlet near the gap between the production tubing and cable was zero (Figure 6.27), and that the inadequate cement slurry volume fraction was located along this gap (Figure 6.26).

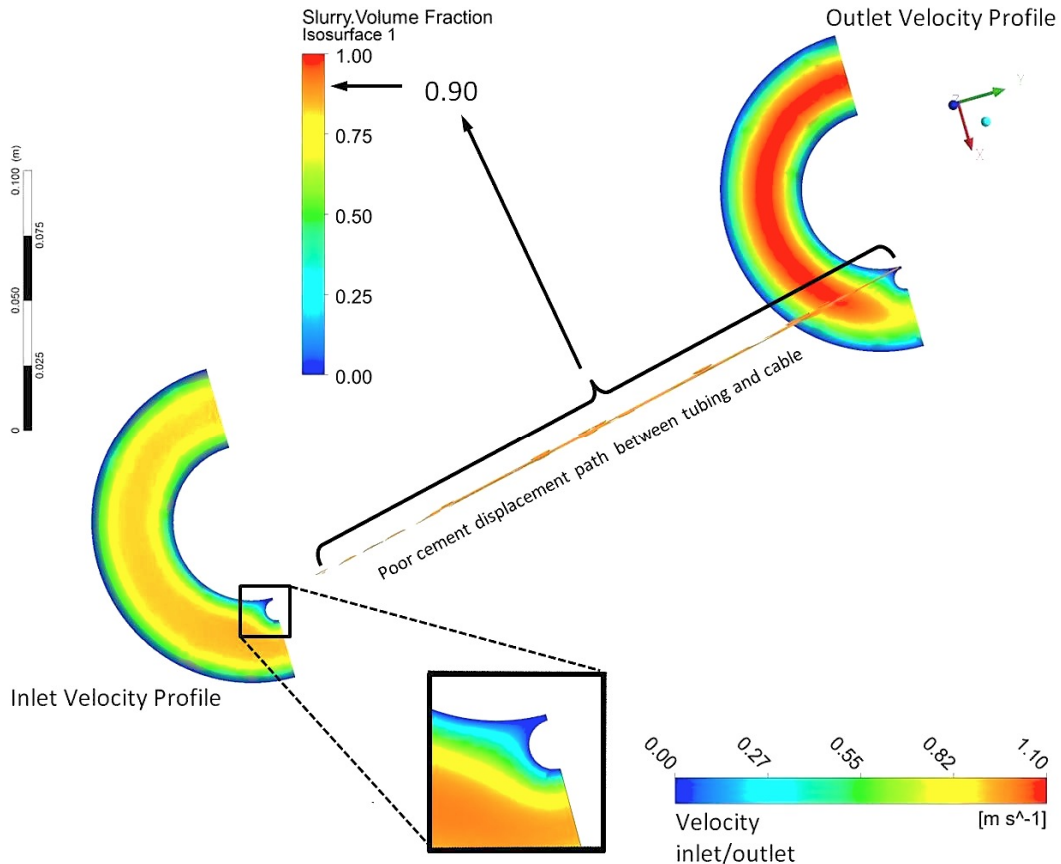


Figure 6.26 VOF simulation results for the axis-symmetrical model of one cable aligned with the tubing and borehole section. Output at times  $t = 89.00$  s, while the cement slurry is displacing through the annulus. The snapshot shows  $ISVF = 0.90$  and velocity profiles of inlet and outlet faces.

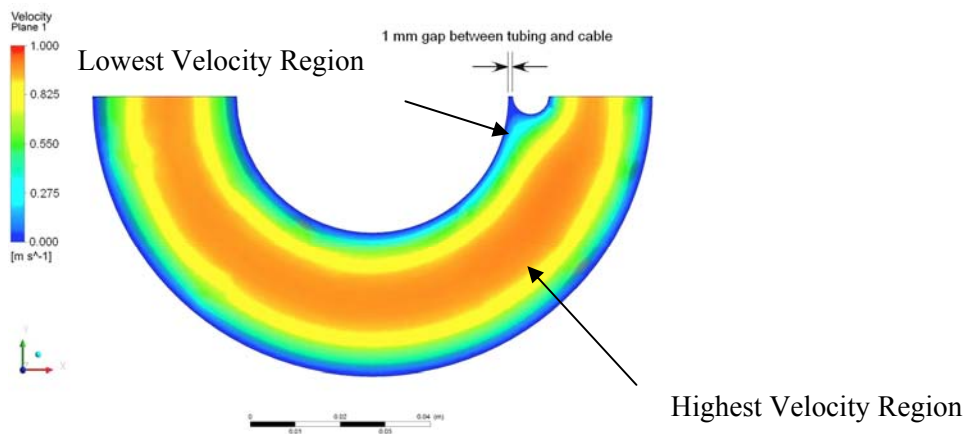
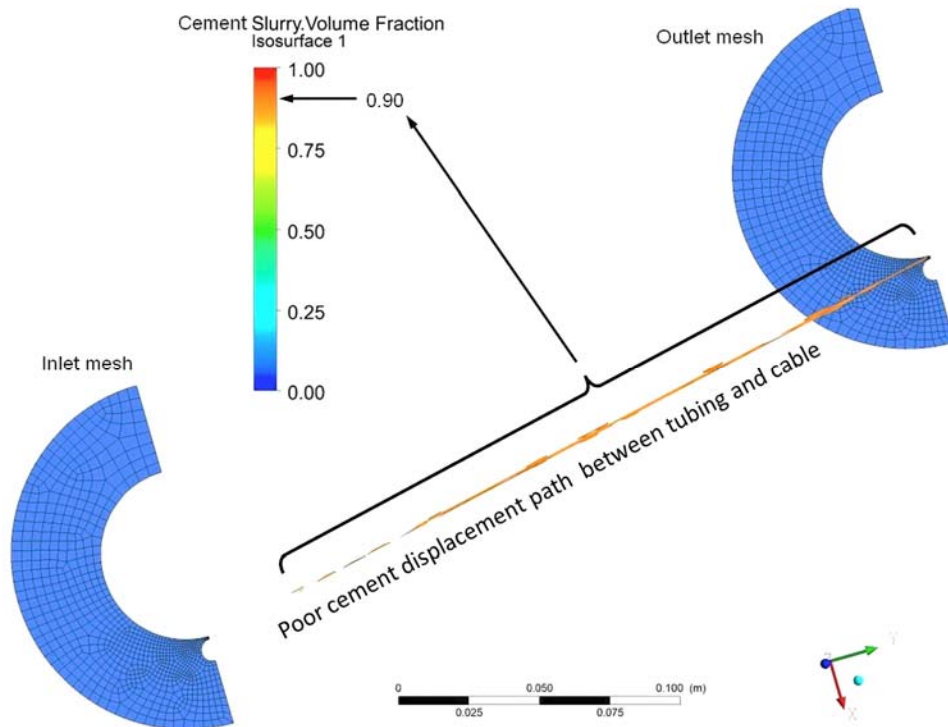


Figure 6.27 VOF simulation results for the axis-symmetrical model of one cable aligned with the tubing and borehole section. Output at times  $t = 89.00$  s, while the cement slurry is displacing through the annulus. The snapshot shows cement slurry velocities on a cross-section of the model.

#### 6.4.4.4 Discussion

Post assessment of the cement job revealed that native fluid invasion occurred when the cement slurry was displacing the fresh-water spacer. Because the lowest velocity regions with values near zero are located on this gap, the mixture of preflush-water, native fluid and cement slurry could not be removed from the gap (Figure 6.28). This could result in pockets of volumes without cement at all and/or a cement mixture with poor quality (highly permeable) between the production tubing and cables paralleled to the tubing.



t = 20.25 s

Figure 6.28 VOF simulation results for the axis-symmetrical model of one cable aligned with the tubing and borehole section. Output at time  $t = 90.00$  s, while the cement slurry is displacing through the annulus. The snapshot shows cement slurry volume fraction and ISVF = 0.90.

One of the main outcomes of this model was the location of the ISVF-90% in one quadrant of the cross-section of the model (Figure 6.29). It is standard practice that the cables of the sensors are placed on one quadrant through the entire length of the observation well allowing them to be protected and to minimize the risk of damage during the installation.

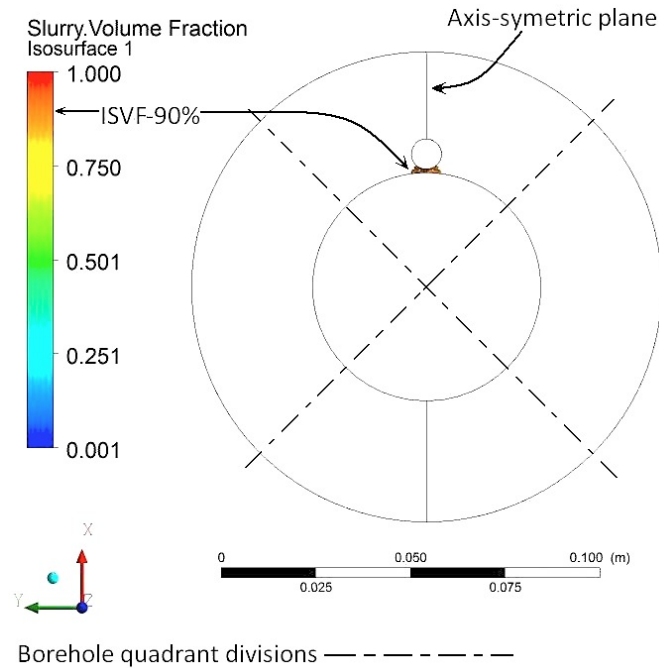


Figure 6.29 VOF simulation results for the axis-symmetrical model of one cable aligned with the tubing and borehole section. Output at time  $t = 90.00$  s, while the cement slurry is displacing through the annulus. The snapshot shows the annular distribution of the ISVF with value of 0.90.

Current standard practice for designing and installing multiple cables of sensors on an observation well focused on the reduction of risk during installation, and minor to zero emphasis is dedicated to the flow design of this elements. This study has exposed the importance of the flow design for downhole elements of integrated observation wells used for MMV activities for CO<sub>2</sub> geological storage.

This problem can be solved by placing the cables in perpendicular or semi-perpendicular direction to annular flow, increasing the shear forces needed to mobilize the fresh-water spacer or native fluid from the gap between the outside diameter of the tubing and the cable (s) and reducing the longitudinal space of the gap. Transient modeling of this geometry was attempted with CFD techniques, but the fraction of millimeter grid resolution required to model the gap of one millimeter resulted in a discretization of a non-structural mesh with more than half million nodes (~1,900,000 elements). This size of modeling required a computer capability that was unavailable within this research study. Figure 6.30 shows the geometrical configuration and discretization of a cable aligned diagonal to the axis of the tubing and spaced one millimeter from the outside diameter of the tubing. Also, Figure 6.30 (e) presents preliminary results of velocity on a cross-section of this model for the first time step, where it was noticed a significant enhance on the velocity near the cable and tubing that could result in better cement

displacement efficiency. However, these preliminary results are an illustration for future studies because additional tests for grid independence are need to confirm these results.

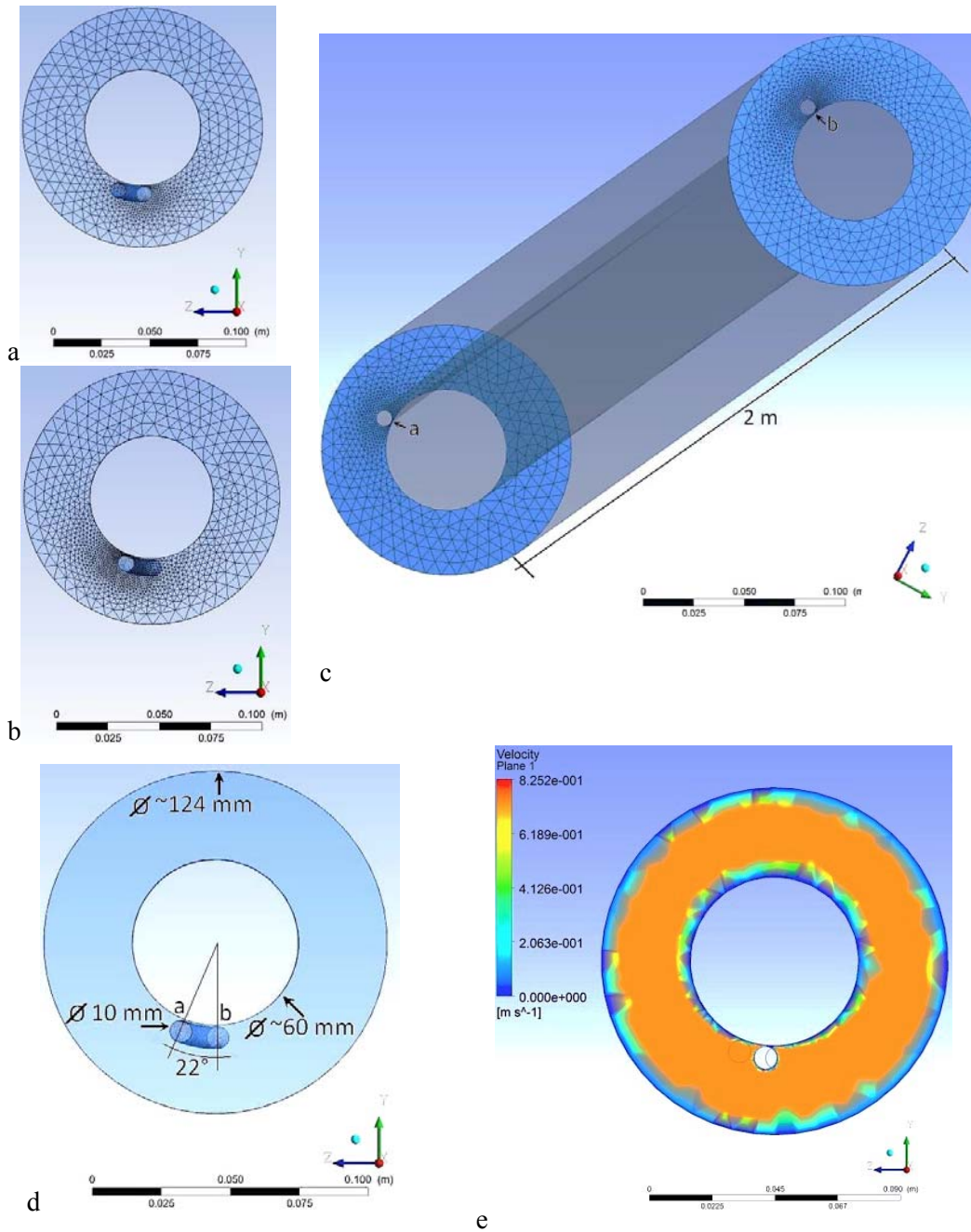


Figure 6.30 Mesh for the preliminary 3D model of one cable aligned diagonal with the tubing and borehole section. (a) Outlet, (b) Inlet, (c) isometric view of the model, (d) Cross-section of cable alignment, and (e) velocity profile of cross-section of the model, output time = .0022 s.

The simulations presented in this section have shown that if a cable is placed near and parallel to the axis of the tubing, there is a high risk of having a zone of poor quality cement (micro-annulus path) between the tubing and cable. This model like any other

model presents a likely outcome based on the geometrical conditions and fluid properties. In reality the installation of only one cable will not meet this condition accurately, where the cable is aligned parallel to the tubing and it is separated 1 mm through the entire tubing string of hundreds of meters<sup>5</sup>. However, an integrated observation well used for MMV activities for CO<sub>2</sub> geological storage will have multiple sensors and cables deployed at different geological targets. The deployment of these multiple cables could meet the conditions of this model, where the space between cables and parallel alignment could be almost constant through the entire tubing string, as illustrated in Figure 6.9 (page 93) for the case of the Penn West installation.

For installation of multiple sensors it is recommended to pack cables in stainless steel capillary lines of 6.35 mm (¼ inches) of diameter. This will eliminate the possible spaces between cables enhancing the cement flow during completion and reduce the risk of damage during installation. The additional cost associated for the use of stainless steel capillary lines is minimum compared to the cost of mitigation activities in the case of the development of a micro-annulus path or cable damage during installation. Also, the use of steel capillary lines could help to fix the cables in a position perpendicular or semi-perpendicular direction to the annular flow, resulting in a cement flow enhancement.

#### **6.4.5 Sensor housing system and tubing conveyed**

The sensor housing system for permanent downhole sensors is a key element to protect the sensor body and to access direct contact to the geological formation of interest. However, without an adequate flow design, the geometry of the sensor housing lowers the local cement displacement efficiency during the cement completion because its geometry reduces the annular space, resulting in flow impedance near the location of the sensor. The scope of this section is to study the extendedness of the flow impedance near the sensor housing standoff geometry used in the observation well in the Pembina Cardium CO<sub>2</sub> Monitoring Pilot. Figure 6.31 shows the as-is CAD drawings of sensor housing system, including a preliminary 3D drawing.

---

<sup>5</sup> CO<sub>2</sub> geological storage will occur at a depth greater 1000 m, where the minimum condition of pressures and temperatures for its supercritical conditions are found.

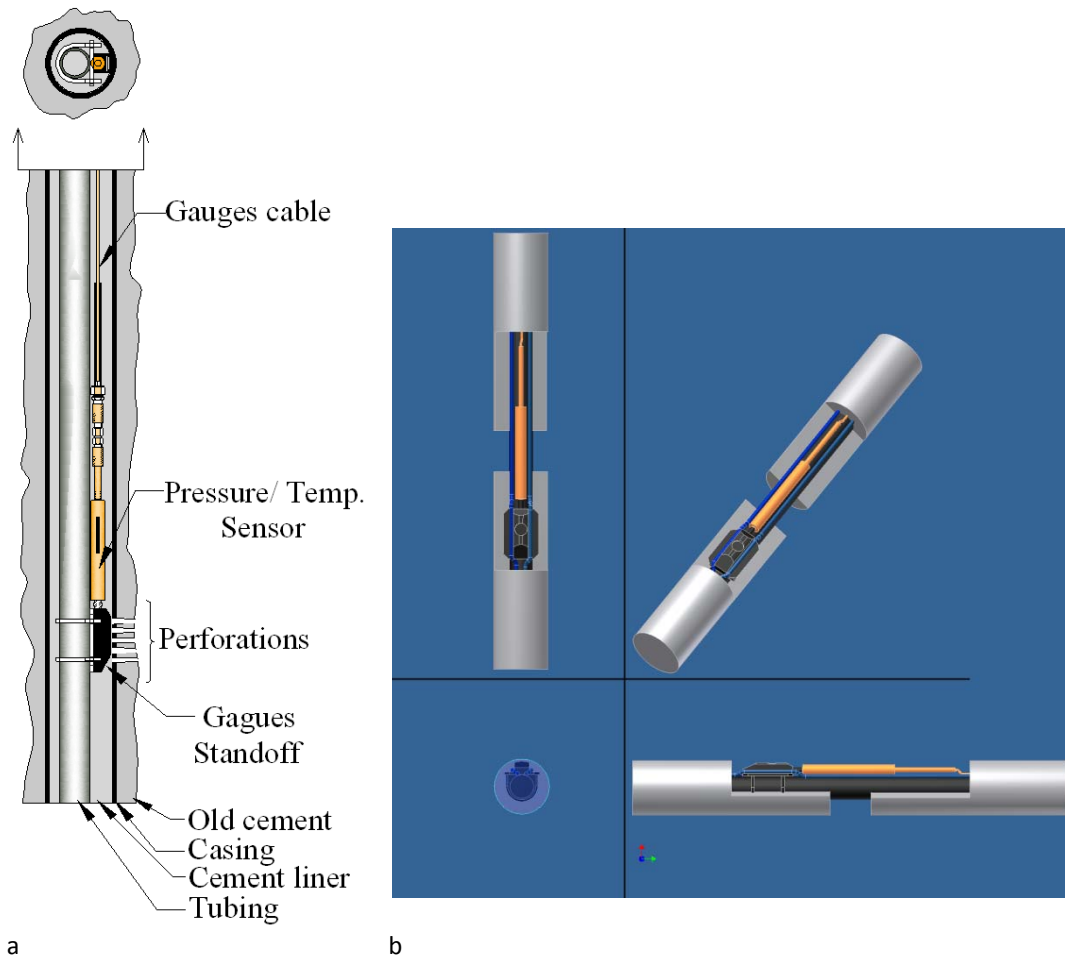
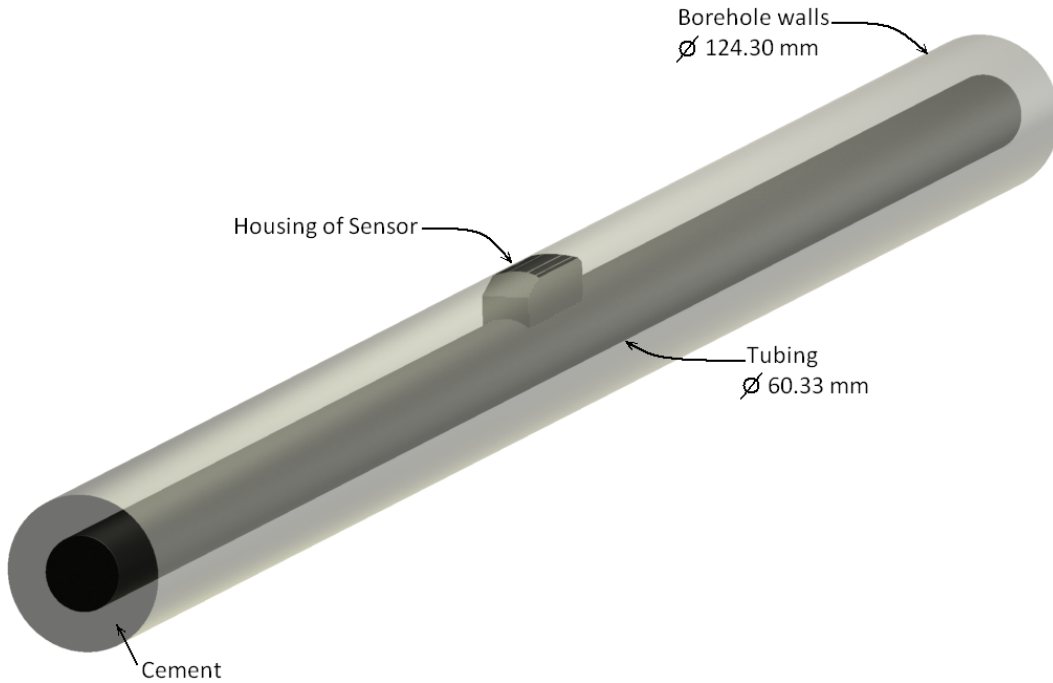


Figure 6.31 Sensor housing system: (a) as-is CAD drawing, (b) preliminary 3D drawings.

#### 6.4.5.1 Geometry and grid

The geometry of the housing was simplified, excluding the detail of screws, bolts, cables and electrical components, and preserving the gross shape of the housing standoff, which was the mayor element that could induce significant local flow impedance near the sensor housing system. It was also assumed that the standoff was in full contact with the borehole wall to minimize short edges, and sharp angles, which could compromise the numerical convergence.



*Figure 6.32 3D geometrical configuration of the sensor housing and tubing conveyed within the 1.7 m of borehole section.*

Figure 6.32 illustrates the geometry of the sensor housing and tubing conveyed within a borehole section of 1.70 m in length. The axis-symmetry condition of this model was used to reduce its volume in half and save some computational time. A geometrical discretization of the 3D axis-symmetrical model was made for the computational fluid dynamics analysis. Unstructured tetrahedral cells were generated to define the model. A view of the generated grid can be seen in Figure 6.33.

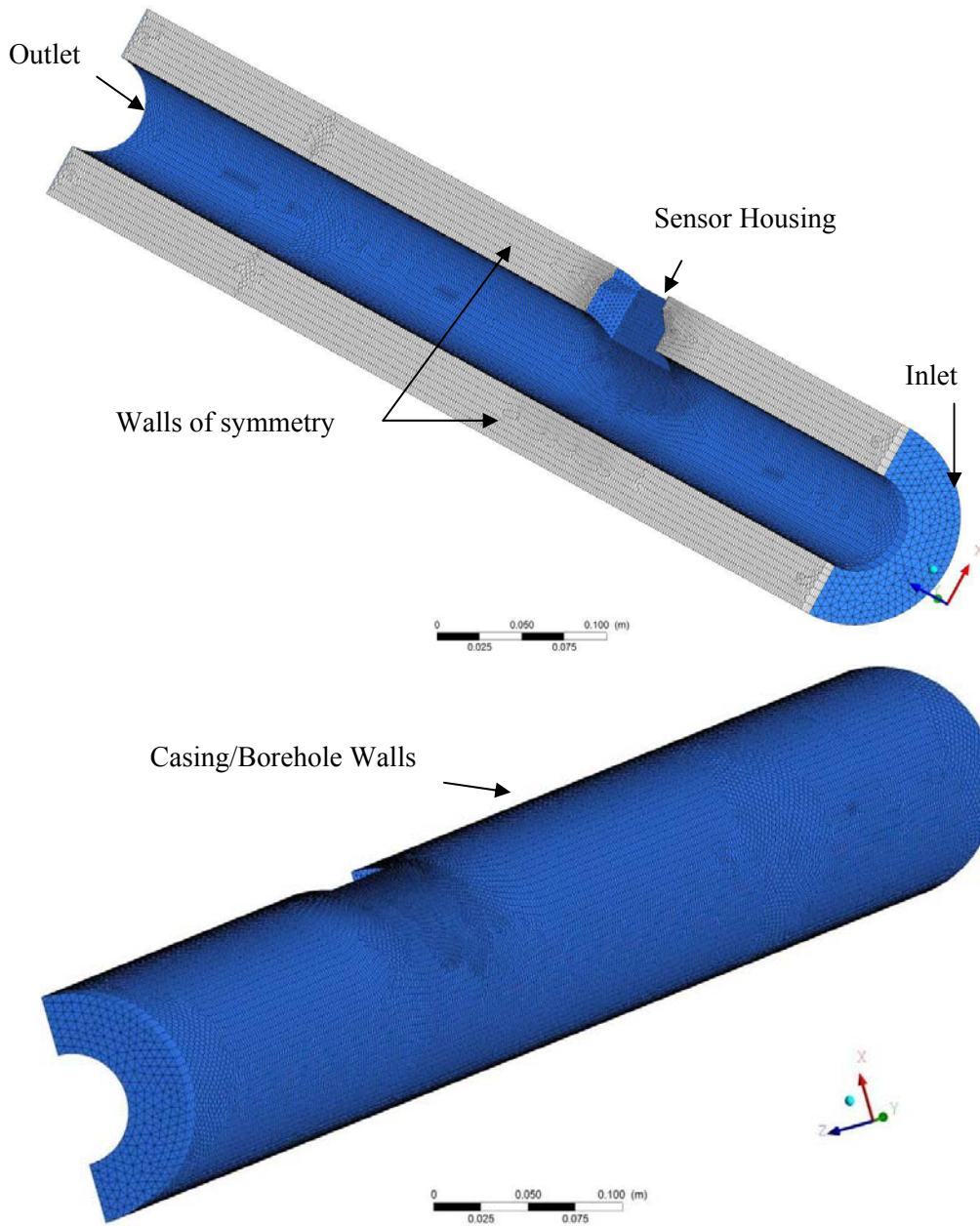


Figure 6.33 Sketch of Mesh for the axis-symmetric 3D sensor housing model duplicate from the Pembina Cardium CO<sub>2</sub> monitoring observation well.

#### 6.4.5.2 Numerical Solution Control

These simulations were also conducted on a computer cluster of 16 nodes, which specifications were presented in the previous section. The time step used in the unsteady calculation was set to  $9.58 \times 10^{-4}$  s, according to Equation 6.4. A total of 4.0 to 3.5 s of flow time was simulated, requiring approximately 576 hours (24 days) of computation time. A mesh with 134,212 nodes and 715,007 elements was used on this analysis.

Extensive grid size and boundary placement dependence tests were also carried out with several grid spacing and boundary location. Also, the integral quantity selected for this section was the iso-surface area of the cement slurry volume fraction with value of 0.90 or ISFV -90%. To confirm the trend of ISFV-90% in a different spatial dimension of the models, the cement slurry volume fraction with value of 0.95 or ISFV -95% was also monitored.

#### **6.4.5.3 Results**

Figure 6.34 and Figure 6.35 show simulation results of the unsteady displacement of cement displacing a freshwater spacer. The cement slurry volume fraction is presented in a color map format, from which the color “orange” corresponds to the iso-surface with cement slurry volume fraction with value of 0.90 (ISFV-90%). Also, the velocity streamlines are presented in these figures in a color map format.

Throughout the entire simulations it was observed that the velocity streamlines were moving parallel to the borehole walls except near the sensor standoff, reflecting the flow impedance that this type of geometry induced during the cement circulation of the case study.

From a different view, the Figure 6.36 presents the sequence of time steps of the cement displacement simulation with results of volume fraction, including the integral quantity (ISFV-90%). From which, it is observed that the cement phase displaced most of the fresh-water-spacer phase, except from the zones behind the sensor standoff where more of the ISFV-90% was located.

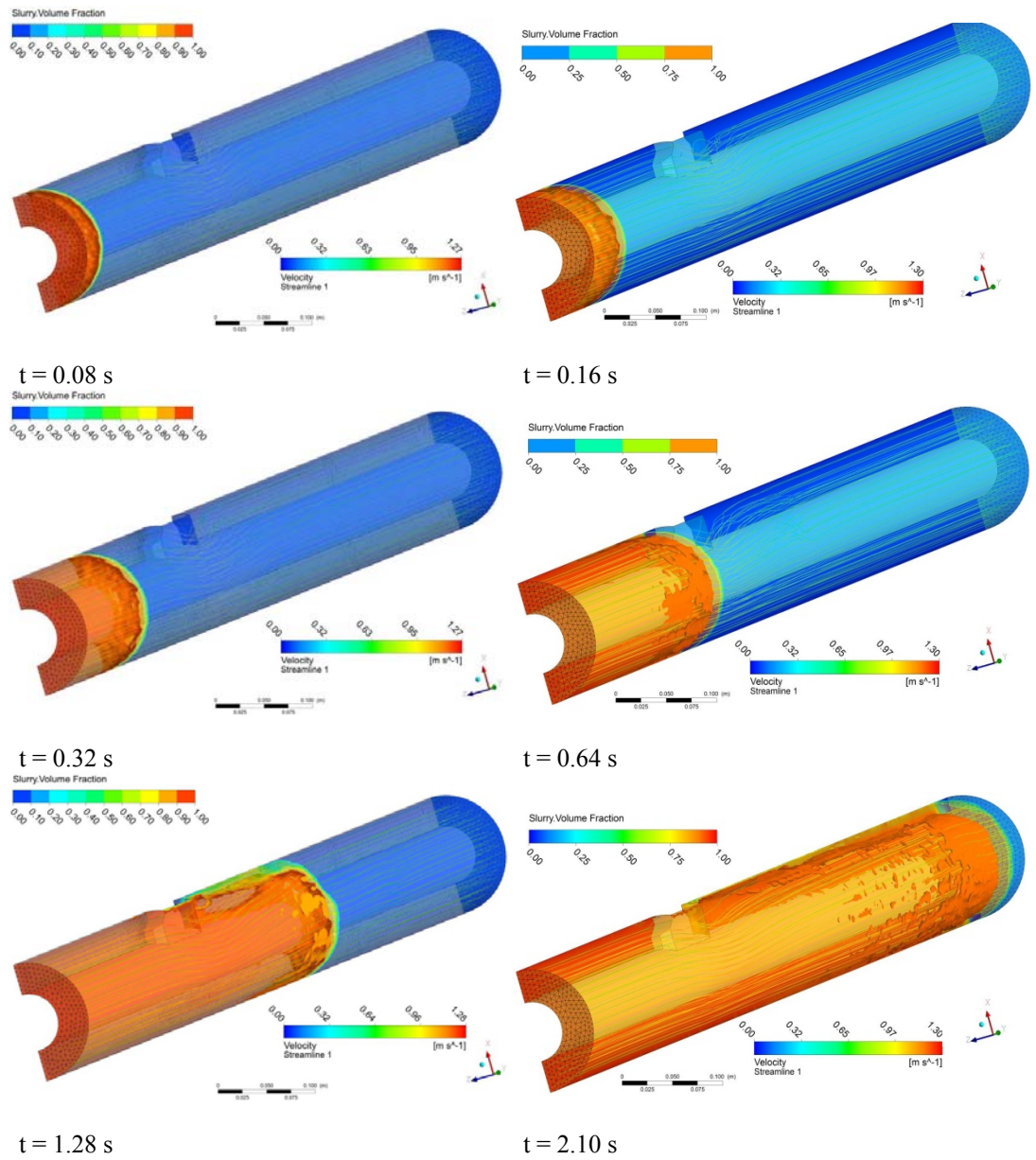


*Figure 6.34 VOF simulation results for the axis-symmetrical model of one sensor housing standoff installed at the Pembina Cardium CO<sub>2</sub> pilot. Output at times  $t = 0.08, 0.16, 0.32, 0.64, 1.28$  and  $2.10$  s, while the cement slurry is displacing through the annulus. Each snapshot shows cement slurry volume fraction, ISVF = 0.90, and annular velocity streamlines.*

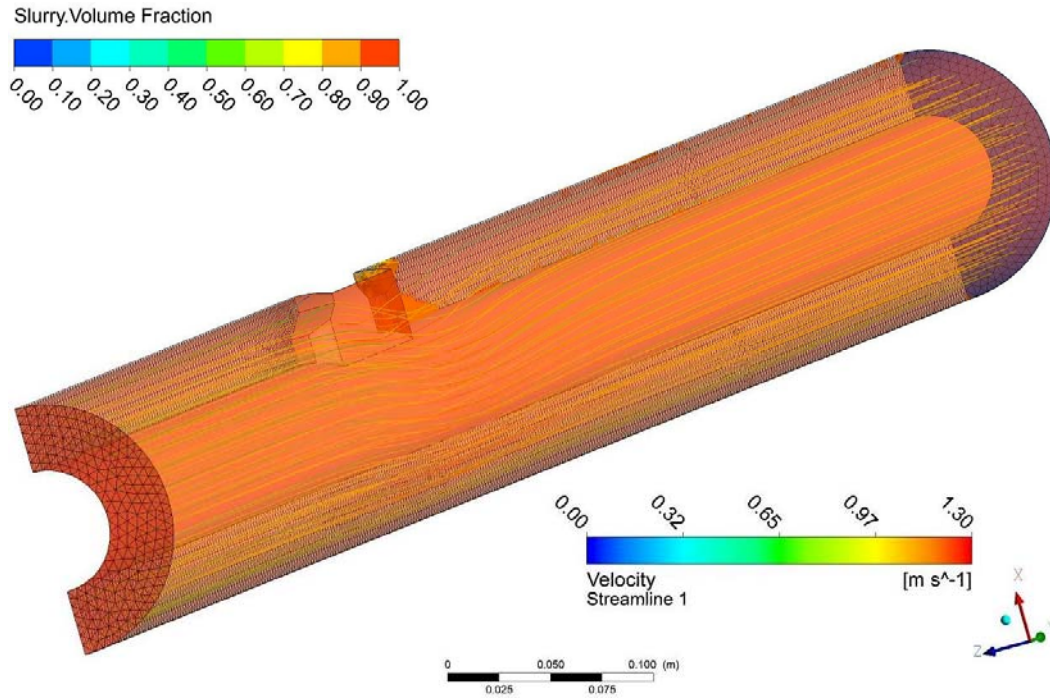


Figure 6.35 VOF simulation results for the axis-symmetrical model of one sensor housing standoff installed at the Pembina Cardium CO<sub>2</sub> pilot. Output at times  $t = 3.50$  s, while the cement slurry is displacing through the annulus. Each snapshot shows cement slurry volume fraction, ISVF = 0.90 (light orange), and annular velocity streamlines.

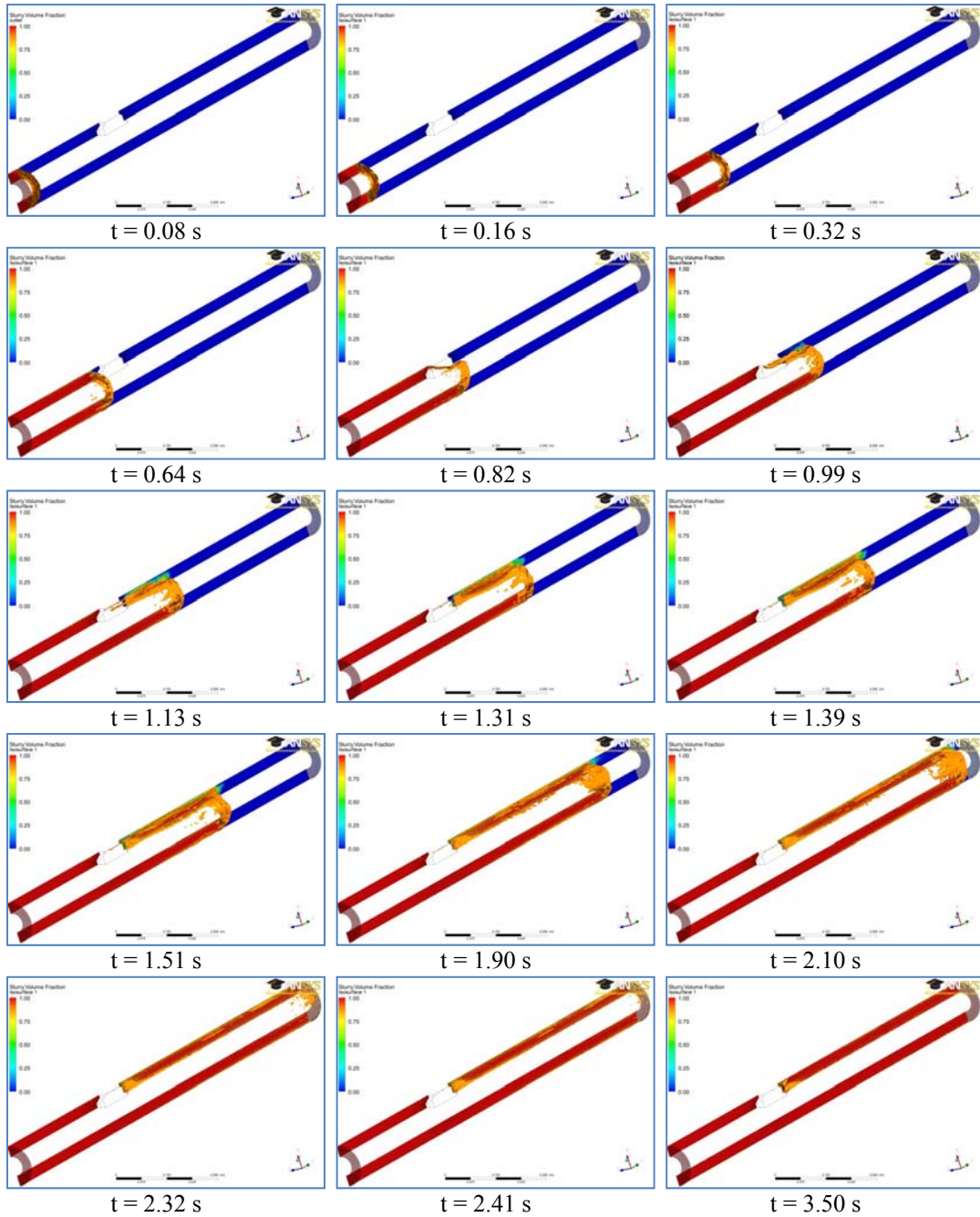
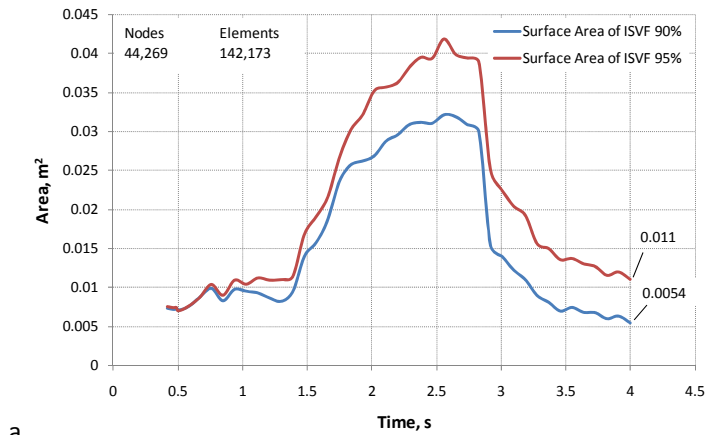
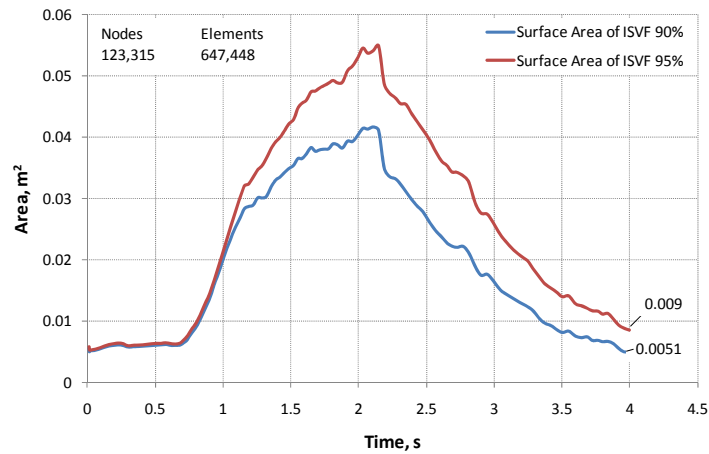


Figure 6.36 VOF simulation results for the axis-symmetrical model of one sensor housing standoff installed at the Pembina Cardium CO<sub>2</sub> pilot. Output at times  $t = 0.08, 0.16, 0.32, 0.64, 0.82, 0.99, 1.13, 1.31, 1.39, 1.51, 1.90, 2.10, 2.32, 2.41$  and  $3.50$  s, while the cement slurry is displacing through the annulus. Each snapshot shows cement slurry volume fraction and ISVF = 0.90 (orange).

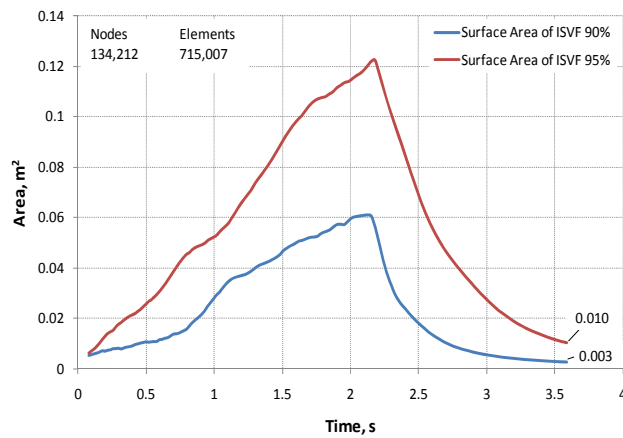
Figure 6.37 summarizes the evolution of the integral quantity through the 4.00 s of the simulation. The integral quantity value was reasonable equal on the several grid spacing meshes. Figure 6.37 (c) shows the integral quantity for the finest mesh, for which the peak value of the area of the iso-surface with volume fraction with value 0.90 (ISVF-90%) was  $0.06 \text{ m}^2$ , and it was reached at 2.20 s when the cement slurry displaced the majority of the fresh-water-spacer phase. The post-peak values shown a significant reduction on ISVF-90% in short period of time, and it was followed by a creep trend with a residual value of  $6 \times 10^{-3} \text{ m}^2$  (twice the axi-symmetry area of  $3.00 \times 10^{-3} \text{ m}^2$ ) at simulation time of 3.50 s.



a



b



c

Figure 6.37 Summary surface area of the ISVF-90% and ISVF-95% (integral quantities) – flow time results for different grid spacing meshes for the axi-symmetrical models of one sensor housing standoff on the tubing conveyed and borehole section. (a) 44,269 nodes mesh, (b) 123,315 nodes mesh, and (c) 134,212 nodes mesh.

#### 6.4.5.4 Discussion

From these simulations, it is observed that the sensor housing geometry used at the observation well in the Pembina Cardium CO<sub>2</sub> Monitoring Pilot has an inadequate flow design. It has a blocky shape with sharp angles between faces that impeded the continuity of the streamlines. Figure 6.38 shows that at 0.60 s the cement slurry front was balanced, but after facing the flow impedance caused by the sensor housing at 0.82 s a fingering effect occurred on the cement slurry front. At 0.99 s, the fingering of the cement slurry front was expanding on three quadrants of the borehole cross-section, displacing the fresh-water spacer from these quadrants. At the same time on the remainder quadrant that was located downstream of the sensor housing, the freshwater-spacer phase was displaced partially leaving a mixture of poor quality cement behind.

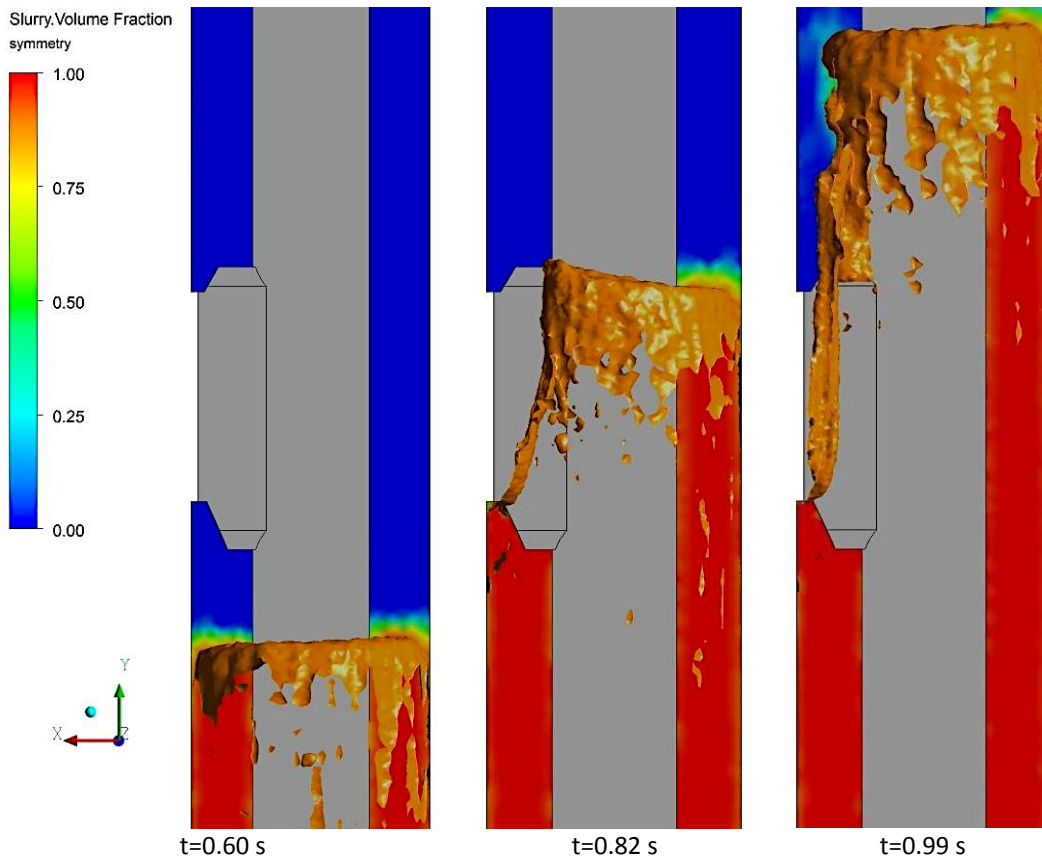


Figure 6.38 VOF simulation results for the axis-symmetrical model of one sensor housing installed at the Pembina Cardium CO<sub>2</sub> pilot. Output at times  $t = 0.60, 0.82$  and  $0.99$  s, while the cement slurry is displacing through the annulus. The snapshot shows the annular distribution of the ISVF with value of 0.90.

One of the main outcomes to highlight from these simulations is the location of the ISVF-90% which was located on one quadrant of the cross-section of the borehole (Figure

6.39). Because it is standard practice to locate the cables of the sensing element downstream of the sensor housing standoff to protect them during installation, the cable were also located on the same quadrant increasing the risk of having a poor quality cement column on the same quadrant ( Figure 6.40).

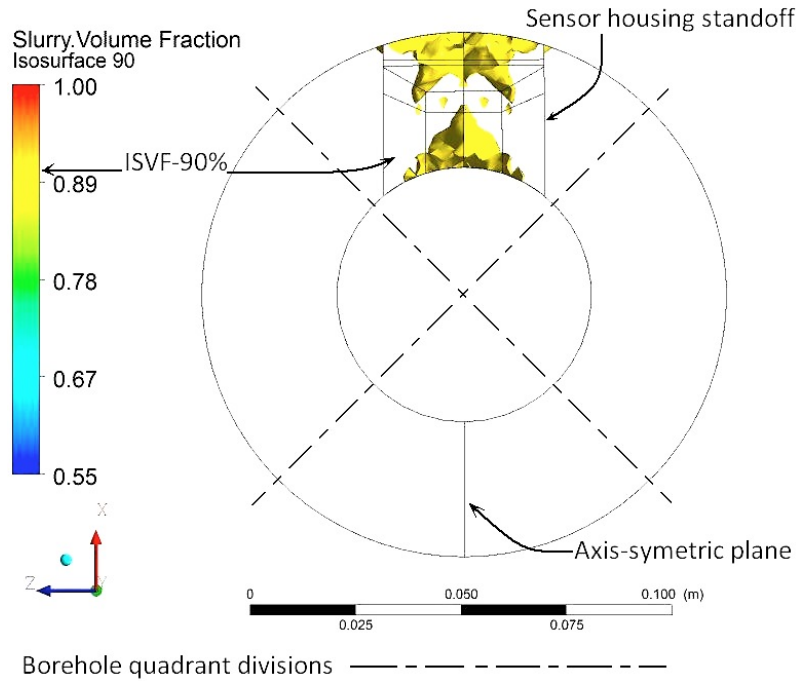


Figure 6.39 VOF simulation results for the axis-symmetrical model of one sensor housing installed at the Pembina Cardium CO<sub>2</sub> pilot. Output at times  $t = 3.50$  s, while the cement slurry is displacing through the annulus. The snapshot shows the annular distribution of the ISVF with value of 0.90.

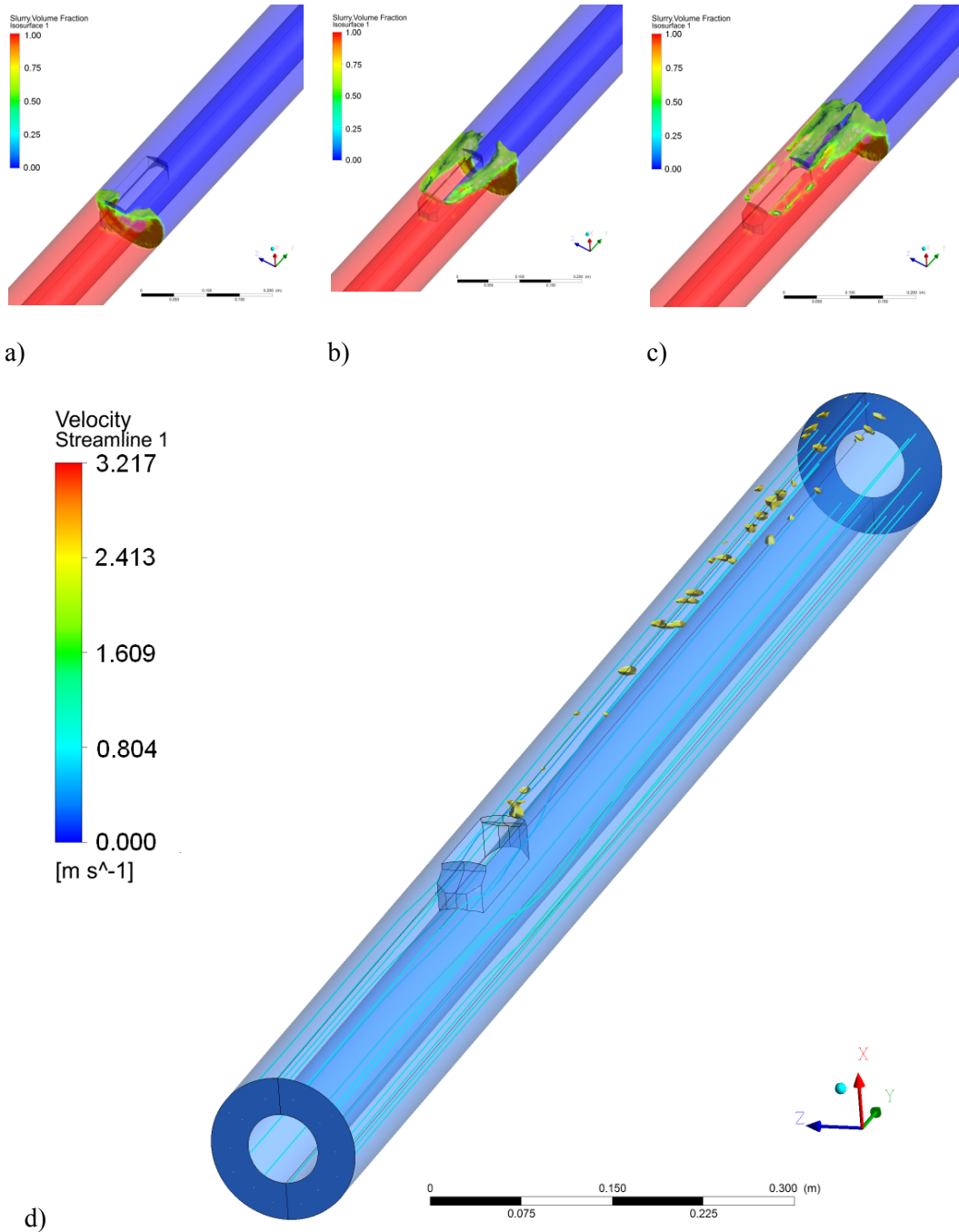


Figure 6.40 Summary of VOF simulation results for the 3D model of the sensor housing standoff, tubing conveyed and borehole sections. Output at time  $t = 0.64$  (a),  $0.82$  (b),  $0.99$  (c) and  $3.50$  (d) s, while the cement slurry is displacing through the annulus. Each snapshot shows the annular distribution of ISVF with value of 0.90.

#### **6.4.6 Sensor housing, tubing conveyed with flow deflector fins**

The outcomes from previous simulations mainly concluded that the geometry configuration of the sensor housing used in Penn West was not the best fit for the cement displacement flow conditions. Therefore, the remaining scope of this study is to evaluate novel geometrical configurations of the sensor housing system that could reduce the poor quality cement column micro-annulus path for similar sensor housing systems. This section focused on a conceptual sensor housing geometry, which is an element that can be re-shaped to enhance the flow of cement slurry near the sensor during the completion of the observation well.

##### ***6.4.6.1 Geometry and grid***

Early results from this study have shown most low cement displacement efficiency regions were located on one quadrant of the borehole cross-section; therefore, integrated flow deflector fins (stand-off devices) were integrated into the geometry of the sensor housing system of this model. This first approach focused on the movement of cement slurry around the sensor housing by adding flow deflector fins down and up stream of the sensor housing. Figure 6.41 illustrates the conceptual 3D configuration of the sensor housing with five flow deflector fins.

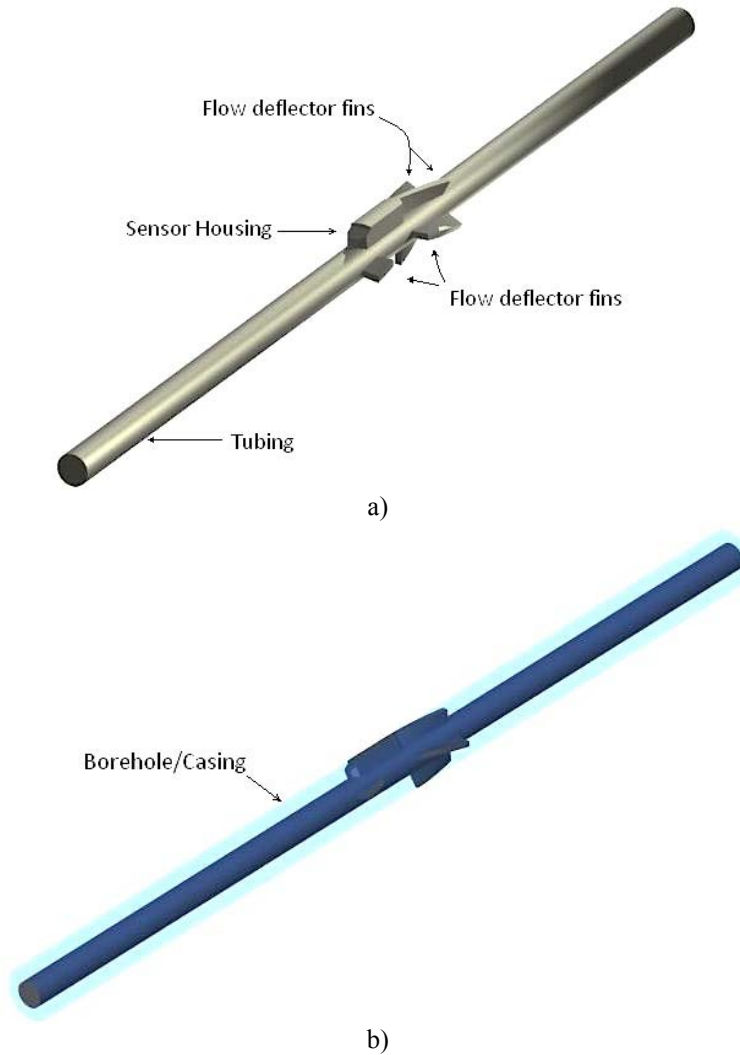


Figure 6.41 3D geometrical boundary conditions of the borehole and tubing conveyed with the sensor housing and five flow deflector fins.

The dimensions of these fins that could enhance the cement displacement were selected from the parametric study conducted by Yao and Robello [77] on the effect on fin width, fin length, fin angle for various Non-Newtonian fluid properties. Based on the fluid properties of this case study (Table 6.1, page 100) the configurations of flow deflector fins used for this study are shown in Figure 6.42. Each fin has  $7^\circ$  of deviation from vertical position and 12 mm width. There are four long fins (127 mm length) located at downstream and one short fin (50 mm length) at the upstream of the sensor housing. It is expected that these dimensions could cause a small pressure drop of 50 Pa, according to [77]. The configurations of the fins were the result of extensive steady state simulations of flow valance around the sensor housing system.

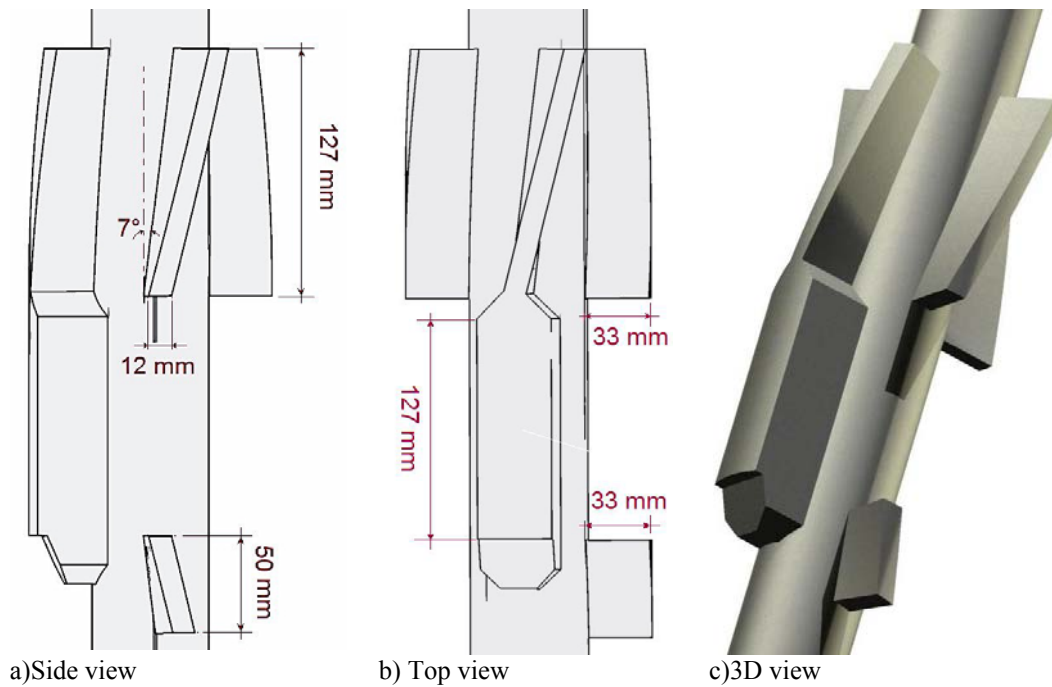


Figure 6.42 Geometry of the conceptual sensor housing and five flow deflector fins.

A geometrical discretization of this 3D model was made for the computational fluid dynamics analysis. Unstructured tetrahedral cells were generated to define the model. A view of the generated grid can be seen in Figure 6.43.

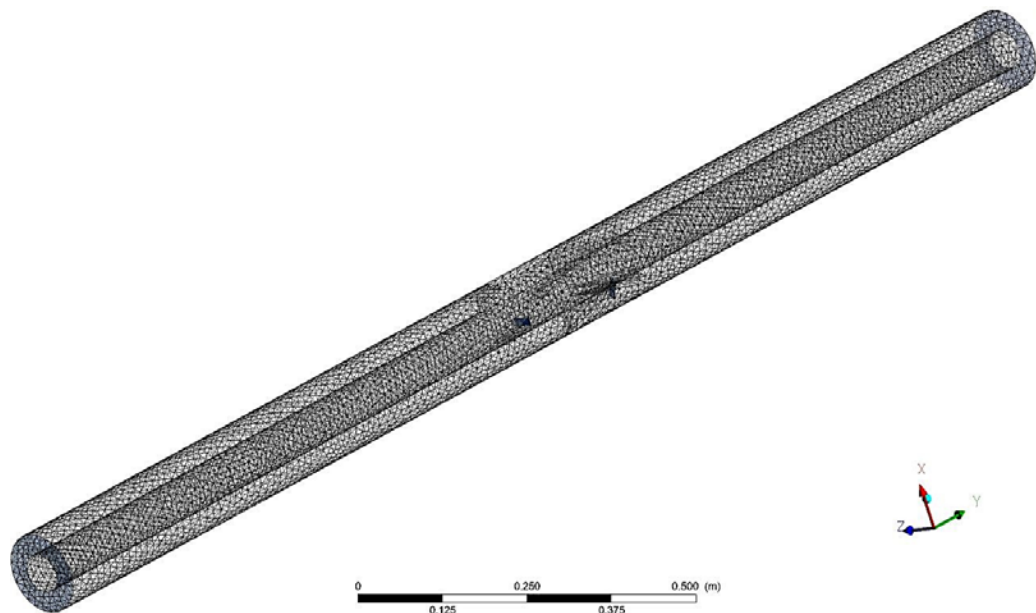


Figure 6.43 Sketch of Mesh of the conceptual 3D sensor housing system with five flow deflector fins.

#### **6.4.6.2 Numerical solution control**

The simulation was conducted on a workstation with Microsoft Windows XP 64, Intel Xeon (3.4 GHz) and 8 GB of memory, but parametric study to define the geometry configuration of this model used a computer closer that was described in the previous section. The time step used in the unsteady calculation was set to  $4.03 \times 10^{-3}$  s, according to Equation 6.4. A total of 4 s of flow time was simulated, requiring approximately 216 hours (9 days) of computation time. A mesh with 21,688 nodes and 101,538 elements was used on this analysis.

Because this was a conceptual model, partial grid size dependence tests were carried out with two grid spacing, monitoring the profile variation and the integrity quantity from one grid to the other. Also, the integral quantity selected for this section was the iso-surface area of the cement slurry volume fraction with value of 0.90 or ISFV -90%. To confirm the trend of ISFV-90% in a different spatial dimension of the models, the cement slurry volume fraction with value of 0.95 or ISFV -95% was also monitored.

#### **6.4.6.3 Results**

Figure 6.44 illustrates the effect on the flow re-direction that the fins induced on the annular flow near the sensor housing system. The upstream flow lines were parallel to the borehole, but through and downstream of the sensor housing system and fins the streamlines were following the direction of the long fins ( $7^\circ$  of deviation from vertical position).

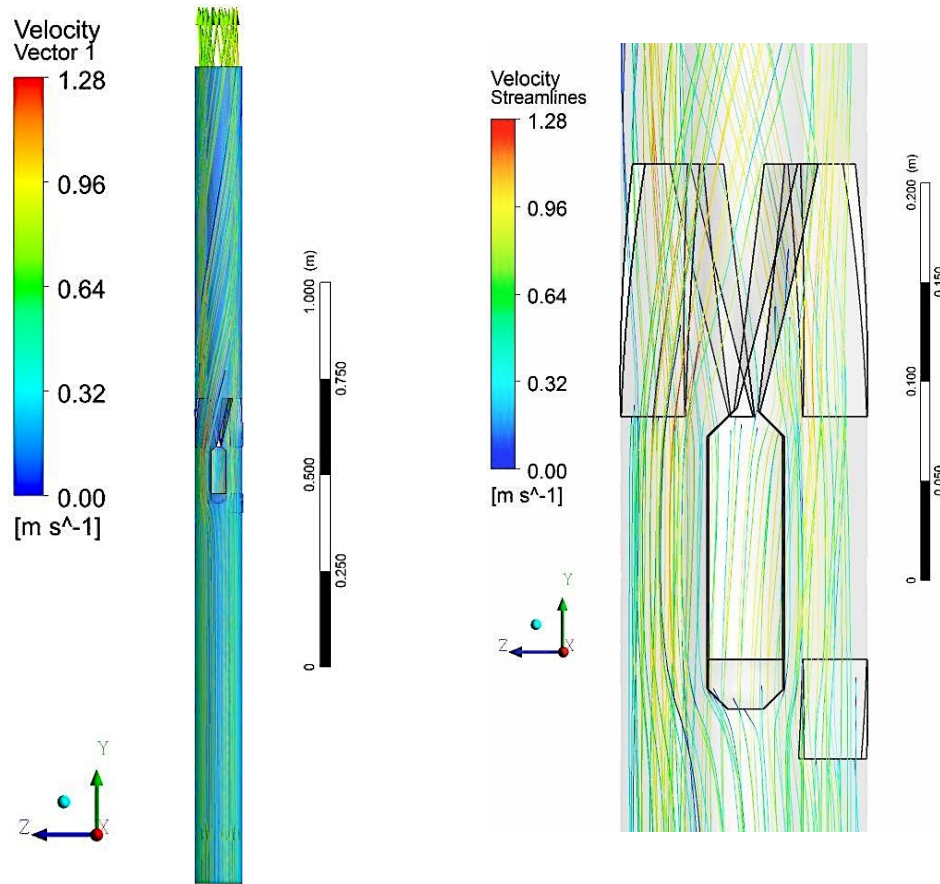


Figure 6.44 VOF simulation results for the 3D model of the sensor housing with five flow deflector fins, tubing conveyed and borehole section of 2.2 m length. Output at time  $t = 4.00$  s, while the cement slurry is displacing through the annulus. The snapshots show cement slurry velocity streamlines.

Figure 6.45 shows simulation results of the unsteady displacement of cement displacing fresh-water spacer. The cement slurry volume fraction is presented in a color map format, from which the color “orange” corresponds to the iso-surface with volume fraction of cement slurry with value of 0.90 (ISVF-90%).

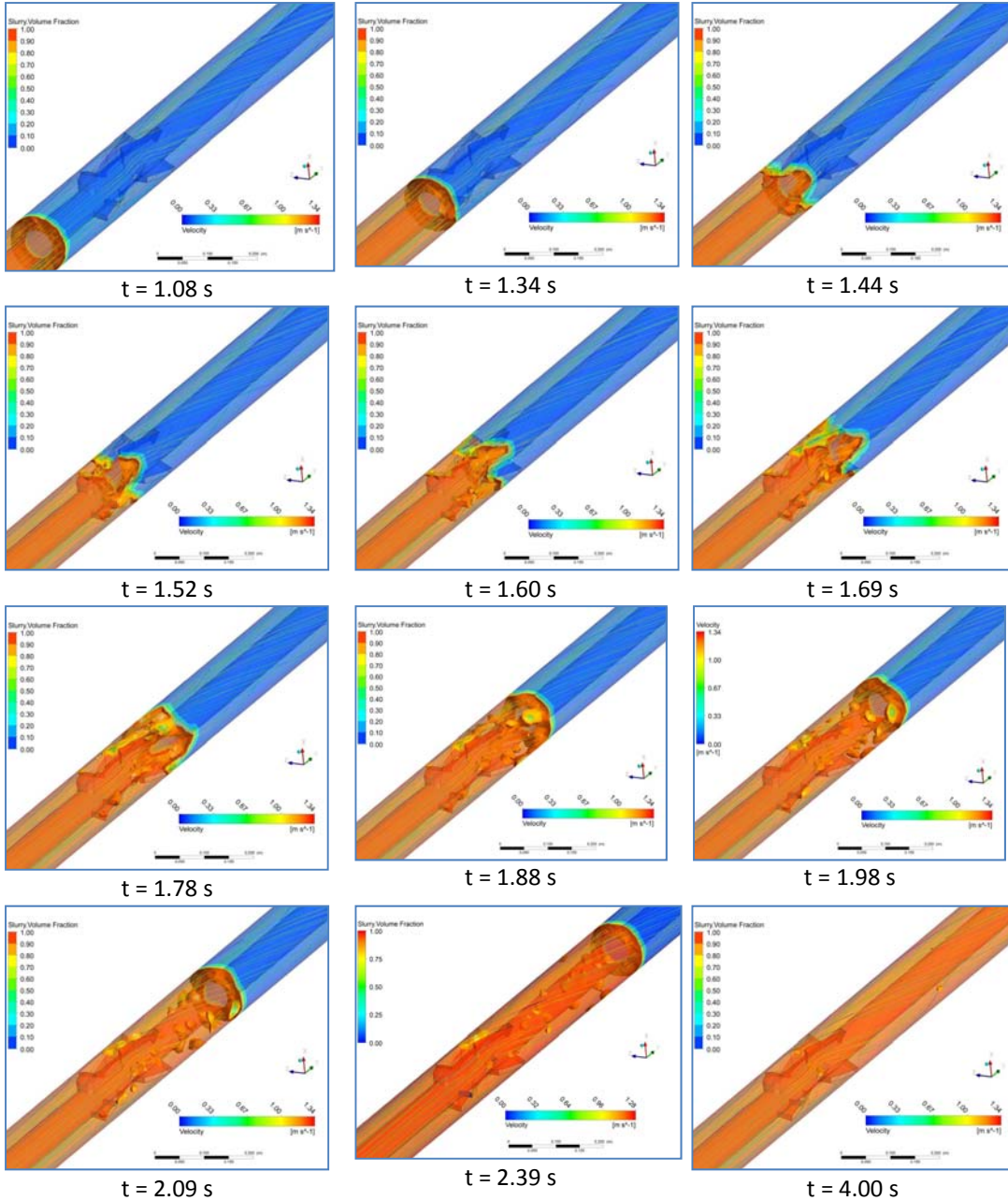


Figure 6.45 VOF simulation results for the 3D model of the sensor housing with five flow deflector fins, tubing conveyed and borehole section of 2.2 m length. Output at time  $t = 1.08, 1.34, 1.44, 1.52, 1.60, 1.69, 1.78, 1.88, 1.98, 2.09, 2.20, 2.39$  and  $4.00$  s, while the cement slurry is displacing through the annulus. Each snapshot shows cement slurry volume fraction, ISVF = 0.90, and velocity streamlines.

These series of snapshots reveal that the functionality of the fins to deflect flow was positive; however, the faces of sensor housing and fins do not follow the streamlines resulting in the generation of turbulent flow on the cement slurry phase.

In Figure 6.45 at 1.34 seconds shows that the flow was moving parallel to the borehole walls, and the cement slurry phase was displacing homogeneously the fresh-water-spacer phase. However, at second 1.44 seconds the sensor housing body caused fingering on the cement slurry displacement front. This non-homogeneous displacement of flow is deflected by the fins as observed at second 1.60. The change of flow direction on the downstream of the sensor housing broke and distributed the fingering of cement slurry front that without fins it tends to form a poor quality cement columns behind or downstream of the sensor housing standoff. At 4 s it is observed that most of the ISVF-90% zones were located on the sensor housing phases perpendicular to the flow directions. Future sensor housings and fins prototypes and models cannot have sharp transition between faces. These modifications could increase the cement displacement efficiency and reduce possible turbidity on the cement slurry phase; thus, reducing the risk of development of micro-annulus.

Figure 6.46 shows the evolution of the integral quantity through the 4 s of the simulation. The peak value of the ISVF -90% was  $0.045 \text{ m}^2$ , and it was reached at 1.88 s when the cement slurry displaced the majority of the fresh-water-spacer phase. In general, the post-peak trend shown a smooth reduction of ISVF-90%, but at 2.80 s there was significant reduction of the value of the integral quantity with a residual value of  $0.0023 \text{ m}^2$ . During the post-peak or flushing period there were some small increments of the integral quantities at s 2.29 and 2.61. These small fluctuations occur when volumes of fresh-water-spacer phase left behind were broken into smaller volumes and vice versa during this flush period (i.e., the surface area of  $1 \text{ m}^3$  of water is  $6 \text{ m}^2$ ; but two  $0.5 \text{ m}^3$  of water have a total surface area of  $8 \text{ m}^2$ ).

After comparing the integral quantity of this model with flow deflector and the previous mode with just the sensor housing at the same final time step, there was a small reduction of the residual ISVF-90% value between these two models. This shows that the induction of flow deflector near the sensor housing slightly improved on the cement displacement efficiency. It is expected that after smoothing the sensor housing and fins geometry the displacement efficiency will improve significantly. The subsequent chapter of this study focuses on the development of a novel sensor housing system and flow deflector fins.

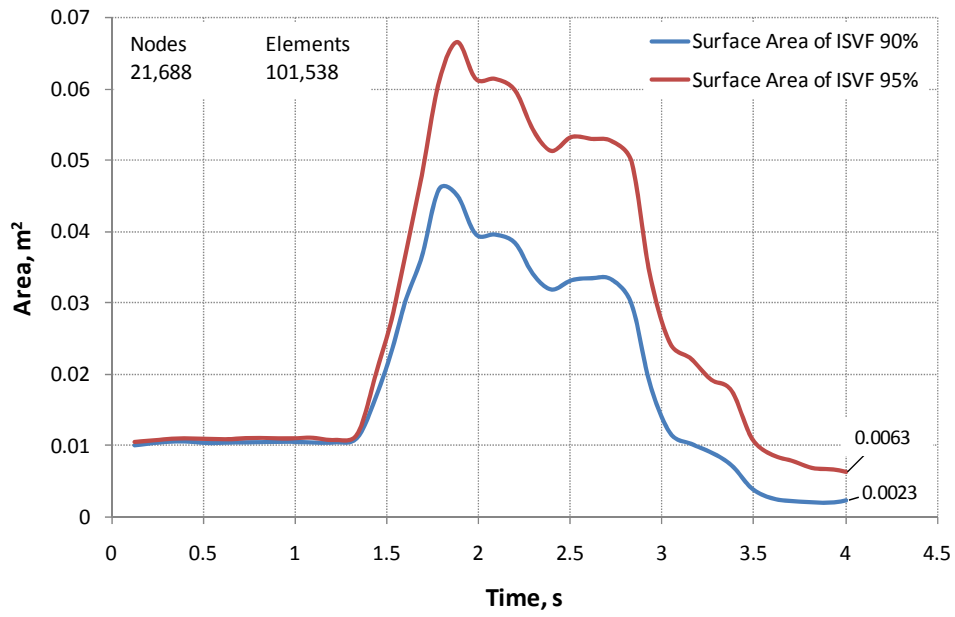


Figure 6.46 Surface area of ISVF 90 % and ISVF 95% (integral quantities) – flow time results for the 3D model of the sensor housing with five flow deflector fins, tubing conveyed and borehole section of 2.2 m length.

#### 6.4.6.4 Discussion

The results presented above show that this new configuration can distribute the mixture (poor quality cement) of cement front and fresh-water-spacer phase in the four quadrants of the borehole cross-section and not in one quadrant as previous configurations (Figure 6.47). As a result, this could reduce the risk of the development of a micro-annulus paths on the cement column after hardening.

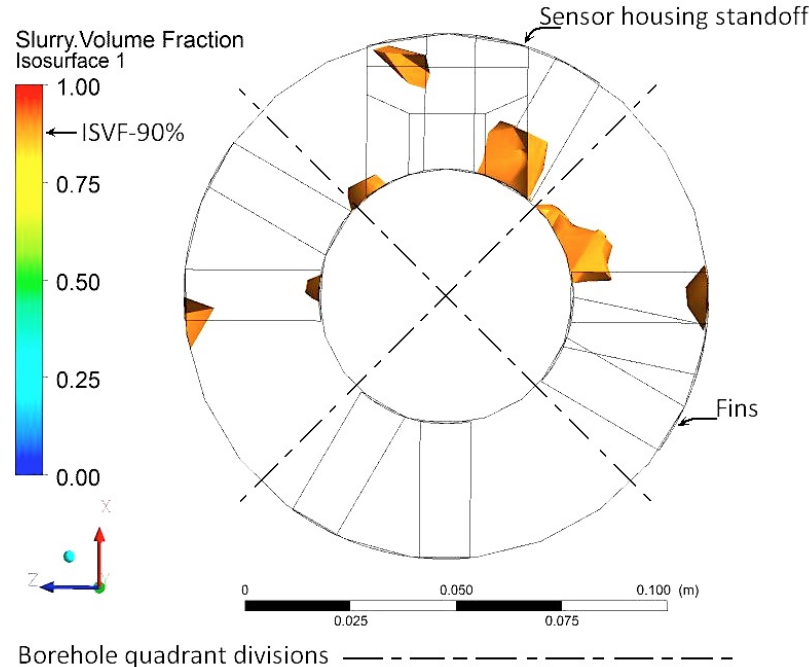


Figure 6.47 VOF simulation results for the 3D model of the sensor housing with five flow deflector fins, tubing conveyed and borehole section of 2.2 m length. Output at time  $t = 4.00$  s, while the cement slurry is displacing through the annulus. The snapshot shows the annular distribution of ISVF with value of 0.90.

The configuration of the conceptual model presented on this section was the result of preliminary simulations of different number of fins and configuration. Figure 6.48 shows preliminary results of one model with four deflector fins at the downstream of the sensor housing standoff. These four flow deflector fins redirect the flow in the same direction of the fins, but blocky shape of the sensor standoff affected the cement displacement efficiency of one flow deflector fin as illustrated on Figure 6.48 (d). A fifth fin was included to solve this defect of the system.

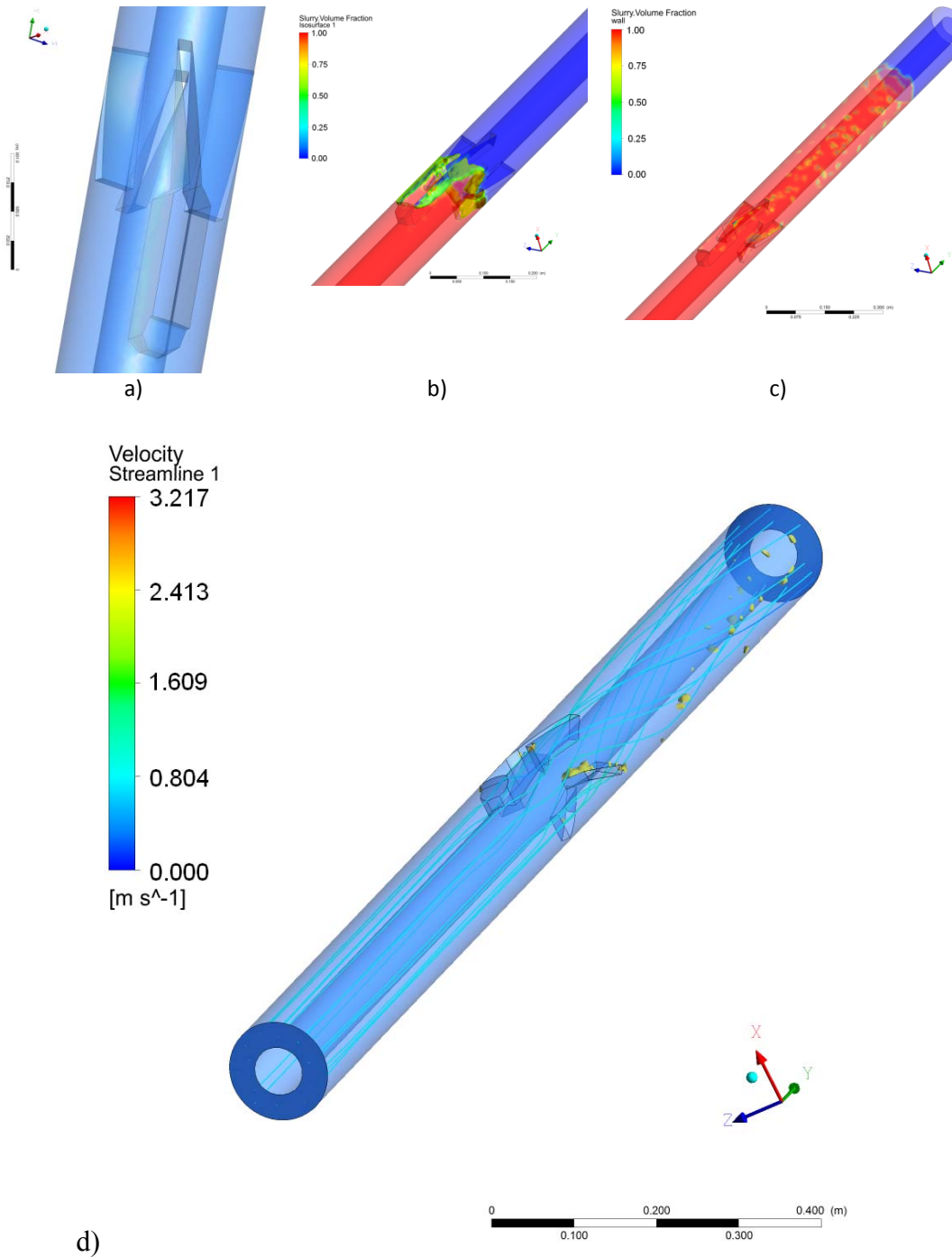


Figure 6.48. Summary of VOF simulation results for the 3D model of the sensor housing with four flow deflector fins, tubing conveyed and borehole sections. Output at time  $t =$  (a), 0.00 (b), 1.55 (c) and 2.47 (d) 4.00 s, while the cement slurry is displacing through the annulus. Each snapshot shows the annular distribution of ISVF with value of 0.90.

Figure 6.49 shows the evolution of the integral quantity through the 4 s of the simulation for the model with four flow deflector fins. The peak value of the ISVF -90% was  $0.093 \text{ m}^2$ , and it was reached at 2.29 s when the cement slurry displaced the majority of the

fresh-water-spacer phase. In general, the post-peak trend shown a smooth reduction of ISVF-90%, but at 2.80 s there was significant reduction of the surface area of the integral quantity with a residual value of 0.016 m<sup>2</sup>. During the post-peak or flushing period there was a small increment of the integral quantities at 2.74 s.

Comparing the integral quantities between this preliminary model with four fins and the model with five fins, it is observed that the integral quantity of this preliminary model was double at peak value and one order of magnitude higher at the residual value than the model with five flow deflector fins. The insertion of the fifth fin at the upstream from the sensor housing increased the velocities near the downstream fin where pockets of ISVF-90% were left behind. The positive results of the sensor housing with five flow deflector fins were presented early in this section.

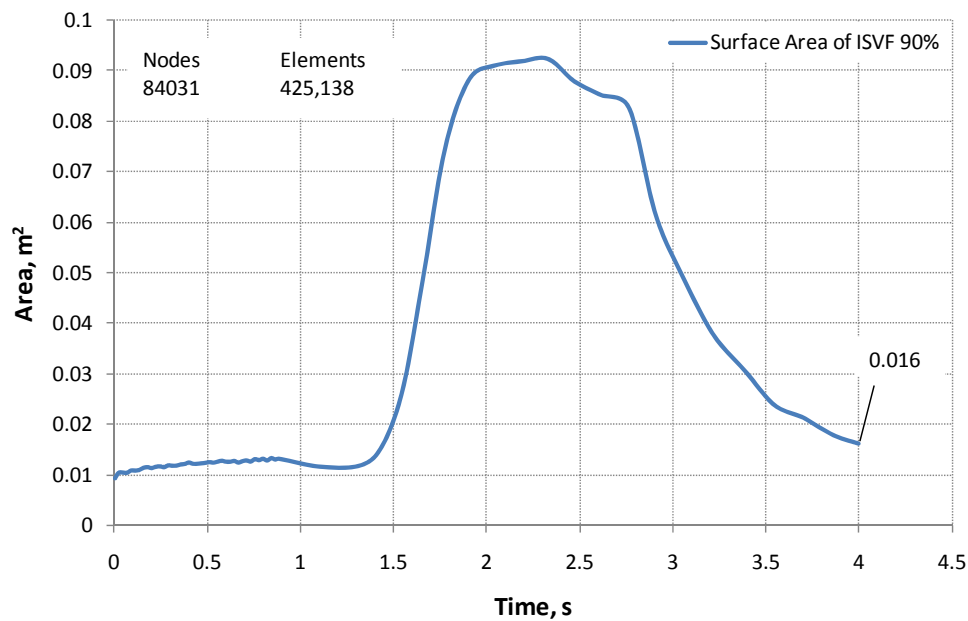


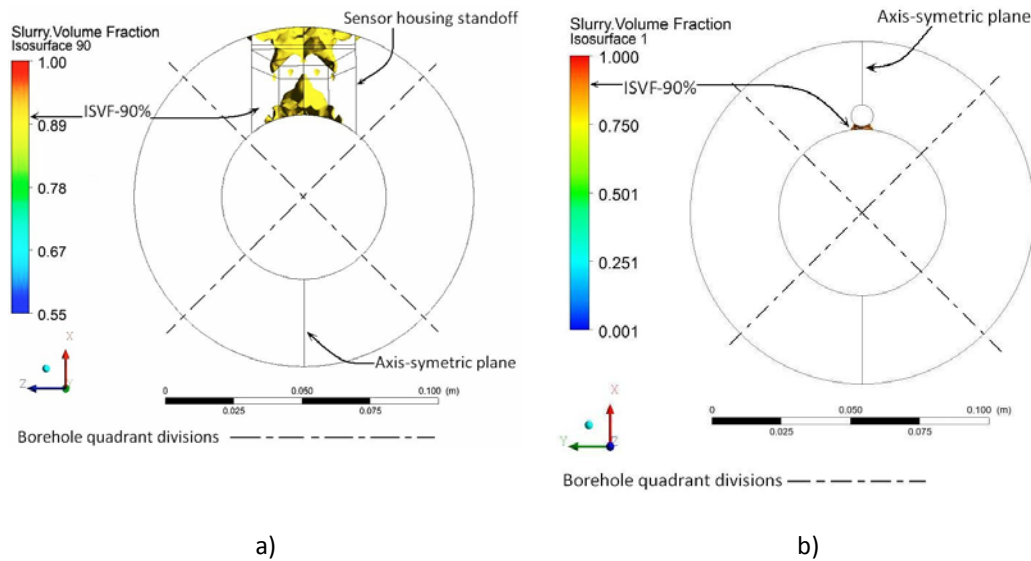
Figure 6.49 Surface area of ISVF 90 % (integral quantity) – flow time results for the 3D model of the sensor housing with four flow deflector fins, tubing conveyed and borehole section of 2.2 m length.

#### 6.4.7 Summary and Conclusions

The observation wells used for MMV activities for CO<sub>2</sub> geological storage will require multiple integrated instrumentation to be deployed at the containment, above-containment, and near surface geological horizons. The timing and intensity of MMV activities on these multiple geological horizons must be different and independent of each

other. Therefore hydraulic isolation between sensors deployed in an observation well is very crucial for MMV activities. Many sensors in the observation well for the Pembina Cardium CO<sub>2</sub> Monitoring Pilot were not hydraulic isolated after cement hardened. Therefore, the remaining scope of this thesis focuses on the development on a new sensor housing that could substantially improve hydraulic isolation between multiple downhole sensors.

The annular flow impedance and low cement displacement efficiency caused by the presence of the sensor housing bodies have a point located effect within the entire length of the borehole. However, sensor elements require cables to transfer the signal from the downhole location to the surface, and typically these cables are placed near and about the sensor housing and on the same quadrant of the borehole cross-section, which is the same location where the poor quality cement column tends form. Multiple cables could cause zones of poor quality cement between the production tubing and the cables. The overlapping of the cable and the sensor housing bodies could increase the risk of the development of micro-annulus paths that could hydraulically communicate multiple sensors of the integrated system.



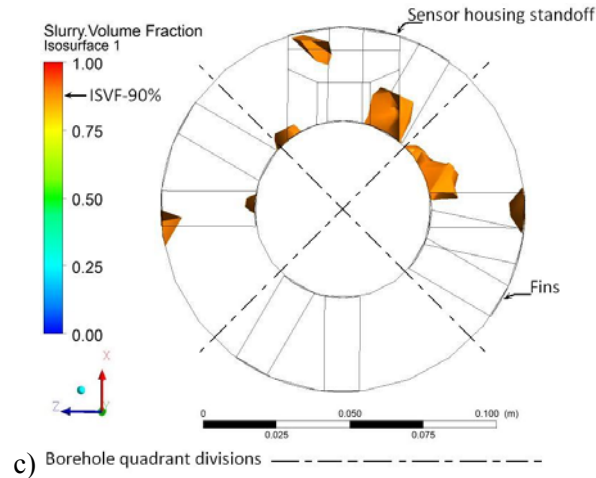


Figure 6.50 Summary of VOF simulation results of the three models of the tubing conveyed and borehole sections with: (a) the sensor housing standoff; and (b) one cable aligned parallel to tubing with 1 mm gap; (c) the sensor housing with five flow deflector fins. Output at time  $t = 89.00$  (a), 3.5 (b) and 4.00 (c) s, while the cement slurry is displacing through the annulus. Each snapshot shows the annular distribution of ISVF with value of 0.90.

The results suggest that the zones of poor quality cement that could lead to a micro-annulus path were likely to be located on one quadrant of the borehole cross-section (Figure 6.50 (a)). This is critical because on the same quadrant multiple cables and capillary lines were installed (Figure 6.50 (b)). The risk of developing a poor quality cement column that could lead to a micro-annulus path can be reduced if the annular flow near the sensor housing is redirected with flow deflector fins. The results of a conceptual model show the new distribution of the ISVF-90 (zones of poor quality cement) on the four quadrant of the cross-section of the borehole. The risk of having these zones of poor quality cement hydraulically connected between them was reduced because they are not longer sharing the same quadrant.

## **CHAPTER 7 CFD Modelling of a Novel Outside Casing Conveyed Low Flow Impedance Sensor Housing System.**

The results and conclusions of previous sections show that there is a need of a novel sensor housing system with flow design fundamentals for permanent downhole monitoring tool for CCS activities. This new housing system should reduce the risk of internal-zonal fluid communication, resulting in independent and fully isolated in-situ pressure and temperature measurements. The study of a new sensor housing system of this chapter follows the similar approach of the previous section, where individual elements of the sensor housing system are analysed using computational fluid dynamics technique. This chapter focuses on the configuration of three elements of the novel system, which are the sensor housing, the flow deflector fins and the casing conveyed geometry.

### **7.1 Modelling description and computation method**

This section provides a generic description and the computation method of the models presented in this chapter. The mathematical model, boundary conditions and fluid properties were the same of the modelling that was described in Chapter 6.

#### **7.1.1 Geometry and grid**

Each observation well design is unique but for this study, a mid-size borehole and casing conveyed geometry was chosen, with an outside and inside casing diameter of 200 mm and 114.30 mm, respectively, to illustrate how CFD techniques could be used to assess the flow mechanics efficiency of the sensor housing geometries within a borehole during cement placement. Details of the geometrical discretization are presented in the description section of each model.

#### **7.1.2 Mathematical model**

A two-phase transient simulation based on standard laminar flow and VOF method was used. The time dependent term scheme used was the first order implicit. The pressure-velocity coupling was calculated through the PISO scheme. Least squared cell based gradient, PRESTO! pressure, second order upwind momentum, geo-reconstruct volume fraction and quadratic upwind interpolation (QUICK) energy were used as spatial

discretization settings. Because the circulated fluids were moving against gravitational forces, the formulation of implicit body force was used.

### **7.1.3 Boundary conditions**

In the same way as the geometry is unique so are the boundary conditions for each observation well. The preliminary models of this chapter have the same boundary conditions that were described in Chapter 6. This helps to compare the effectiveness of the novel sensor housing system.

All of the surfaces were set at zero-slip walls, except for the inlet and the outlet. The inlet was set as a uniform constant velocity inlet of 0.737 m/s. Using UDF, the outlet was set as a transient pressure that increased with a pressure gradient of 3.535 kPa per second. The models were initialized in a steady state conditions with a primary fresh-water spacer fluid (density: 1.00 g/cm<sup>3</sup>). After the velocity and pressure profiles within the models were initialized, the models were switched to transient conditions where the fresh-water spacer fluid was followed by a CO<sub>2</sub>-resistant cement slurry (density: 1.76 g/m<sup>3</sup>), with rheological parameters: power law index,  $n = 0.9839$ , consistency,  $K = 0.0619 \text{ Pa s}^{(0.9839)}$ .

### **7.1.4 Numerical solution control**

The simulations were conducted on a workstation with Microsoft Windows XP 64, Intel Xeon (3.4 GHz) and 8 GB of memory. The models were also dominated by convection, the minimum time step used in the simulations was a function of grid size in particular the minimum volume cell (see Equation 6.4).

The integral quantity selected for this section was also the iso-surface area of the cement slurry volume fraction with value of 0.90. This represented the regions or zones within the annular space where there was inadequate cement slurry volume fraction (ISVF). To confirm the trend of ISFV-90%, the cement slurry volume fraction with value of 0.95 and 0.98 or ISFV-95% and 08% were also monitored in some of the models.

### **7.1.5 Approach**

The first two sections present the study of the cement slurry displacement through a: (1) novel sensor housing; and (2) a parametric analysis of flow deflector fins. The results of these two sections represent the initial phase of a modelling effort that attempts to provide an improved understanding of the annular flow within a borehole with complex sensor housing geometries.

The third section of this chapter combines the novel sensor housing and the optimum flow deflector fins in one single model that could restore cement homogeneity around downhole sensor housings and mitigates the formation of a micro-annulus alongside sensor cables that run to surface.

A total of nine simulations are presented on this chapter, requiring approximately 672 hours of computation time.

## 7.2 Low flow impedance sensor housing geometry

The previous designs of the sensor housing systems presented in Chapter 5 did not include a pre-design flow mechanics assessment stage; thus, these housing geometries induced greater flow impedance into the system.

The flow impedance generated in previous sensor housings originated on the geometrical configuration of the housing. These housings had a rectangular type structure, where faces formed sharp or orthogonal angle between them, resulting on the creation of vortices that broke the continuity of the annular streamlines and imbalanced the displacing front of the cement slurry. This created fingers on the displacing front that led to inadequate cement slurry displacement that could result in a micro-annulus path.

The presence of a micro-annulus path in an observation well for CO<sub>2</sub> geological storage field is not acceptable because super-critical CO<sub>2</sub> is a powerful solvent [78] with viscosities of one order of magnitude lower than water under the same conditions<sup>6</sup> that may result in containment leakage to the surface or above horizons and hydraulic communication between downhole tools. The scope of this section is to study a novel low flow impedance sensor housing that could reduce the risk of the development of micro-annulus paths on observation wells.

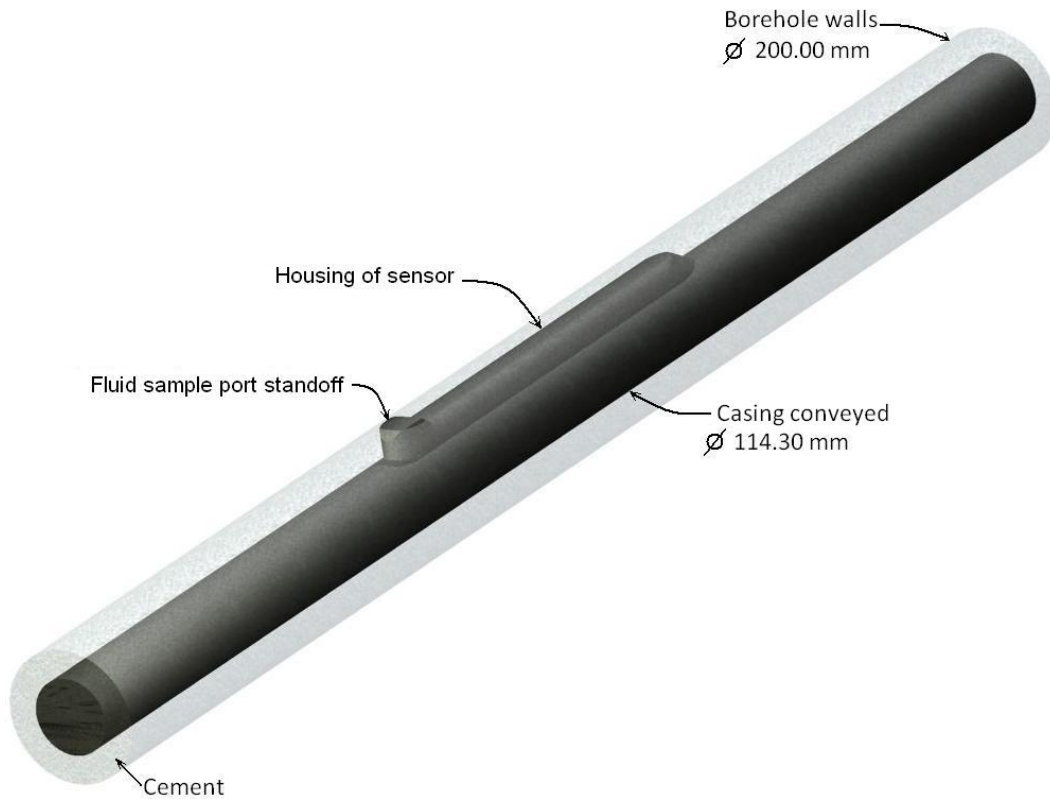
### 7.2.1 Geometry and grid

Figure 7.1 illustrates the 3D configuration of a novel sensor housing system for permanent downhole installations. The outside surfaces of this housing were smooth without any sharp or orthogonal angles between them. The sensor housing was long and narrow, and it could carry two measurement devices with enough space for cable joint or connection for multiple sensors at different depths. The fluid sample port standoff of the sensor was the only element that was in full contact with the borehole walls, and the two main objectives of this element was to protect the sensor housing during the installation and to have direct hydraulic communication with the borehole wall.

Figure 7.1 depicts an isometric view of the model of the novel sensor housing system. Figure 7.2 presents some dimensions of the novel sensor housing used in the CFD model.

---

<sup>6</sup> At 20 MPa of pressure and 55 °C of temperature, which are conditions found on the sedimentary bases of Alberta.



*Figure 7.1 3D geometrical configuration of the novel sensor housing and the casing conveyed within the 2 m of a borehole section.*

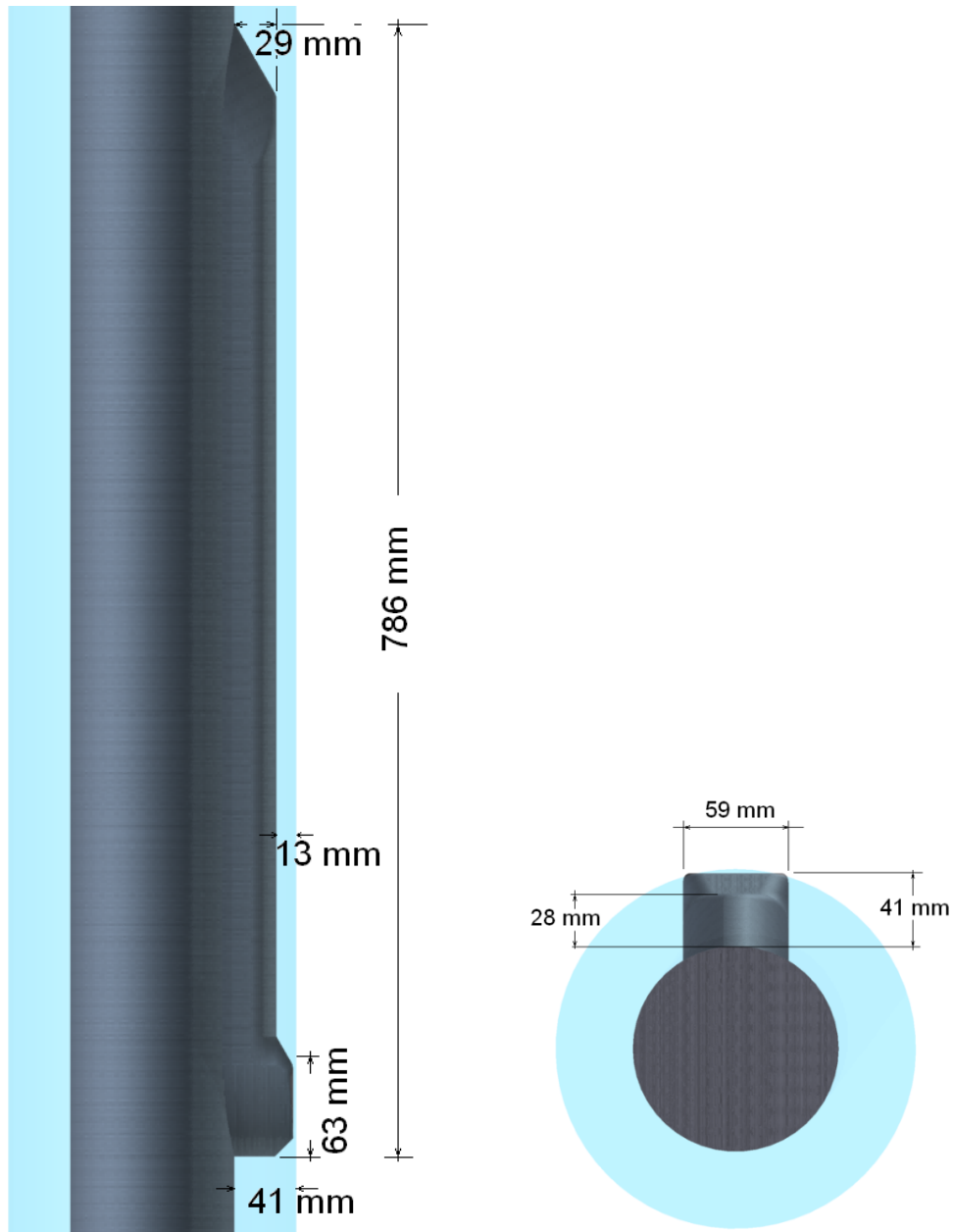


*Figure 7.2 Sketch of the novel sensor housing with some dimensions.*

A geometrical discretization of this 3D model was made for the computational fluid dynamics analysis. Unstructured tetrahedral cells were generated to define the model. A view of the generated grid can be seen in Figure 7.3.

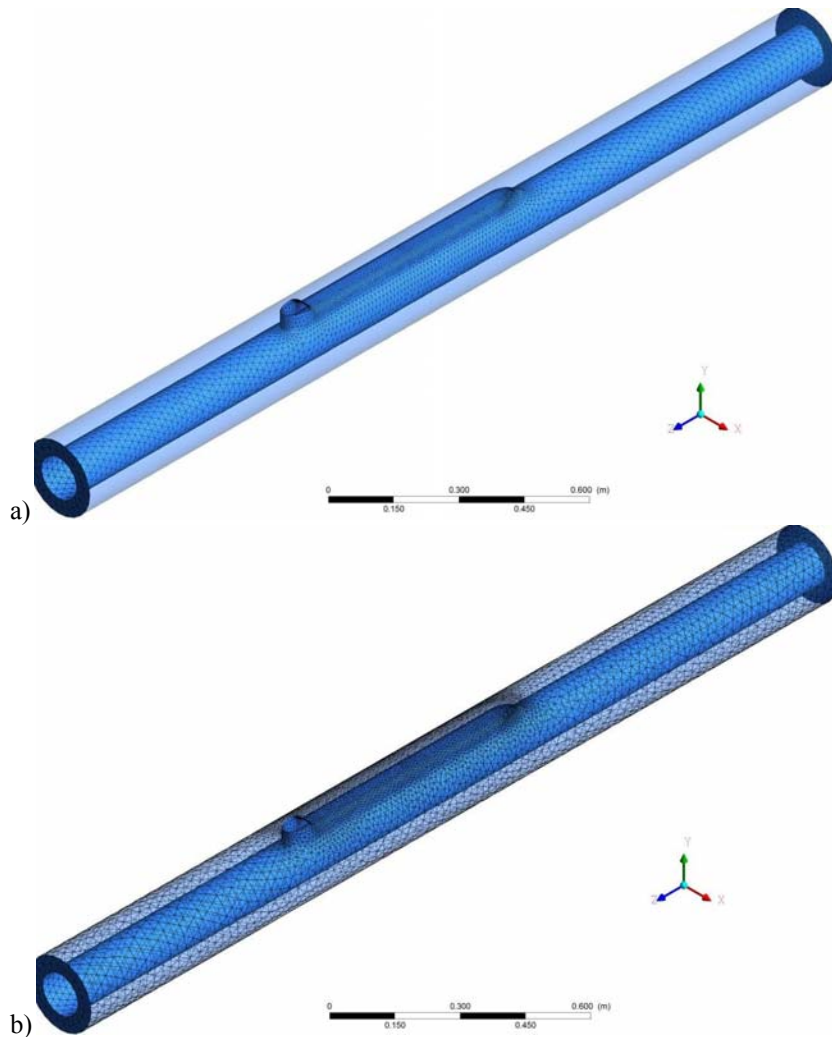


Figure 7.3 Mesh for the 3D model of (a) the novel sensor housing system and the casing conveyed (b) within the 2 m of a borehole section.

### 7.2.2 Numerical solution control

The time step used in the unsteady calculation was set to  $7.3 \times 10^{-4}$  s. A total of 6 s of flow time was simulated, requiring approximately 72 hours (3 days) of computation time. A mesh with 22,250 nodes and 103,702 elements was used on this analysis.

### 7.2.3 Results

Figure 7.4 shows the simulation results of the unsteady displacement of cement displacing fresh-water spacer. The cement slurry volume fraction is presented in a color map format, of which the color “dark orange” corresponds to the iso-surface with cement slurry volume fraction with value of 0.90 (ISVF-90%).

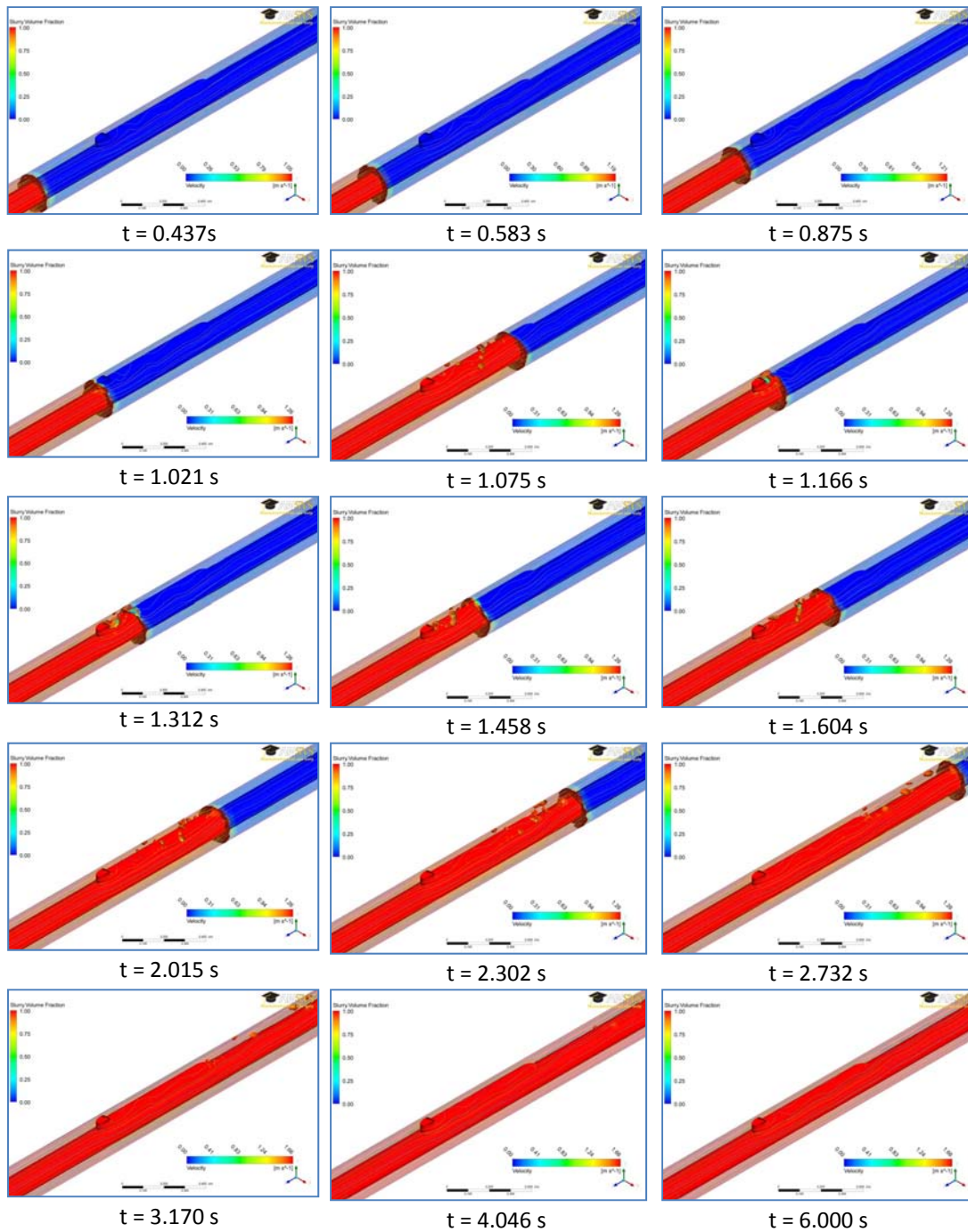


Figure 7.4 VOF simulation results for the 3D model of the novel sensor housing and the casing conveyed within the borehole section of 2.00 m length. Output at time  $t = 0.437, 0.583, 0.875, 1.021, 1.075, 1.166, 1.312, 1.458, 1.604, 2.015, 2.302, 2.732, 3.170, 4.046$  and  $6.000$  s, while the cement slurry is displacing through the annulus. Each snapshot shows cement slurry volume fraction, ISVF = 0.90, and velocity streamlines.

Throughout the entire simulation, it was observed that the cement phase displaced most of the water-spacer phase. The time for the water-spacer to be displaced by the cement slurry from the inlet to the outlet was 3.00 s, but the simulation time ran until the integral quantity stabilized at 6.00 s.

Figure 7.5 shows the evolution of the integral quantity through the entire circulation period of 6.00 s. The peak area value of the iso-surface with volume fraction with value of 0.90 (ISVF-90%) was 0.0393 m<sup>2</sup>, and it was reached at 2.00 s when the cement slurry front was at the sensor housing top. This shows that this new sensor housing induced a low flow impedance; thus, the displacement efficiency was enhanced because the front of the cement slurry stabilized soon after passing the top of the sensor housing. The post-peak of the ISVF-90% was followed by a reduction of the integral quantity before the cement front reached the outlet at 3.00 s, then it was preceded by a significant drop of the ISVF values reaching a stabilized residual value of  $8.1 \times 10^{-5}$  m<sup>2</sup> at 6 s. Comparing the residual integral quantity of this model with the sensor housing of Chapter 5, the novel sensor housing was two orders of magnitude lower than the sensor housing of chapter 5, meaning that less poor quality cement regions were left near the novel sensor housing. This provided another evidence of the positive impact that the new sensor housing geometry has on the cement displacement efficiency.

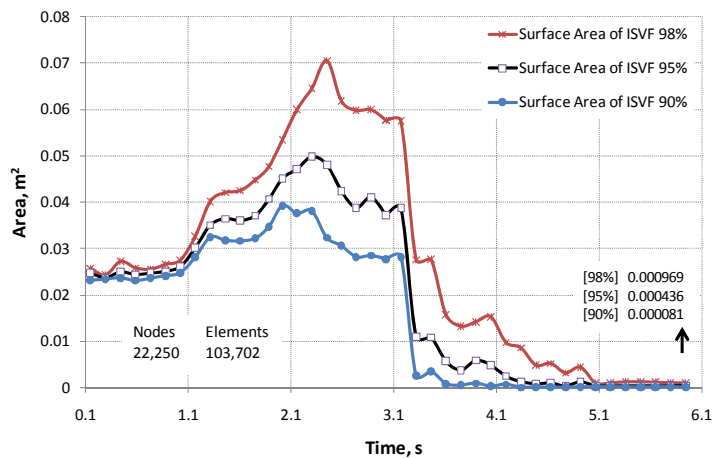


Figure 7.5 Surface area of the ISVF = 90, 95 and 98 percent (integral quantities) – flow time results for the 3D model of the novel sensor housing and the casing conveyed within the borehole section of 2.00 m length.

## 7.2.4 Discussion

Because the displacement efficiency of the cement slurry was greater than previous models, the integral quantity zones of ISVF-90% were too small to display. Therefore, the integral quantity of ISVF-95% was selected to display the location of zones with poor quality cement (Figure 7.6). These results suggest that any sensor housing could generate mild annular flow impedance, and as previous models indicated, the location of poor quality cement zones were located in one quadrant of the borehole cross-section which was positioned downstream of the sensor housing.

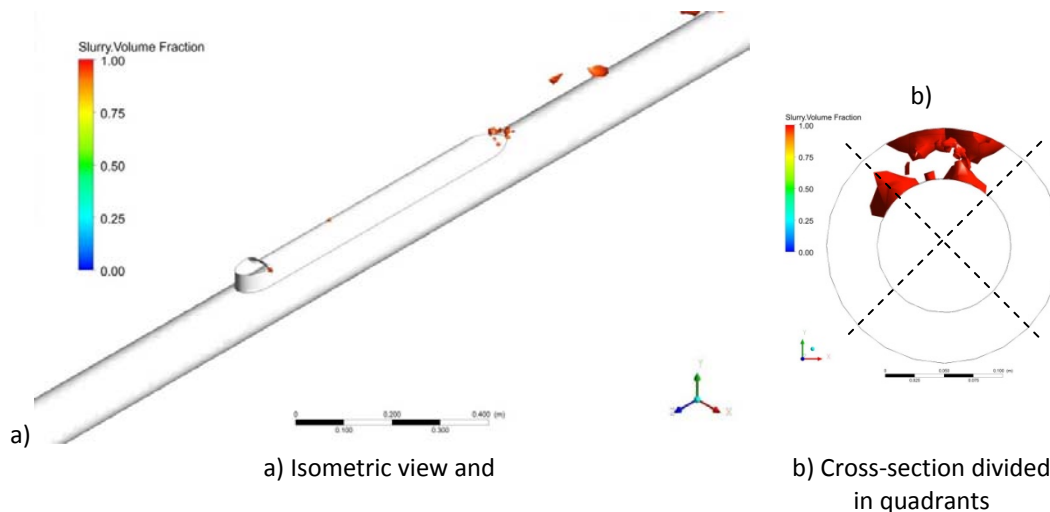


Figure 7.6 VOF simulation results for the 3D model of the novel sensor housing and the casing conveyed within the borehole section of 2.00 m length. Output at time  $t = 3.17$  s, while the cement slurry is displacing through the annulus. These snapshots show the annular distribution of the ISVF with value of 0.95.

Although, the cement displacement efficiency with this novel sensor housing was almost hundred percent, the overlapping effect of the annular flow impedance resulted from the cables, the capillary lines and other elements of the downhole instrumentation system could increase the quantity of poor quality cement zones located in the same quadrant. If more inadequate cement slurry volume fractions develop on one quadrant, the risk of having ISVF regions hydraulically connected between them could increase, resulting in the development of micro-annulus path. To reduce this risk, results from Chapter 5 suggested that the annular flow should be redirected with the integration of flow deflector fins that could be located near the novel sensor housing. The following section studies the optimum fins configuration for the novel sensor housing.

### **7.3 Flow deflector fins optimization**

The results of the previous section showed that the novel sensor housing improved the displacement of the cement slurry through the annulus. However, the regions of the inadequate cement slurry volume fractions that could lead to zones of poor quality cement were concentrated in the same quadrant of the annular cross-section, where the sensor housing was located. Also, generally the cables are located on the same quadrant to reduce the risk of damaging them during installation, but this could increase the risk of the development of a micro-annulus path as discussed in Chapter 5.

The objective of this new sensor housing system is to prevent the creation of micro-annulus by having cement contacting all surfaces of the downhole component (casing, sensor housing, sensor cables, and the formation itself). The cement could not do this naturally, as every obstruction or irregular shaped component that is located within the flow path of the cement could result in a non-homogenous flow regime. Preliminary analysis, from Chapter 5, of a conceptual model showed that the introduction of flow deflector fins could balance the distribution of the ISVF regions in the cross-section of the annular space. This section studies how the fins integrated with the novel sensor housing could balance the small annular flow impedance that the novel sensor housing induces.

Because this is a novel application where flow deflector fins are integrated to a sensor housing, the author initially studied the effect of the fins in two opposite locations of the sensor housing: (1) at the lower level of the fluid sample port standoff; and (2) at the upper level of the sensor housing top.

### 7.3.1 Fins at level of the fluid sample port standoff

#### 7.3.1.1 Geometry and grid

Figure 7.7 and Figure 7.8 illustrate the 3D configuration, the side view and the cross-section of the model of this section. This section studies the effect of three flow deflector fins located at the lower part of the sensor housing. The geometry of the fins was simplified for this preliminary model and it was assumed that these were in full contact with the borehole walls.

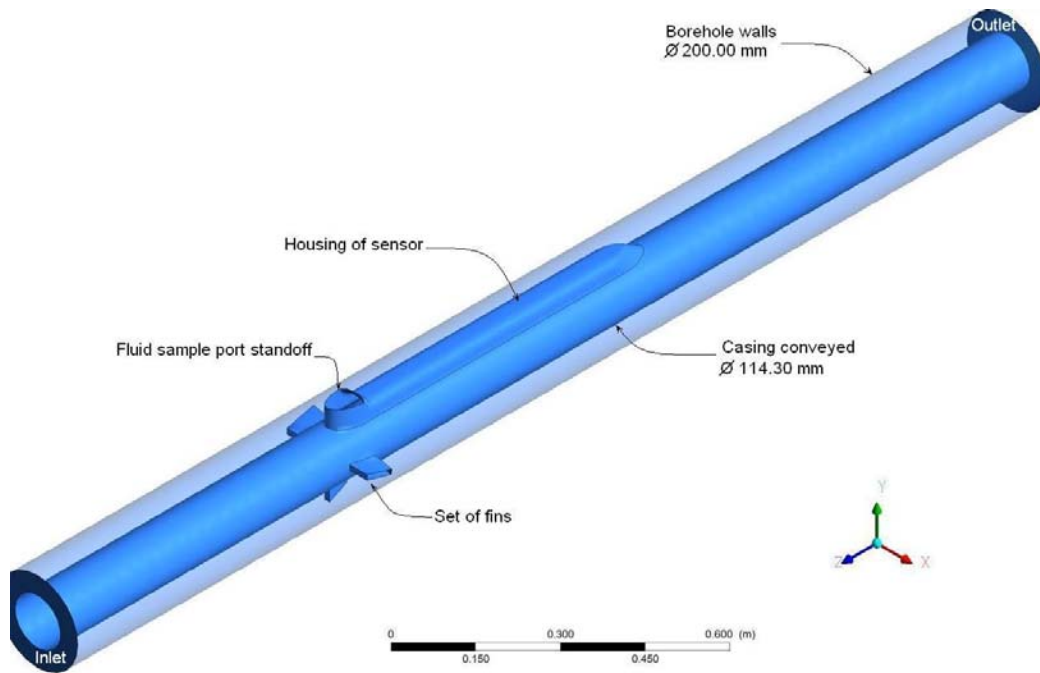


Figure 7.7 3D geometrical configuration of the low flow impedance sensor housing with three flow deflector fins located upstream of the sensor housing.

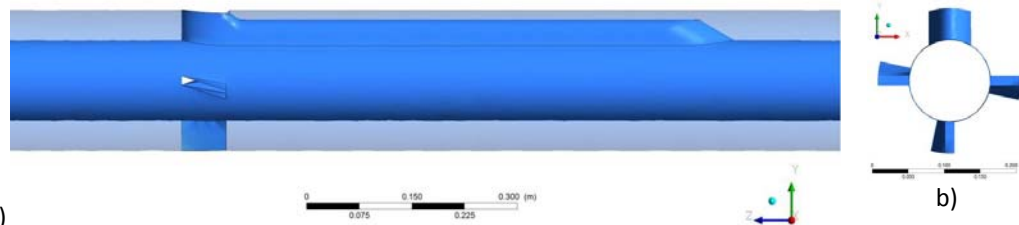


Figure 7.8 Illustration of the three upstream flow deflector fins and the novel sensor housing: a) side view b) cross-section

The dimensions of these fins were selected from the parametric study conducted by Yao and Robello [77] on the effect on fin width, fin length, fin angle for various Non-

Newtonian fluid properties. Based on the fluid properties presented early in this chapter (page 147) the configurations of flow deflector fins used for this study are shown in Figure 7.9. Each fin has  $8.5^\circ$  of deviation from the vertical position and 12.7 mm width and 66.7 mm length.

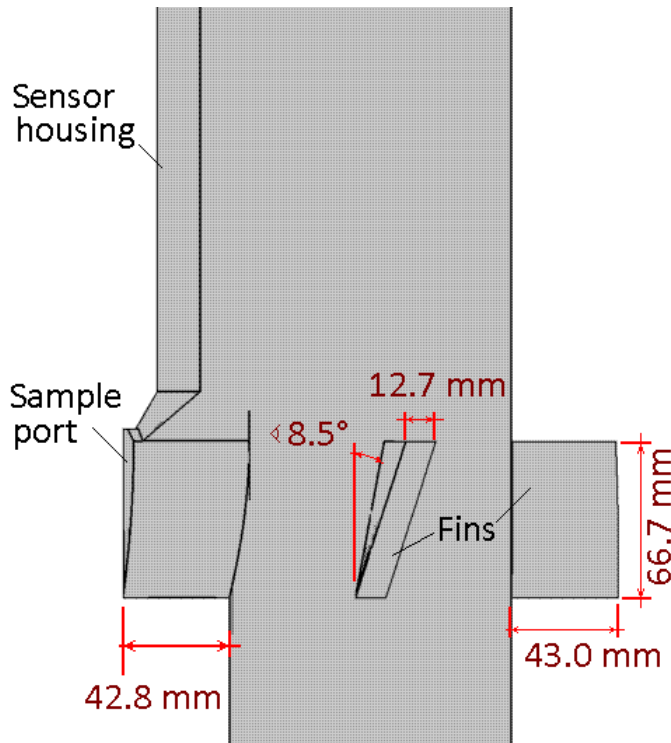


Figure 7.9 Sketch of the three flow deflector fins located at the level of the fluid sample port standoff.

A geometrical discretization of the 3D model was made for the CFD analysis. Unstructured tetrahedral cells were generated to define the model. A view of the generated grid can be seen in Figure 7.10.

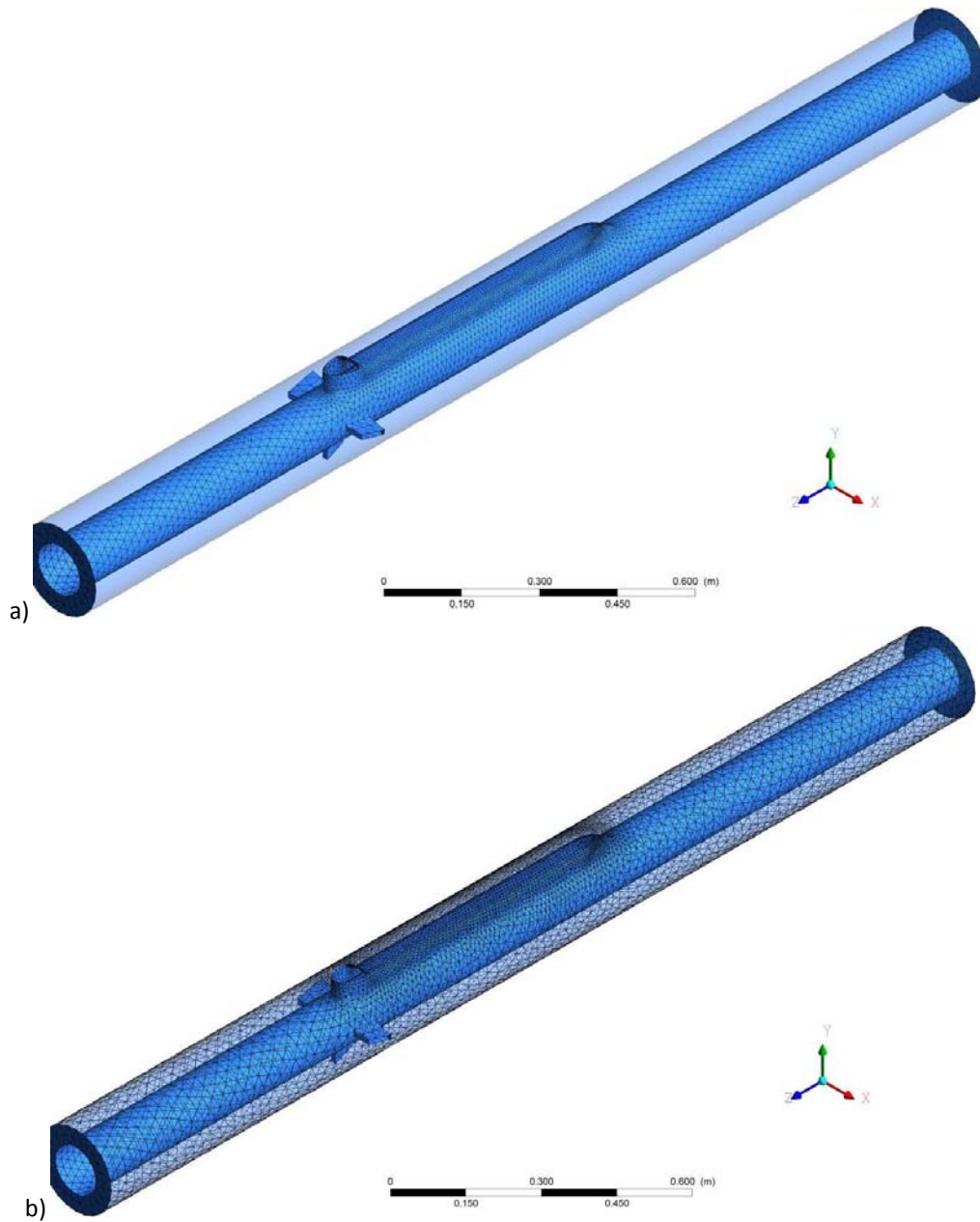


Figure 7.10 Mesh for the 3D model of (a) the novel sensor housing system and the casing conveyed with three upstream flow deflector fins (b) within the 2.50 m of a borehole section.

### 7.3.1.2 Numerical solution control

The time step used in the unsteady calculation was set to  $7.5 \times 10^{-4}$  s. A total of 4.00 s of flow time was simulated, requiring approximately 72 hours (3 days) of computation time. A mesh with 22,969 nodes and 106,908 elements was used on this analysis.

### 7.3.1.3 Results

Figure 7.11 shows the simulation results of the unsteady displacement of cement displacing fresh-water spacer. The cement slurry volume fraction is presented in a color map format, of which the color “dark orange” corresponds to the iso-surface with cement slurry volume fraction with value of 0.90 (ISVF-90%).

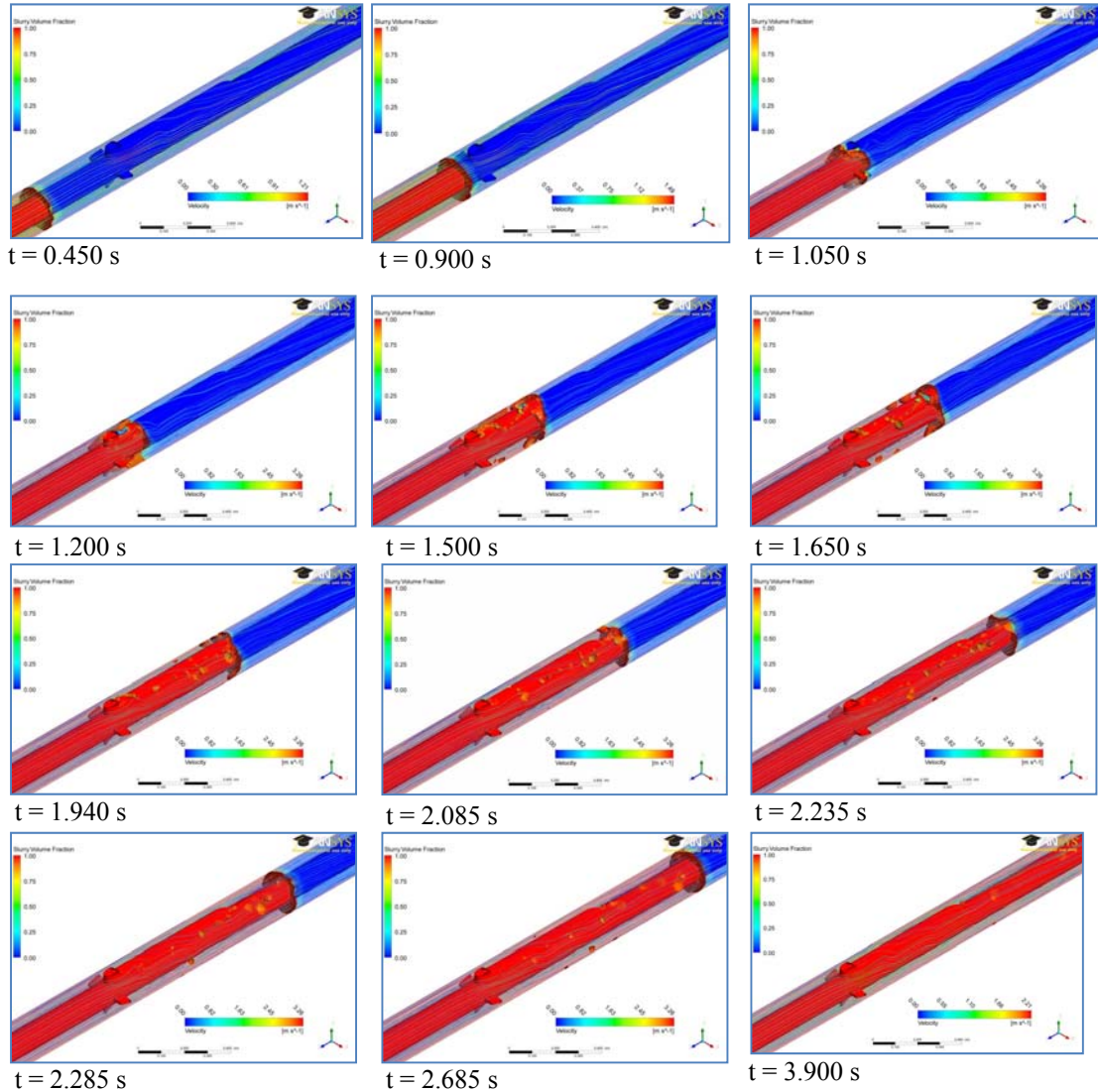


Figure 7.11 VOF simulation results for the 3D model of the novel sensor housing and the casing conveyed with three upstream flow deflector fins within the borehole section of 2.50 m length. Output at time  $t = 0.450, 0.600, 0.900, 1.050, 1.200, 1.500, 1.650, 1.940, 2.085, 2.235, 2.285, 2.685$  and  $3.900$  s, while the cement slurry is displacing through the annulus. Each snapshot shows cement slurry volume fraction, ISVF = 0.90, and velocity streamlines.

Throughout the whole simulation, it is observed that the cement phase displaced most of the water-spacer phase except for small volumes of ISVF (mixture of cement slurry and water-spacer) that are left downstream of the sensor housing. These series of figures also show that the fins are mildly deflecting the downstream annular flow, distributing the ISVF-90% in downstream annular space.

The time for the water-spacer to be displaced by the cement slurry from the inlet to the outlet was 3.00 s (Figure 7.11), but the simulation time ran until the integral quantity stabilized at 4.00 s.

Figure 7.12 shows the evolution of the integral quantity through the entire circulation period of 4.00 s. The peak area value of the iso-surface with volume fraction with value of 0.90 (ISVF-90%) was  $0.0714 \text{ m}^2$ , and it was reached at 1.35 s when the cement slurry front was passing through the set of flow deflector fins. The results suggest that this type of flow deflector fins induced higher annular flow impedance than the novel sensor housing. The post-peak values of the integral quantity ISVF-90% showed a reduction trend until the cement front reached the outlet at 3.00 s. Then, this trend was followed by a significant drop of the ISVF values reaching a stabilized residual value of  $5.7 \times 10^{-4} \text{ m}^2$  at 4.00 s. The residual integral quantity of this model was one order of magnitude higher than the model with the sensor housing alone because some of the faces of the fins had sharp edges, and this induced some flow impedance into the system.

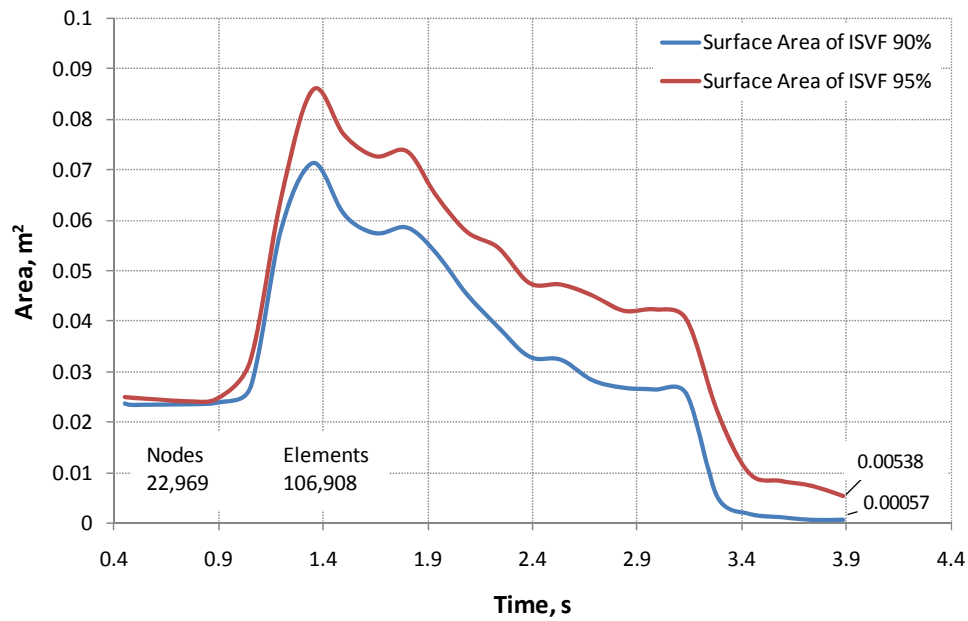
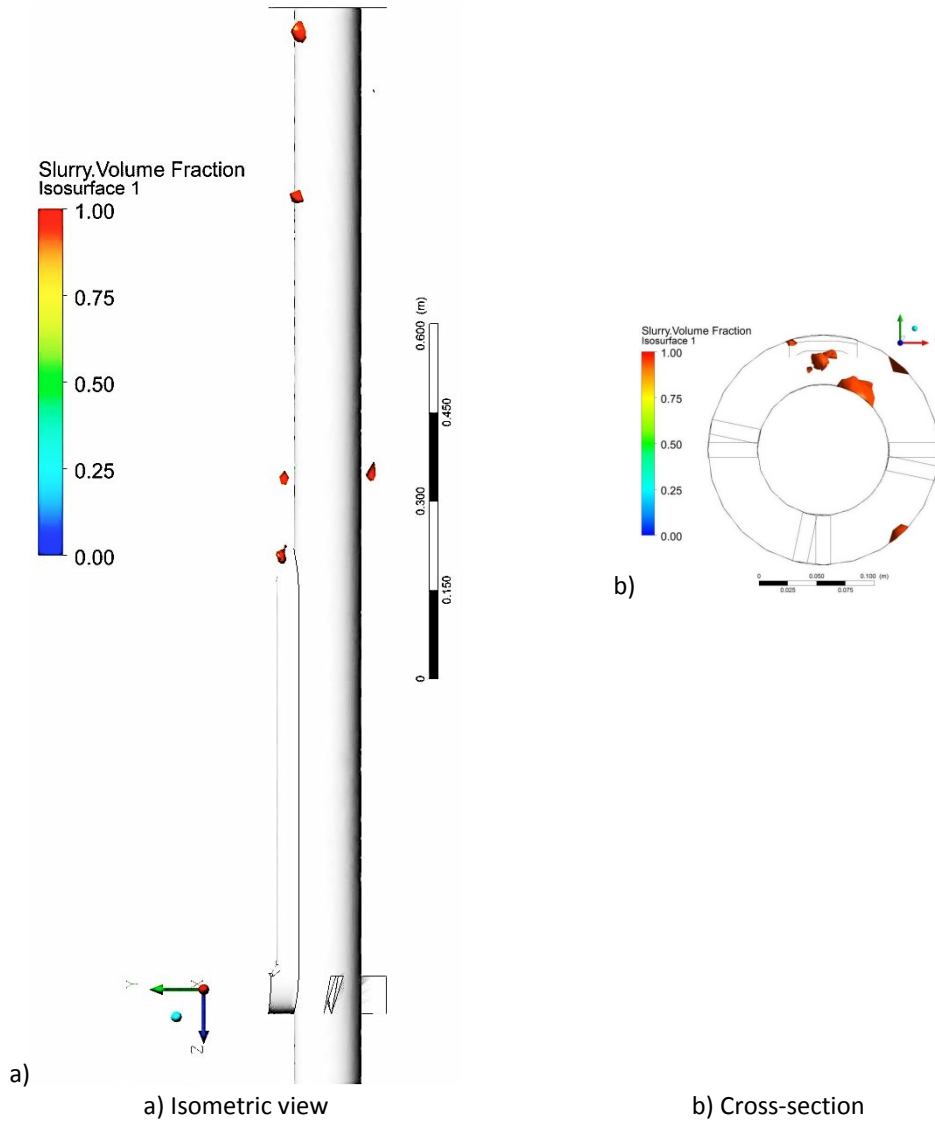


Figure 7.12 Surface area of the ISVF = 90, 95 and 98 percent (integral quantities) – flow time results for the 3D model of the novel sensor housing and the casing conveyed with three upstream flow deflector fins within the borehole section of 2.00 m length.

#### 7.3.1.4 Discussion

The results presented in this section suggest that this type of flow deflector fins located near the sample port standoff distributed the ISVF in all of the quadrants of the cross-section of the borehole (Figure 7.13). On the other hand, the residual integral quantity was higher than the previous model reducing of the cement displacement efficiency.



*Figure 7.13 VOF simulation results for the 3D model of the novel sensor housing and the casing conveyed with three upstream flow deflector fins within the borehole section of 5.00 m length. Output at time  $t = 3.90$  s, while the cement slurry is displacing through the annulus. These snapshots show the annular distribution of the ISVF with value of 0.95.*

The flow deflector fins are elements that could add annular flow impedance if the flow dynamic properties of their geometry are inadequate. Figure 7.14 shows some close-ups of the simulation outputs. In this figure it can be observed that at 1.20 s the locations and configuration of the flow deflector fins induced a significant flow impedance into the system. Some pockets of ISVF-90% were left behind the displacement front at 1.50 s of circulation; this was an indication that the front and back faces of the fins had sharp edges that were not preserving the streamlines of the annular flow. Also, the location of this set of fins was not the optimal because the new redirection of flow could not be maintained

through the downstream of the sensor housing. More zones of poor quality cement were located in the quadrant above the sensor housing, and they were not displaced to different a quadrant. The next section assesses a model with three flow deflector fins at the top-end of the sensor housing that could equally distribute the poor quality cement zones in the annular space.

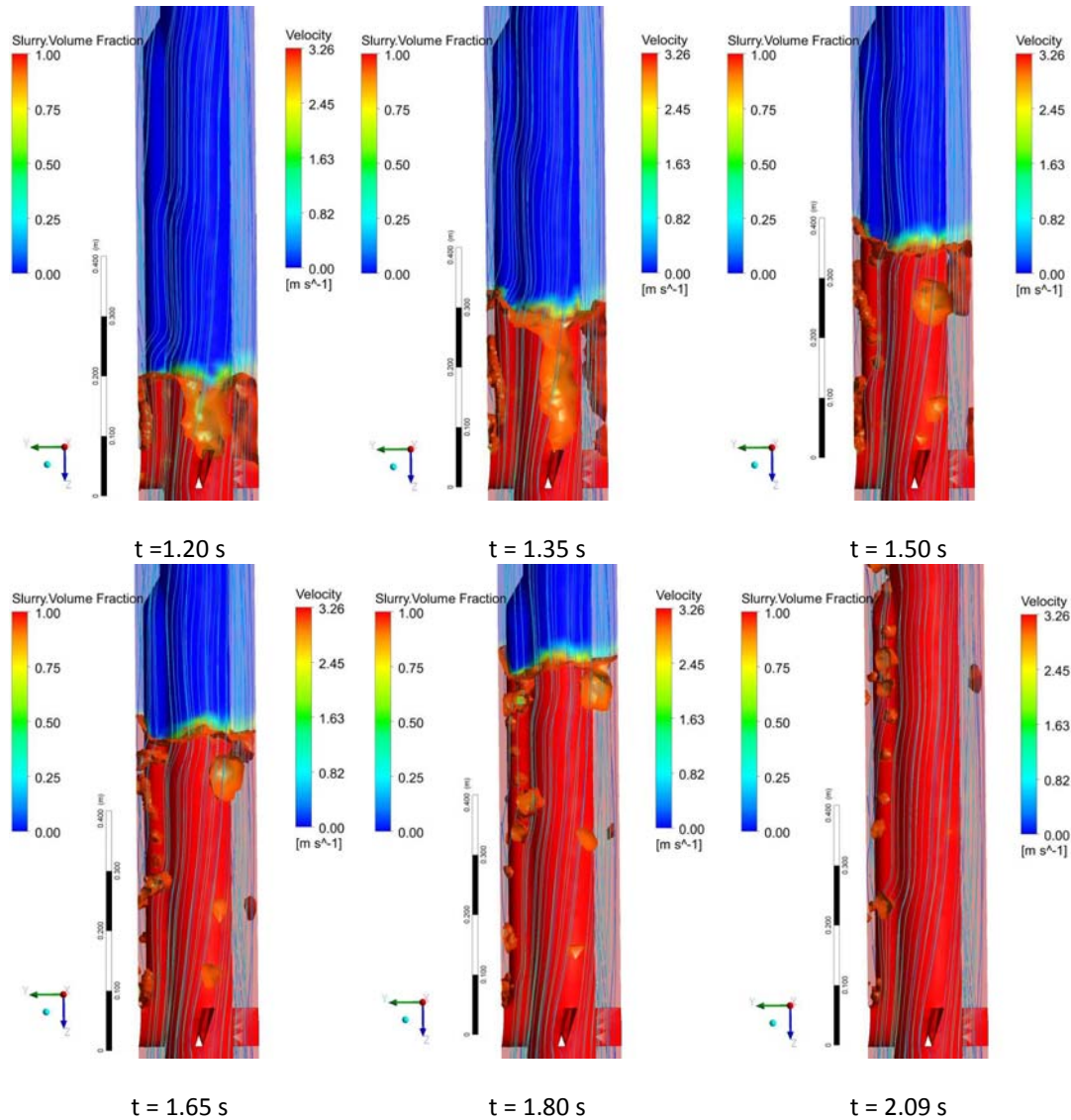


Figure 7.14 VOF simulation results for the 3D model of the novel sensor housing and the casing conveyed with three upstream flow deflector fins within the borehole section of 2.00 m length. Output at time  $t = 1.20, 1.35, 1.50, 1.65, 1.80$  and  $2.90$  s, while the cement slurry is displacing through the annulus. Each snapshot shows cement slurry volume fraction, ISVF = 0.90, and velocity streamlines.

### 7.3.2 Fins at top-end of sensor housing

This section utilized the same three flow deflector fins that were presented in the previous section. Although, the previous results suggested that this type for fin's geometry were inducing a higher annular flow impedance than the novel sensor housing, the scope of this section is the assessment of the impact of this set of fins on the annular flow in a different location of the novel sensor housing.

#### 7.3.2.1 Geometry and grid

Figure 7.15 illustrates the 3D configuration of the model used in this section. This section studied the effect of three flow deflector fins located at top-end of the sensor housing. The fins were moved downstream; thus, the model required a borehole and casing segment of 5 m length to capture the effect of the fins on the downstream sector of the annular space. The geometry of the fins was simplified and it was assumed that they were in full contact with the borehole walls.

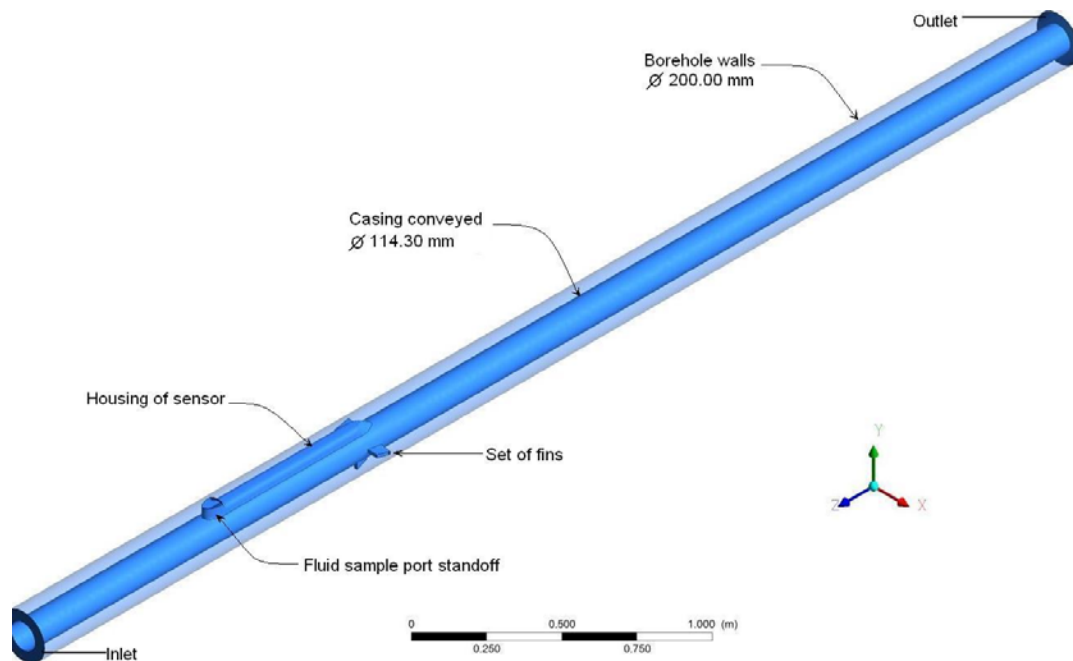


Figure 7.15 3D geometrical configuration of low flow impedance sensor housing with three flow deflector fins downstream of sensor housing.

A geometrical discretization of the 3D model was made for the CFD analysis. Unstructured tetrahedral cells were generated to define the model. A view of the generated grid can be seen in Figure 7.16.

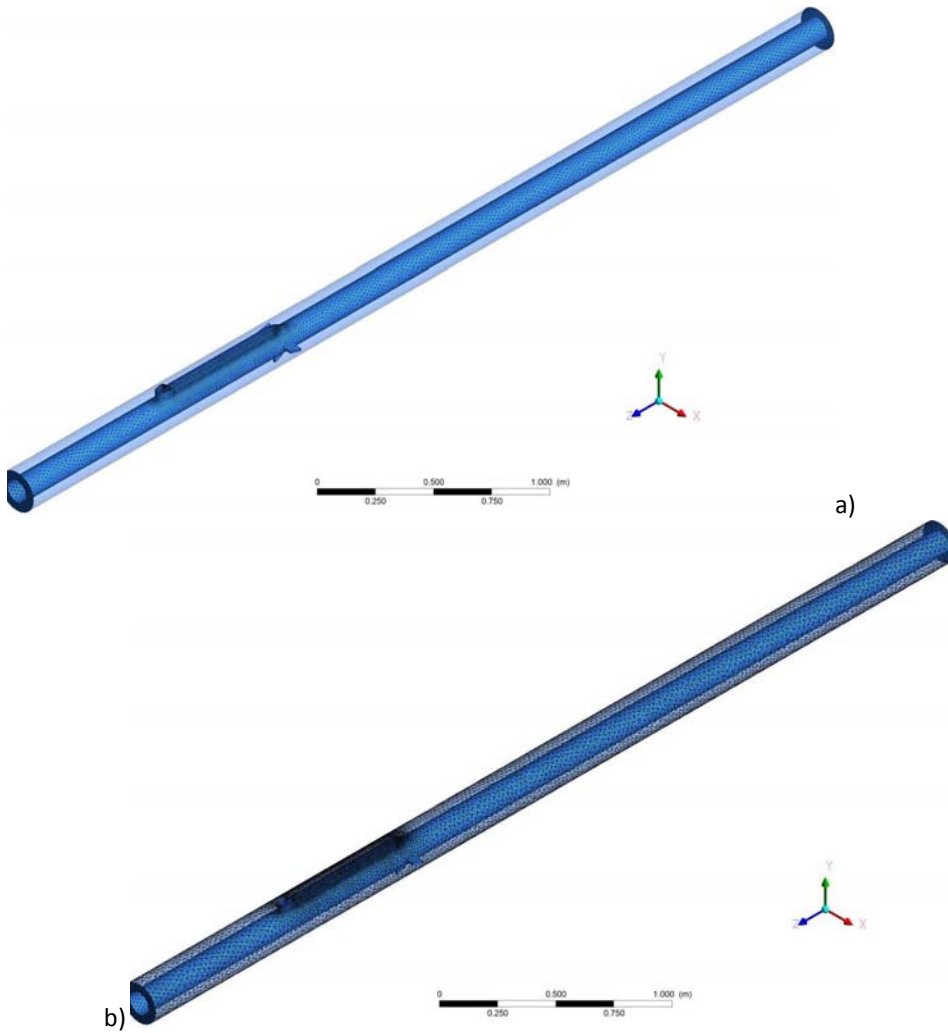


Figure 7.16 Mesh for the 3D model of (a) the novel sensor housing and the casing conveyed with three downstream flow deflector fins (b) within the 5.00 m of a borehole section.

### 7.3.2.2 Numerical solution control

The time step used in the unsteady calculation was set to  $1.3 \times 10^{-3}$  s. A total of 10.00 s of flow time was simulated, requiring approximately 48 hours (2 days) of computation time. A mesh with 33,707 nodes and 153,953 elements was used on this analysis.

### 7.3.2.3 Results

Figure 7.17 shows the simulation results of the unsteady displacement of cement displacing fresh-water spacer. The cement slurry volume fraction is presented in a color map format, of which the color “dark orange” corresponds to the iso-surface with cement slurry volume fraction with value of 0.90 (ISVF-90%).

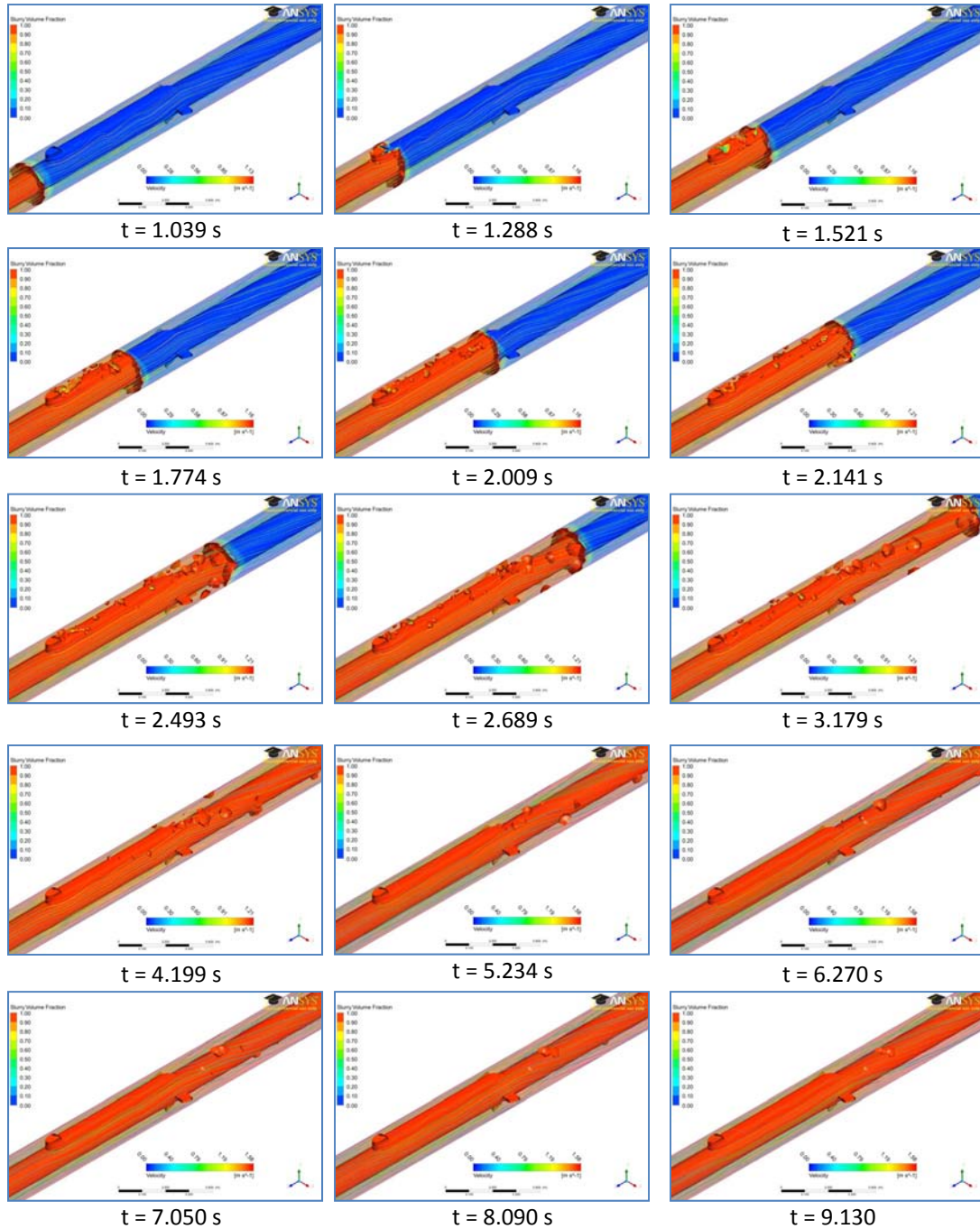


Figure 7.17 VOF simulation results for the 3D model of the novel sensor housing and the casing conveyed with three downstream flow deflector fins within the borehole section of 5.00 m length. Output at time  $t = 1.039, 1.288, 1.521, 1.774, 2.009, 2.141, 2.493, 2.689, 3.179, 4.199, 5.234, 6.270, 7.050, 8.090$  and  $9.130$  s, while the cement slurry is displacing through the annulus. Each snapshot shows cement slurry volume fraction, ISVF = 0.90, and velocity streamlines.

Throughout the whole simulation, it was observed that the cement phase displaced most of the water-spacer phase except for small volumes of ISVF (mixture of cement slurry and water-spacer) that were left downstream of the sensor housing. These series of

figures also show that the fins were deflecting the downstream annular flow approximately 8° deviation from the vertical position, distributing the ISVF-90% in downstream annular space.

The time for the water-spacer to be displaced by the cement slurry from the inlet to the outlet was 6.25 s (Figure 7.17), but the simulation time ran until the integral quantity stabilized at 10.00 s.

Figure 7.18 shows the evolution of the integral quantity through the entire circulation period of 10.00 s. The peak are value of the iso-surface with volume fraction with value of 0.90 (ISVF-90%) was 0.060 m<sup>2</sup>, and it was reached at 2.27 s when the cement slurry front was passing through the set of flow deflector fins located at the top-end of the sensor housing. This shows also that this type of flow deflector fins induced higher annular flow impedance than the novel sensor housing. The post-peak values of the integral quantity ISVF-90% showed a reduction trend until the cement front reached the outlet at 6.25 s, then this trend was followed by a significant drop of the ISVF values reaching a stabilized residual value of 1.79x10<sup>-4</sup> m<sup>2</sup> at 10.00 s. The residual integral quantity of this model with fins located at the top-end of the novel sensor housing was lower (half) than the previous model with fins located at the level of the fluid sample port standoff.

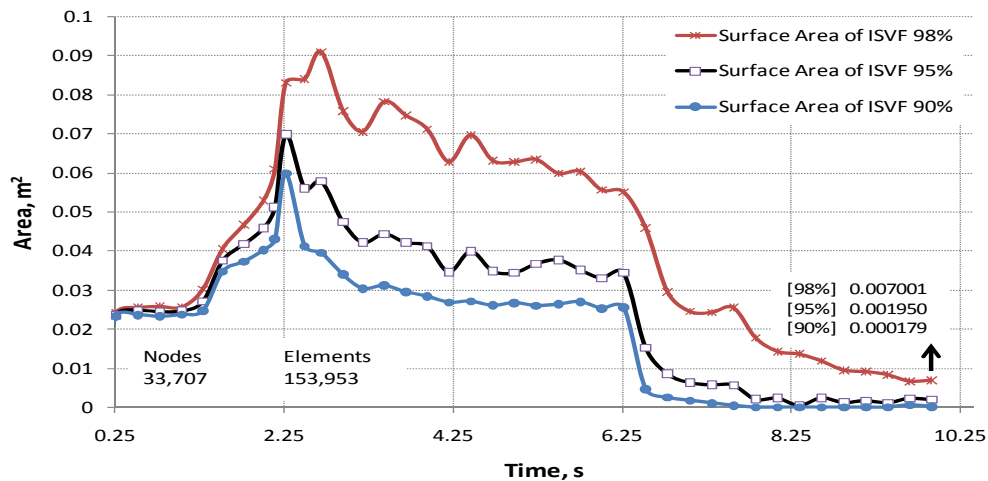
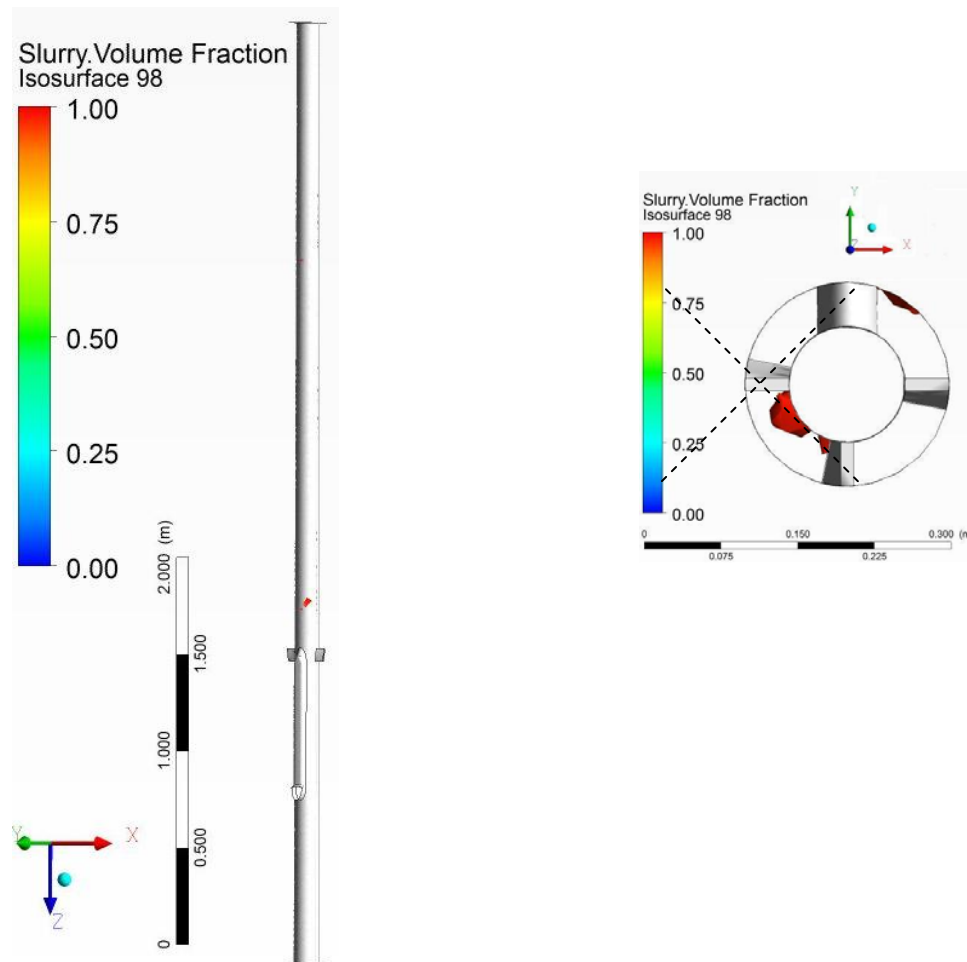


Figure 7.18 Surface area of the ISVF = 90, 95 and 98 percent (integral quantities) – flow time results for the 3D model of the novel sensor housing and the casing conveyed with three downstream flow deflector fins within the borehole section of 5.00 m length.

### 7.3.2.4 Discussion

The results presented in this section suggest that when this type of flow deflector fins were located at the top-end of the novel sensor housing these could distribute the ISVF regions in all of the quadrants of the cross-section of the borehole (Figure 7.19). However, the residual integral quantity was higher than the model with the sensor housing alone, reducing of the cement displacement efficiency. It seems more effective to place this type of flow deflector fins downstream of the novel sensor housing.



a) Isometric view

b) Cross-section

Figure 7.19 VOF simulation results for the 3D model of the novel sensor housing and the casing conveyed with three downstream flow deflector fins within the borehole section of 5.00 m length. Output at time  $t = 9.91$  s, while the cement slurry is displacing through the annulus. These snapshots show the annular distribution of the ISVF with value of 0.98.

#### **7.3.2.5 Summary and conclusion**

These preliminary results suggested that the geometry design of the set flow deflector fins was governed by the upstream fins. The reason behind this is that the sensor housing located downstream of the fins represent the major flow impedance on the system that imbalance the cement slurry front; thus, these fins could balance the cement slurry front. However, the upstream sets of fins require additional design to reduce the annular flow impedance. Therefore, the following section focus on the study of multiple configurations of the upstream fins.

### 7.3.3 Fins located at the upstream from the sensor housing

As stated previously, the optimal fin geometrical configuration is governed by the fins located at the upstream of the sensor housing. This section studies four models with different types of flow deflector fins located upstream of the novel sensor housing. The scope of this study is to identify the suitable configuration of the flow deflector fins for the sensor housing system by means of CFD techniques.

#### 7.3.3.1 Type-I fin

The geometry of the fins from the prior models had a "blocky" shape with sharp angular edges resulting in high annular flow impedance. The Type-I fins presented in this section have smooth surfaces that could preserve the stream lines of the annular flow during circulation.

##### 7.3.3.1.1 Geometry and grid

Figure 7.20 illustrates the 3D configuration of the model used in this section. This section studied the effect of four flow deflector Type-I fins located at the upstream of the sensor housing sample port. The geometry of sensor housing was simplified to focus on the geometry and configuration of the fins. The set of fins and fluid sample port standoff were simplified by assuming that these elements were in full contact with the borehole walls. These simplifications eliminated small gaps (mm scale) of point located elements, but preserved the large elements of the system (cm scale) that dominate the fluid phase displacement.

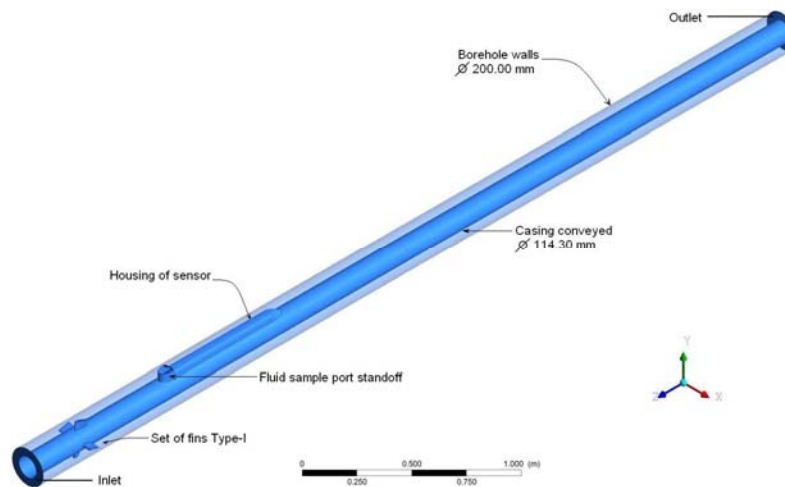


Figure 7.20 3D geometrical configuration of the low flow impedance sensor housing with four flow deflector fins (Type-I) located at 483 mm upstream of the sensor housing sample port within the borehole section of 5.00 m length.

According to [77] and based on the fluid properties presented early in this chapter (page 147) the configurations of flow deflector fins used for this study are shown in Figure 7.21. Each fin had  $8.5^\circ$  of deviation from the vertical position and 12.7 mm width and 65.5 mm length.

The set of fins were located at the upstream distance of approximately seven times the fin's length (483 mm) from the sensor fluid sample port standoff. Because the scope of this preliminary model focused on the flow mechanic assessment of the set of fins, it was important to isolate the fins from potential boundary effects from the sensor housing geometry.

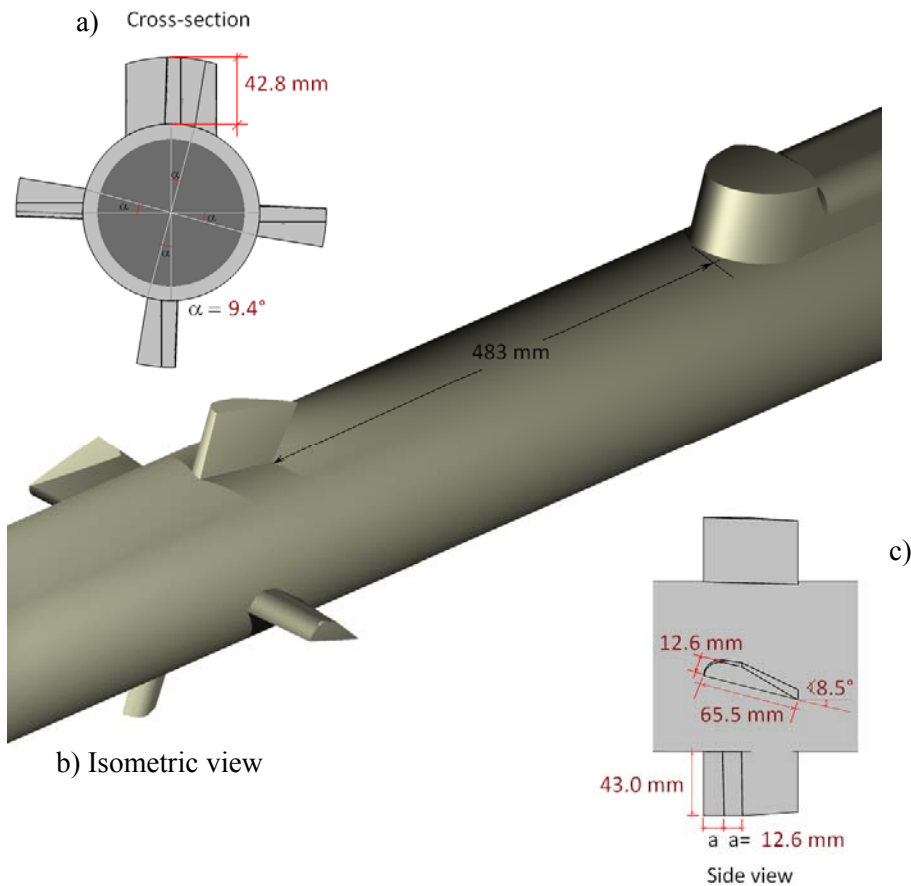


Figure 7.21 Sketch of: (a) the cross-section; (b) the isometric view; (c) and the side view of four flow deflector Type-I fins located at 483 mm from the fluid sample port standoff.

A geometrical discretization of the 3D model was made for the CFD analysis. Unstructured tetrahedral cells were generated to define the model. A view of the generated grid can be seen in Figure 7.22.

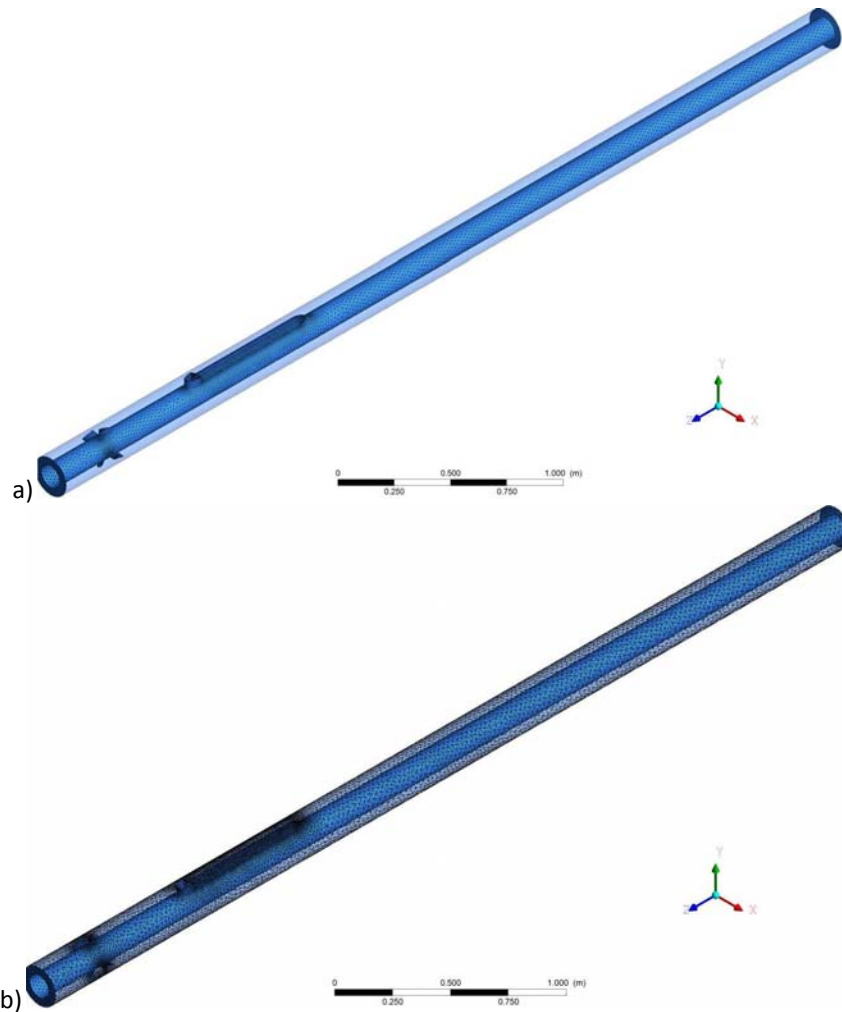


Figure 7.22 Mesh of (a) 3D model of the novel sensor housing and the casing conveyed with four flow deflector fins (Type-I) located at 483 mm upstream of the fluid sample port standoff (b) within the 5.00 m of a borehole section.

#### 7.3.3.1.2 Numerical solution control

The time step used in the unsteady calculation was set to  $1.3 \times 10^{-3}$  s. A total of 10,000 s of flow time was simulated, requiring approximately 96 hours (4 days) of computation time. A mesh with 38,871 nodes and 180,073 elements was used on this analysis.

#### 7.3.3.1.3 Results

Figure 7.23 shows the simulation results of the unsteady displacement of cement displacing fresh-water spacer. The cement slurry volume fraction is presented in a color map format, of which the color “dark orange” corresponds to the iso-surface with cement slurry volume fraction with value of 0.90 (ISVF-90%).

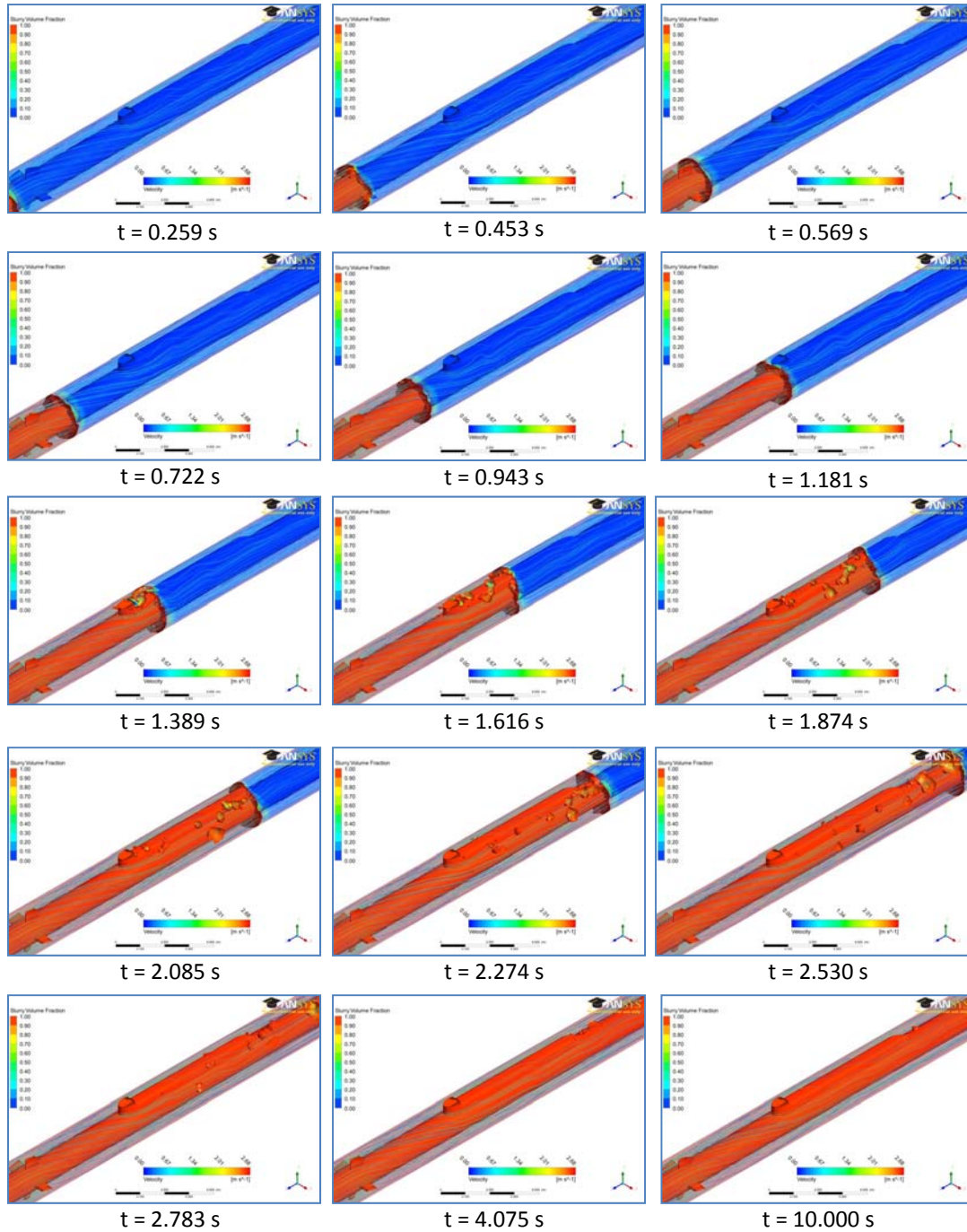


Figure 7.23 VOF simulation results for the 3D model of the novel sensor housing and the casing conveyed with four flow deflector fins (Type-I) located at 483 mm upstream of the sensor housing within the borehole section of 5.00 m length. Output at time  $t = 0.259, 0.453, 0.569, 0.722, 0.943, 1.181, 1.389, 1.616, 1.874, 2.085, 2.274, 2.530, 2.783, 4.075$  and  $10.00$  s s, while the cement slurry is displacing through the annulus. Each snapshot shows cement slurry volume fraction, ISVF = 0.90, and velocity streamlines.

Throughout the whole simulation, it was observed that the cement phase displaced most of the water-spacer phase. The results of Figure 7.23 suggest that the Type-I fins

preserved the annular stream lines of the cement slurry, but the deflection of stream lines of 8.5 from vertical position was not preserved through the entire model. This was an indication that second set of flow deflector fins at the downstream of the sensor housing were required.

The fluid sample port standoff was the major flow impedance of the sensor housing. At 1.389 s, the inhomogeneous cement slurry front passed the standoff, leaving pockets of poor quality cement behind. Then these ISVF regions were deflected and displaced at a short distance from the cement slurry front, meaning that these were moving with similar velocity gradients than the displacement front.

The time for the water-spacer to be displaced by the cement slurry from the inlet to the outlet was 6.40 s, but the simulation time ran until the integral quantity stabilized at 10.00 s.

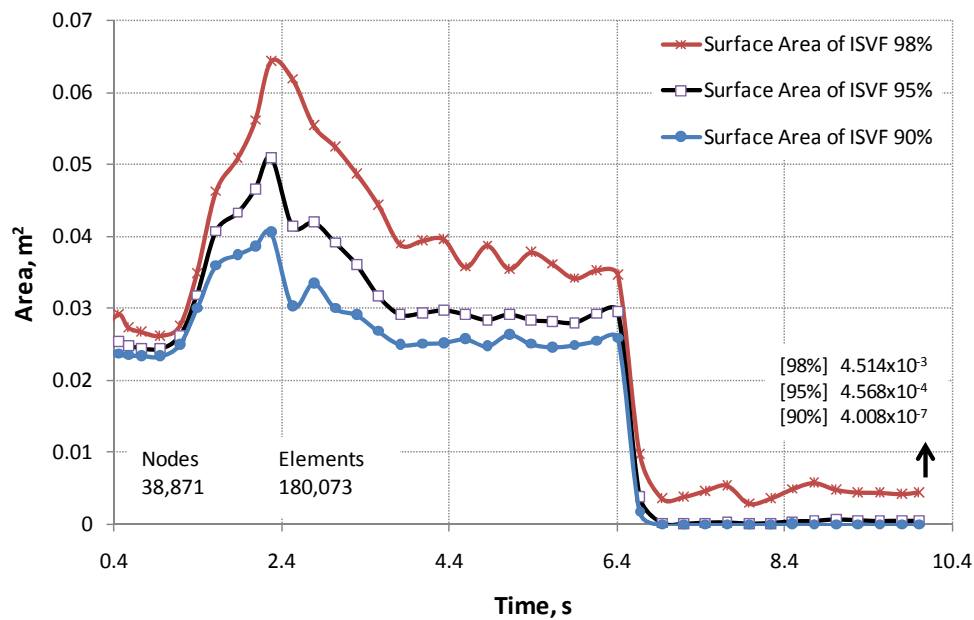


Figure 7.24 Surface area of the ISVF = 90, 95 and 98 percent (integral quantities) – flow time results for the 3D model of the novel sensor housing and the casing conveyed with four flow deflector fins (Type-I) located at 483 mm upstream of the sensor housing within the borehole section of 5.00 m length.

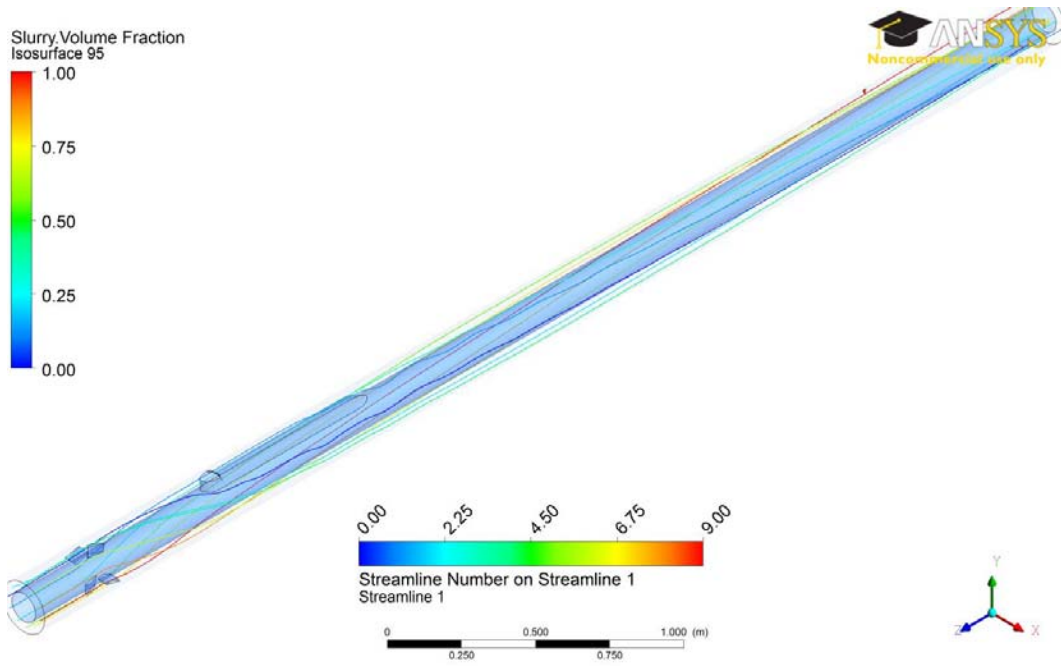
Figure 7.24 shows the evolution of the integral quantities through the entire circulation period of 10.00 s. The peak area value of the iso-surface with volume fraction with value of 0.90 (ISVF-90%) was  $0.041 \text{ m}^2$ , and it was reached at 2.27 s when the cement slurry

front was passing through the top-end of the sensor housing. Because the peak value did not occur when the displacement front passed through the set of fins, the results suggest that this type of flow deflector maintained a lower flow impedance when compared to the model with the sensor housing alone. The post-peak values of the integral quantity ISVF-90% showed a reduction trend until the cement front reached the outlet at 6.25 s, then this trend was followed by a significant drop of the ISVF values reaching a stabilized residual value of  $4.01 \times 10^{-7} \text{ m}^2$  at 10.00 s. The residual integral quantity of this model with Type-I fins was three orders of magnitude lower than the previous model with three fins located at the top-end of the sensor housing.

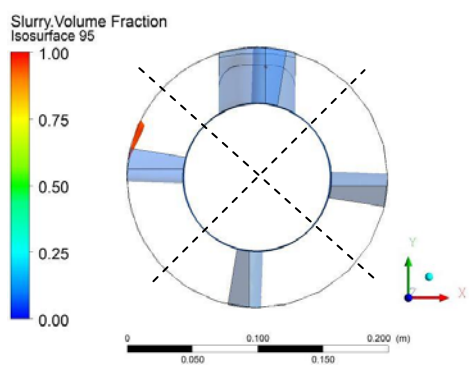
#### 7.3.3.1.4 Discussion

Because the zones of ISVF-90% at the end of the simulation were small and few, the inadequate cement volume fraction with value of 0.98 was used to illustrate the locations and distribution of the poor quality cement zones. The results presented in this section suggest that this type of flow deflector fins distributed the ISVF zones in all of the quadrants of cross-section of the borehole. Despite that, the flow deflection was not preserved through the entire model (Figure 7.25). To preserve the redirection of the annular flow a second set of flow deflector fins at the downstream of the sensor housing is required.

The shape of the Type-I fins was ideal from the flow mechanics perspective; however, there is an associated risk of bending the slim parts of the fins during installation, and the ability to manufacture of this shape could be challenged. The following models explore other shapes with more robust fins of uniform thickness and trimmed edges.



Isometric view



Cross-section divided in quadrants

Figure 7.25 VOF simulation results for the 3D model of the novel sensor housing and the casing conveyed with four flow deflector fins (Type-I) located at 483 mm upstream of the sensor housing within the borehole section of 5.00 m length. Output at time  $t = 10.00$  s, while the cement slurry is displacing through the annulus. These snapshots show the annular distribution of the ISVF with value of 0.98.

### 7.3.3.2 Type-II fin

The scope of this section is to evaluate the model with set of Type-II fins that have uniform thickness. The purpose of this new geometrical configuration is to eliminate thin components of the previous model of fins and reduce the risk of bending the fins during installation.

#### 7.3.3.2.1 Geometry and grid

Figure 7.26 and Figure 7.27 illustrate the 3D configuration, the side view and the cross-section of the model of this section. The geometry of the fins was simplified and it was assumed that they were in full contact with the borehole walls. Because the main objective of this model is to focus on the Type-II fins set, the length of the model was reduced in half to save some computational time.

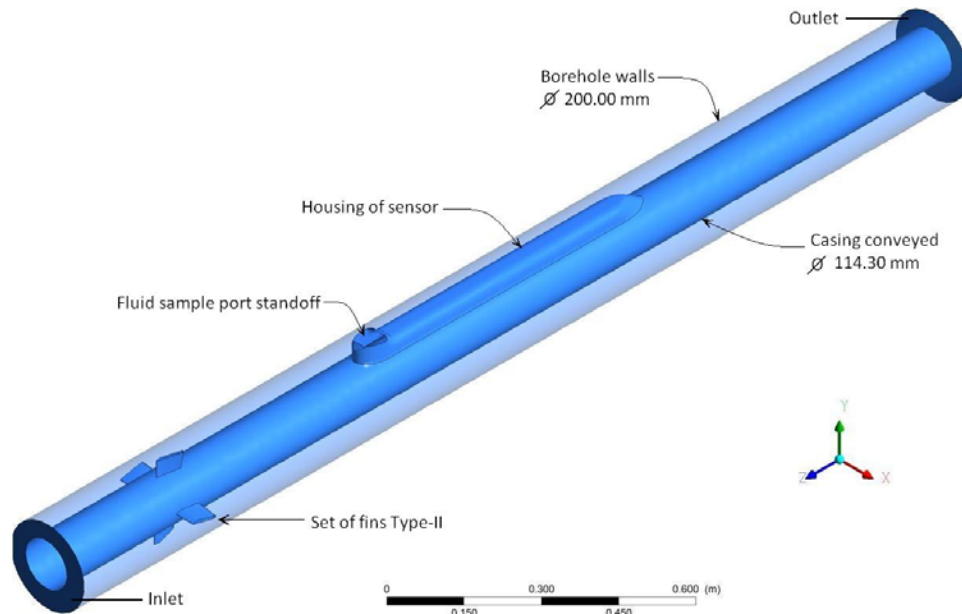


Figure 7.26 3D geometrical configuration of the low flow impedance sensor housing with four flow deflector fins (Type-II) located at the upstream of the sensor housing.

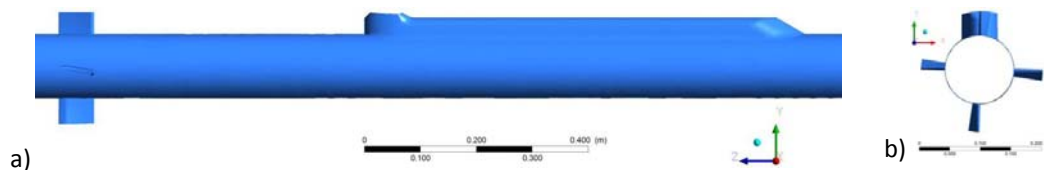


Figure 7.27 Illustration of the four upstream flow deflector fins (Type-II) and the novel sensor housing: (a) side view (b) cross-sectional view

According to [77] and based on the fluid properties presented early in this chapter (page 147) the configurations of flow deflector fins used for this study are shown in Figure 7.28. Each fin has  $8.5^\circ$  of deviation from the vertical position and 6.2 mm width and 60.0 mm length.

The set of fins were located at a upstream distance of approximately seven times the fin's length (483.0 mm) from the sensor housing sample port. Because the scope of this model focused on the flow mechanic assessment of the set of fins, it was important to isolate the fins from potential boundary effects from the sensor housing geometry.

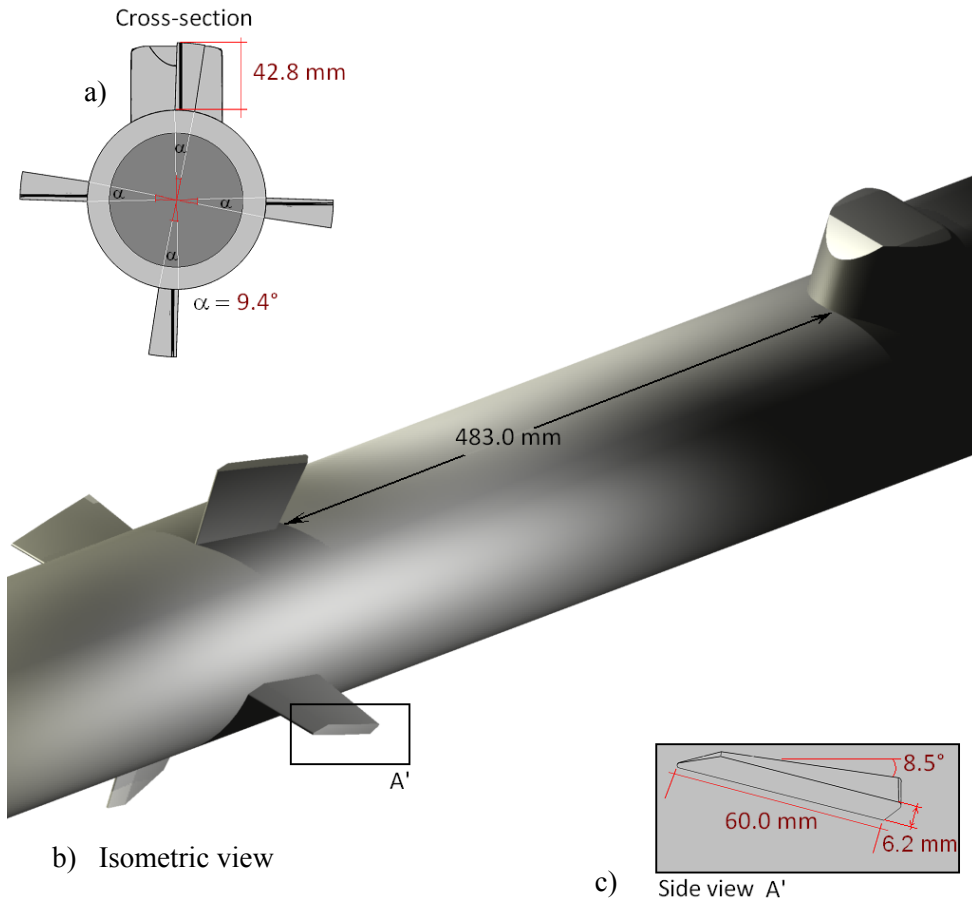


Figure 7.28 Sketch of: (a) the cross-section; (b) the isometric view; (c) and the side views of four flow deflector Type-II fins located at 483 mm from the fluid sample port standoff.

A geometrical discretization of the 3D model was made for the CFD analysis. Unstructured tetrahedral cells were generated to define the model. A view of the generated grid can be seen in Figure 7.29.

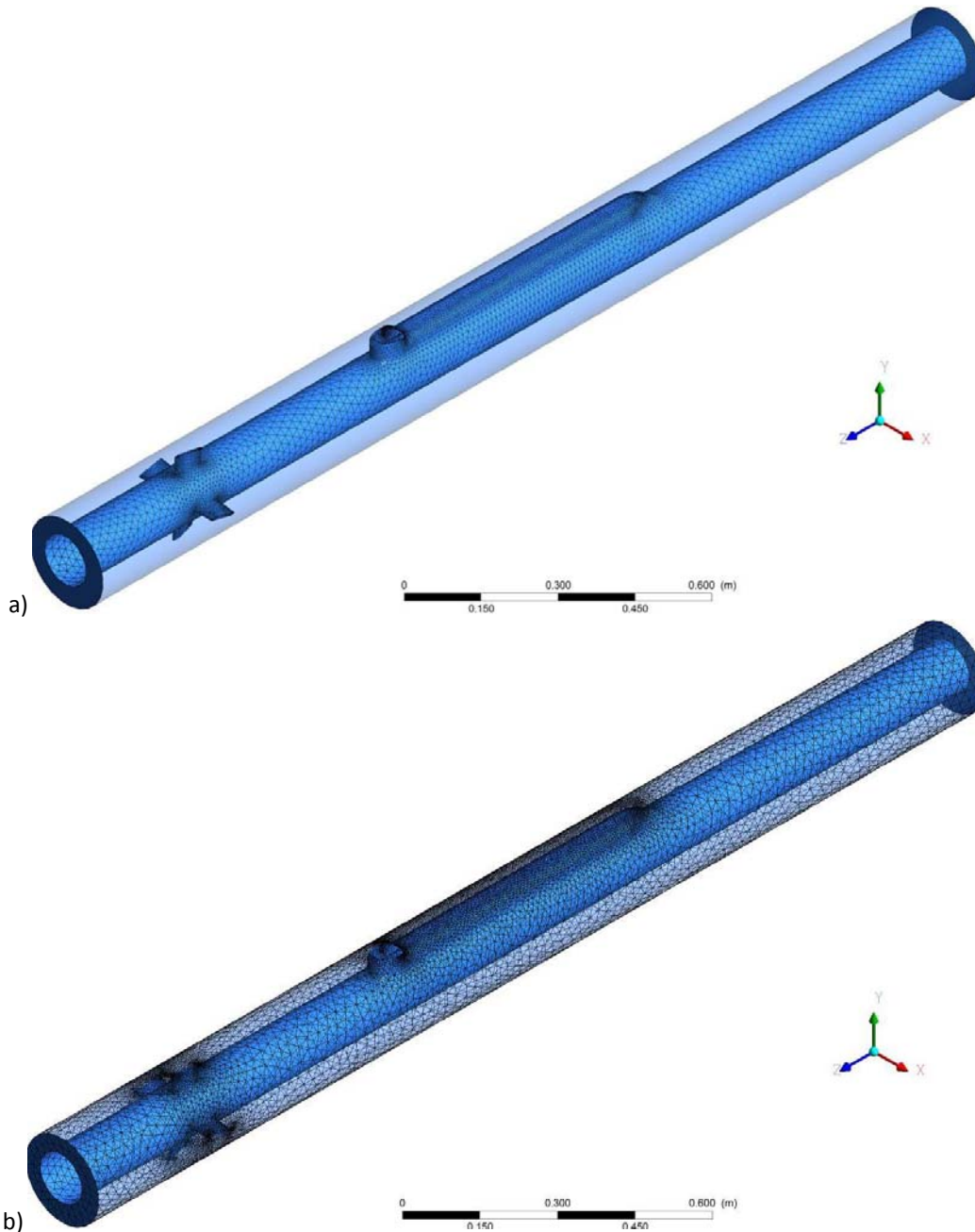


Figure 7.29 Mesh for the 3D model of (a) the novel sensor housing and the casing conveyed with four flow deflector fins (Type-II) located at 483.0 mm upstream of the sensor housing (b) within the 2.50 m of a borehole section.

### 7.3.3.2.2 Numerical solution control

The time step used in the unsteady calculation was set to  $5.0 \times 10^{-4}$  s. A total of 4.00 s of flow time was simulated, requiring approximately 72 hours (3 days) of computation time. A mesh with 56,395 nodes and 282,218 elements was used on this analysis.

#### 7.3.3.2.3 Results

Figure 7.30 shows the simulation results of the unsteady displacement of cement displacing freshwater spacer fluid. The cement slurry volume fraction is presented in a color map format, of which the color “dark orange” corresponds to the iso-surface with cement slurry volume fraction with value of 0.90 (ISVF-90%).

Throughout the entire simulation, it was observed that the cement phase displaced most of the spacer fluid phase. These series of snapshots also show that the Type-II fins induced mild flow impedance. At 0.82 s of circulation, pockets of poor quality cement were left behind in the cement slurry front, indicating that some modifications were required to smooth the fin’s tail.

At 1.66 s of circulation, several zones of ISVF-90% were observed downstream of the standoff of the sensor housing. The major flow impedance was caused by the fluid sample standoff that resulted in the formation of zones of poor quality cement.

These results also suggest that a second set of fins was required at the downstream of the sensor housing because the deflection of the annular flow of  $8.5^\circ$  from vertical position was not preserved through the entire model.

The time for the water spacer to be displaced by the cement slurry from the inlet to the outlet was 3.200 s, but the simulation time ran until the integral quantity stabilized at 4.000 s.

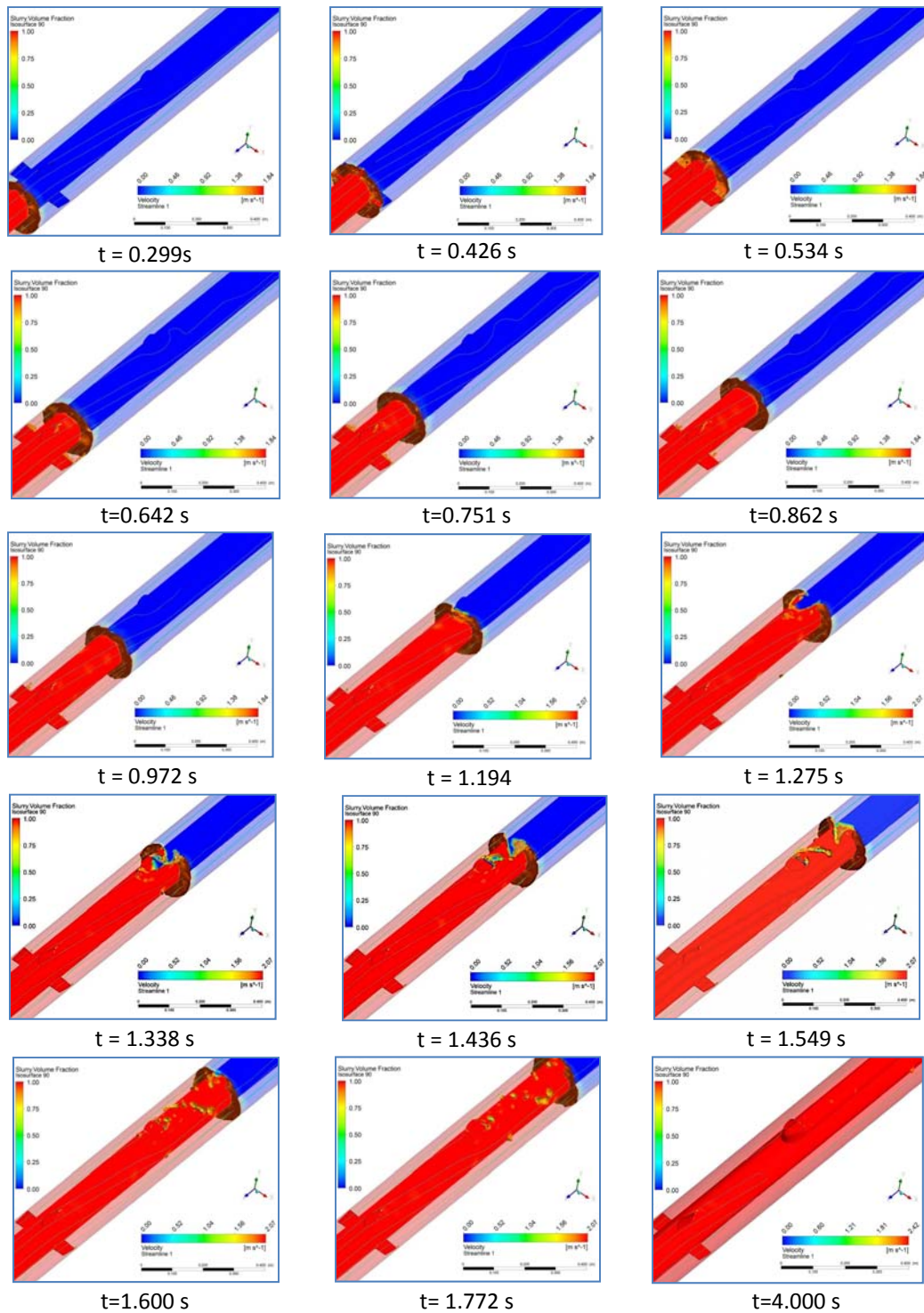


Figure 7.30 VOF simulation results for the 3D model of sensor housing with four flow deflector fins (Type-II). Output at time  $t = 0.299, 0.426, 0.534, 0.642, 0.751, 0.862, 0.972, 1.194, 1.275, 1.338, 1.436, 1.549, 1.600, 1.772$  and  $4.000$  s, while the cement slurry is displacing through the annulus. Each snapshot shows cement slurry volume fraction,  $ISVF = 0.90$ , and velocity streamlines.

Figure 7.31 shows the evolution of the integral quantity through the entire circulation period of 4.000 s. The first peak area value of the iso-surface with volume fraction with value of 0.90 (ISVF-90%) was 0.035 m<sup>2</sup>, and it was reached at 0.534 s when the cement slurry front was passing through the set of fins. Then, the integral quantity followed a reduction trend until the cement slurry front reached the fluid sample standoff. At 1.100 s, the values of ISVF-90% started to increase until the second peak value of 0.036 m<sup>2</sup> occurred at 2.210 s. These two peak values were equal (with reason), which means that the set of Type-II fins and sensor housing produce relatively equal annular flow impedance into the system.

The post-peak values of the integral quantity ISVF-90% showed a reduction trend until the cement front reached the outlet at 3.200 s, then this trend was followed by a significant drop of the ISVF values reaching a stabilized residual value of 2.94x10<sup>-3</sup> m<sup>2</sup> at 4.000 s. The peak integral quantity value (0.036 m<sup>2</sup>) of this model with Type-II fins was reasonably equal to the peak value (0.041m<sup>2</sup>) from the model with Type-I.

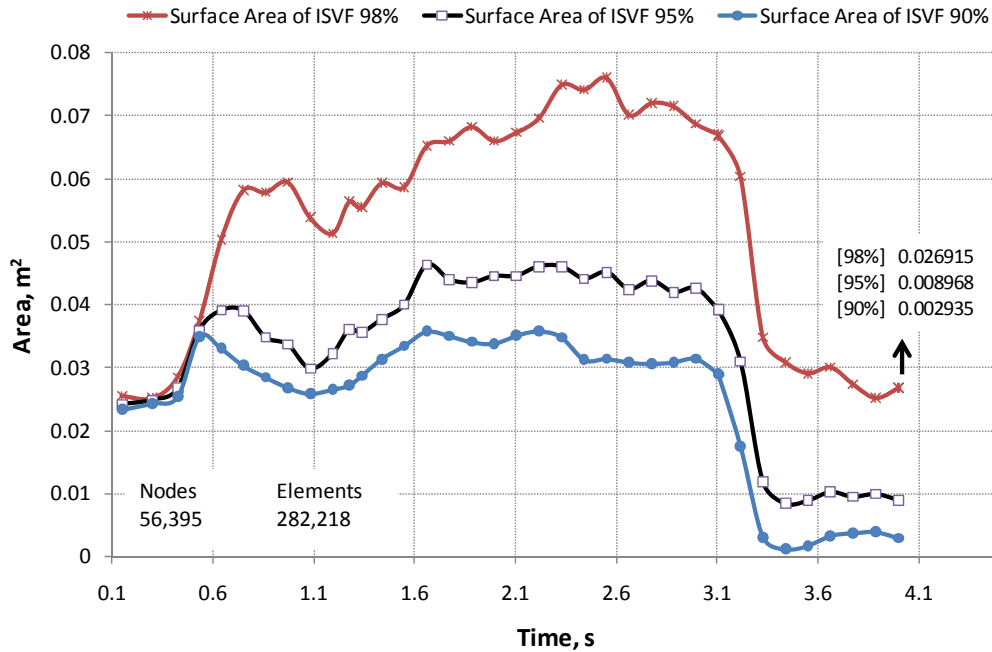


Figure 7.31 Surface area of the ISVF = 90, 95 and 98 percent (integral quantities) – flow time results for the 3D model of the novel sensor housing and the casing conveyed with four flow deflector fins (Type-II) located at 483.0 mm upstream of the sensor housing within the borehole section of 5.00 m length.

### 7.3.3.2.4 Discussion

The zones of ISVF-90% at the end of the simulation were small and few; thus, the inadequate cement volume fraction with value of 0.98 was used to illustrate the locations and distribution of the poor quality cement zones (See Figure 7.32). The results presented in this section suggest that uniform thickness with trimmed edges fins (Type-II) distributed the ISVF in all of the quadrants of the borehole cross-section. Despite that, the flow deflection was not preserved through the entire model. To preserve the redirection of the annular flow a second set of flow deflector fins at the downstream of the sensor housing is required

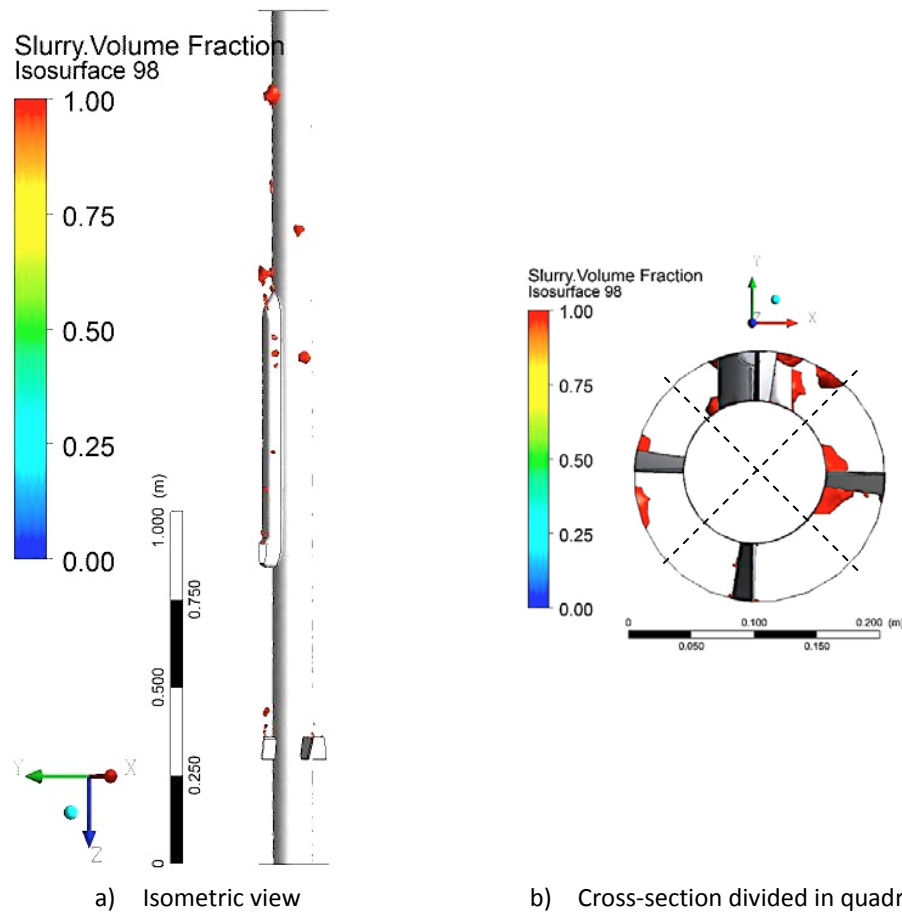
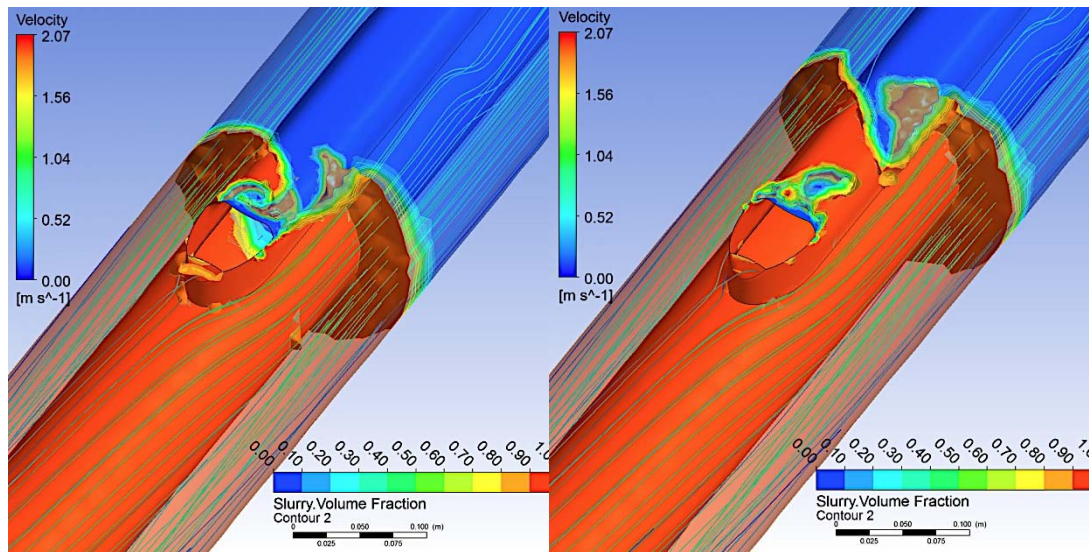


Figure 7.32 VOF simulation results for the 3D model of the novel sensor housing and the casing conveyed with four flow deflector fins (Type-II) located at 483.0 mm upstream of the sensor housing within the borehole section of 2.50 m length. Output at time  $t=4.00$  s, while the cement slurry is displacing through the annulus. These snapshots show the annular distribution of the ISVF with value of 0.98.



t = 1.338

t = 1.436

Figure 7.33 VOF simulation results for the 3D model of the novel sensor housing and the casing conveyed with four flow deflector fins (Type-II) located at 483.0 mm upstream of the sensor housing within the borehole section of 2.50 m length. Output at time t 1.338 and 1.436 s, while the cement slurry is displacing through the annulus. Each snapshot shows cement slurry volume fraction, ISVF = 0.90, and velocity streamlines.

The hydraulic link between the fluid sample port and borehole wall (formation) at each monitoring depth is important for MMV activities, and this hydraulic connection must be isolated from near horizons within the borehole to ensure in situ measurements. In this study, the CFD results indicate that the geometry of the standoff used induces significant flow impedance into the system that can be balanced with the integration of the fins without plugging the sample port. The deflection of the annular flow of  $8.5^\circ$  from the vertical position induced spiral motions with closed streamlines on the back face of fluid sample standoff at 1.338 s, resulting in the development of pockets of poor quality cement that were later displaced during circulation, as illustrated in the following time step at 1.436 s (see Figure 7.33). Because it was convenient to have a hydraulic connection between the borehole wall and the fluid sample standoff, the formation of small vortices on the back face of the standoff was anticipated. This could trap small pockets of poor quality cement that may result in a high permeable zone after the cement hardened.

The flow deflector Type-II fins with uniform thickness and trimmed edges had mild flow impedance, which was similar to the flow impedance generated from the ideal Type-I fins. Figure 7.34 illustrates the cement slurry displacement front passing through the

frontal and caudal edges of the fins at 0.426 s and 0.534 s, respectively. The frontal and caudal edges did not cause an imbalance of the displacement front, but the tail edges produced some small pockets of poor quality cement that were displaced through the circulation period.

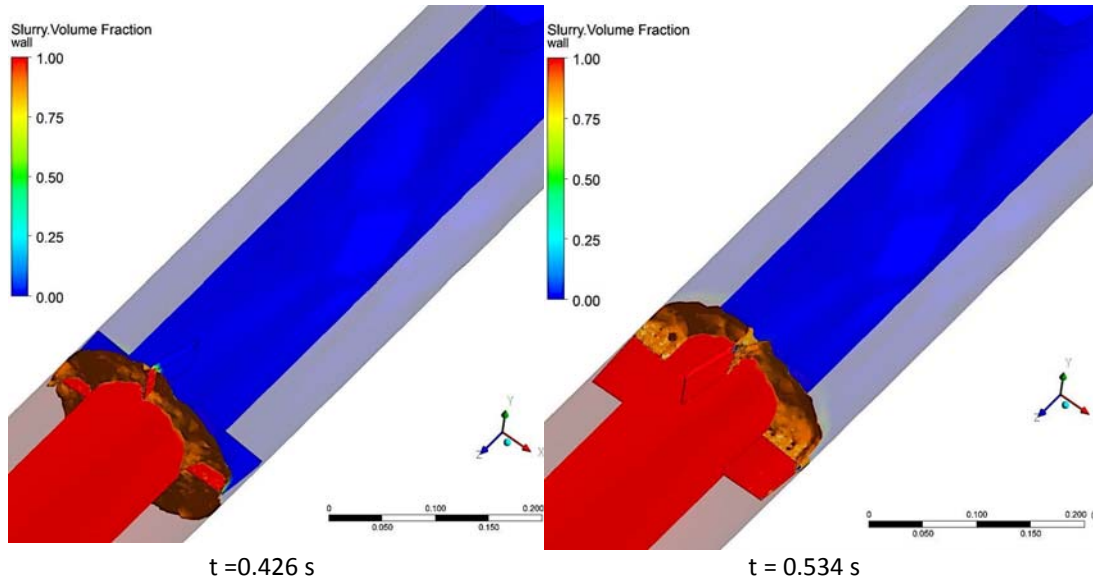


Figure 7.34 VOF simulation results for the 3D model of the novel sensor housing and the casing conveyed with four flow deflector fins (Type-II) located at 483.0 mm upstream of the sensor housing within the borehole section of 2.50 m length. Output at time  $t = 0.426$  and  $0.534$  s, while the cement slurry is displacing through the annulus. Each snapshot shows cement slurry volume fraction and  $ISVF = 0.90$ .

All the models with flow deflector fins presented in the last two sections and in Chapter 5 assumed that the fins were in full contact with the borehole walls. This assumption simplified the models and reduced the computational time. However, because there was not clearance between the borehole wall and the fins, there is a high risk of damaging these types of fins including the sensor housing during installation. The following two section study models with uniform thickness fins that have a clearance of 50% and 30% of the annular space.

### 7.3.3.3 *Type-III fin*

Previous results suggest that fins with uniform thickness and trimmed edges are an optimal solution to deflect the annular flow, enhance the cement circulation and distribution of poor quality cement zones. The next phase of this modeling effort focuses on the clearance between the fins and the borehole wall and a correction of the cement slurry rheology for a larger clearance.

A large clearance resulted from the use of short (in height) fins to reduce the risk of damaging the fins during installation, but short fins are the less effective in deflecting the annular flow. Therefore, this and the following section assess the fluid mechanics properties of two reasonably high and low clearances between the fins and the borehole wall. This section studies a model with fins that have a clearance of 50% of the annular space (42.8 mm) between the casing and the borehole walls.

The rheology of the cement slurry used in previous model was inherited from the OW for the Pembina Cardium CO<sub>2</sub> monitoring pilot. This was helpful to illustrate how the CFD technique was used to evaluate the preliminary simulations of the novel sensor housing system. However the models of this chapter have a clearance between casing and borehole walls 30% greater than the clearance between the tubing and borehole walls of the OW for the Penn West site. Therefore, a correction of the cement slurry rheology was required to appropriately evaluate the effect that the annular clearance has on the fins configuration. The new boundary conditions of this and the following models includes the CO<sub>2</sub>-resistant cement slurry with rheological parameter: power law index,  $n = 0.589$ ,  $K = 0.819 \text{ Pa s}^{(0.589)}$ . These fluid properties were taken from wellbore completion report of a well installed in a CO<sub>2</sub>-EOR field with similar dimensions and clearance [79].

#### 7.3.3.3.1 Geometry and grid

Figure 7.35 and Figure 7.36 illustrate the 3D configuration and side view of the model of this section. Because the main objective of this model focuses on the effect of the fin's height on the downstream flow of the sensor housing, the length of the model was 5.00 m.

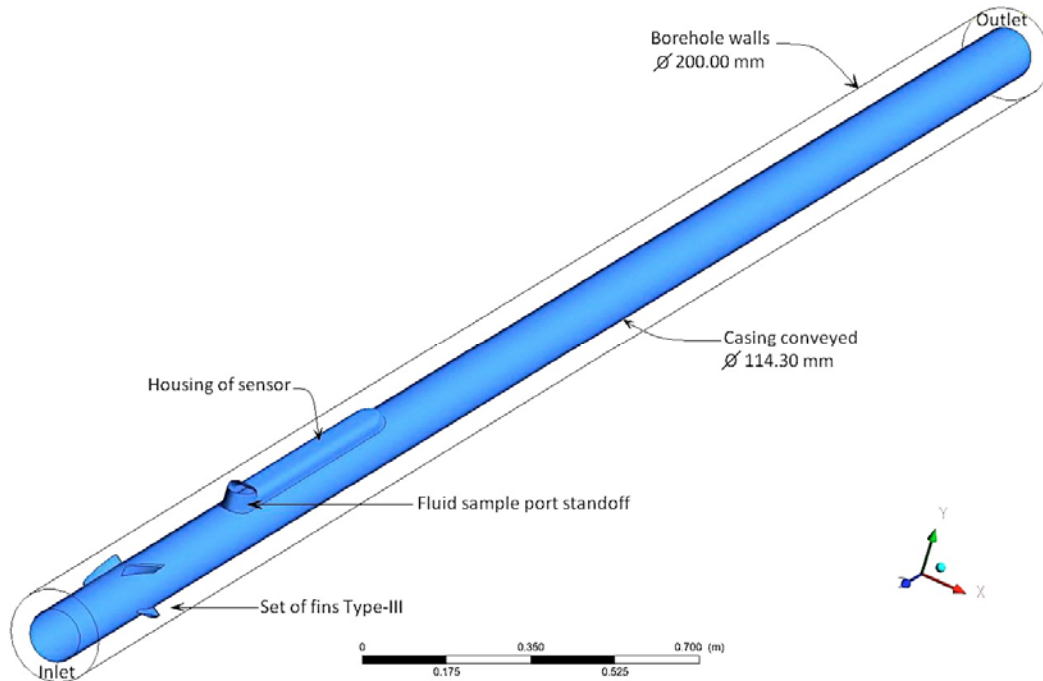


Figure 7.35 3D geometrical configuration of the low flow impedance sensor housing with four flow deflector fins (Type-III) located at 420 mm upstream of the sensor housing.

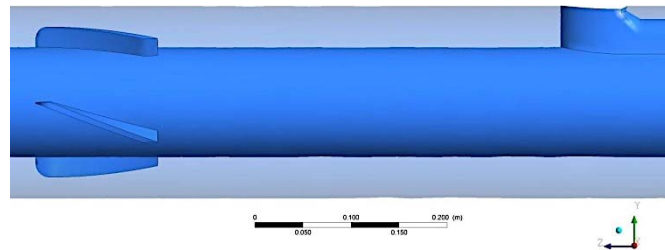


Figure 7.36 Illustration of four upstream flow deflector fins (Type-III) and the novel sensor housing.

The height of flow deflector fin of this model was approximately 50% (21.0 mm) of the annular space (42.8 mm) between the casing and the borehole walls. In order to compensate the reduction in size of the fin's height, the length and the deflection angle of the fins were increased by two times from dimension of the previous models.

The configurations of flow deflector fins used for this part of the study are shown in Figure 7.37. Each fin had  $16^\circ$  of deviation from the vertical position, 6.0 mm width and a projection length of 127.0 mm.

The set of Type-III fins were located at the upstream distance of approximately three times the fin's length (420.0 mm) from the fluid sample port standoff. Because the scope of this model focused on a fluid mechanics assessment of the set of Type-III fins, it was

important to isolate the fins from possible boundary effects from the sensor housing geometry.

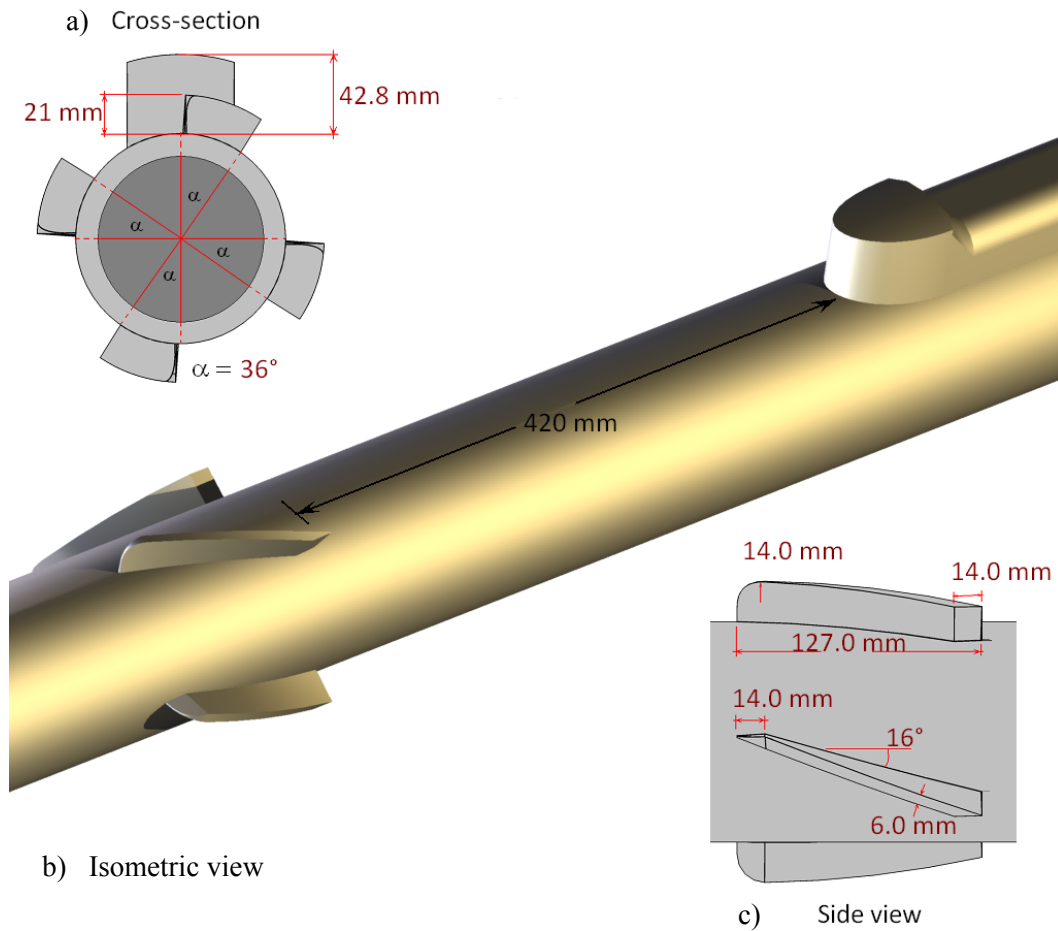


Figure 7.37 Sketch of: (a) the cross-section; (b) the isometric view; (c) and the side view of four flow deflector Type-III fins located at 420 mm from the fluid sample port standoff.

A geometrical discretization of the 3D model was made for the CFD analysis. Unstructured tetrahedral cells were generated to define the model. A view of the generated grid can be seen in Figure 7.38.

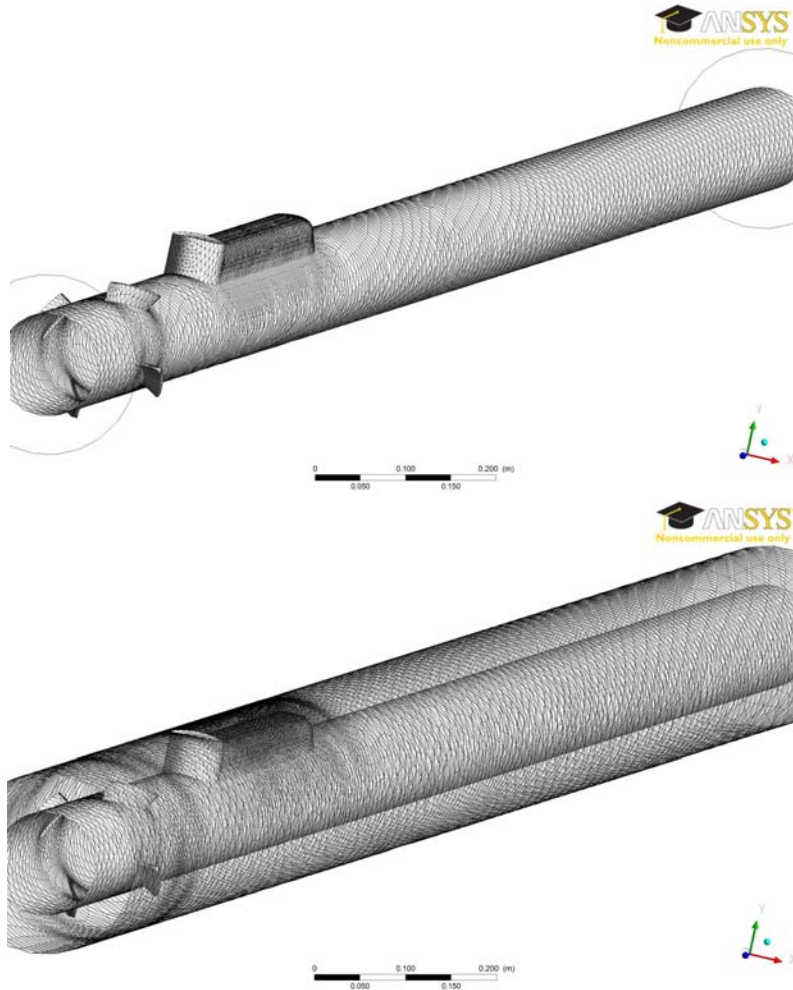


Figure 7.38 Mesh for the 3D model of (a) the novel sensor housing and the casing conveyed with four flow deflector fins (Type-III) located at 420 mm upstream of the sensor housing (b) within the 5.00 m of a borehole section.

#### 7.3.3.3.2 Numerical solution control

The time step used in the unsteady calculation was set to  $6.9 \times 10^{-4}$  s. A total of 10.00 s of flow time was simulated, requiring approximately 120 hours (5 days) of computation time. A mesh with 41,851 nodes and 198,000 elements was used on this analysis.

#### 7.3.3.3.3 Results

Figure 7.39 shows the simulation results of the unsteady displacement of cement displacing fresh-water spacer. The cement slurry volume fraction is presented in a color map format, of which the color “dark orange” corresponds to the iso-surface with cement slurry volume fraction with value of 0.90 (ISVF-90%).

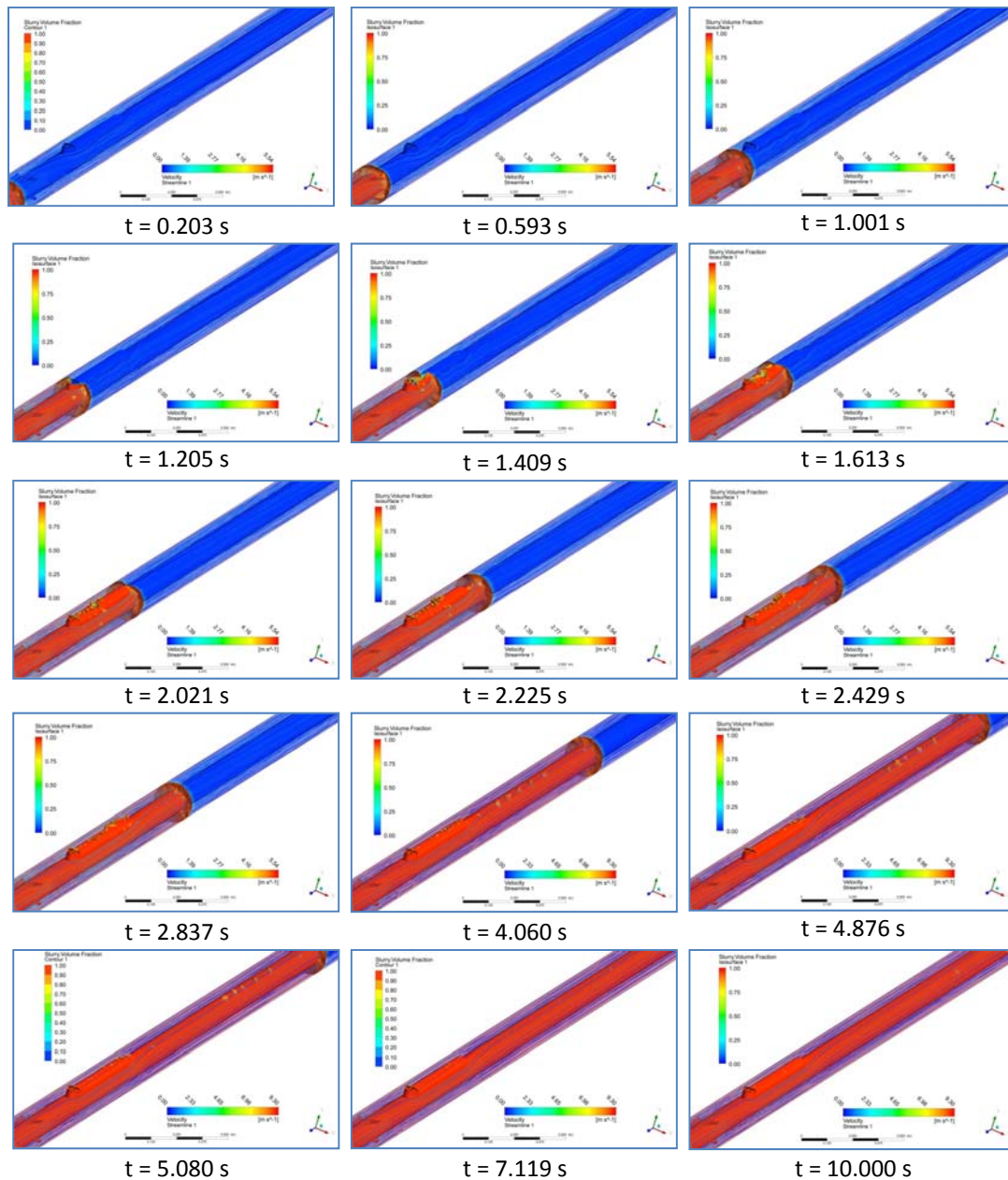


Figure 7.39 VOF simulation results for the 3D model of the novel sensor housing and the casing conveyed with four flow deflector fins (Type-III) located at 420 mm upstream of the sensor housing within the borehole section of 5.00 m length. Output at time  $t = 0.203, 0.593, 1.001, 1.205, 1.409, 1.613, 2.021, 2.225, 2.429, 2.837, 4.060, 4.876, 5.080, 7.119$  and  $10.000$  s, while the cement slurry is displacing through the annulus. Each snapshot shows cement slurry volume fraction, ISVF = 0.90, and velocity streamlines.

Just like in other models, it was observed that the cement phase displaced most of the water-spacer phase. These series of figures also show that the fins were mildly deflecting the downstream annular flow. The results suggest that the fins were not tall enough to deflect the viscous cement slurry phase. Additional simulation results of the unsteady displacement of cement displacing fresh-water spacer from a different angle and grey color map format are presented in Appendix B.

The time for the water-spacer to be displaced by the cement slurry from the inlet to the outlet was 6.100 s, but the simulation time ran until the integral quantity stabilized at 10.000 s.

On Figure 7.40 the evolution of the integral quantity is shown through the entire circulation period of 10.000 s when using the Type-III fins. The first peak area value of the iso-surface with volume fraction with value of 0.90 (ISVF-90%) was 0.034 m<sup>2</sup>, and it was reached at 0.593 s when the cement slurry front was passing through the set of fins. Then, the integral quantity of this model followed a reduction trend until the cement slurry front reached the fluid sample port standoff. At 1.100 s, the values of ISVF-90% started to increase until the second peak value of 0.048 m<sup>2</sup> occurred at 2.633 s. The first peak value was lower than the second peak value, which means that the set of Type-III fins were not enhancing the cement circulation on the sensor housing system section.

The post-peak values of the integral quantity ISVF-90% showed a reduction trend until the cement front reached the outlet at 6.100 s, then this trend was followed by a significant drop of the ISVF values reaching a stabilized residual value of  $1.58 \times 10^{-3}$  m<sup>2</sup> at 10.000 s.

The first peak value of the ISVF-90% (0.034 m<sup>2</sup>) of this model with Type-III fins was equal (with reason) to the previous peak values of 0.041 m<sup>2</sup> and 0.036 m<sup>2</sup> from the models with Type-I and Type-II fins, respectively. This means that the shape of the Type-III was inducing a mild annular flow impedance into the system.

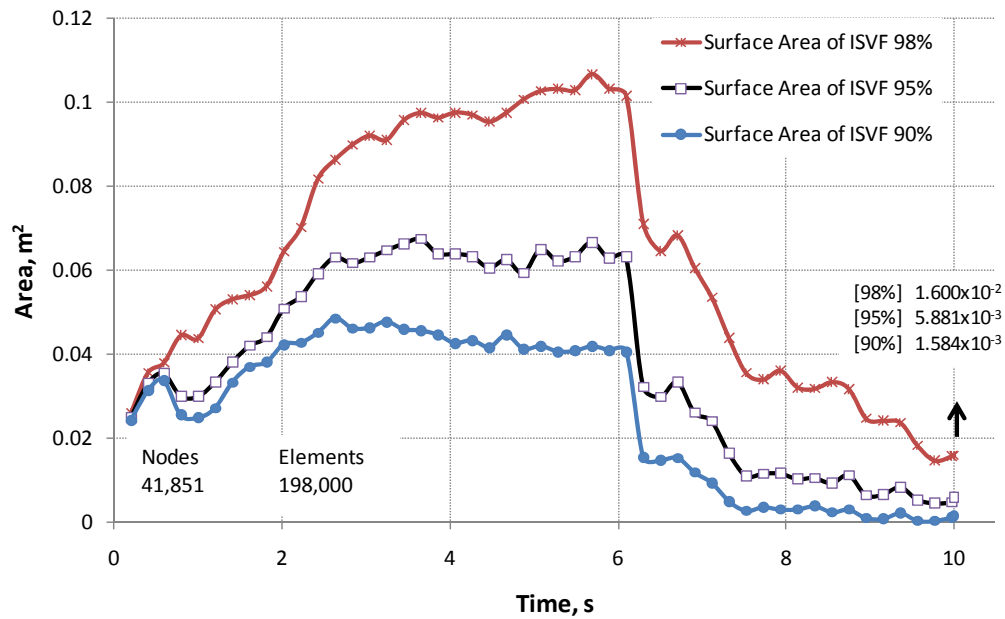
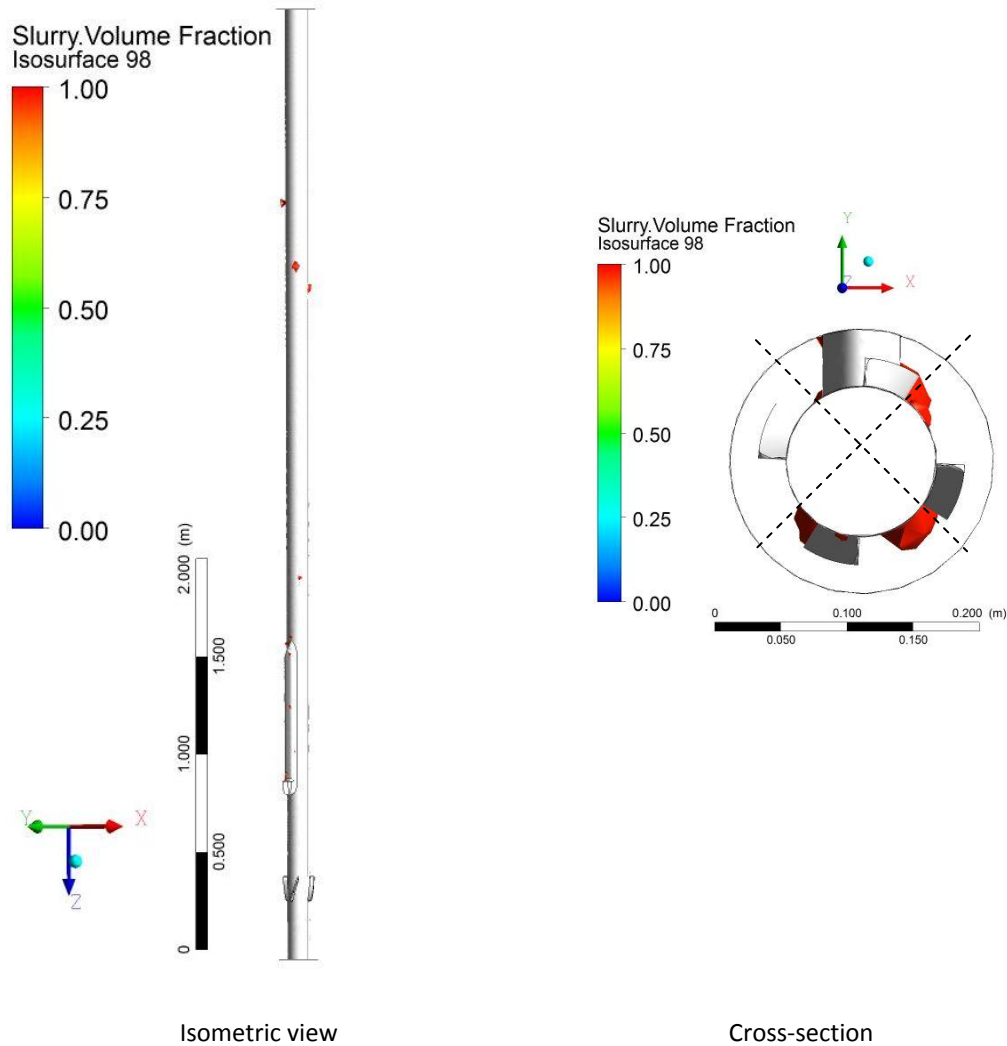


Figure 7.40 Surface area of the ISVF = 90, 95 and 98 percent (integral quantities) – flow time results for the 3D model of the novel sensor housing and the casing conveyed with four flow deflector fins (Type-III) located at 420 mm upstream of the sensor housing within the borehole section of 5.00 m length.

#### 7.3.3.3.4 Discussion

The zones of ISVF-90% at the end of the simulation were small and few; thus, the inadequate cement volume fraction with value of 0.98 was used to illustrate the locations and distribution of the poor quality cement zones (See Figure 7.41). The results presented in this section suggest that uniform thickness with trimmed edges fins distributed the ISVF regions in all of the quadrants of the borehole cross-section. Despite that, the flow deflection was not preserved through the entire model. As previously mentioned, to preserve the redirection of the annular flow a second set of flow deflector fins at the downstream of the sensor housing is required.



Isometric view Cross-section

Figure 7.41 Surface area of the ISVF = 90, 95 and 98 percent (integral quantities) – flow time results for the 3D model of the novel sensor housing and the casing conveyed with four flow deflector fins (Type-III) located at 420 mm upstream of the sensor housing within the borehole section of 5.00 m length. These snapshots show the annular distribution of ISVF with value of 0.98.

The selection of the cement slurry and spacer rheological properties, including their characterization, is part of a large scale design, execution and evaluation of a cement job [32], and it is not in the scope of this study. However is important to highlight that the rheological properties of the displaced fluids have a significant impact on the effectiveness of the fins on deflecting the annular flow. Figure 7.42 illustrates the different flow pattern induced by the flow deflector Type-III fins when the main annular fluid was fresh-water spacer and cement slurry at 0.407 s and 10.000 s, respectively. Through the entire model, the Newtonian fluid (spacer) was deflected on the same direction of the set of fins deviation. On the other hand, the non-Newtonian fluid (cement

slurry) was just deflected in the space between the set of fins and the sample port of the sensor housing. Once the cement slurry reached the body of the sensor housing the downstream annular flow was straightened back.

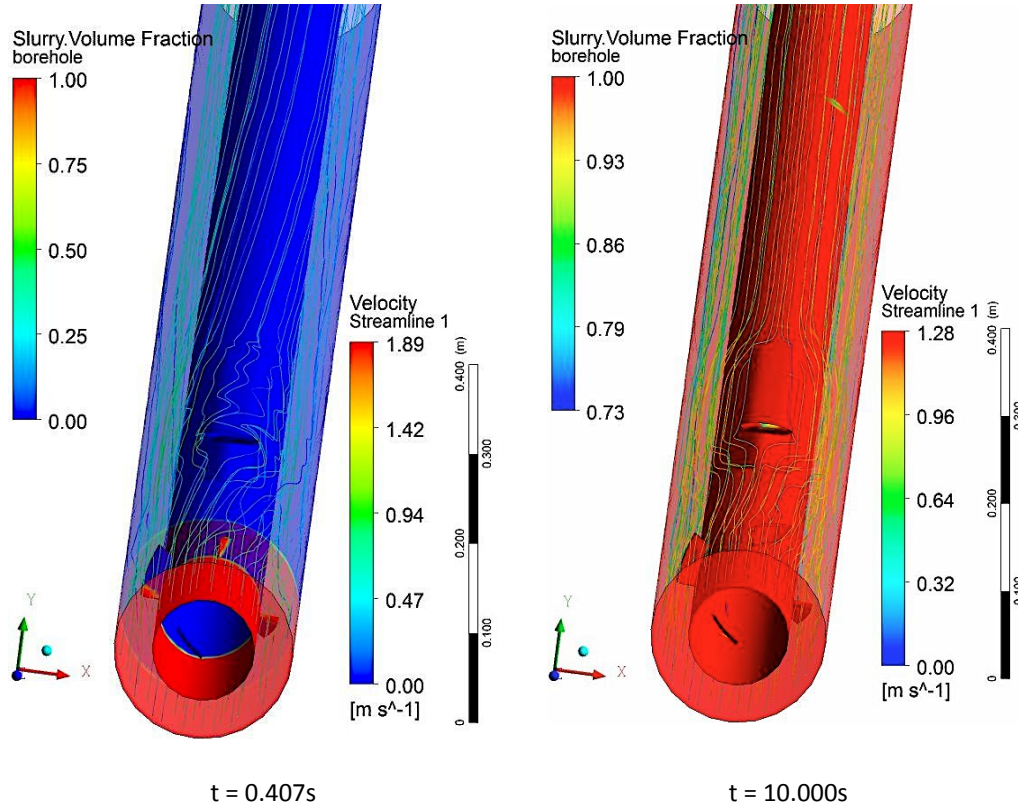


Figure 7.42 VOF simulation results for the 3D model of the novel sensor housing and the casing conveyed with four flow deflector fins (Type-III) located at 420 mm upstream of the sensor housing within the borehole section of 5.00 m length. Output at time  $t = 0.407$  and  $10.000$  s, while the cement slurry is displacing through the annulus. Each snapshot shows cement slurry volume fraction, ISVF = 0.90, and velocity streamlines.

The following section evaluates the effect of using taller fins on the downstream annular flow of the novel sensor housing system.

### 7.3.3.4 Type-IV fin

This section studies a model with fins with similar dimension to the previous model, but the clearance (11.8 mm) between the Type-IV fins and the borehole walls is 30% of the annular space (42.8 mm) between the casing and the borehole walls. This small clearance is acceptable for installations in vertical observation well, but for inclined wellbores the fins under these conditions could be dragged, get deformed or fallen apart, preventing further downward movement of casing during installation [32, 80]. To quantify this risk, additional structural analysis on the fins will be required for incline wellbores.

#### 7.3.3.4.1 Geometry and grid

Figure 7.43 and Figure 7.44 illustrate the 3D configuration and the side view of the model of this section. Because the main objective of this model focuses on the effect of the fin's height on the downstream flow of the sensor housing, the length of the model was 5.00 m.

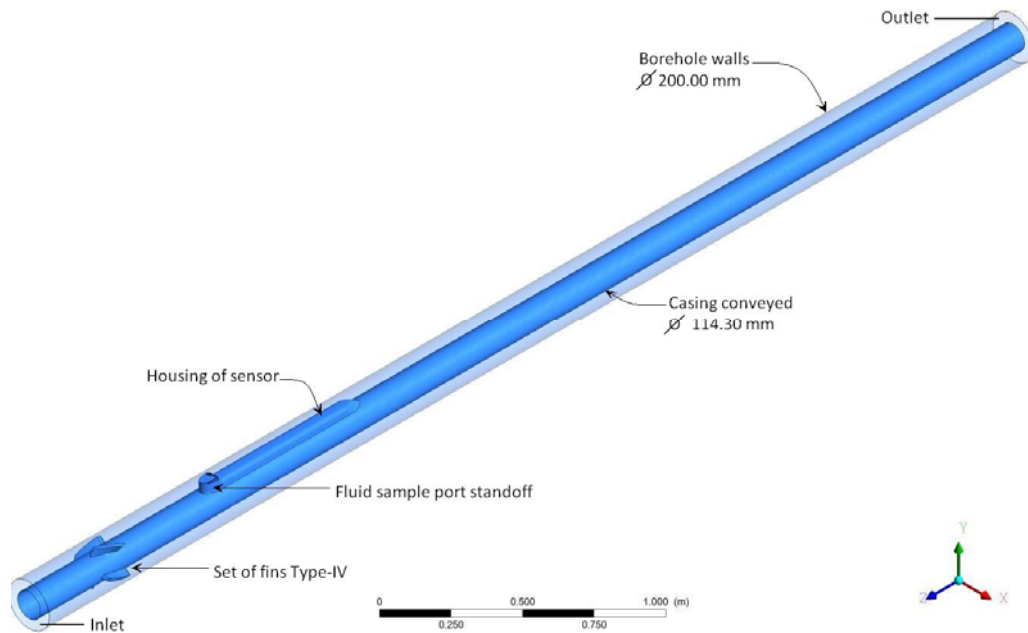
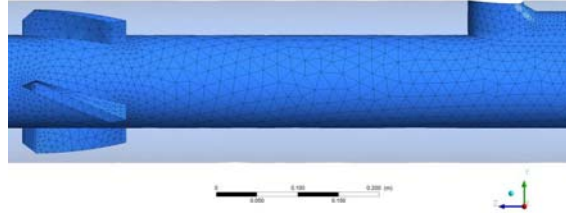


Figure 7.43 3D geometrical configuration of the low flow impedance sensor housing with four flow deflector fins (Type-IV) located at 420.0 mm from the fluid sample port standoff.



*Figure 7.44 Illustration of four upstream flow deflector fins (Type-IV) and the novel sensor housing.*

The height of each of the flow deflector fins of this model was approximately 70% (31.0 mm) of the annular space (42.8 mm) between the casing and the borehole walls. In order to compensate the reduction the fin's height, the length and the deflection angle of the Type-IV fin was increased two times from the Type-II fin, which was 42.8 mm height, with zero clearance.

The configurations of the flow deflector Type-IV fins used for this study are shown in Figure 7.45. Each fin had  $16^\circ$  of deviation from the vertical position and 11.5 mm width and a projection length of 127.0 mm.

The set of fins were located at a upstream distance of approximately three times the fin's length (420.0 mm) from the sensor housing sample port. Because the scope of this model focused on the flow mechanics assessment of the set of Type-IV fins, it was important to isolate the fins from possible boundary effects from the sensor housing geometry.

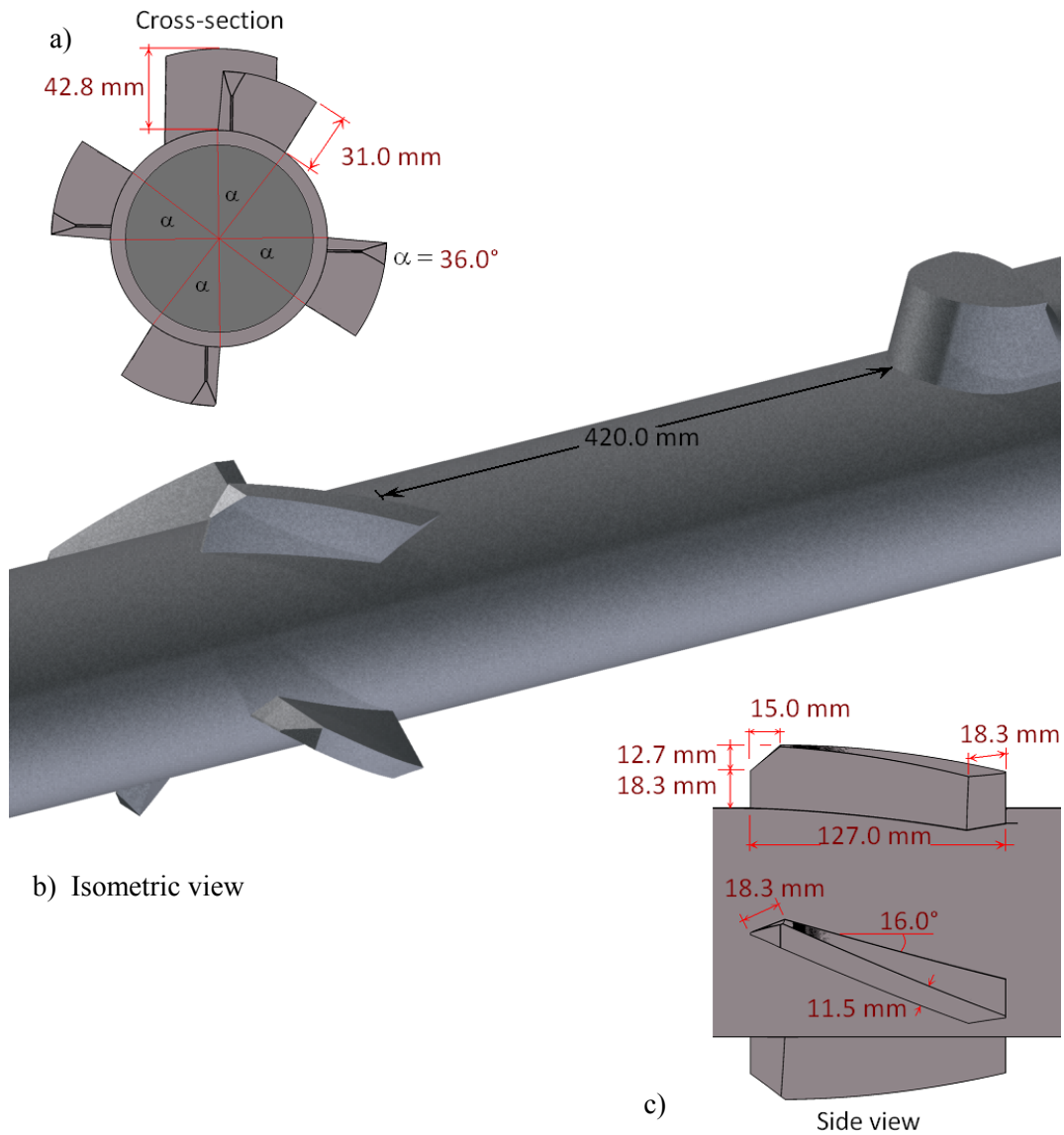


Figure 7.45 Sketch of: (a) the cross-section; (b) the isometric view; (c) and the side view of four flow deflector Type-IV fins located at 420.0 mm from the fluid sample port standoff.

A geometrical discretization of the 3D model was made for the CFD analysis. Unstructured tetrahedral cells were generated to define the model. A view of the generated grid can be seen in Figure 7.46.



Figure 7.46 Mesh for the 3D model of (a) the novel sensor housing system and the casing conveyed with four flow deflector fins (Type-IV) located at 420.0 mm upstream of sensor housing (b) within the 5.00 m of a borehole section.

#### 7.3.3.4.2 Numerical solution control

For the model with Type-IV fins, the time step used in the unsteady calculation was set to  $7.2 \times 10^{-4}$  s. A total of 10,000 s of flow time was simulated, requiring approximately 96 hours (4 days) of computation time. A mesh with 40,812 nodes and 190,844 elements was used on this analysis.

#### 7.3.3.4.3 Results

Figure 7.47 shows the simulation results of the unsteady displacement of cement displacing fresh-water spacer. The cement slurry volume fraction is presented in a color map format, of which the color “dark orange” corresponds to the iso-surface with cement slurry volume fraction with value of 0.90 (ISVF-90%).

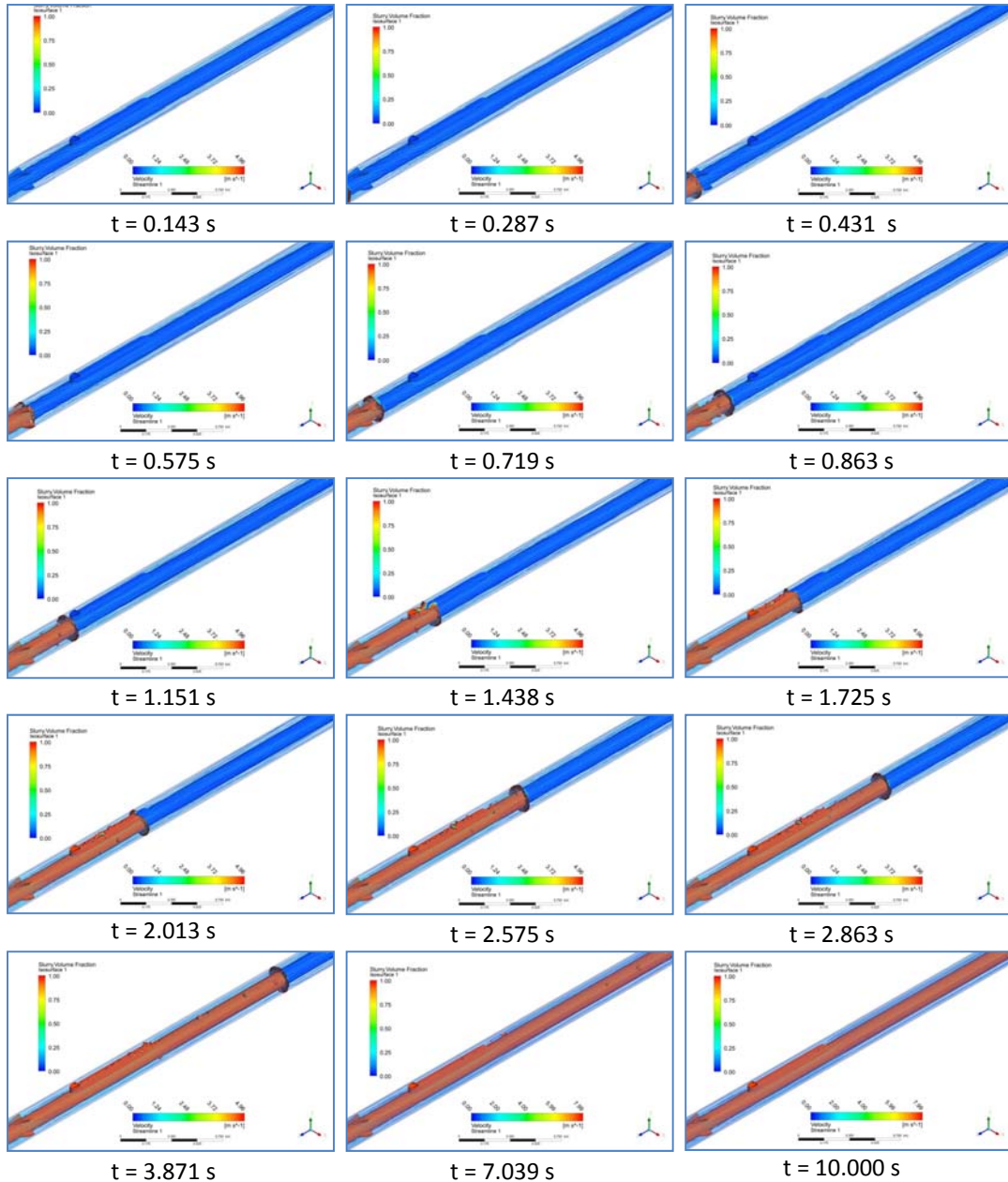


Figure 7.47 VOF simulation results for the 3D model of the novel sensor housing and the casing conveyed with four flow deflector fins (Type-IV) located at 420.0 mm upstream of the sensor housing within the borehole section of 5.00 m length. Output at time  $t = 0.143, 0.287, 0.431, 0.575, 0.719, 0.863, 1.151, 1.438, 1.725, 2.013, 2.575, 2.863, 3.871, 7.039$  and  $10.000$  s, while the cement slurry is displacing through the annulus. Each snapshot shows cement slurry volume fraction, ISVF = 0.90, and velocity streamlines.

Throughout the entire simulation, it was observed that the cement phase displaced most of the water-spacer phase. These series of figures also show that the Type-IV fins were mildly deflecting the downstream annular flow. The results suggest that the fins were not tall enough to deflect the viscous cement slurry phase through the sensor housing body. This confirms the need of a second set of flow deflector fins at the downstream of the sensor housing.

The time for the water-spacer to be displaced by the cement slurry from the inlet to the outlet was 6.607 s, but the simulation time ran until the integral quantity stabilized at 10.000 s.

Figure 7.48 shows the evolution of the integral quantity through the entire circulation period of 10.000 s. The first peak area value of the iso-surface with volume fraction with value of 0.90 (ISVF-90%) was  $0.032 \text{ m}^2$ , and it was reached at 0.431 s when the cement slurry front was passing through the set of Type-IV fins. Then, the integral quantity followed a reduction trend until the cement slurry front reached the fluid sample standoff. At 1.007 s, the values of ISVF-90% started to increase until the second peak value of  $0.044 \text{ m}^2$  occurred at 2.287 s. The first peak value was lower than the second peak value.

The post-peak values of the integral quantity ISVF-90% showed a reduction trend until the cement front reached the outlet at 6.607 s, then this trend was followed by a significant drop of the ISVF values reaching a stabilized residual value of  $1.61 \times 10^{-3} \text{ m}^2$  at 10.000 s.

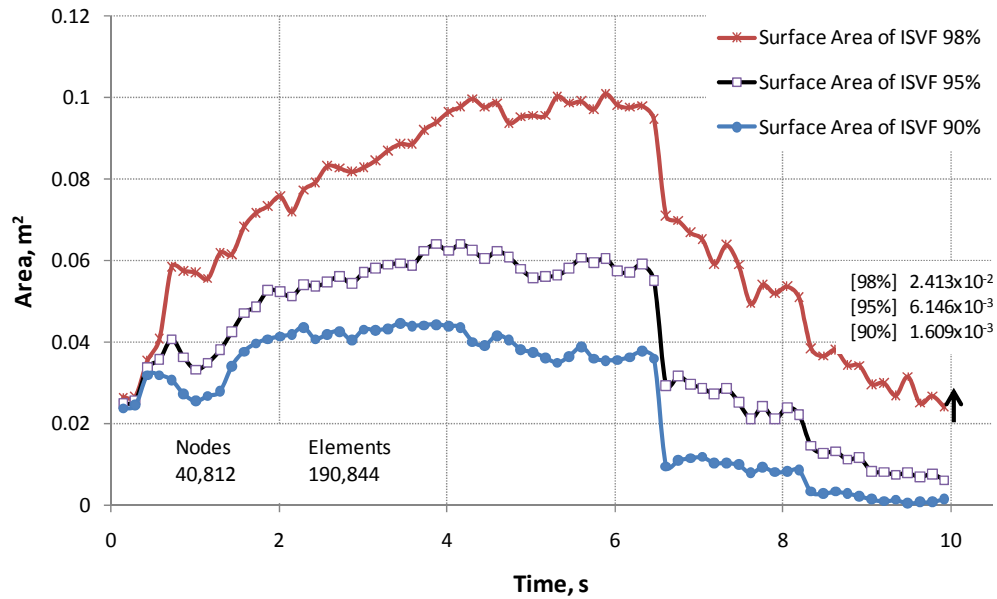
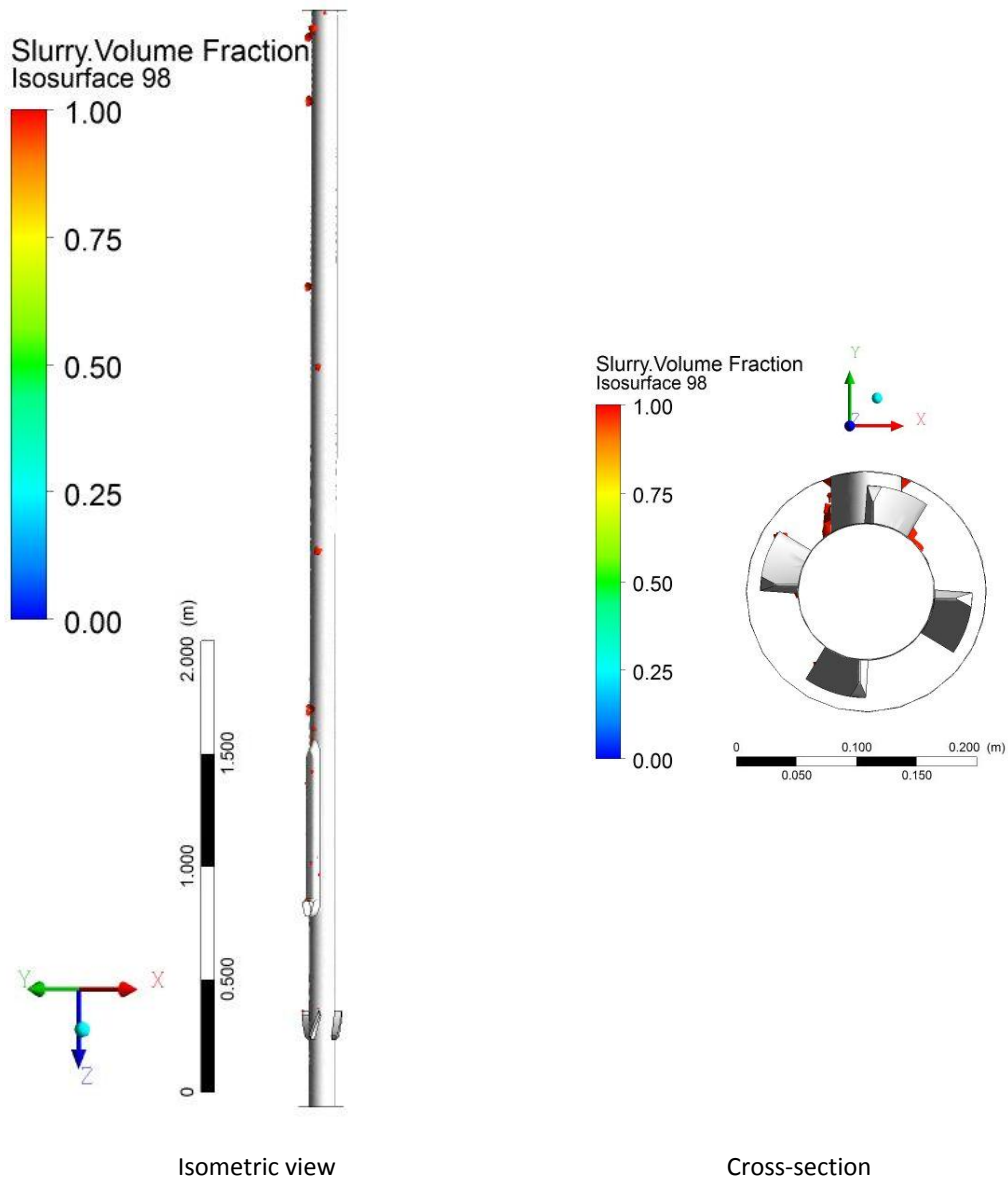


Figure 7.48 Surface area of the ISVF = 90, 95 and 98 percent (integral quantities) – flow time results for the 3D model of the novel sensor housing and the casing conveyed with four flow deflector fins (Type-IV) located at 420.0 mm upstream of the sensor housing within the borehole section of 5.00 m length.

#### 7.3.3.4.4 Discussion

The zones of ISVF-90% at the end of the simulation were small and few; thus, the inadequate cement volume fraction with value of 0.98 was used to illustrate the locations and distribution of the poor quality cement zones (See Figure 7.49). The results presented in this section suggest that uniform thickness with trimmed edges fins, like The Type-IV fins, distributed the ISVF regions in all of the quadrants of the borehole cross-section. Despite that, the flow deflection was not preserved through the entire model. To preserve the redirection of the annular flow a second set of flow deflector fins at the downstream of the sensor housing is required.



Isometric view Cross-section

*Figure 7.49 VOF simulation results for the 3D model of the novel sensor housing and the casing conveyed with four flow deflector fins (Type-IV) located at 420.0 mm upstream of the sensor housing within the borehole section of 2.50 m length. Output at time  $t=4.00$  s, while the cement slurry is displacing through the annulus. These snapshots show the annular distribution of the ISVF with value of 0.98.*

Figure 7.50 illustrates the different flow pattern induced by the flow deflector fins when the main annular fluid was fresh-water spacer and cement slurry at 0.407 s and 10.000 s, respectively. Through the entire model, the Newtonian fluid (spacer) was deflected in the same direction of the set of fins deviation. On the other hand, the non-Newtonian fluid (cement slurry) was just deflected in the space between the set of fins and the fluid

sample port standoff. Once the cement slurry front reached the body of the sensor housing the downstream annular flow was straighten back.

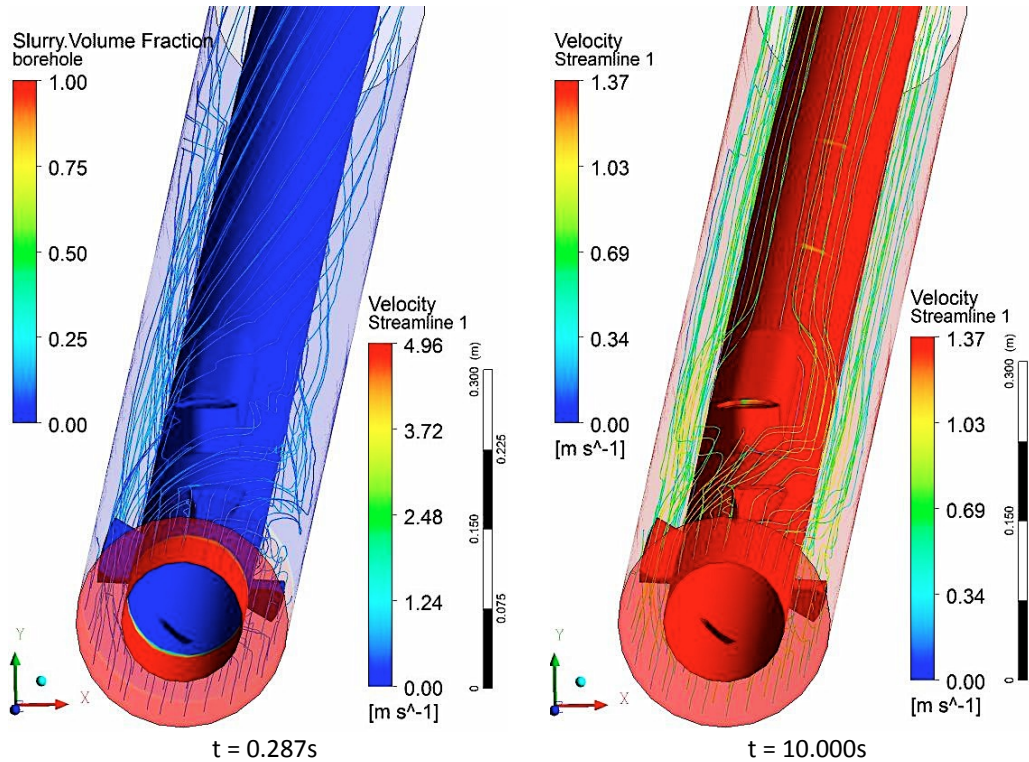


Figure 7.50 VOF simulation results for the 3D model of the novel sensor housing and the casing conveyed with four flow deflector fins (Type-IV) located at 420.0 mm of upstream of the sensor housing within the borehole section of 5.00 m length. Output at time  $t = 0.287$  and  $10.00$  s, while the cement slurry is displacing through the annulus. Each snapshot shows cement slurry volume fraction,  $ISVF = 0.90$ , and velocity streamlines.

These results suggest that the optimal set of Type-IV fins induce a short annular flow deflection on the cement slurry phase. In order to maximize annular deflection into the sensor housing body, this set of fins could be placed closer to the sensor housing body and rotated, so the tail edge of one fin matches the downstream fluid sample port standoff. This rotation could help to enforce the direction of the annular flow. To confirm the effectiveness of these modifications a quick steady state simulation was conducted. Figure 7.51 presents the results of the velocity streamlines of the main model of this section and the modified model. These results verify that placing the set of fins closer to the sensor housing streamlines help to deflect flow on top of the sensor housing body; thus, enhancing the distribution of poor quality cement in the annular space.

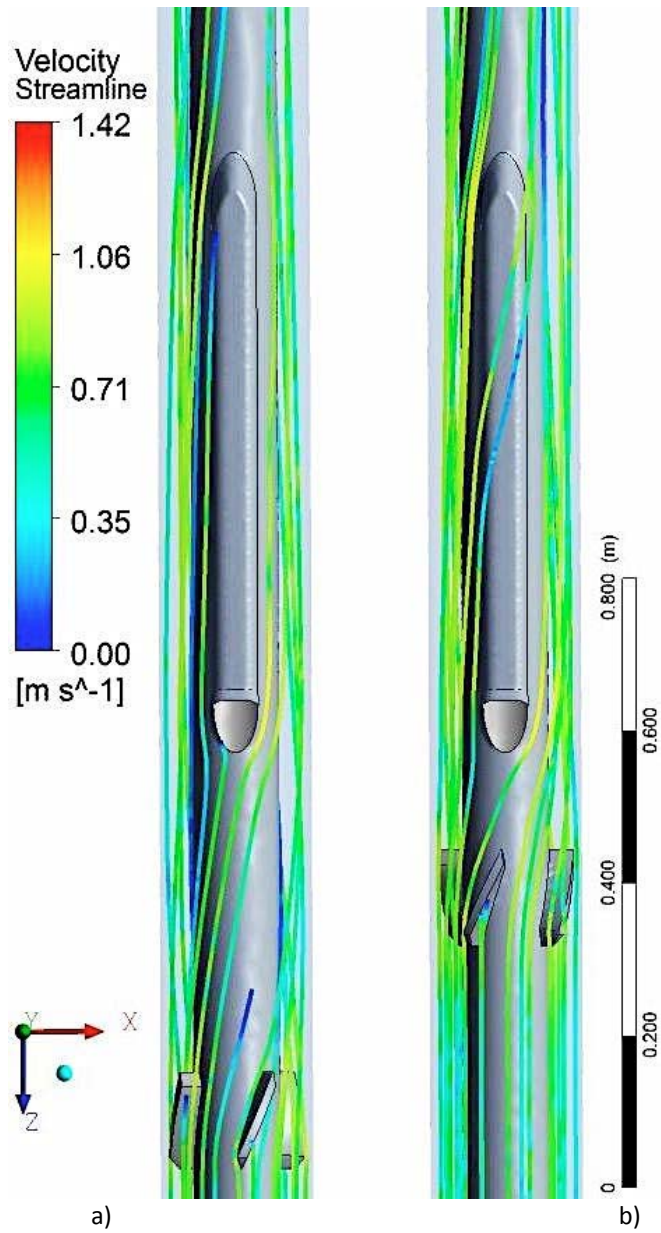


Figure 7.51 VOF steady state simulation results for the 3D model of the novel sensor housing and the casing conveyed with four flow deflector fins (Type-IV) located: (a) at 420.0 mm and (b) 127.0 mm from the upstream of the sensor housing within the borehole section of 5.00 m length. Each snapshot shows the velocity streamlines.

#### **7.3.4 Summary and Conclusion on Deflector Fin Designs**

This section studied geometrical configuration of four different types flow deflector fins for the novel sensor housing with CFD techniques. The optimal geometrical configuration from all four types of fins was found in Type-IV fin. The set of four Type-IV fins should be located at the one fin's length distance from the sensor housing to obtain better flow deflection on the top face of the novel sensor housing. While the results from the simulator have proven the applicability of CFD techniques on these settings, substantial refining of the simulation grid will be required in any future pre-design phase of downhole sensor housing installations.

From the fluid mechanics perspective, the appropriate geometrical configuration of the fin is unique for the boundary conditions, dimension of the annular space and fluid properties (i.e., rheology). The computational effort presented in this section show how CFD techniques can be used to assist on the design phase of complex downhole sensor housing configurations where more attention is required. For future applications in the pre-design phase of sensor housing systems, the Type-IV fin represents a generic shape that can be re-assessed with additional CFD modeling.

To ensure good flow deflection in the downstream of the sensor housing, the optimal set of fins selected from this section should be installed at the downstream and upstream of the novel sensor housing system. The following section studies a CFD model with this new configuration.

## **7.4 Analysis of sensor housing and flow deflector fins geometry/configuration**

The final phase of the modelling effort of this chapter, which attempts to provide an improved understanding of the annular flow within a borehole with complex sensor housing geometries, utilizes the results of previous model to assess the novel sensor housing and flow deflector fins geometry and configuration for the outside casing conveyed sensor housing system.

The previous two sections assessed the optimum geometrical configuration of the novel sensor housing and the set of fins via CFD modelling techniques. The results suggest that a upstream and downstream set of fins are required to distribute the poor quality cement zones on the four quadrant of the borehole cross-section. Both sets of Type-IV fins should be located at one fin's length distance from the sensor housing. The scope of this section is to assess the annular flow behaviour of a borehole section with this configuration during the cement displacement.

### **7.4.1 Geometry and grid**

Figure 7.52 illustrates the 3D configuration of the model of this section.

The height of each of the flow deflector fins of this model was approximately 70% (31.0 mm) of the annular space (42.8 mm) between the casing and the borehole walls. The configurations of flow deflector fins used for this study are shown in Figure 7.53. Each fin had 18 ° of deviation from the vertical position, 11.5 mm width and a projection length of 127.0 mm.

The two sets of fins were located at the upstream and downstream of the sensor housing at distance of one time the fin's length (127.0 mm).

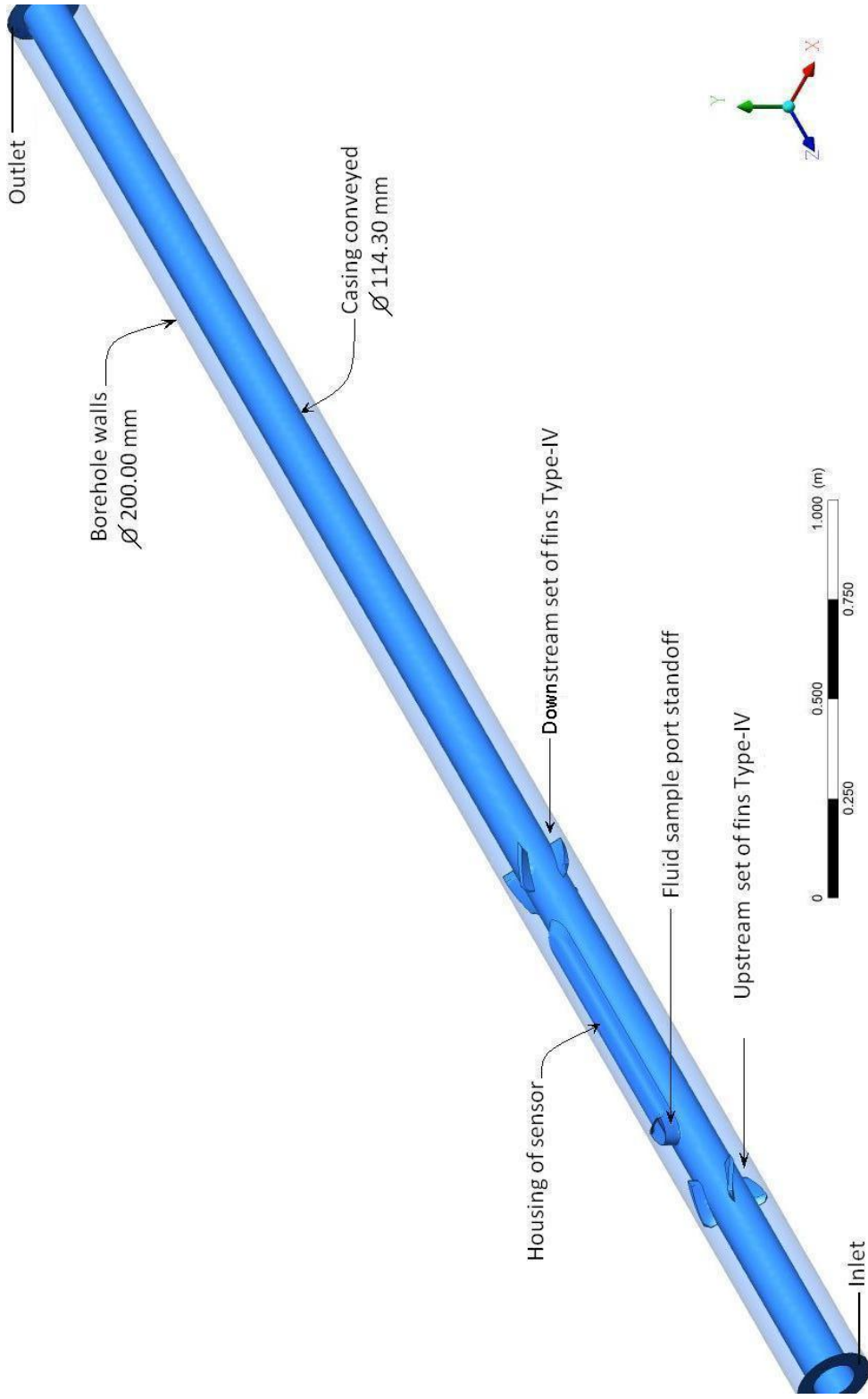


Figure 7.52 3D geometrical configuration of the low flow impedance sensor housing with two sets of four flow deflector fins (Type-IV) located at 127.0 mm down- and up- stream of the sensor housing.

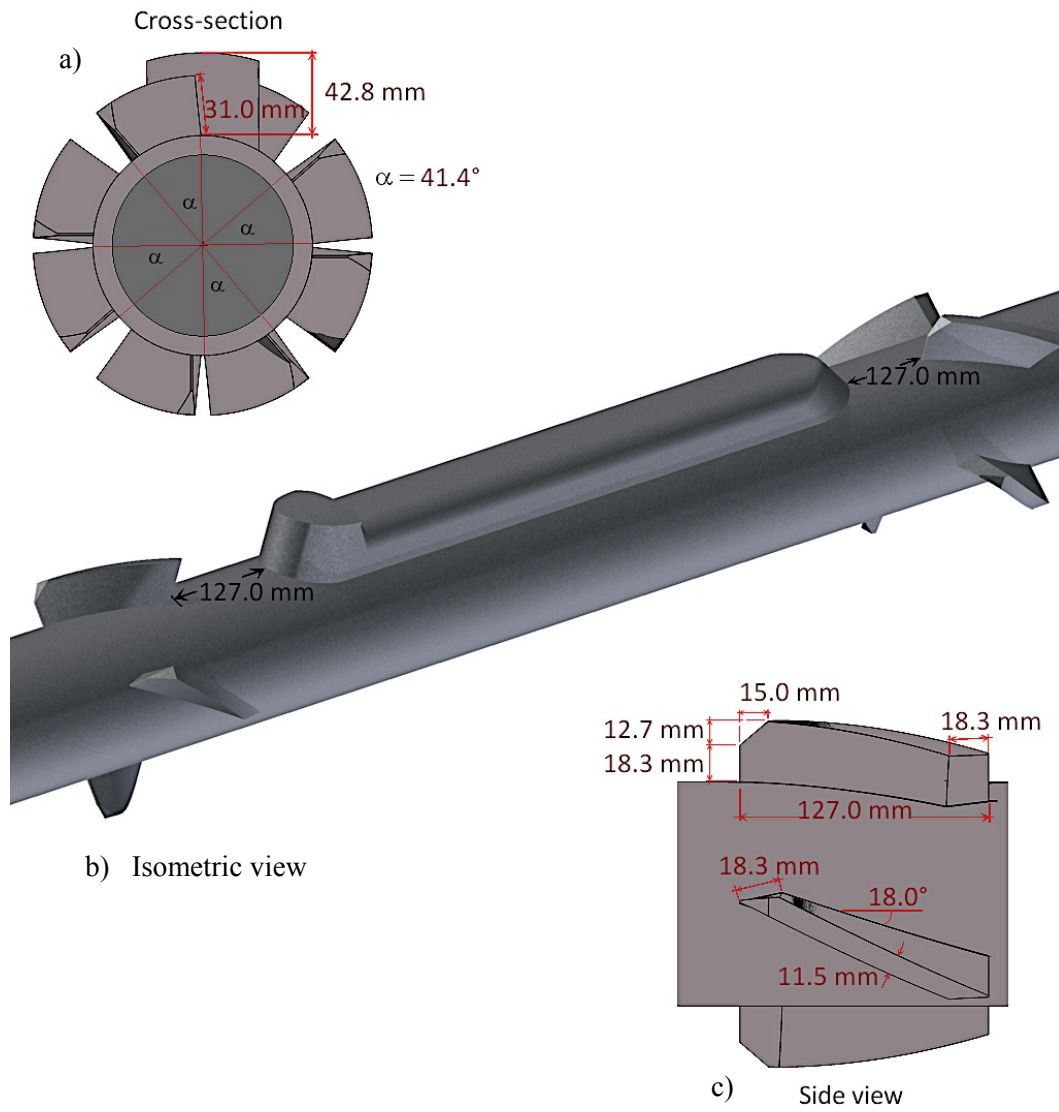


Figure 7.53 Sketch of: (a) the cross-section; (b) the isometric view; (c) and the side view of two set of four flow deflector Type-IV fins located at 127.0 mm from the fluid sample port standoff.

A geometrical discretization of the 3D model was made for the CFD analysis. Unstructured tetrahedral cells were generated to define the model. A view of the generated grid can be seen in Figure 7.54.



Figure 7.54 Mesh for the 3D model of (a) the novel sensor housing system and the casing conveyed with two sets of four flow deflector fins (Type-IV) each located at 127.0 mm down and up stream of sensor housing (b) within the 5.00 m of a borehole section.

#### 7.4.2 Numerical solution control

The time step used in the unsteady calculation was set to  $6.2 \times 10^{-4}$  s. A total of 10.00 s of flow time was simulated, requiring approximately 96 hours (4 days) of computation time. A mesh with 50,394 nodes and 240,209 elements was used on this analysis.

### 7.4.3 Results

Figure 7.55 shows the simulation results of the unsteady displacement of cement displacing fresh-water spacer. The cement slurry volume fraction is presented in a color map format, of which the color “dark orange” corresponds to the iso-surface with cement slurry volume fraction with value of 0.90 (ISVF-90%).

Throughout the whole simulation, it was observed that the cement phase displaced most of the water-spacer phase. These series of figures also show that the tow set of fins were deflecting the upstream and downstream annular flow near the sensor housing.

The fresh-water spacer was circulated mainly to prevent commingling with earlier circulated fluid (i.e., mud or brine) and to remove the film of mud at the formation walls [32]. At 0.719 s of circulation, the borehole section was mainly dominated by the fresh-water spacer fluid which was deflected up to  $18^\circ$  from a vertical position by the downstream and upstream sets of fins, increasing the flow path trajectory and contact time of the spacer fluid with the annular walls near the sensor housing; thus, the cleaning and cement-walls bonding during circulation was enhanced. This initial phase of the cement circulations was important for the final objective of the novel sensor housing system of enhancing cement displacement and reducing the risk of developing a micro-annulus path between near monitoring points or to the surface.

The cement slurry front passed the first set of flow deflector fins at 0.959 s with an homogeneous displacement front, but soon after passing the fluid sample standoff at 1.319 s of circulation some fingers and small ISVF pockets were develop and left behind the cement slurry front. Figure 7.55 also shows the time period (1.439 s to 2.020 s) when the cement slurry front was passing through the sensor housing body. The streamlines revealed that the high viscous cement slurry phase was displacing parallel to the sensor housing; thus, the ISVF pockets developed at the standoff were displaced downstream in the same quadrant that the sensor housing body was located.

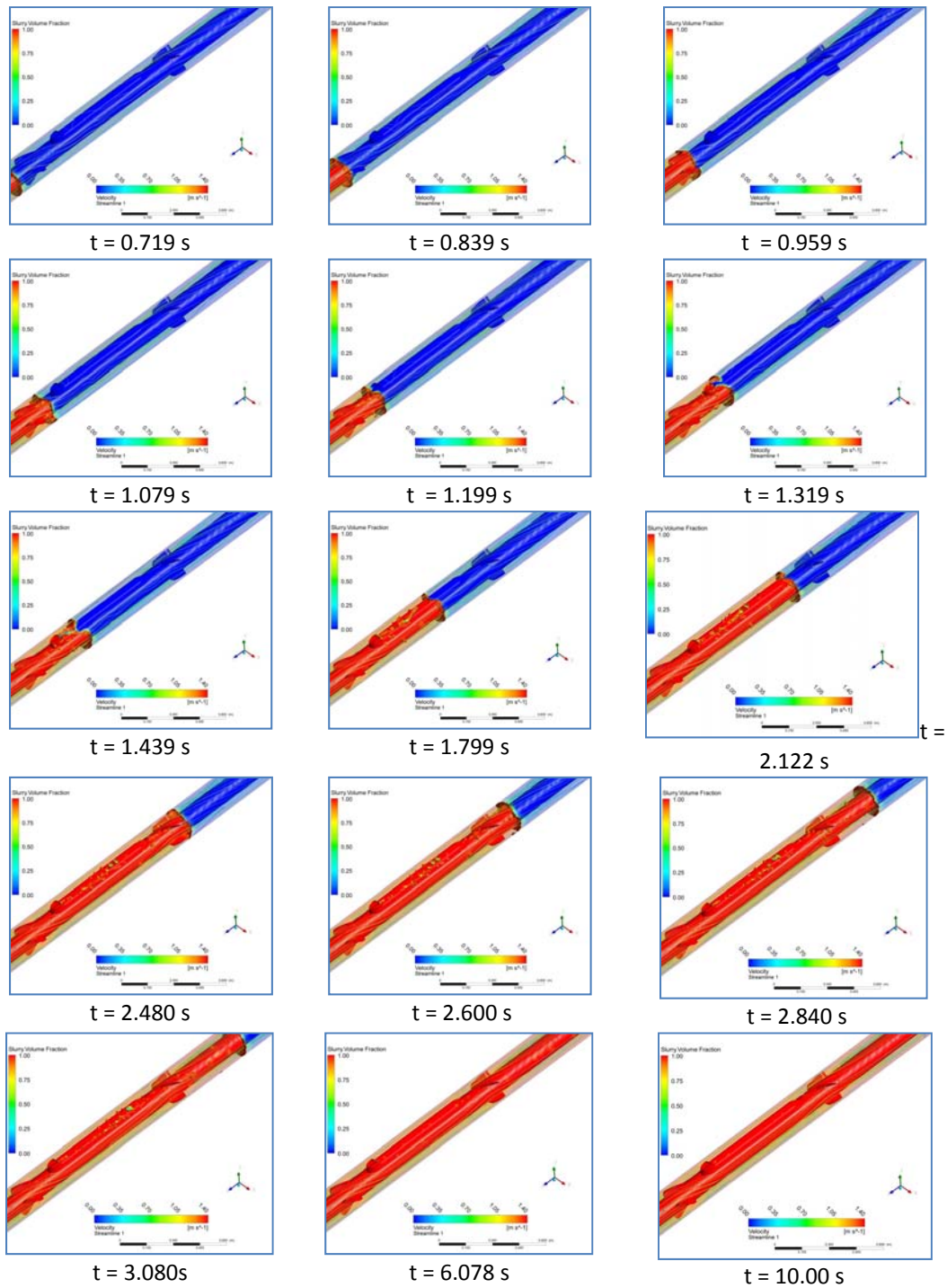


Figure 7.55 VOF simulation results for the 3D model of the novel sensor housing and the casing conveyed with two sets of four flow deflector fins (Type-IV) each located at 127.0 mm of the down- and up- stream of the sensor housing within the borehole section of 5.00 m length. Output at time  $t = 0.719, 0.839, 0.959, 1.079, 1.199, 1.319, 1.439, 1.799, 2.122, 2.480, 2.600, 2.840, 3.080, 6.078, 10.000$  s, while the cement slurry is displacing through the annulus. Each snapshot shows cement slurry volume fraction, ISVF = 0.90, and velocity streamlines.

Figure 7.55 also illustrates the time period when the cement slurry front was passing through the second set of flow deflector fins. The cement front stabilized after passing the downstream end of the sensor housing at 2.122 s of circulation. This homogeneous front passed through the second set of fins at 2.480 s, deflecting the streamlines of the cement slurry phase at 18° from the vertical position. At 2.600 s of cement displacement, the homogeneous displacement front trajectory became approximately parallel to the borehole axis.

The inadequate cement slurry volume fraction pockets resulted from the standoff flow impedance were left behind the displacement front. The distance between the displacement front and the ISVF pockets was increasing every time step. This means that velocity gradients above the sensor housing were significantly lower than the displacement front. Without the second set of fins located downstream the sensor housing these poor quality cement zones could be displaced downstream on the same quadrant where the sensor housing was located, increasing the risk of hydraulic communication between a near sensor. However, the results of this model suggest that the second set of fins deflected these ISVF zones to a different quadrant; thus, the same quantity of ISVF regions were distributed in entire downstream annular space, reducing the risk of hydraulic communication between the ISVF regions.

The results suggest that the two sets of fins could enhance the cleaning and the distribution of the ISVF zones. Additional simulation results of the unsteady displacement of cement displacing fresh-water spacer from a different angle and grey color map format are presented in Appendix D.

Figure 7.56 shows the evolution of the integral quantity through the entire circulation period of 10.000 s. The peak area value of the iso-surface with volume fraction with value of 0.90 (ISVF-90%) was 0.059 m<sup>2</sup>, and it was reached at 2.480 s when the cement slurry front was passing through the downstream set of fins. The post-peak values of the integral quantity ISVF-90% showed a reduction trend until the cement front reached the outlet at 6.438 s, then this trend was followed by a significant drop of the ISVF values reaching a stabilized residual value of 8.88x10<sup>-4</sup> m<sup>2</sup> at 10.000 s.

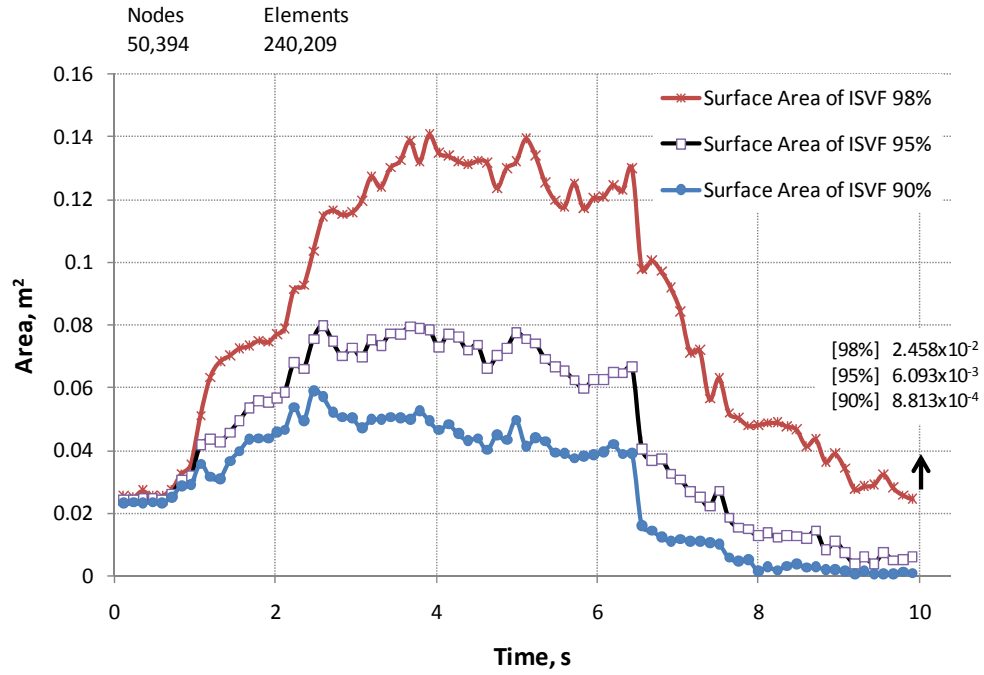


Figure 7.56 Surface area of the ISVF = 90, 95 and 98 percent (integral quantities) – flow time results for the 3D model of the novel sensor housing and the casing conveyed with two sets of four flow deflector fins (Type-IV) each located at 127.0 mm from the down- and up- stream of the sensor housing within the borehole section of 5.00 m length.

#### 7.4.4 Discussion

Because the zones of ISVF-90% at the end of the simulation were small and few, the inadequate cement volume fraction with value of 0.98 was used to illustrate the locations and distribution of the poor quality cement zones (Figure 7.57). The results presented in this section suggest that the two set of fins distributed the ISVF regions in all of the quadrants of the borehole cross-section. To preserve the redirection of the annular flow the second set of flow deflector fins was integrated at the downstream of the sensor housing

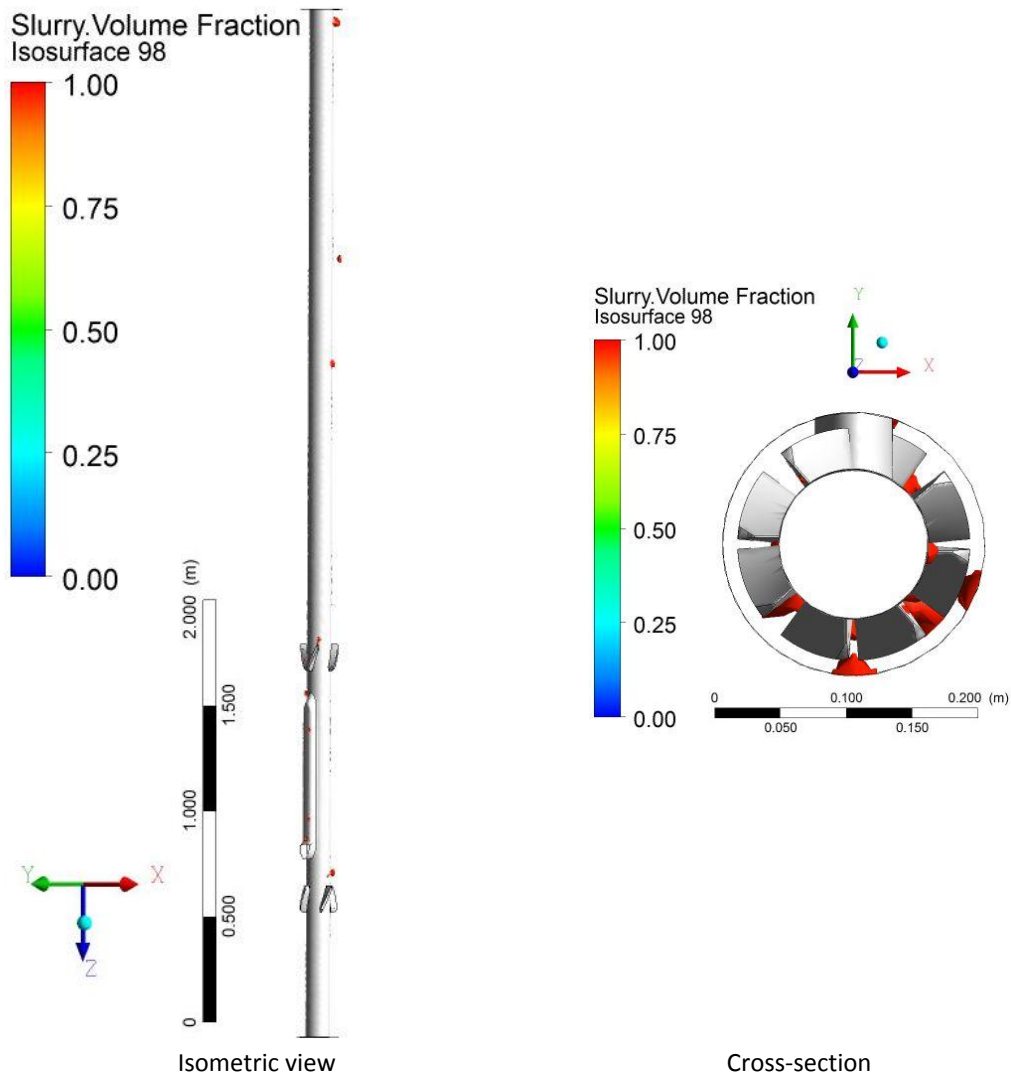


Figure 7.57 VOF simulation results for the 3D model of the novel sensor housing and the casing conveyed with two sets of four flow deflector fins (Type-IV) each located at 127.0 mm from the down- and up- stream of the sensor housing within the borehole section of 5.00 m length. Output at time  $t = 10.00$  s, while the cement slurry is displacing through the annulus. These snapshots show the annular distribution of the ISVF with value of 0.98.

Figure 7.58 illustrates the different flow pattern induced by the flow deflector Type-IV fins when the main annular fluid was fresh-water spacer and cement slurry at 0.839 s and 10.000 s, respectively. The Newtonian fluid (fresh-water spacer) was deflected on the same direction that the set of fins through the entire model.

On the other hand, the non-Newtonian fluid (cement slurry) was just deflected in two locations: (a) in the space between the first set of fins and the fluid sample port standoff; and (b) at the downstream of the second set of flow deflector fins. Both annular flow deflections of the cement slurry phase had a short trajectory before the streamlines of the highly viscous cement slurry were realigned to the vertical position.

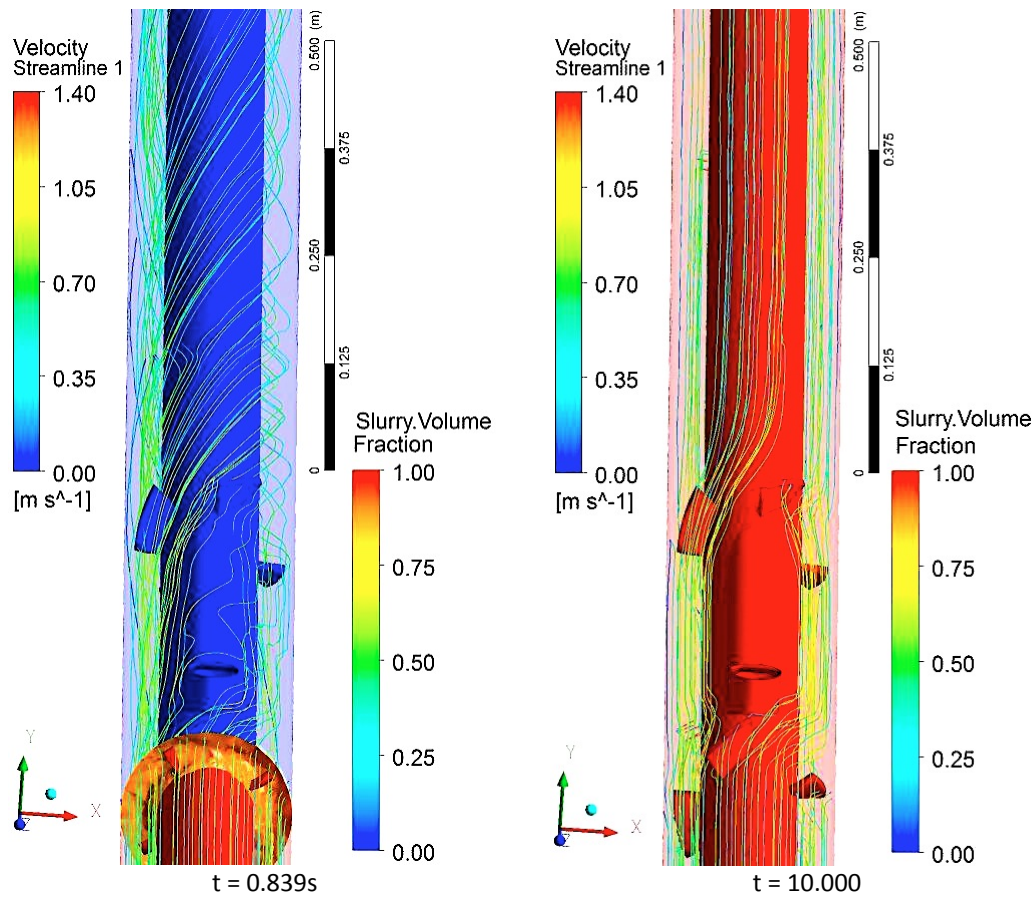


Figure 7.58 VOF simulation results for the 3D model of the novel sensor housing and the casing conveyed with two sets of four flow deflector fins (Type-IV) each located at 127.0 mm from the down and up stream of sensor housing within the borehole section of 5.00 m length. Output at time  $t = 0.839$  and  $10.000$  s, while the cement slurry is displacing through the annulus. Each snapshot shows cement slurry volume fraction,  $ISVF = 0.90$ , and velocity streamlines.

The scope of this research did not include fluid rheological or cement slurry design because these are part of a large-scale well cement design. However, it is important to highlight that the efficiency of the optimal flow deflector fins and novel sensor housing

are impacted by the rheological properties of the circulated fluids. Figure 7.59 illustrates the relationship between the shear rate and shear strength ( $\tau$ ) that define the rheological properties of the fluids used in the model of this section, previously mentioned. The shear strength properties of the cement slurry are two orders of magnitude higher than the fresh-water spacer, resulting in different annular flow behavior in the borehole conditions of the models. An example of this is presented in Figure 7.60, where two different velocity profiles resulted at 0.120 s and 9.798 s when the fresh-water spacer and cement slurry fluids were pacing at the same sampling plane, respectively.

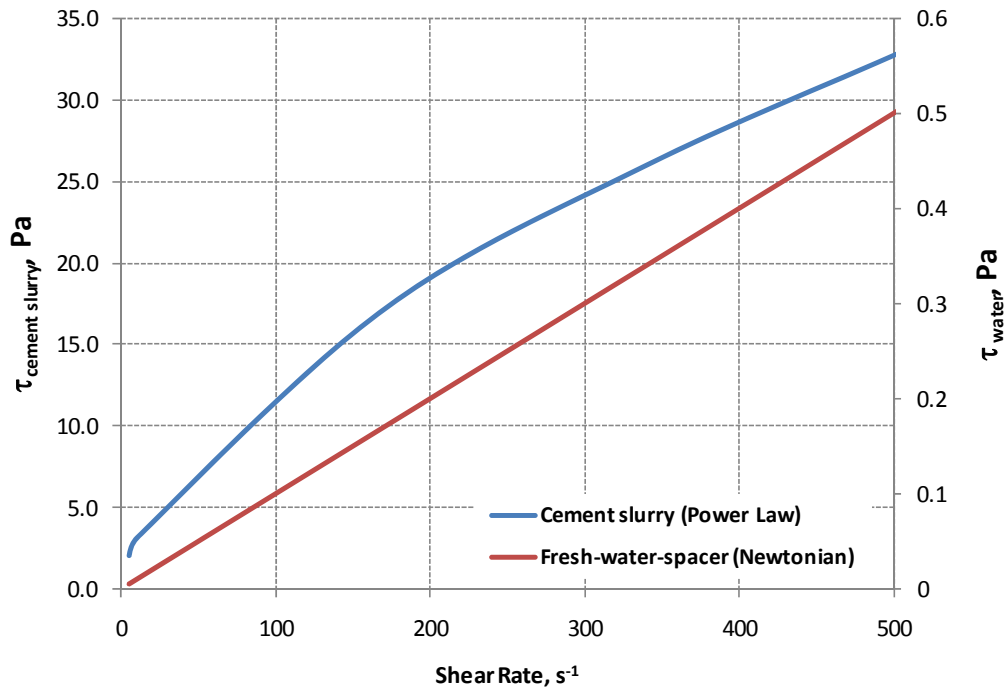
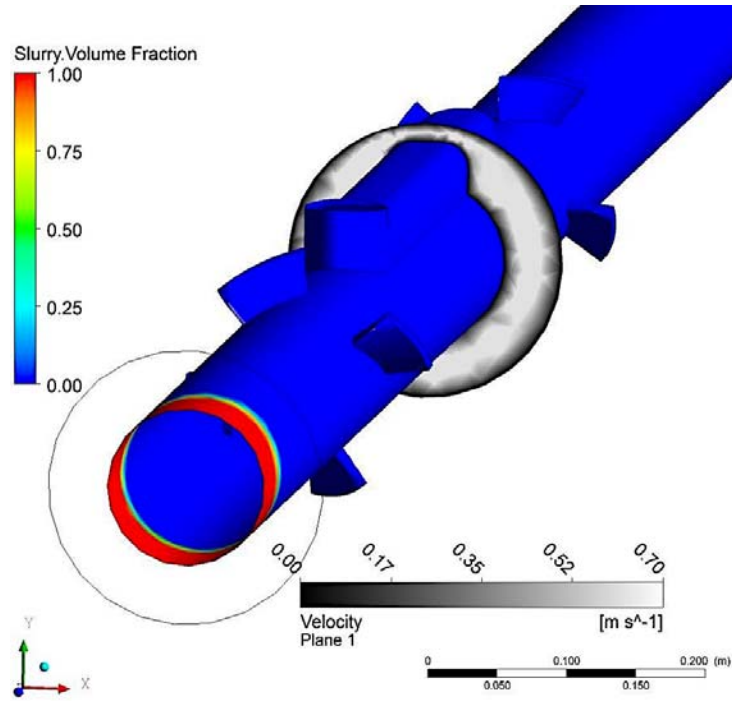
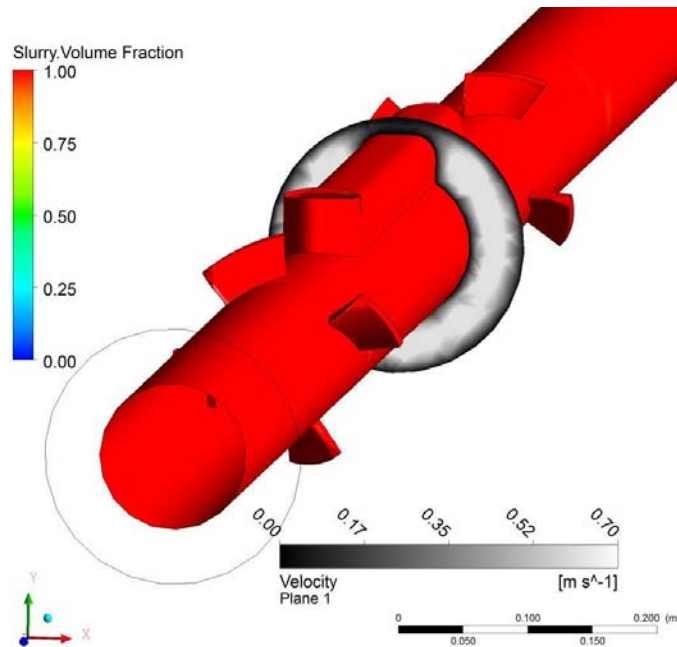


Figure 7.59 Rheological properties of cement slurry and fresh-water spacer fluids.



t = 0.120s



t = 9.798s

Figure 7.60 VOF simulation results for the 3D model of the novel sensor housing and the casing conveyed with two sets of four flow deflector fins (Type-IV) each located at 127.0 mm of down and up stream of sensor housing within the borehole section of 5.00 m length. Output at time  $t = 0.120$  and  $9.798$  s, while the cement slurry is displacing through the annulus. Each snapshot shows cement slurry volume fraction and the velocity profile of a sampling plane in grey color map.

The reduction of annular space affects the cement displacement efficiency. There are several analytical studies that can assess these conditions when long sections (global scale) of tubing/casing are placed eccentric into the borehole, resulting in the reduction of annular space and affecting the cement displacement efficiency [61, 62, 81, 82]. However these analytical techniques cannot be used to assess annular flow behavior with complex geometrical configurations.

Integrated observation wells are important components for the direct measurements of the MMV activities for CO<sub>2</sub> geological storage, and they are comprised of multiple sensors at the containment and the burden levels. The sensor housing systems of these observations wells could induce a local reduction of annular space in short section of the borehole, and computation fluid dynamic techniques provide a better prediction of the annular flow behaviour under these complex borehole configurations. Without this computational effort the sensor housing system configuration could increase the risk of the development of micro-annulus paths that could hydraulically connect multiple monitoring depths, affecting the direct “in-situ” measurements of the Formation. Based on the results of the design simulations, a patent application was submitted for the final design and the technology has been licensed to Opsens. The Opsens Zero-Vortex-Gauge (ZVG) system could restore cement homogeneity around downhole sensor housings and mitigates the formation of a micro-annulus path alongside the sensor cables that run to the surface. Extensive computational fluid dynamics modelling and design has resulted in a field-proven system that greatly reduces the risk of inter-zonal fluid communication, resulting in independent and fully isolated sensors that determine more accurately, in-situ pressure and temperature measurements [83]. Copy of the filed patent is presented in Appendix D.

## **7.5 Conclusions**

The observation wells required for MMV activities for CO<sub>2</sub> geological storage are comprised of permanent multiple-instrument strings with complex wellbore configurations. The annular multi-phase flow behaviour in particular the cement slurry phase circulation through this complex wellbore configurations are not well understand, advancements in numerical simulations help to increase the understanding of multi-phase flow around downhole sensor housing systems. The chapter illustrates how CFD techniques could be used to assess the flow mechanics efficiency of the sensor housing geometries within a borehole during cement placement.

The results of this detailed wellbore numerical modeling were used to enhance the planning and operations of cement placement around deep downhole monitoring sensor housing systems and to identify difficulties of cement placement. As an outcome of this study, a new outside casing conveyed low flow impedance sensor housing system and method was developed and patented.

## **CHAPTER 8 Conclusions and Recommendations**

### **8.1 Summary**

The province of Alberta is committed to developing its oil and gas resources situated in the Alberta Basin in a responsible manner to minimize impacts on the environment. One of the major platforms for reducing carbon dioxide (CO<sub>2</sub>) emissions from large point sources is carbon capture and geological storage (CCS). Early carbon storage research and development efforts in Canada and elsewhere began with “value-added” projects such as CO<sub>2</sub>-enhanced oil recovery (EOR) or CO<sub>2</sub> enhanced coalbed methane (ECBM), where the increase in production helps to offset the cost of CO<sub>2</sub> and of its potential long-term storage. These projects provide a valuable opportunity to assess appropriate measurement, monitoring and verification (MMV) protocols for the geological storage component of CCS technologies. MMV operations provide confidence that CO<sub>2</sub> has been injected and stored in an environmentally sound and safe manner. Multiple integrated monitoring instrumentation systems are being deployed in CO<sub>2</sub> field demonstration research projects around the world and will provide experience that can be used in regulatory regimes for future commercial CO<sub>2</sub> sequestration scale projects.

This dissertation focus on the design, deployment and assessment of performance and hydraulic integrity of a sophisticated multi-instrument string deployed in an observation well and a surface tiltmeter array, a near surface monitoring, technologies used in two CO<sub>2</sub> geological storage pilot projects.

#### **8.1.1 Observation well**

The Pembina field was chosen from several fields within Alberta, Canada, for a geological carbon dioxide (CO<sub>2</sub>) storage pilot study, in which the injection of CO<sub>2</sub> was combined with enhanced oil recovery (EOR). As part of the project, an existing wellbore within the study area was used as a dedicated observation well. The design and initial results during cementing of this observation well were reviewed. The experience of implementing monitoring technologies was analyzed in order to assess existing knowledge for deploying downhole instrumentation used for monitoring and verification of CO<sub>2</sub> movements in the subsurface. Analysis indicates that the observation well allows direct monitoring and measurements at reservoir level of multiple variables through geophysical, geochemical, and geomechanical instrumentation, as well as the opportunity

to carry out wellbore integrity studies under "in-situ" conditions. A post-cement job and completion analysis that couples downhole measurements, analytical and numerical simulation was conducted to improve future installations. Downhole pressure gauges captured the dynamics of cement displacement and were key elements during post-cement job review and assessments of future well integrity.

The deployment of the instrumentation in the monitoring well was successful, although the cement job failed with constant leakage of reservoir fluid occurring afterwards – a micro-annulus path was developed within the 400 m of the cement column. The problem was solved by punching a hole in the tubing and injecting a dense brine. However, during this process four pressure sensors and two temperature sensors were lost and geophone cables were damaged.

During the post-cement job review the native fluid invasion event was confirmed with the recorded downhole pressure and temperature measurement. Sensor bodies used to diagnose cement displacement do not have a large effect on the pressure response during cement circulation. Density, volumes, and flow rate have a large impact on circulation pressures.

There were two events that lead to the development of micro-annulus path at the OW : (1) the native fluid invasion that contaminated the fresh-water spacer and cement slurry during circulation; and (2) the inadequate flow design of the downhole components of the OW. It was not possible to determine which event had a larger influence on the development of the micro-annulus in the OW because the inside annular space of the production tubing was also cemented, limiting the post-diagnostic of the downhole condition with logging techniques. Analytical and numerical simulations suggest that the most provable location of the micro-annulus path is the annular space between the cables/capillary-lines and tubing.

The observation wells used for MMV activities for CO<sub>2</sub> geological storage will require multiple integrated instrumentation to be deployed at the containment, above-containment, and near surface geological horizons. The timing and intensity of MMV activities on these multiple geological horizons must be different and independent of each other. Therefore hydraulic isolation between sensors deployed in an observation well is very crucial for MMV activities. Many sensors on the observation well for the Pembina Cardium CO<sub>2</sub> Monitoring Pilot were not hydraulically isolated after cement hardened due to the micro-annulus path developed during the cement job. Computational fluid

dynamics (CFD) techniques were used to better understand the parameters affecting the wellbore environment during cement circulation. A total of 13 CFD simulations were conducted, requiring approximately a combined total of 2200 hours (92 days) of computation time.

The evidence and results presented suggest that the geometry of the sensor housing used in the observation well for the Pembina Cardium CO<sub>2</sub> Monitoring Pilot generated a significant annular flow impedance. This affected the cement displacement efficiency near and above the sensor body (downstream), resulting in a mixture (poor cement) of cement slurry with fresh-water spacer and invaded native fluid. Then, the volumes of this mixture that were left in the annular space could not harden when the circulation stopped, and this resulted in the development of a micro-annulus path.

The sensor housing systems of these observations wells could induce a local reduction of annular space in short section of the borehole, and computation fluid dynamic techniques provide a better prediction of the annular flow behaviour under these complex borehole configurations. Without this computational effort the sensor housing system configuration could increase the risk of the development of micro-annulus paths that could hydraulically connect multiple monitoring depths, affecting the direct “in-situ” measurements of the Formation.

The CFD results suggest that the annular flow impedance and low cement displacement efficiency caused by the presents of the sensor housing bodies have a point located effect within the entire length of the borehole. However, sensor elements required cable to transfer the signal from the downhole location to the surface, and typically these cables are place near and about the sensor housing and on the same quadrant of the borehole cross-section, which is the same location where the poor quality cement column tends form. Multiple cables could cause zones of poor quality cement between the production tubing and the cables. The overlapping of the cable and the sensor housing bodies could increase the risk of the development of micro-annulus paths that could hydraulically communicate multiple sensors of the integrated system. The simulation results also suggest that this risk can be reduce with a novel sensor housing integrated with two set of flow deflector fins located at the down- and up- stream of the sensor housing. The new configuration derived from using CFD techniques and extensive design has resulted in a patented system that greatly reduces the risk of inter-zonal fluid communication, ensuing independent and fully isolated in-situ pressure and temperature measurements.

From a fluid mechanics perspective, the appropriate geometrical configuration of the fin is unique for the boundary conditions, dimension of the annular space and fluid properties (i.e., rheology). The computational effort presented in this dissertation demonstrates how CFD techniques can be used to assist on the design phase of complex downhole sensor housing configurations where more attention is required. While the results from the simulator have proven the applicability of CFD techniques on these settings, substantial refining of the simulation grid will be required in any future pre-design phase of downhole sensor housing installations.

### **8.1.2 Surface tiltmeter array**

This research also include the performance assessment of the surface tiltmeter array, an indirect-near-surface measurement technology, deployed in CSEMP—a CO<sub>2</sub> enhanced coal-bed methane pilot project located also in the Pembina Field. The experience and analyses gained from the installations provide valuable insight for CO<sub>2</sub> geological storage monitoring and risk/performance assessment.

The deployment of the surface tiltmeter array was successful, but the standard of practice used to design and install arrays does not include a pre-evaluation of the site conditions. The surface tiltmeter array installed at the CSEMP pilot site was designed and deployed with standards used for oil and gas operational sites where large surface deformations are expected; however, the primary purpose of the CSEMP pilot was to demonstrate that CO<sub>2</sub> storage in Ardley coals is viable as a greenhouse gas reduction mechanism; thus, small surface deformations were expected

Surface tiltmeters are sensitive to reservoir deformations from CO<sub>2</sub> injection as shown here by tiltmeter measurements, but surface processes also impact the instrument responses. Many surface effects are cyclical and elastic in nature allowing the desired reservoir signal trends to show through when measurement periods are appropriately chosen. If an injection interval corresponds closely to a period of heavy rain and ice thaw, then the desired signal would be lost in extraneous sources. If the injection and measurement period are long enough for the temporary signal spike to return back to the baseline, then the signal may often be extracted. The analysis depends upon the total change in tilt from one time to another. Deformation that occurs in between those two measurement points, as long as it is elastic and has time to return to the baseline, has no impact on the results.

Tiltmeter technology for short-term (hours) applications as a fracture diagnostic tool has been successfully applied in the oil and gas industry since 1996. Fracture mapping is much longer than short-term noise (e.g., traffic) and shorter than long-term external effects associated with seasonal changes or site and instrumentation drift. This characteristic allows the fracture signals to be extracted even in the presence of significant amounts of noise. The results of the fracture mapping, using surface tiltmeter array and downhole tiltmeters, for the hydraulic fracture operation in CSEMP was successful.

This long term surface tiltmeter array reservoir monitoring (months) application, which at the time was possibly the first of its kind to interpret the deformation of coal from tiltmeters due to CO<sub>2</sub> injection, could capture a positive maximum deformation of approximately 2 mm after injecting 850 tonnes of CO<sub>2</sub> in the Ardley coals at a depth of 400 m. Extensive examination of the tilt signature was conducted to extract the reservoir response during the CO<sub>2</sub> injection. It is expected that for a surface deformation greater than 5 mm the signature of reservoir response can overcome the external effects in long-term reservoir monitoring.

## **8.2 Conclusions**

Over the tenure of the Penn West CO<sub>2</sub> Monitoring Project, a detailed analysis of every aspect of the OW completion, cementing behavior, annular flow behavior both the cement and the injected brine, its impact on the integrity of downhole systems. Synthesis of this information will provide the basis for recommendations regarding the deployment of downhole technology in OWs used for the monitoring and verification of CO<sub>2</sub> movement.

The application of the innovated FRS, permanently cemented at different depths, has proved to be effective technology for geochemical monitoring at economic cost. One additional advantage of the FRS design is its use as a “bubble” tube pressure sensor that can be used to confirm the BHP of the pressure gauges permanently installed within the OW.

Downhole pressure gauges capture the dynamics of cement displacement, and they are key element during a post-job review and future well integrity assessment. They provide a good diagnostic of boundary conditions of cement displacement operations, but does not allow evaluation of the efficiency of the operations. It is the integration of complex

3D CAD models of downhole instrumentation assemblies with computational fluid dynamics simulators that provides a powerful framework to examine the movement of fluids and cement relative to completion geometry.

The results of this detailed wellbore numerical modeling were used to enhance the planning and operations of cement placement around deep downhole monitoring sensor housing systems and to identify difficulties of cement placement. As an outcome of this study, a new outside casing conveyed low flow impedance sensor housing system and method was developed and patented.

The experience and analyses gained from CSEMP provide valuable insight of advantage and disadvantage of this type of technology. The most obvious result from the reservoir monitoring analysis at Pembina is that there is a large amount of movement in the tiltmeter tools that is not related to the injection, which complicates the analysis. The author considers that the current state of this technology cannot be used as an indirect measurement of CO<sub>2</sub> migration. The tools have potential, but more research and tool development is required to overcome the installation issues and the effect of the ambient variables that are unique for each site.

### **8.3 Recommendations and future work**

#### **8.3.1 Observation well**

Many of the observation wells with an integrated multi-instrumentation system are deployed with tubing hanging inside of pre-cased boreholes. Pre-cased boreholes are used to guarantee zonal isolation during primary cement operations where cement is placed between the casing and formation. However, the main objective of a cement operation for this type of observation well is to hydraulically isolate the response of each sensor within the borehole. To obtain this zone isolation, cement slurry placement is constrained by two distinct envelopes — the cement circulation envelope, and the cement displacement efficiency envelope.

For each depth, the cement circulation envelope determines the minimum pore pressure profile and the maximum fracture pressure profile during the placement to avoid influx or fracturing. The cement displacement efficiency envelope is constrained by the flow rate at each depth, which helps to avoid cement channeling or contamination for a given wellbore geometry. Analytical results suggest that to prevent the invasion of the well by native fluid, the preflush fluid should be dense enough to balance the reservoir pressure

and prevent any influx into the wellbore. Also, It is recommended to include cement circulation simulation reports as part of the pre-cement placement design phase for observation wells. This will help to highlight potential problems in design and execution, as well as solutions for the same.

Advancements in both measurement techniques and numerical simulations are helping to increase the understanding of multi-phase flow in downhole sensor housing systems. CFD simulators are powerful instruments that require substantial computer power and time-consuming computational time. The author recommends the use of computer cluster to increase the size of the models, but this does not save computational time because the computational technique is the same for a computer cluster or a workstation. The author initially intended to model the full-size wellbore, but the large scale ratio ( $10^5$ ) between the length and the diameter of the wellbore and the limited computer power and computational time required for this scale of modelling limited the extent of this research.

The parametric study of rheological properties was not in the scope of this research, but it is recommended to evaluate the impact of the cement displacement in large range of different cement types.

The current assumption that laminar flow is established during the circulation that allows reducing the simulation effort to 5 m long sections will have to be validated. Future CFD simulations should include turbulence models k-e.

### 8.3.2 Surface tiltmeter array

Compared to hydraulic fracturing, images of surface deformation during CO<sub>2</sub> injection are strongly affected by sensor motion due to sources other than the CO<sub>2</sub> injection, including rainfall and possible temperature effects. Constructing deeper sites and using a denser tiltmeter array could substantially mitigate these effects. During analysis of hydraulic fracture treatments, sensor motion on time scales shorter and longer than the treatment are removed, minimizing effects of temperature, rainfall, sensor drift, etc. Since the time scale of the reservoir motion due to the longer term CO<sub>2</sub> injection cannot be predicted beforehand (for instance, the injected fluid may move to a shallower depth partway through injection, causing a drastic change in signals), the temperature- and rainfall- induced motion cannot currently be distinguished from reservoir-sourced motion and is not removed when interpretations are made for long-term injection. The following recommendations are made to improve the sensitivity of surface tiltmeter arrays for long-term applications in CO<sub>2</sub> enhanced coal-bed methane projects:

- Dramatic elevation changes are likely to be largely due to weather-related effects on the tiltmeter sites. It is highly recommended that a local weather monitoring station be installed in conjunction with tiltmeter arrays deployed for long-term reservoir monitoring projects.
- Temperature calibration for expected ground temperature variations is highly recommended for long-term surface tiltmeter applications.
- For long-term application of MMV activities for CO<sub>2</sub> geological storage, a modified installation designing such as great burial depth of the tiltmeter is required. For reservoir monitoring at the Pembina, tiltmeter sites at a depth of 6 m were found to be inadequate. Twelve metres deep is recommended to limit the site movement due to rainfall, temperature changes, and other environmental effects. Additional research is required for this issue.
- Increase the number of tilt sites by using a denser array, to ensure all changes in the surface shape are captured by the tiltmeters.
- Adding GPS to the array provides a reference position that is stable over long periods (more than 30 days) and is not subject to drift. For any monitoring that will occur over a period of several months or more, adding GPS will improve the results.

- Expose the tools to longer periods of CO<sub>2</sub> injection and production to characterize and verify the operation of the tools and array.
- There is some potential to filter the tiltmeter data to remove effects that are not likely to be sourced from at or near the injection depth. This option is currently being developed

## CHAPTER 9 References

1. IPCC, ed. *Carbon Dioxide Capture and Storage*. ed. B. Metz, et al. 2005, Cambridge University Press: UK. 431.
2. IPCC, *Eighth Session of IPCC Working Group III and Twenty Fourth Session of the IPCC*. 2005: Montreal.
3. Zambrano-Narvaez, G. and R.J. Chalaturnyk, *Design and Deployment of an Integrated Instrumentation System in a Monitoring Well at the Penn West CO<sub>2</sub>-EOR Pilot*, in *7<sup>th</sup> International Symposium of Field Measurements in Geomechanics*. 2007, ASCE: Boston, MA.
4. Stevens, S.H. and J.J. Gale, *Geologic CO<sub>2</sub> sequestration may benefit upstream industry*. Oil and Gas Journal, 2000. **98**: p. 5.
5. Gale, J.J., *Geological storage of CO<sub>2</sub>: What's known, Where are the gaps and What more needs to be done*, in *6th International Conference on Greenhouse Gas Control Technologies*, J.J. Gale and Y. Kaya, Editors. 2002: Kyoto, Japan. p. 207-212.
6. McPherson, B.O.L. and B.S. Cole, *Multiphase CO<sub>2</sub> flow, transport and sequestration in the Powder River Basin, Wyoming*. Journal of Geochemical Exploration, 2000(69-70): p. 5.
7. Zhou, W., et al., *The IEA Weyburn CO<sub>2</sub> Monitoring and Storage Project - Modelling of the Long-Term Migration of CO<sub>2</sub> from Weyburn*, in *7<sup>th</sup> International Conference on Greenhouse Gas Control Technologies (GHGT-7)*, E.S. Rubin, D.W. Keith, and C.F. Gilboy, Editors. 2004, Elsevier: Vancouver, Canada. p. 721-729.
8. (IEA), *Technology Roadmaps: Carbon capture and storage*. 2009, International Energy Agency. p. 52.
9. (IEA), *Carbon Capture and Storage: Legal and Regulatory Review, 2*, Editor. 2011, International Energy Agency. p. 108.
10. Chalaturnyk, R.J. and W.D. Gunter, *Geological Storage of CO<sub>2</sub>: Time frames, Monitoring and Verification*, in *7th International Conference on Greenhouse Gas Control Technologies (GHGT-7)*, E.S. Rubin, D.W. Keith, and C.F. Gilboy, Editors. 2004, Elsevier: Vancouver, Canada. p. 623-632.
11. Zambrano-Narvaez, G. and W.D. Gunter, *Tiltmeter array and baseline monitoring at CSEMP: Report 1*. 2006, Alberta Research Council: Edmonton, Alberta. Canada. p. 1-2.
12. Winthagen, P., P. Arts, and B. Shroots, *Monitoring Subsurface CO<sub>2</sub> Storage*. *Oil and Gas Science and Technology*, 2005. **60**(3): p. 573-582.
13. Robertson, K., J. Findsen, and S. Messner, *International Carbon Capture and Storage Projects Overcoming Legal Barriers*, in *2006/1236 Report*. 2006, DOE/NETL.
14. Zambrano-Narvaez, G. and R. Chalaturnyk, *Case study of the cementing phase of an observation well at the Pembina Cardium CO<sub>2</sub> monitoring pilot, Alberta*,

- Canada. *International Journal of Greenhouse Gas Control*, 2011(Accepted for publication).
15. Lim, G., Y. Liu, and W.D. Gunter, *Reservoir Simulation Modelling for the Penn West Pembina CO<sub>2</sub>-EOR Site (Task 6.1.) Progress Report*. 2007, Alberta Research Council.
  16. Dashtgard, S., et al., *Local-Scale Baseline Geological Reprint for the Pembina-Cardium CO<sub>2</sub>-Enhance Oil Recovery Site*. 2006, Report AGS - AEUB 9: Edmonton, Alberta.
  17. Hitchon, B., ed. *Pembina Cardium CO<sub>2</sub> Monitoring Pilot at CO<sub>2</sub>-EOR Project, Alberta, Canada*. 2009, Geoscience Publishing: Edmonton. 392.
  18. *Pembina Cardium CO<sub>2</sub> Monitoring Pilot, a CO<sub>2</sub> EOR Project, Alberta, Canada*, ed. B. Hitchon. 2009, Edmonton, Alberta, Canada: Geoscience Publishing. 392.
  19. Robinson, J.R., et al., *CSEMP Pilot Test and Monitoring Designs at the enerPLUS Site - South Buck Lake*, in *Final Report*. 2004, Alberta Research Council/Tessaract Corporation: Edmonton, Alberta, Canada.
  20. Gunter, W.D., M.J. Mavor, and J.R. Robinson, *CO<sub>2</sub> Storage and Enhanced Methane Production: Field Testing at Fenn-Big Valley, Alberta, Canada, with Application*, in *7th International Conference on Greenhouse Gas Control Technologies*, E.S. Rubin, D.W. Keith, and C.F. Gilboy, Editors. 2005, Elsevier: Vancouver, BC, Canada. p. 413-421.
  21. Wong, S., et al., *Enhanced Coalbed Methane and CO<sub>2</sub> Storage in Anthracitic Coals - Micro-Pilot Test At South Qinshui, Shanxi, China*. *International Journal of Greenhouse Gas Control*, 2007. **1**(2): p. 215-222.
  22. Gunter, W.D., et al., *Recommended Practices for CO<sub>2</sub>-Enhanced Coal Bed Methane Pilot Tests in China*. 2008: Canadian International Development Agency 275.
  23. Mavor, M.J., W.D. Gunter, and J.R. Robinson, *Alberta Multiwell Micro-Pilot Testing for CBM Properties, Enhanced Methane Recovery and CO<sub>2</sub> Storage Potential*, in *SPE Annual Technical Conference and Exhibition*, SPE, Editor. 2004, SPE paper 90256: Houston, Texas, USA. p. 14.
  24. Mavor, M.J., et al., *Testing for CO<sub>2</sub> Sequestration and Enhanced Methane Production from Coal*, in *SPE Gas Technology Symposium*, SPE, Editor. 2002, SPE paper 75680: Calgary, Alberta. p. 14.
  25. McCrank, J. and D.C. Lawton. *Seismic characterization of a CO<sub>2</sub> flood in the Ardley coals, Alberta, Canada*. in *Leading Edge*. 2009. Tulsa, OK: Society of Exploration Geophysicists.
  26. Blyth, A., et al., *Geological and hydrogeological characterization and monitoring of a CO<sub>2</sub> storage - enhanced CBM production micro-pilot test site in the Pembina area, west-central Alberta Plains, Canada*. 2006, Alberta Research Council.
  27. Mavor, M.J. and J. Faltonson, *Enerplus 102 Pembina 7-28-46-7 W5M CO<sub>2</sub> Micro-Pilot Analysis, Final Report of CSEMP project*. 2008, Alberta Research Council: Edmonton, AB. p. 100 pages.

28. Jimenez, J., R. Chalaturnyk, and B. Gunter, *Preliminary Design of Wellbore Monitoring Configuration at the Penn West CO<sub>2</sub>-EOR Pilot Monitoring*. 2005. p. 26.
29. Coueslan, M., *Processing and Interpretation of Time-lapse Vertical Seismic Profile Data from the Penn West CO<sub>2</sub> Monitoring Project*, in *Geophysics*. 2007, University of Calgary: Calgary.
30. McRae, J.B. and T. Simmonds. *Long-term stability of vibrating wire instruments. One manufacture's perspective*. in *3rd International Symposium of Field Measurements in Geomechanics*. 1991. Osla, Norway: Rotterdam: A.A. Balkema.
31. Crawford, S.B. and R.F. Legget, *Ground temperature investigation in Canada*. *Engineering Journal*, 1957. **40**(3): p. 263-269.
32. Nelson, E.B. and D. Guillot, *Well Cementing*. Second ed. 2006, Sugar Land, Texas: Schlumberger.
33. Melrose, J.C., et al. *Water-Rock Interaction in the Pembina Field, Alberta*. in *Paper SEP 6049 prepared for the 51th Annual Fall Technical Conference*. 1976. New Orleans.
34. Duncan, G., *Completion practices. Guidelines for selection of specific tools and equipment for EOR application, including packers, seals, flow control artificial, lift and downhole monitoring*, in *World Oil*. 1995. p. 77-87.
35. Duncan, G., *Nitrogen determination of bottomhole pressure*, in *World Oil*. 1997. p. 125-126.
36. Miller, C.W. and J.M. Zerzan. *Downhole pressure changes measured with fluid filled capillary tube*. in *paper SPE 8233 prepared for the Technical Conferences and Exhibition*. 1979. Las Vegas, Nevada, USA.
37. Okada, Y., *Internal Deformation Due to Shear and Tensile Faults in a Half-Space*. 1992, *Bulletin of the Seismological Society of America*. p. 1018-1040.
38. Green, A.E. and I.N. Sneddon. *The Distribution of Stress in the Neighbourhood of a Flat Elliptical Crack in an Elastic Solid*. in *Cambridge Philosophical Society*. 1949.
39. Du, Y., P. Segall, and H. Gao, *Dislocations in Inhomogeneous Media Via a Modulus Perturbation Approach: General Formulation and Two-Dimensional Solutions*. *Journal of Geophysical Research*, 1994. **99**(B7): p. 767-779.
40. Wang, R., F. Lorenzo Martin, and F. Roth, *Computation of deformation induced by earthquakes in a multi-layered elastic crust*. *Computer and Geosciences*, 2003. **29**(2): p. 198-207.
41. Du, J., et al., *Mapping Fluid Flow in a Reservoir Using Tiltmeter-Based Surface Deformation Measurements*, *SPE paper 96897*, in *Presented at the SPE Annual Technical Conference and Exhibition*. 2005: Dallas, TX.
42. Davis, E., D. Astakhov, and C. Wright, *Monitoring and Diagnostic Technologies. Precise Deformation Monitoring by High Resolution Tiltmetre*. *Geophysical Exploration*, 2001. **54**(6): p. 425-432.

43. Davis, E., et al., *Precise Tiltmeter Subsidence Monitoring Enhances Reservoir Management*, in *SPE/AAPG Western Regional Meeting*. 2000: Long Beach, California.
44. Pinnacle Technologies, I., *Fracture Mapping Results for Enerplus in the Pembina Field*. 2006, Pinnacle Technologies, Inc. p. 33.
45. GRI, *Effect of Layered Formations on Tiltmeter Hydraulic Fracture Mapping*. 1999, Gas Technology Institute Technological Report.
46. Apruzzese, J., *Fracture Mapping and Reservoir Monitoring Observations for Enerplus in the Pembina Field*. 2007, Pinnacle Technologies Inc.: Houston. p. 23.
47. Apruzzese, J., *Existing Data: Possible Improvements and Usages for Post Fracture Period at Enerplus Pembina Field*. 2007, Pinnacle Technologies Inc.: Houston. p. 27.
48. Pinnacle Technologies, I., *Fracture Mapping Results for Enerplus in the Pembina Field*. 2007, Pinnacle Technologies Inc.: Calgary. p. 23.
49. Blair, D.P., *Rise times of attenuated seismic pulses detected in both empty and fluid-filled cylindrical boreholes*. *Geophysics*, 1984. **49**(4): p. 398-410.
50. Peng, C., C.H. Cheng, and M.N. Toksoz. *Cased borehole effects on downhole seismic measurements*. in *55th EAEG meeting*. 1994. Stavanger.
51. Vincent, P.D., et al., *Evaluating the effect of the joining platform on seismic data acquired by geophones mounted to rigid media*. *Journal of Applied Geophysics*, 2009. **68**(2): p. 146-150.
52. Piot, B.M. and M. Loizzo, *Reviving the Job Signature Concept for Better Quality Cement Jobs*, in *Drilling Conference*, IADC/SPE-39350, Editor. 1998, IADC/SPE: Dallas, Texas.
53. Liu, G., *Software assists wellbore cleanup*, in *Hart's E&P*. 2003, Hart Engery Publishing, LP: Houston, Texas. p. 3.
54. Brehme, J., A.D. Bain, and A. Valencia, *Use of Pressure Gauges in Liner Running Strings during Liner Cementing Operations*, in *SPE/IADC Drilling Conference*, SPE-79906, Editor. 2003: Amsterdam, The Netherlands.
55. Beirute, R.M., *The phenomenon of free fall during primary cementing*, in *59th Annual Technical Conference*, SPE-13045, Editor. 1984, SPE: Houston, Texas.
56. Johns, J.E., et al., *Locating and Repairing Casing Leaks With Tubing in Place - Ultrasonic Logging and Pressure-Activated Sealant Methods*, in *Offshore Europe 2007*, SPE, Editor. 2007: Aberdeen, Scotland, U.K.
57. Jones, P.H. and D. Bedine, *Oil-Well Cementing*, in *Drilling and Production Practice*, API, Editor. 1940: Los Angeles, California. p. 45 - 63.
58. Teplitz, A.J. and W.E. Hasebroek, *An Investigation of Oil-Well Cementing*, in *Drilling and Production Practice*, API, Editor. 1946: Shreveport, LA. p. 76 -103.
59. McLean, R.H., C.W. Manry, and W.W. Whitaker, *Displacement Mechanics in Primary Cementing*, in *SPE California Regional Meeting*, AIME, Editor. 1967, SPE: Santa Barbara, California. p. 251-260.

60. API, *Specification for Bow-Spring Casing Centralizers (API Spec 10D)*. 2002: Washington, D.C., USA.
61. Bittleston, S.H., J. Ferguson, and I.A. Frigaard, *Mud removal and cement placement during primary cementing of an oil well*. Journal of Engineering Mathematics, 2002. **43**: p. 229-253.
62. Moyes-Gonzalez, M.A., et al., *Transient effects in oilfied cementing flows: Qualitative behaviur*. European Journal of Applied Mathematics, 2007. **18**: p. 477-512.
63. Terani, M.A., S.H. Bittleston, and P.J.G. Long, *Flow instabilities during annular displacement of one non-Newtonian fluid by another*. Experiments in Fluids, 1993(14): p. 246-256.
64. Jaeger, J.C., N.G.W. Cook, and R.W. Zimmerman, *Fundamentals of Rock Mechanics*, ed. 4th. 2008: Blackwell. 475.
65. Zimmerman, R.W. and G.S. Bodvarsson, *Hydraulic Conductivity of Rock Fractures*. Transport in Porous Media, 1996. **23**: p. 1-30.
66. Bilgesu, H.I., et al., *Computational Fluid Dynamics (CFD) as a Tool to Study Cutting Transport in Wellbores*, in *SPE Eastern Regional Meeting*, SPE-78716, Editor. 2002: Lexington, Kentucky.
67. Calis, H.A.P., et al., *CFD modelling and experimental validation of pressure drop and flow profile in a novel structured catalytic reactor packing*. Chemical Engineering Science, 2001. **56**(4): p. 1713-1720.
68. Frankiewicz, T. and C.-M. Lee, *Using Computational Fluid Dynamics (CFD) Simulation to Model Fluid Motion in Process Vessels on Fixed and Floating Platforms*, in *Annual Technical Confernece and Exhibition*, SPE-77494, Editor. 2002: San Antonio, Texas.
69. Suarez, L., et al., *3D CFD Simulation of Rotary Gas-Separator Performace Under Two-Phase-Flow Condition*, in *Latin American and Caribbean Petroleum Engineering Conference*, SPE-94959, Editor. 2005, SPE: Rio de Janeiro, Brazil.
70. Xu, J., et al., *Prediction of Turbulent Friction in Rod Pumped Wells*, in *Permian Basin Oil and Gas Recovery Conference*, SPE-39800, Editor. 1998: Midland, Texas.
71. ANSYS, I. <<http://www.ansys.com/products/cfx.asp>>. 2008.
72. Hirt, C.W. and B.D. Nichols, *Volume of Fluid (VOF) Method for the Dynamics of Free Boundaries*. Journal of Computational Physics, 1981. **39**: p. 201-225.
73. O'Halloran, S.P., et al. *Experimental Measurements and Numerical Simulations of Two-Phase Stratified, Wavy and Slug Flow in a Narrow Rectangular Channel*. . in *2005 ASME Fluids Engineering Division Summer Meeting and Exhibition*. 2005. Houston, TX, USA: ASME.
74. *Production Casing Cement Proposal*, in *AMOCO HB A-108 PEM 100/07-11-048-09W5/0*. 2005, BJ Services Company Canada.
75. Fluent\_Inc, *ANSYS Fluent Multiphace User's Guide*. 2007: Lebanon, NH.
76. Lange, C.F., *Applied Computational Fluid Dynamics Course*. 2009.

77. Yao, D. and S.G. Robello. *Annular Pressure Loss Predictions for Various Stand-off Devices*. in *2008 IADC/SPE Drilling Conference*. 2008. Orlando, Florida: IADC/SPE 112544.
78. Heidaryan, E., et al., *Viscosity of pure carbon dioxide at supercritical region: Measurement and correlation approach*. *The Journal of Supercritical Fluids*, 2010. **Article in Press**.
79. Service, T.W., *Trycan Cement Proposal*. 2009, Trycan: Edmonton.
80. Halliburton, *Canadian Red Book*. 2000.
81. Lajeunesse, E., J. Martin, and D. Salin, *3D Instability of Miscible Displacements in a Hele-Shaw Cell*. *Phys. Rev. Lett.*, 1997. **79**(26): p. 5254-5257.
82. Moyers-Gonzalez, M.A., *Transient effects in oilfield cementing flows*, in *Mathematics*. 2006, The University of British Columbia: Vancouver. p. 192.
83. Zambrano-Narvaez, G., R.J. Chalaturnyk, and P. Lang, *Outside Casing Conveyed Low Flow Impedance Sensor Gauge System and Method*, U.S.P.T.O. P1396PC00, Editor. 2011: USA-PCT.

## **APPENDIX A: The standard operation procedures used for the CSEMP**

### **Surface tiltmeter site drilling Procedure**

The following is the standard operating procedure (SOP) for drilling surface tiltmeter sites. Sites vary in depth from 10 feet to 40 feet. Following the proper drilling procedure is necessary to maintain good relations with the regulatory agencies, landowners and our clients.

- **Background**

Surface tiltmeter tools measure the inclination or “tilt” that results from the deformation (movement) of the earth during a hydraulic fracture treatment. The induced tilt signal infers a fracture orientation (fracture azimuth, dip and volume). The measured signals can be as small as one nanoradian, or one part in a billion. One nanoradian of tilt is equivalent to laying a beam from New York to the Los Angeles and picking it up at one end a ¼ inch. The surface of the Earth naturally moves miniscule amounts every day due to:

- Thermal fluctuations (heating & cooling of the earth)
- Solid Earth Tides (due to the Earth’s rotation with respect to the sun and moon, similar to ocean tides)
- Cultural Noise - Any surface movement that causes the ground to deform (traffic, cattle, storage tanks, pump units, flow lines)

Surface tiltmeters are deployed below the surface to avoid the “noise” due to thermal fluctuations and cultural noise on the surface. The surface tools are usually installed at a depth between 10 – 40 feet. The actual depth depends on the depth of the hydraulic fracture and the amount of surface “noise.”

The surface tiltmeter tools are installed in an array of tools. The number of tools in an array depends on the depth of the fracture and surface considerations. The array usually consists of between 12 and 40 surface sites/tools. The tilt signal from each surface tool is used to form a tilt deformation pattern resulting from a hydraulic fracture. **Figure A.1** depicts a typical map of a Surface Tiltmeter Array.

- **Materials**

1. Site Markings
  - Stakes, flagging, and/or white paint

2. Inner pipe
    - 3" ID or larger PVC pipe & matching PVC cap
    - Typically use 4" Schedule 40 PVC pipe & cap
  3. Outer pipe
    - 8" ID or larger PVC pipe & matching PVC cap
    - Typically use 8" Schedule 40 PVC pipe & cap
  4. Tremmie Pipe, if needed
    - ½" ID or larger PVC pipe
    - Typically use 1" PVC pipe
  5. Pinnacle ID Sticker and/or Tags
    - ID sticker/tag will contain contact phone number and address
  6. PVC glue
  7. Cement containing:
    - Water
    - Cement
    - Sand and/or gravel
    - Bentonite or other viscosifier (optional)
- **Surveying and Staking**
    1. Mark proposed tiltmeter sites with stakes, flagging and/or white paint.
    2. Record exact location using GPS.
    3. Have client representative and/or landowner approve proposed sites.
    4. Take down detailed directions to the site.
    5. Call in a "Line Locate" from the One Call Center in the State/Province where the work is being done.
    6. Once a confirmation number and an "all clear" have been issued for all sites, drilling may commence.
  - **Drilling**

Procedure below outlines drilling procedure for a Typical Surface Tiltmeter Site. Unless otherwise stated, all pipe sizes refer to typical sizes referenced in the above **Materials** section.

1. Inner pipe preparation:
  - Glue an end cap to the bottom of the first joint of 4" PVC.
  - If site is to be deeper than 20', connect two sections of 4" PVC together with a coupling. Use a PVC glue to seal and secure sections.
  - Optional* - Threaded couplings may also be used for the 4" pipe, but must be sealed with silicone  
or PVC glue.
  - Note: All PVC pipe and connections must be water-tight.
2. Drill an 8" or larger diameter borehole to depth as needed.
  - Depths range from 10 – 40'
3. If site is wet, prepare 1" PVC pipe to be used as a tremmie pipe. If needed, the tremmie pipe will be run along side the 4" PVC for cementing purposes.
4. Fill bottom 3 – 6" of borehole with cement or grout.
5. Drop 4" PVC casing into borehole, leaving 12" to 18" of pipe above ground level. Bottom of pipe should be landed into cement. If needed, the tremmie pipe should be run into borehole along side 4" PVC.

6. Pump cement slurry or grout into hole. Reciprocate pipe to ensure full coverage and good bond. If the site is wet, use tremmie pipe.  
Cement slurry is to contain:
  - Water
  - Cement
  - Sand and/or gravel
  - Bentonite or other viscosifier (optional)
7. Stop cement at least 6' from the surface. If site was wet, pull out tremmie pipe.  
Note: Cement must cover lower half of inner pipe but cannot extend closer than 6' from the surface.
8. The 4" PVC pipe may need to be anchored in place overnight to prevent vertical movement.
9. Install Outer pipe:  
Place 6 – 8' section of 8" PVC pipe around existing 4" pipe with 24" of pipe protruding above ground. Do not cement the 8" PVC pipe, just center it around 4" pipe. Hold it in place with soil backfill.  
*Optional:* Some bentonite can be placed around the base to prevent water inflow.  
The outer pipe is installed to isolate the inner pipe from surface "noise" and to allow dry storage of tiltmeter accessories (battery, cables, etc.)
10. Completely fill and level the excavated hole using fill dirt/soil (use backhoe if necessary).
11. Place Pinnacle ID sticker or tag with contact phone number and address in plain sight. (Make sure site is labeled with site number)
12. Make notes of how each well installation went, whether there were any problems (i.e. soil collapsed in hole, thief zones, difficulties with tremmie pipe, wet site, etc.). These notes will help determine the quality of tiltmeter data.

**Figure A.1**, below, illustrates the cross-section view of a typical Surface Tiltmeter Site.

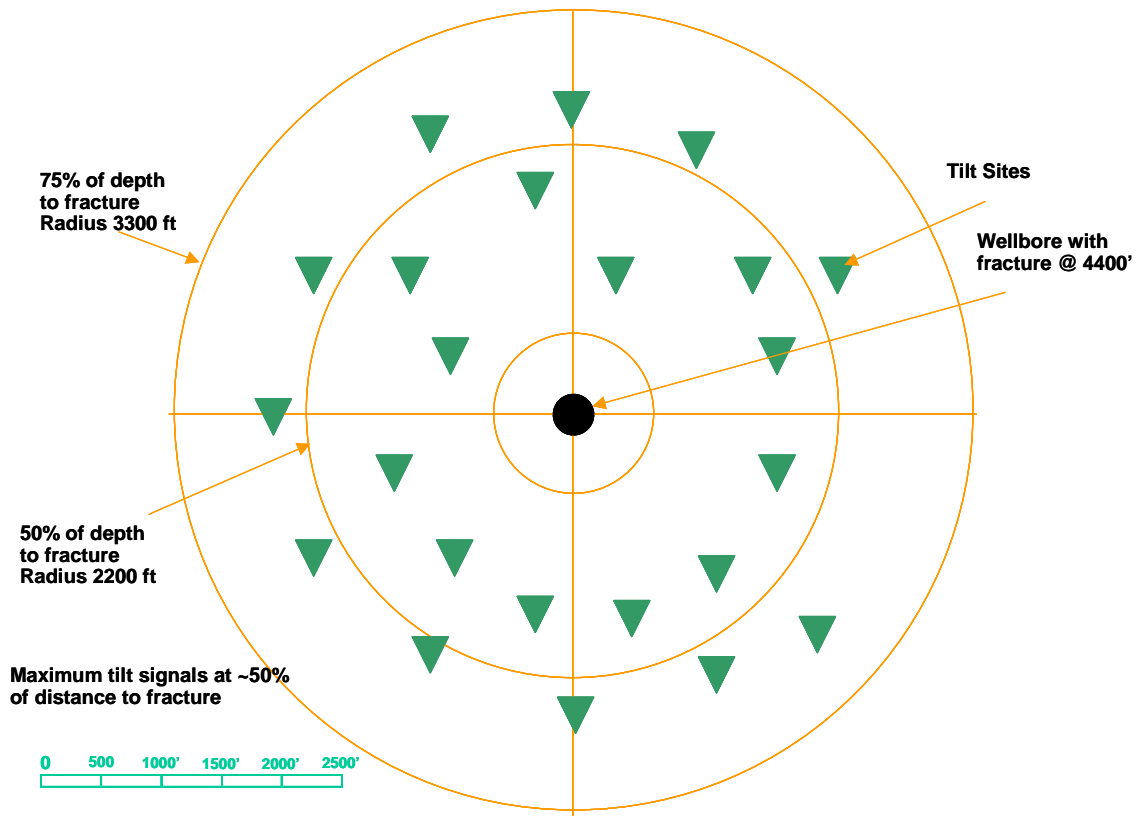
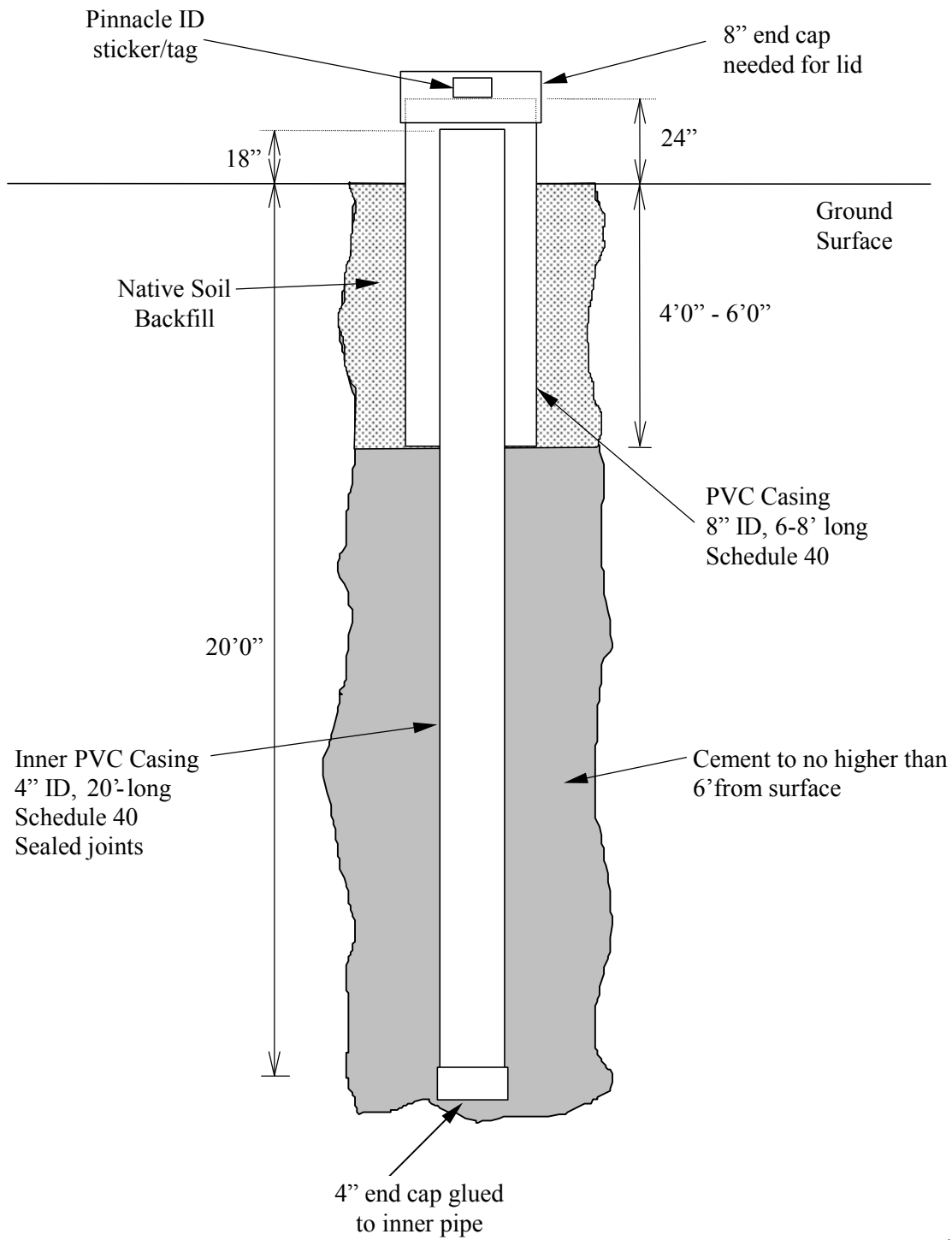


Figure A.1 Typical Surface Tiltmeter Array, Map View



Note: Not to scale.

Figure A.2 Cross-section of a Typical Surface Tiltmeter Site

## **Surface Tiltmeter Site Abandonment and Reclamation Procedure**

The following is the standard operating procedure (SOP) for abandonment of surface tiltmeter sites. It is preferred that the sites not be abandoned in the event that future work is done in the area; however, if this is not the case the sites should be reclaimed at the earliest time possible following making this decision. Properly handling this is necessary to maintain good relations with the regulatory agencies, landowners and our clients.

- **Abandonment**

1. Pull the outer pipe (use a backhoe if necessary).
2. Break apart inner pipe at joint approximately 8' from the surface. The minimum requirement is that the pipe be cut below 4' (plow depth).
3. Fill the inner pipe to within 4' of the surface using bentonite chips.

- **Reclamation**

1. Completely fill and level the excavated hole using fill dirt/soil (use backhoe if necessary).
2. Pack the soil as much as possible to prevent settling.
3. Generally cleanup around the site (leave site picked up and clean).
4. Have site rechecked at later date to insure that no subsidence has occurred around the hole (especially after wet weather).

- **Reporting**

1. Document abandonment procedure including amount of bentonite used, contractors used, dates, etc.
2. Texas only - Within 30 days a letter must be sent to the Texas Railroad Commission stating the all the sites were abandoned according to the above procedure including the dates and name of the operator. The letter should include a plat of the project area including the county, survey lines, scale and northerly direction. A Texas Water Commission letter stating the protection depths must also be attached (this can be taken from the drilling permit application for a well in the area).
3. For other States and Countries the drilling and abandonment requirement should be obtained before starting the project.

## APPENDIX B: Additional simulation results of model with Type-IV fin

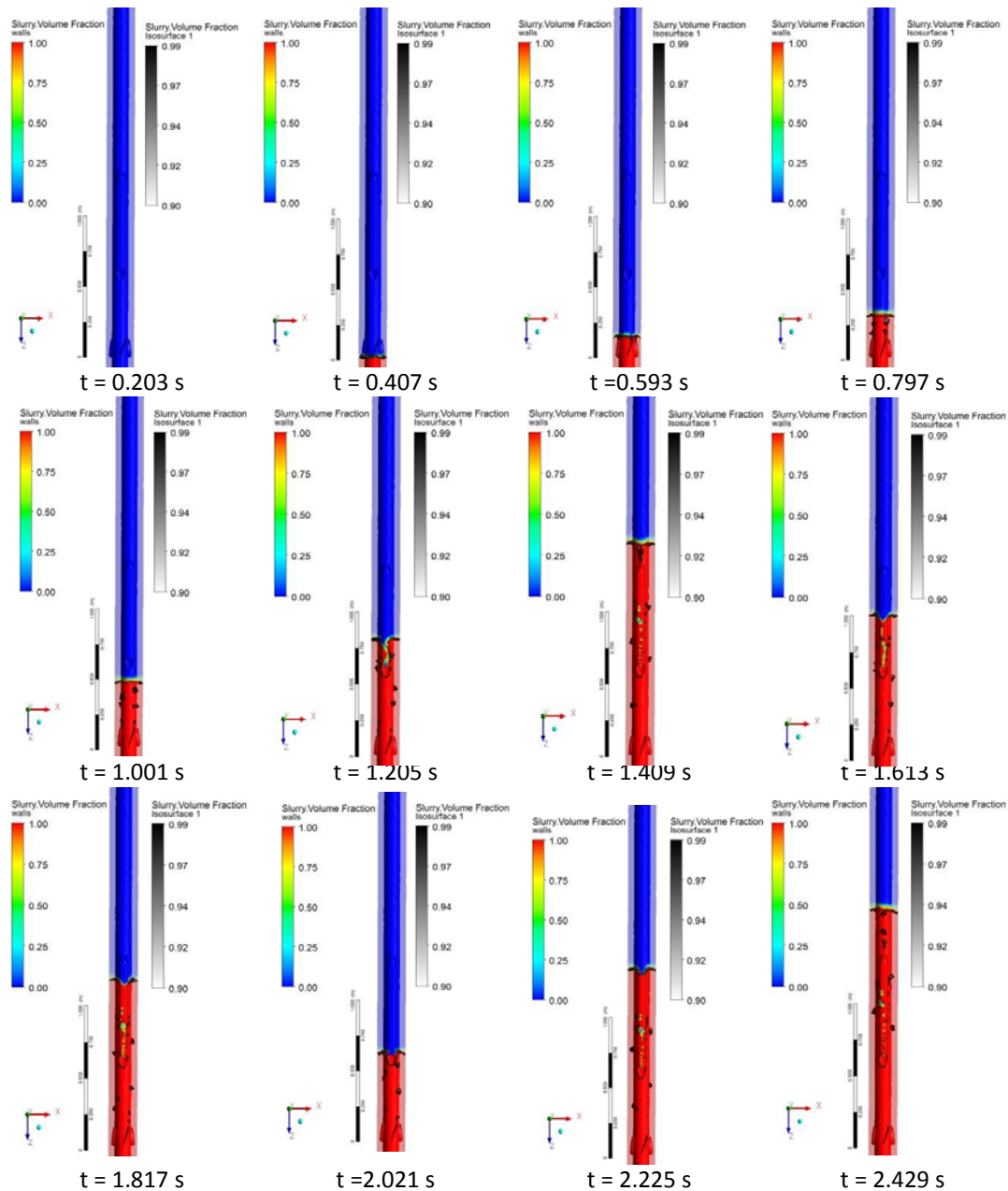


Figure B.1 VOF simulation results of 3D model of novel sensor housing and tubing conveyed with four flow deflector fins (Type-III) located at 30 centimetres upstream of the sensor housing within a borehole section of 5.00 m length. Output at time  $t = 0.203, 0.407, 0.593, 0.797, 1.001, 1.205, 1.409, 1.613, 1.817, 2.021, 2.225$  and  $2.429$  s, while the cement slurry is displacing through the annulus. Each snapshot shows cement slurry volume fraction, ISVF from 0.90 to 0.99 (grey color map).

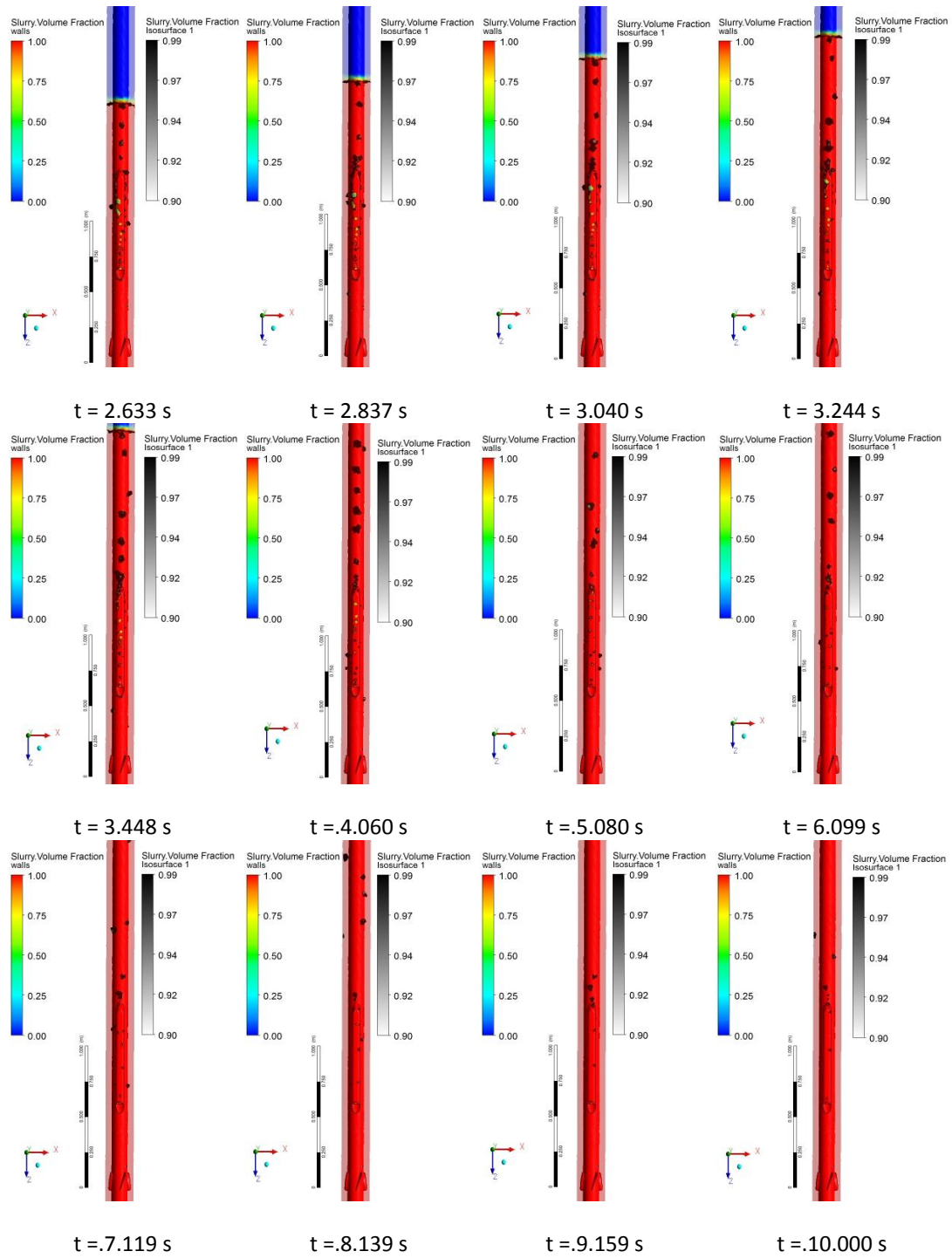


Figure B.2 VOF simulation results of 3D model of novel sensor housing and tubing conveyed with four flow deflector fins (Type-III) located at 30 centimetres upstream of the sensor housing within a borehole section of 5.00 m length. Output at time  $t = 2.633, 2.837, 3.040, 3.244, 3.448, 4.060, 5.080, 6.099, 7.119, 8.139, 9.159$  and  $10.00$  s, while the cement slurry is displacing through the annulus. Each snapshot shows cement slurry volume fraction, ISVF from 0.90 to 0.99 (grey color map).

## **APPENDIX C: Patent P1396PC00 - Outside casing conveyed low flow impedance sensor gauge system and method**

### **ABSTRACT**

The present document describes a sensing apparatus for lowering into a well and cementing therein at a certain depth. The sensing apparatus comprises an elongated casing and a sensor device protruding from an outside surface of the elongated casing for generating measurement data and sending the data to the surface of the well using a cable extending from the sensor device along the outside surface of the casing. A flow of cement is provided between the outside surface of the casing and the well for cementing the casing in place and isolating different layers of the well. Presence of the sensor device and the cable creates an obstruction within the flow path of the cement which may result in the formation of micro-annulus around the sensor device and the cable. In order to address this problem, a plurality of fins is provided around the casing, the fins being shaped to cause a straight flow of cement received at the fins to rotate around the longitudinal axis of the casing when exiting the fins for increasing cement flow between the elongated casing and its surrounding environment to mitigate micro-annulus formation. Another means to address this problem is to provide cable attachments which distance the cable from the casing and thereby let cement flow between the cable and the casing also mitigating micro-annulus formation.

### **CROSS-REFERENCE TO RELATED APPLICATIONS**

[0001] This application claims priority from U.S. Provisional Application No. 61/297518 Filed on January 22, 2010, which is incorporated herein by reference in its entirety.

### **TECHNICAL FIELD**

[0002] The present disclosure relates to downhole reservoir surveillance systems, and more particularly to sensing apparatus for being cemented at given elevations or zones inside a well so as to mitigate hydraulic communication between the zones.

### **BACKGROUND**

**[0003]** Downhole reservoir surveillance systems often consist of sensors (pressure & temperature) that are lowered into a well and cemented in place at specific elevations to make contact with the geological formation of interest, for the sake of measuring in-situ pressure and temperature. Often, these sensors are packaged in steel housings that are usually welded to the outside of the casing, and designed for mechanical protection of the delicate sensor. This way, the sensor is carried downhole with the casing that it is attached thereto. A signal cable runs from the sensor (downhole) to the surface, to convey the sensor measurements.

**[0004]** In many installations, more than one sensor is lowered into the same well, with each designed to measure physical phenomena within a zone of interest. In these types of installations, prevention of hydraulic communication between two or more zones of interest is preferable for measurement precision. The sensors are thus typically cemented in place within the wellbore, and it is the cement that acts as a barrier for migration of in-situ fluids from zone to zone. In this case, the potential for leakage in between zones however still remains due to the micro annulus formation around the sensor and the sensor signal cables from lower zones passing through upper zones of interest (since they run all the way up to surface). Therefore, if not cemented properly, the surrounding environment of the sensor(s) and the cables connected thereto may create a micro-annulus in which gas or liquid is able to travel, thus compromising the zonal isolation.

**[0005]** There is thus a need for a downhole surveillance system and method with improved downhole sensing apparatus which addresses at least some of the above noted limitations association with the prior art.

## **SUMMARY**

**[0006]** The system described herein provides a means to prevent the creation of a micro-annulus along the sensor cable. The goal is to have cement contacting all surfaces of the downhole components (casing, sensor housing, sensor cables, and the formation itself).

**[0007]** The cement will not do this naturally, as every obstruction or irregular shaped component that is located within the flow path of the cement will result in a non-homogenous flow regime. This, in turn, will result in volumes around the sensor housing and cables where there is cement of very poor quality (highly permeable) or no cement at all. These regions are referred to as “inadequate cement slurry volume fractions” (ISVF). The low flow impedance sensor housing system is constituted by a zero-vortex

sensor housing, two sets flow deflector fins, and cable standoffs. The various components of the system address this problem.

**[0008]** In accordance with an embodiment, there is provided a sensing apparatus comprising an elongated casing for lowering from a surface into a well and cementing therein, the elongated casing comprising an outside surface, a lower end and an upper end opposite the lower end; a sensor device protruding from the outside surface, for generating measurement data indicative of an environmental parameter; a cable extending from the sensor device, along the outside surface toward the upper end, for transmitting the measurement data to the surface; and a plurality of fins disposed on the outside surface, the fins being shaped to cause a straight flow of cement received at the fins to rotate around the longitudinal axis of the elongated casing when exiting the fins for increasing cement flow between the elongated casing and the surrounding environment to mitigate micro-annulus formation along the elongated casing.

**[0009]** The casing may comprise a fluid pipe. In an embodiment, the fluid pipe is cylindrical.

**[0010]** In an embodiment, the apparatus further comprises cable attachments positioned along the casing between the sensor device and the upper end of the casing, the cable attachments being at least partially in between the casing and the cable for distancing the cable from the outside surface of the elongated casing.

**[0011]** In an embodiment, the plurality of fins comprises a first set of fins substantially equally spaced annularly on the outside surface between the sensor device and the lower end.

**[0012]** In an embodiment, the plurality of fins comprises a second set of fins provided around the casing and between the sensor device and the upper end of the casing, the fins of the second set being curved to re-rotate the upward flow of cement when exiting the second set of fins for increasing cement flow between the cable and the elongated casing to mitigate micro-annulus formation along the cable.

**[0013]** In an embodiment, the cable is provided at an angle with respect to the longitudinal axis of the elongated casing such that the upward flow of cement exiting the second set of fins is substantially perpendicular to the cable.

**[0014]** The sensor device may be elongated and may comprise a first end adjacent the first set of fins and a second end adjacent the second set of fins. The second set of fins

may be provided between the first cable attachments after the sensor device and the second cable attachment after the sensor device. The cable may extend from the second end of the sensor device and between two adjacent fins of the second set.

**[0015]** Yet in a further embodiment, the sensor device may include an elongated housing and at least one sensor. The at least one sensor may comprise a temperature sensor and a pressure sensor. The at least one sensor may comprise two temperature sensors and two pressure sensors, each temperature sensor forming a pair with a pressure sensor, each pair having an output. The sensor device may comprise a first multiplexer for multiplexing the outputs of the two pairs of sensors and for sending the two outputs on the same cable. In an embodiment, the sensor device may comprise a second multiplexer for multiplexing the output of the first multiplexer with another sensor device of a lower casing in the well. In an embodiment, at least one of the first multiplexer and the second multiplexer comprises a Y splice.

**[0016]** In another aspect, there is provided a sensing apparatus comprising an elongated casing for lowering from a surface into a well and cementing therein, the elongated casing comprising an outside surface, a lower end and an upper end opposite the lower end; a sensor device protruding from an outside surface, for generating measurement data indicative of an environmental parameter; a cable extending from the sensor device, along the outside surface toward the upper end, for transmitting the measurement data to the surface; and cable attachments positioned along the outside surface between the sensor device and the upper end, the cable attachments for attaching the cable thereto at a distance from the outside surface such that cement flows between the elongated casing and the cable to mitigate micro-annulus formation along the elongated casing. In an embodiment, wherein the cable spirals upwardly from the sensor device around the elongated casing.

**[0017]** In a further aspect, there is provided a method for installing a sensing apparatus inside a well, the method comprising: lowering an elongated casing into the wellbore, the elongated casing having a sensor device protruding from an outside surface of the casing, and a signal transmitting cable extending from the sensor device; providing a flow of cement between the casing and an inner wall of the well; rotating the flow of cement around a longitudinal axis of the casing before arriving to the sensor device for increasing cement flow around the sensor device and mitigating micro-annulus formation.

[0018] In an embodiment, rotating comprises redirecting the cement flow around the casing using a plurality of fins around the casing between the sensor device and an end of the elongated casing at which the flow of cement between the casing and the well arrives first.

[0019] In a further embodiment, the method comprises, prior to lowering the elongated casing, lowering another casing into the wellbore, the other casing having an opening which allows fluids pushed downward inside the another casing to flow upward between an exterior surface of the another casing and the inner walls of the well.

[0020] In a further embodiment, the method further comprises rotating the flow of cement across the cable to mitigate micro-annulus formation along the cable.

[0021] In a further embodiment, the method further comprises providing the flow of cement between the elongated casing and the cable.

[0022] Features and advantages of the subject matter hereof will become more apparent in light of the following detailed description of selected embodiments, as illustrated in the accompanying figures. As will be realized, the subject matter disclosed and claimed is capable of modifications in various respects, all without departing from the scope of the claims. Accordingly, the drawings and the description are to be regarded as illustrative in nature, and not as restrictive and the full scope of the subject matter is set forth in the claims.

#### **BRIEF DESCRIPTION OF THE DRAWINGS**

[0023] Further features and advantages of the present disclosure will become apparent from the following detailed description, taken in combination with the appended drawings, in which:

[0024] Figure C.1 is a schematic illustration of a downhole sensing apparatus in accordance with an embodiment;

[0025] Figure C.2 illustrates an exploded view of an exemplary sensor device, in accordance with an embodiment;

[0026] Figure C.3 illustrates the electrical components of a sensing apparatus provided between the surface of the well and at least one lower sensing apparatus in the well, in accordance with an embodiment;

[0027] Figures C.4(a) & C.4(b) illustrate different views of the sensing apparatus of Figure C3;

[0028] Figure C.5 is a flow chart of a method for installation of the downhole sensing apparatus of Figure C.1; and

[0029] Figure C.6 is a partial cut-out view of the ground showing an observation well in which an assembly comprising an embodiment of a sensing apparatus is installed.

[0030] It will be noted that throughout the appended drawings, like features are identified by like reference numerals.

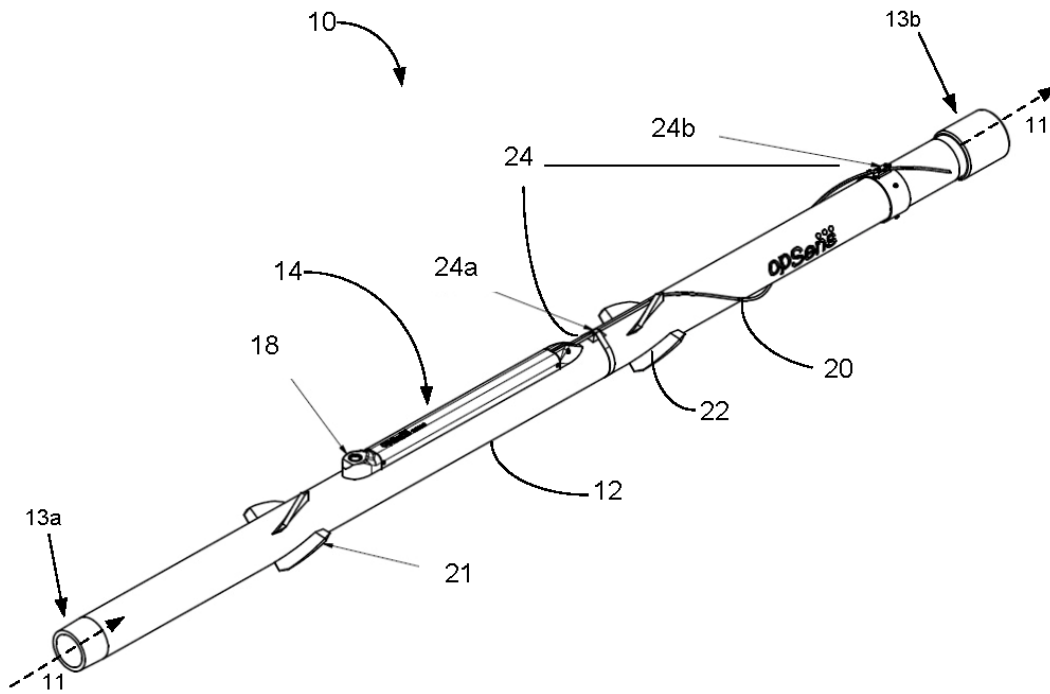


**Figure C.1.**

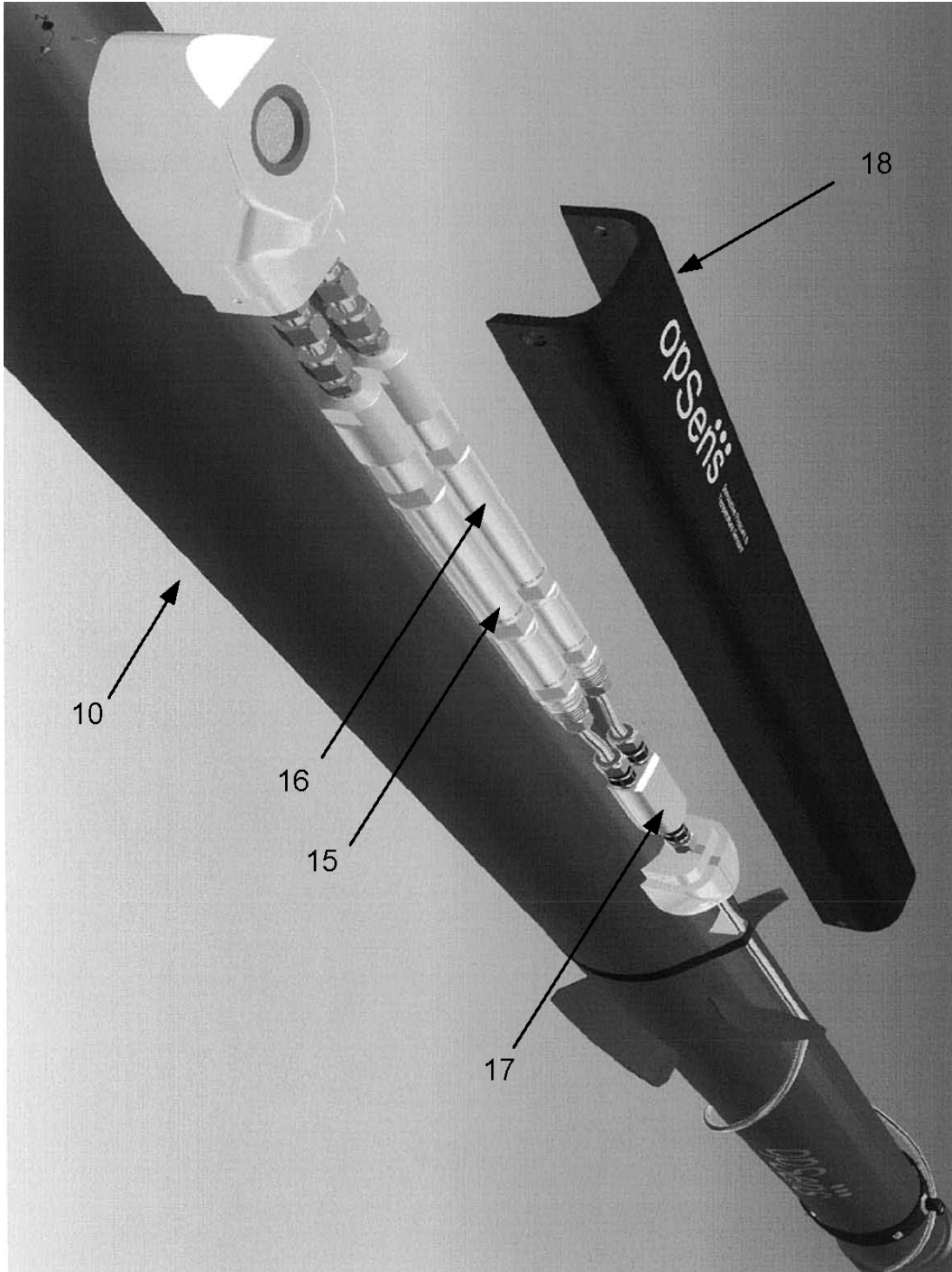


**Figure C.2.**

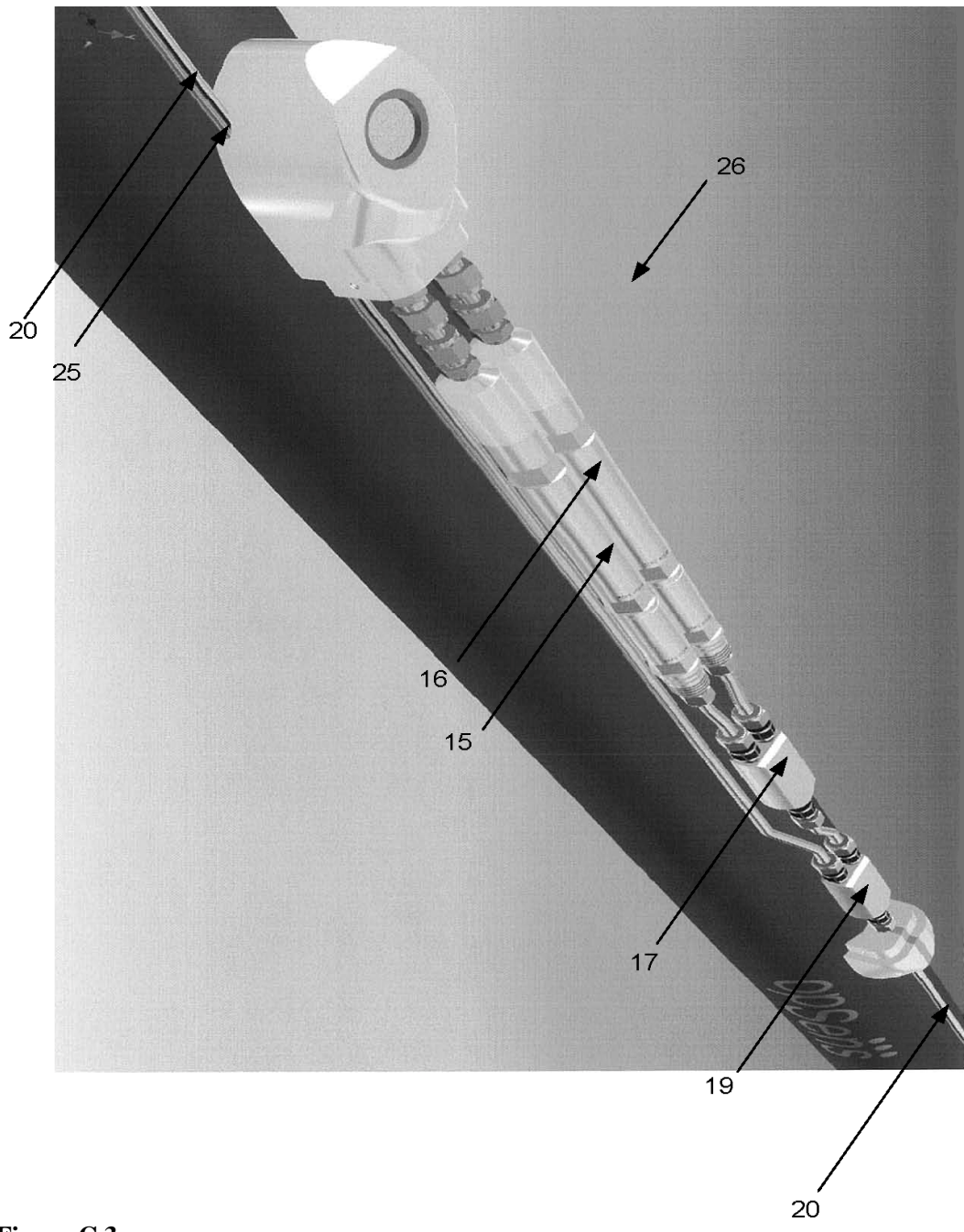


**Figure C.3.**



**Figure C.4 (a).**

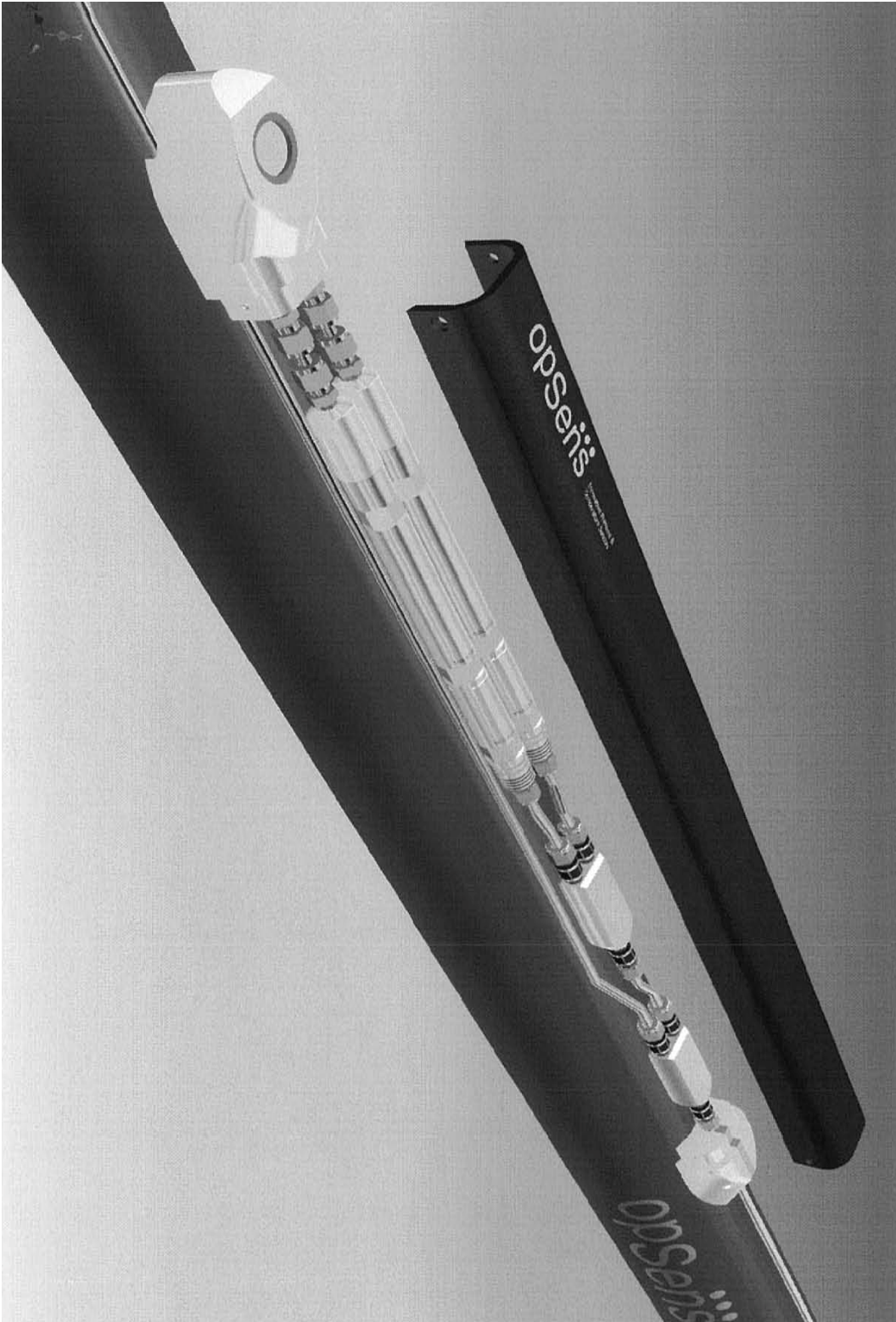
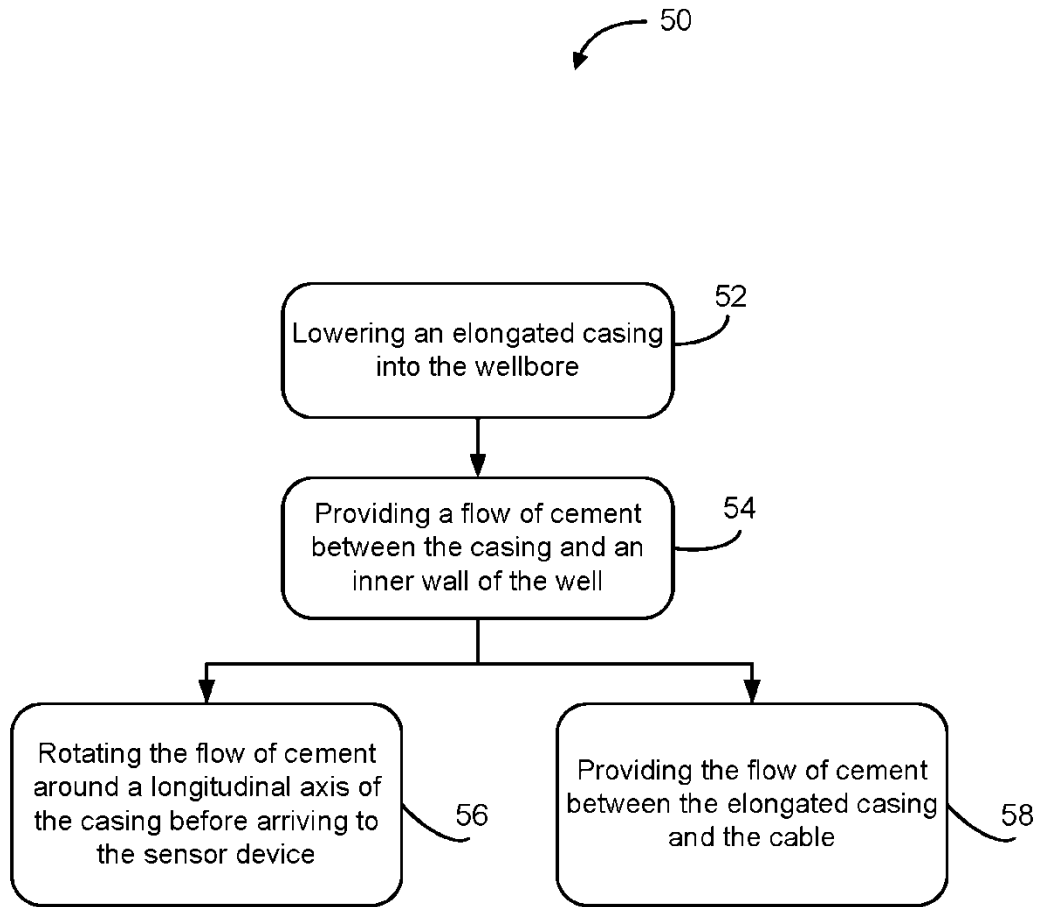


Figure C.4 (b).



**Figure C.5.**

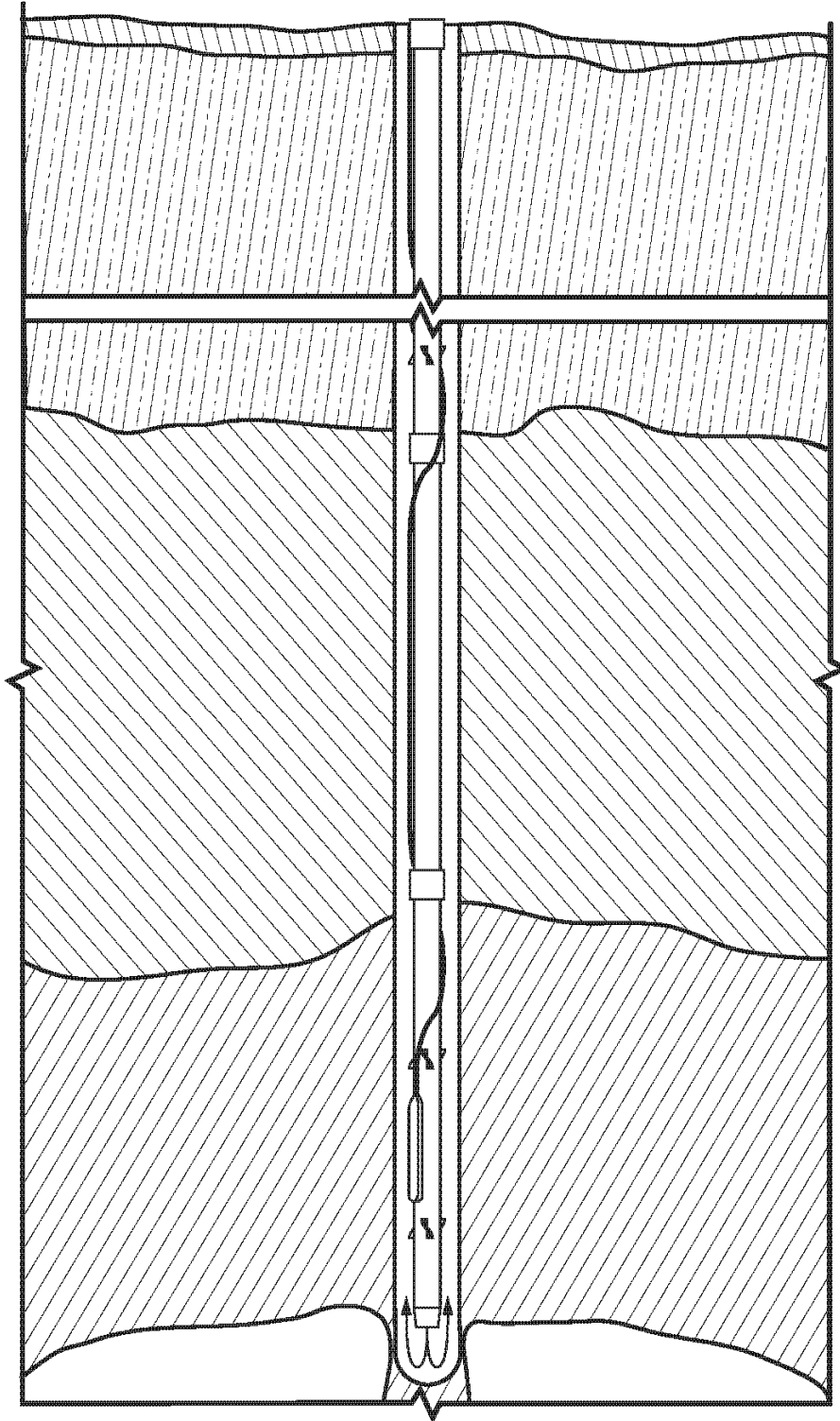


Figure C.6.

## DETAILED DESCRIPTION

[0031] The present document describes a sensing apparatus for lowering into a well and cementing therein at a certain depth. The sensing apparatus comprises an elongated casing and a sensor device protruding from an outside surface of the elongated casing for generating measurement data and sending the data to the surface of the well using a cable extending from the sensor device along the outside surface of the casing. A flow of cement is provided between the outside surface of the casing and the well for cementing the casing in place and isolating different layers of the well. Presence of the sensor device and the cable creates an obstruction within the flow path of the cement which results in the formation of micro-annulus around the sensor device and the cable. In order to address this problem, an embodiment presents a plurality of fins provided around the casing, the fins being shaped to cause a straight flow of cement received at the fins to rotate around the longitudinal axis of the casing when exiting the fins for increasing cement flow between the elongated casing and its surrounding environment to mitigate micro-annulus formation. Another embodiment presented herein discloses cable attachments which distance the cable from the casing and thereby let cement flow between the cable and the casing also mitigating micro-annulus formation.

[0032] Figure 1 illustrates an example of a downhole sensing apparatus **10** in accordance with an embodiment. As shown in the example of Figure 1, the sensing apparatus **10** comprises an elongated casing **12** from which a sensor device **14** partially protrudes. The signal is sent from the sensor device **14** to the surface of the well, into which the sensing apparatus **10** is to be installed, using a cable **20** which extends from the sensor device **14** along the casing **12**.

[0033] In an embodiment, the casing defines a fluid pipe having a lower end **13a** and an upper end **13b** opposite the lower end. In an embodiment, the upper and lower ends include respective helical threads for connecting to other casings in the well.

[0034] One of the methods for cementing a selected casing in the well consists of providing a flow of cement between the exterior surface of the casing and the inner walls of the well (e.g., pumping the cement down and let it circulate back up along the outside of the casing). In one embodiment, the flow of cement is provided upward in the well, whereby, cement is pushed downward inside of the casing **12** to exit the lower end **13a** and be received by a lower casing in the well (not shown). The lower casing includes one

or more openings from which the cement exits and flows upward between the exterior surface of the casing and the inner walls of the well.

[0035] As discussed above, every obstruction or irregular shaped component along the flow path of the cement will result in gaps of no-cement and ISVF areas around the sensing apparatus **10**. In order to reduce/eliminate the occurrence of ISVF around the sensor device **14** and/or cable **20**, embodiments of the invention provide a mechanism which rotates the flow of cement around selected areas of the casing **12**, where an obstruction or irregular shape exists.

[0036] In an embodiment, a first set of fins **21** is provided below the sensor device **14** (between the sensor device **14** and the lower end **13a**). These devices balance the annular flow impedance that the sensor housing induces. The fins may be welded to the outside surface of the casing **12**. The fins **21** are shaped (curved) to receive the straight flow of cement and rotate the latter as it exits the fins **21** in order to eliminate the presence of gaps and ISVF areas around the longitudinal sensor device **14**.

[0037] The number of fins in each set is determined using Computational Fluid Dynamics (CFD) software. The CFD software takes into account casing diameter, cement rheological properties, downhole temperature, pressure, flow rates, etc. The number of fins is at least two. For a regular casing, the number of fins is generally four. In one embodiment, the fins are concentrically spaced around a diameter of the casing **12**. The fins may take on respective shapes and angles with respect to the axis of the casing **12**. The shape and angle of each fin depends on: the rheology and the flow rates of the cement, the geometrical properties of the annular space formed by the sensing apparatus **10** as it is lowered in the wellbore (which includes for example the wellbore diameter), the dimensions of the casing **12**, dimensions of the sensor device **14**, and the location of the fins **21** relative to the location of the sensor device **14** on the casing **12**.

[0038] According to an embodiment, the fins measure between 5 in. and 6 in. long. Also according to an embodiment, the angle made by the fins and the longitudinal axis of the casing is approximately 25 degrees.

### **Cable Attachments**

[0039] In a preferred embodiment, the cable **20** is rotated around the casing **12** and attached to the latter using a set of cable attachment **24** provided between the cable **20**

and the outside surface of the casing to distance the cable from the outside surface of the casing. The cable attachment **24** comprises a cable standoff **24a** and a cable clamp **24b**. The cable standoff **24a** attaches to the cable **20** and is located between the sensor cable and the casing. This prevents the cable from contacting the casing and promotes cement flow between the cable and casing, thus preventing the formation of a micro-annulus. The cable clamp **24b** clamps the sensor signal cable at a 45° angle to the axis of the casing, and also lifts it off the surface of the casing. In conjunction with this device, the cable is wrapped around the casing 360° and held in place with the cable clamp. These devices angle the cable relative to the flow direction of the cement. The flowing cement is forced to pass underneath the cable and minimizes the chance of a micro-annulus formation between the cable and the casing.

**[0040]** In some cases, the rotating flow of cement caused by the first set of fins **21** tends to be re-straightened before reaching the cable and/or cable attachment **24**. In order to eliminate the micro-annulus formation and ISVF areas along the cable **20**, a second set of fins **22** is provided adjacent and above the sensor device **14**, between the sensor device **14** and the upper end **13b** of the casing **12** to re-rotate the flow of cement in order to eliminate the presence of gaps and ISVF areas along the cable. The fins **22** are shaped and positioned so as to “twist” around the casing **12**, in a direction opposite a twisting direction of the cable **20** around the casing **12**. Such opposite twisting directionality between the fins **22** and the cable **20** induce a “cross-flow” of cement over and under the cable **20** (i.e. including within the distance formed between the cable **20** and the casing **12**).

**[0041]** The number, shape and dimension of the fins **22** around the casing is determined in accordance with the parameters discussed above in connection with the fins **21**. The angle/direction of curvature of the fins **22** is preferably the same as that of the fins **21**, whereby the direction of rotation induced by the fins **22** is the same as that induced by the fins **21**. However, the present embodiments may also be implemented with the fins **22** curved in an angle opposite to the angle of curvature of the fins **21**.

### **Sensor Device**

**[0042]** Figure 2 illustrates an exploded view of an exemplary sensor device **14**, in accordance with an embodiment. The sensor device **14** comprises one or more sensors and a housing **18** enclosing the sensors. This protects the sensing elements (pressure/temperature gauge) during the installation, and allows the sensors to be in close

contact to the formation fluid post-cementing. Generally sensor housing configuration with a computation flow analysis could create vortices that result in ISVF and potential micro-annulus. The housing design of OPS Zero-Vortex-Gauge (OPS-ZVG) resulted from mechanical and computational flow analysis reduces all the possible vortices, preserving the streamlines of the flow during cementing.

**[0043]** In the example of Figure 2, the sensor device **14** comprises a temperature sensor and a pressure sensor gauges **15** and **16** (aka sensor pairs). This sensor arrangement provides redundancy in case of failure of one of the gauges. It is also to be noted that additional and different kinds of sensors may also be used without departing from the scope of this document. The outputs of the sensors are fed into a multiplexer **17** for sending the combined measurements on the same cable **20** to the surface of the well.

**[0044]** In some embodiments, each gauge **15** and **16** comprises only a pressure sensor or a temperature sensor.

**[0045]** In cases where more than one sensing apparatus are needed to provide different measurements at different depths of the well, different cables are required that run along different casings to reach the surface of the well. The presence of more than one cable complicates the problem further especially that the additional obstructions (cables and cable attachments) in the flow path of the cement will result in a non-homogenous flow regime. The present embodiments offer a solution to this problem by providing additional multiplexers in the sensor devices of the different sensing apparatuses.

**[0046]** Figure 3 illustrates the electrical components (without the casing) of a sensing apparatus **26** provided between the surface of the well and at least one lower sensing apparatus in the well, in accordance with an embodiment. Figures 4a&4b illustrate different views of the sensing apparatus **26** exemplified in Figure 3.

**[0047]** As shown in Figure 3, the sensor device comprises an opening **25** provided in the lower end thereof for receiving the cable **20** from a lower sensing apparatus. The signal sent on the cable **20** from the lower sensing apparatus and the output of the multiplexer **17** are fed to another multiplexer **19** in order to send all the signals on the same cable **20** passing through different sensing apparatuses of the same well.

### **Sensing apparatus installation**

**[0048]** Figure 5 illustrates a flow chart of one embodiment of a method **50** for installing a sensing apparatus inside a well so as to mitigate the formation of micro-annulus

alongside the sensing device and/or the cable of the sensing apparatus. As per the above, reducing or eliminating the formation of micro-annulus reduces the risks of hydraulic communication between zones inside the well, which can lead to imprecise or faulty measurements especially when multiple sensing devices are used for each zone.

**[0049]** In step **52**, the elongated casing is lowered into a wellbore. In one embodiment of the method **50**, the sensing apparatus is such as that described hereinabove in relation to Figure 1. For example, the casing has a sensor device coupled to a signal transmitting cable, and the signal transmitting cable extends from the sensor device, at a distance along an outside surface of the elongated casing.

**[0050]** In step **54**, a flow of cement is provided between the casing and an inner wall of the well in order to cement the casing in place. In an embodiment, the flow of cement is provided upward in the well, whereby the cement is first pushed downward inside of the elongated casing to be collected by another elongated casing below the elongated casing on which the sensing device is provided. The cement then exits from the lower casing and flows upward between the outside surface of the casing and the inner walls of the well. Therefore, one embodiment comprises lowering another casing into the wellbore prior to lowering the elongated casing. The other casing having an opening which allows fluids pushed downward inside the other casing to flow upward between an exterior surface of the other casing and the inner walls of the well.

**[0051]** In step **56**, the cement is rotated around a longitudinal axis of the casing before arriving to the sensor device for increasing cement flow around the sensor device and mitigating micro-annulus formation. In an embodiment of step **56**, rotating the cement flow comprises redirecting the cement flow around the casing using a plurality of fins around the casing between the sensor device and an end of the elongated casing at which the flow of cement between the casing and the well arrives first. In an embodiment, the fins are positioned concentrically on the outside surface of the casing, with a twisting direction.

**[0052]** Alternatively or in addition to the cement rotation step **56**, the flow of cement is provided between the elongated casing and the cable in step **58**.

**[0053]** The inside diameter of the elongated casing is wiped clean by pumping a wiper-plug down to the bottom (with water). The plug has water on top, and cement underneath

and travels down the casing. As it moves down, more cement is circulated up the annulus of the well to the surface. When it reaches the bottom, it stays there and casing is sealed.

**[0054]** In an embodiment, the fins are twisted opposite a twisting direction of the cable around the casing. This scenario allows the fins to induce a cross-flow of cement within the distance created between the cable and the casing.

**[0055]** Although the casing is illustrated herein as being installed or for installation in an observation well, the casing can be adapted to be used in a production well also. The sensors, fins and cables are simply adapted to the size and environment of the production well.

**[0056]** Figure 6 is a partial cut-out view of the ground showing an observation well **60** in which an assembly **62** comprising an embodiment of a sensing apparatus **10** is installed. The assembly **62** also comprises other fluid pipe casings **64** which are not equipped with a sensor device. The ground is constituted of different types of matter **66, 68, 70, 72** and **74**. The bottom of the observation well **76** provides a return path **78** for the cement (not shown) when it is poured / pushed down the series of casings from the upper end **80** of the first casing near ground level.

**[0057]** While preferred embodiments have been described above and illustrated in the accompanying drawings, it will be evident to those skilled in the art that modifications may be made therein without departing from the scope of this disclosure. Such modifications are considered as possible variants comprised in the scope of the disclosure.

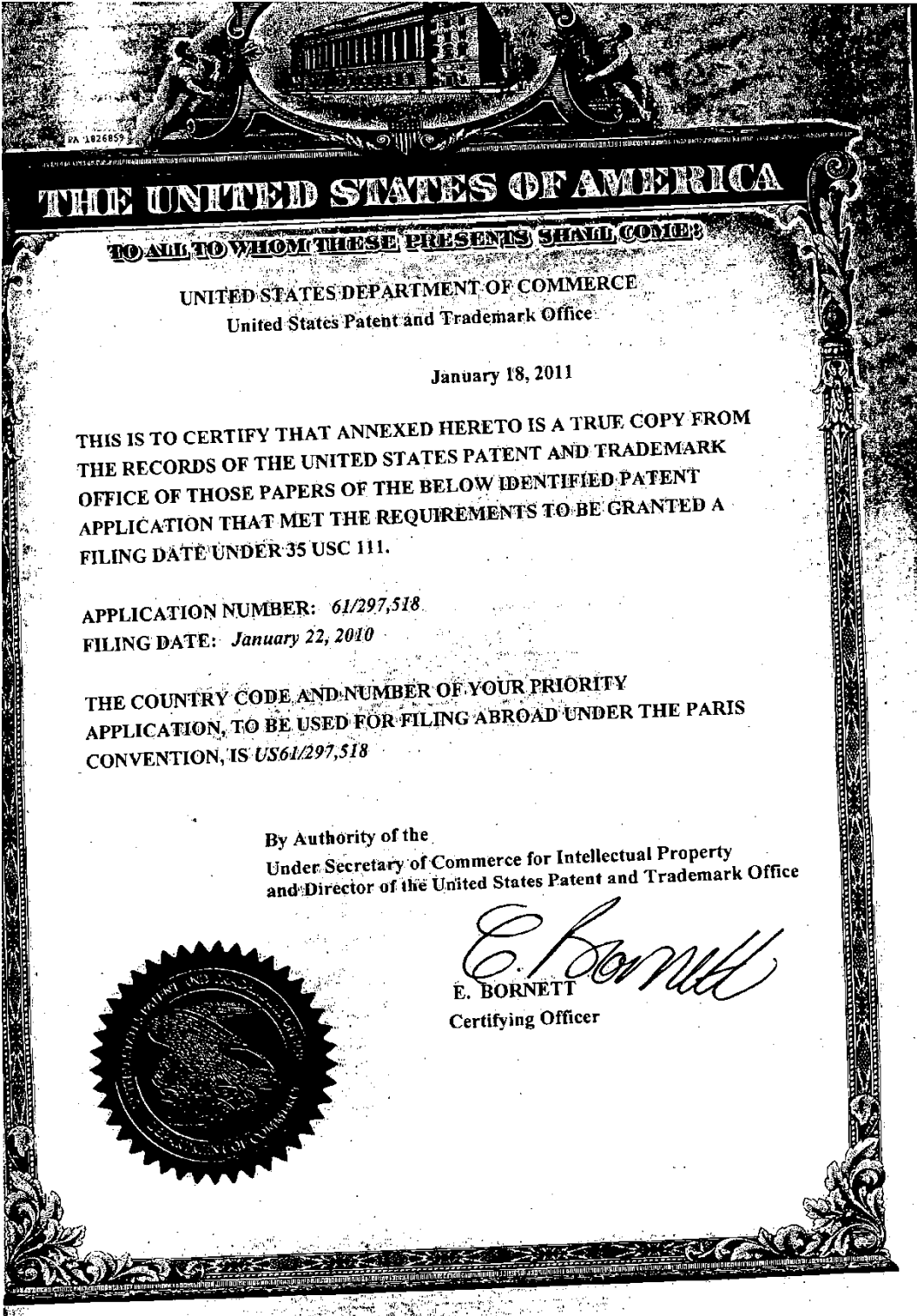
**CLAIMS:**

1. A sensing apparatus comprising:
  - an elongated casing for lowering from a surface into a well and cementing therein, the elongated casing comprising an outside surface, a lower end and an upper end opposite the lower end;
  - a sensor device protruding from the outside surface, for generating measurement data indicative of an environmental parameter;
  - a cable extending from the sensor device, along the outside surface toward the upper end, for transmitting the measurement data to the surface; and
  - a plurality of fins disposed on the outside surface, the fins being shaped to cause a straight flow of cement received at the fins to rotate around the longitudinal axis of the elongated casing when exiting the fins for increasing cement flow between the elongated casing and a surrounding environment to mitigate micro-annulus formation along the elongated casing.
2. The sensing apparatus of claim 1, further comprising cable attachments positioned along the outside surface between the sensor device and the upper end, the cable attachments for attaching the cable thereto at a distance from the outside surface.
3. The sensing apparatus of claim 2, wherein the plurality of fins comprises a first set of fins substantially equally spaced annularly on the outside surface between the sensor device and the lower end.
4. The sensing apparatus of claim 3, wherein the plurality of fins comprises a second set of fins substantially equally spaced annularly on the outside surface between the sensor device and the upper end of the elongated casing, the fins of the second set of fins being curved to re-rotate the flow of cement when exiting the second set of fins for increasing cement flow between the cable and the elongated casing to mitigate micro-annulus formation along the cable.
5. The sensing apparatus of claim 4, wherein the cable is disposed on the outside surface at an angle with respect to a longitudinal axis of the elongated casing such that the upward flow of cement exiting the second set of fins is substantially perpendicular to the cable.

6. The sensing apparatus of claim 4, wherein the sensor device is elongated and comprises a first end adjacent the first set of fins and a second end adjacent the second set of fins.
7. The sensing apparatus of claim 4, wherein the second set of fins is provided between a first cable attachment from the sensor device and a second cable attachment from the sensor device.
8. The sensing apparatus of claim 4, wherein the number of fins on the first set of fins and on the second set of fins respectively is at least two.
9. The sensing apparatus of claim 4, wherein the fins of the second set re-rotate the flow of cement in the same direction of rotation induced by the first set of fins.
10. The sensing apparatus of claim 9, wherein at least one of a shape and a position of the fins are dependent on at least one of the following factors: rheology of the cement, flow rates of the cement, geometrical properties of an annular space formed by the sensing apparatus as it is lowered in the well, dimensions of the casing, dimensions of the sensor device, and the location of the fins relative to the location of a sensor housing on the elongated casing.
11. The sensing apparatus of claim 1, wherein the sensor device includes an elongated housing and at least one sensor.
12. The sensing apparatus of claim 11, wherein the at least one sensor comprises a temperature sensor and a pressure sensor.
13. The sensing apparatus of claim 12, wherein the at least one sensor comprises two temperature sensors and two pressure sensors, each temperature sensor forming a pair with a pressure sensor, each pair having an output.
14. The sensing apparatus of claim 13, further comprising a first multiplexer for multiplexing the outputs of the two pairs of sensors and for sending the two outputs on the same cable.
15. The sensing apparatus of claim 14, further comprising a second multiplexer for multiplexing the output of the first multiplexer with the output of another sensor device of a lower casing in the well.
16. The sensing apparatus of claim 15, wherein at least one of the first multiplexer and the second multiplexer comprises a Y splice.

17. A sensing apparatus comprising:
  - an elongated casing for lowering from a surface into a well and cementing therein, the elongated casing comprising an outside surface, a lower end and an upper end opposite the lower end;
  - a sensor device protruding from an outside surface, for generating measurement data indicative of an environmental parameter;
  - a cable extending from the sensor device, along the outside surface toward the upper end, for transmitting the measurement data to the surface; and
  - cable attachments positioned along the outside surface between the sensor device and the upper end, the cable attachments for attaching the cable thereto at a distance from the outside surface such that cement flows between the elongated casing and the cable to mitigate micro-annulus formation along the elongated casing.
18. The sensing apparatus of claim 17, wherein the cable spirals upwardly from the sensor device around the elongated casing.
19. A method for installing a sensing apparatus inside a well, the method comprising:
  - lowering an elongated casing into the wellbore, the elongated casing having a sensor device protruding from an outside surface of the elongated casing, and a signal transmitting cable extending from the sensor device;
  - providing a flow of cement between the elongated casing and an inner wall of the well;
  - rotating the flow of cement around a longitudinal axis of the elongated casing before arriving to the sensor device for increasing cement flow around the sensor device and mitigating micro-annulus formation.
20. The method of claim 19, wherein rotating comprises:
  - redirecting the cement flow around the elongated casing using a plurality of fins around the casing between the sensor device and an end of the elongated casing at which the flow of cement between the elongated casing and the well arrives first.

21. The method of claim 19, further comprising, prior to lowering the elongated casing, lowering another casing into the wellbore, the another casing having an opening which allows fluids pushed downward inside the another casing to flow upward between an exterior surface of the another casing and the inner walls of the well.
22. The method of claim 19, further comprising rotating the flow of cement across the cable to mitigate micro-annulus formation along the cable.
23. The method of claim 19, further comprising providing the flow of cement between the elongated casing and the cable.



**THE UNITED STATES OF AMERICA**

**TO ALL TO WHOM THESE PRESENTS SHALL COME:**

UNITED STATES DEPARTMENT OF COMMERCE  
United States Patent and Trademark Office

January 18, 2011

THIS IS TO CERTIFY THAT ANNEXED HERETO IS A TRUE COPY FROM THE RECORDS OF THE UNITED STATES PATENT AND TRADEMARK OFFICE OF THOSE PAPERS OF THE BELOW IDENTIFIED PATENT APPLICATION THAT MET THE REQUIREMENTS TO BE GRANTED A FILING DATE UNDER 35 USC 111.

APPLICATION NUMBER: *61/297,518*  
FILING DATE: *January 22, 2010*

THE COUNTRY CODE AND NUMBER OF YOUR PRIORITY APPLICATION, TO BE USED FOR FILING ABROAD UNDER THE PARIS CONVENTION, IS *US61/297,518*

By Authority of the  
Under Secretary of Commerce for Intellectual Property  
and Director of the United States Patent and Trademark Office

*E. Bornett*  
E. BORNETT  
Certifying Officer



## APPENDIX D: Additional simulation results of OPS-ZVG model

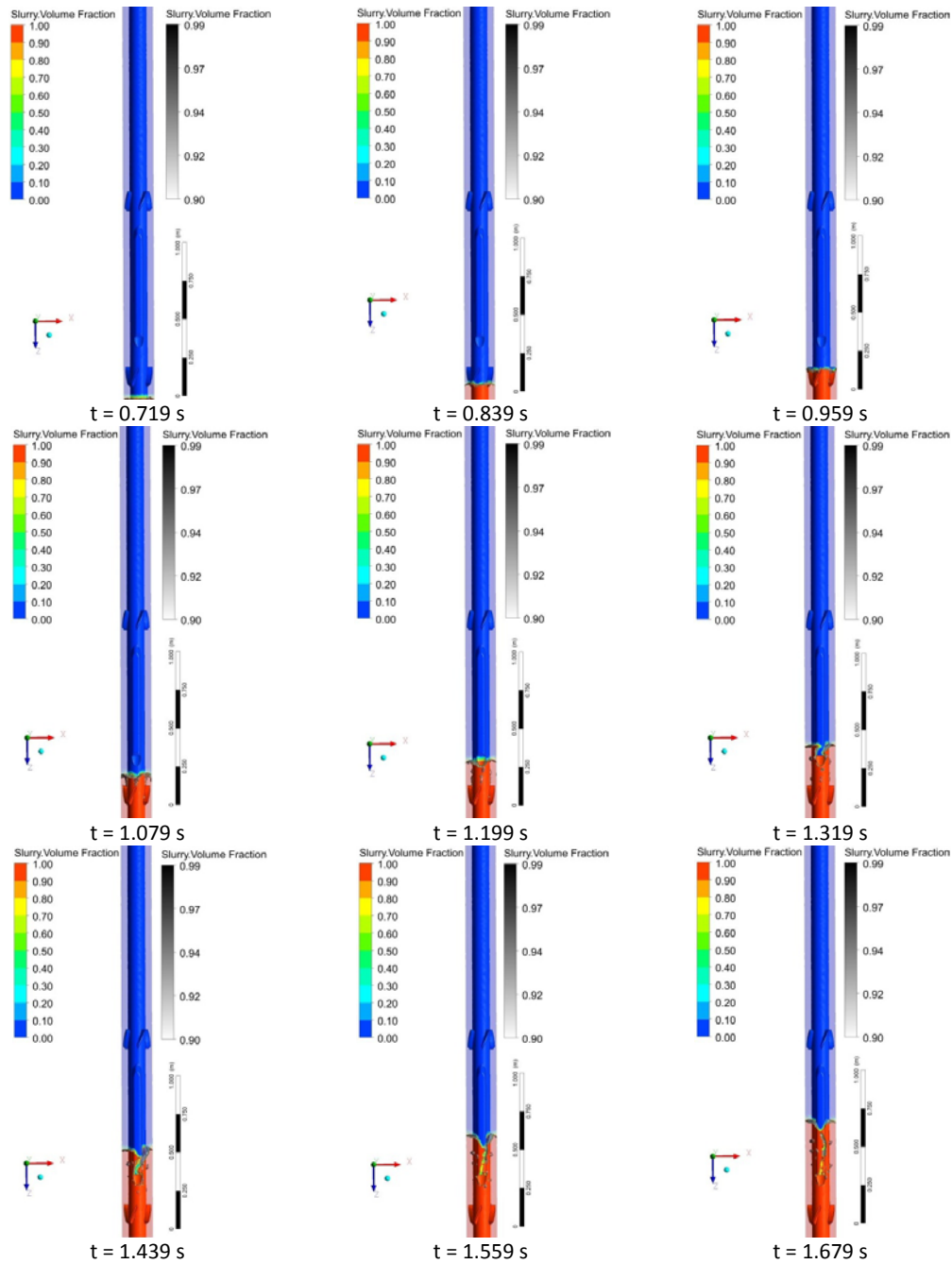


Figure D.1 VOF simulation results of 3D model of novel sensor housing and tubing conveyed with two sets of four flow deflector fins (Type-IV) each located at 127.0 mm down and up stream of the sensor housing within a borehole section of 5.00 m length. Output at time  $t = 0.719, 0.839, 0.959, 1.079, 1.199, 1.319, 1.439, 1.559$  and  $1.679$  s, while the cement slurry is displacing through the annulus. Each snapshot shows cement slurry volume fraction, ISVF from 0.90 to 0.99 (grey color map).

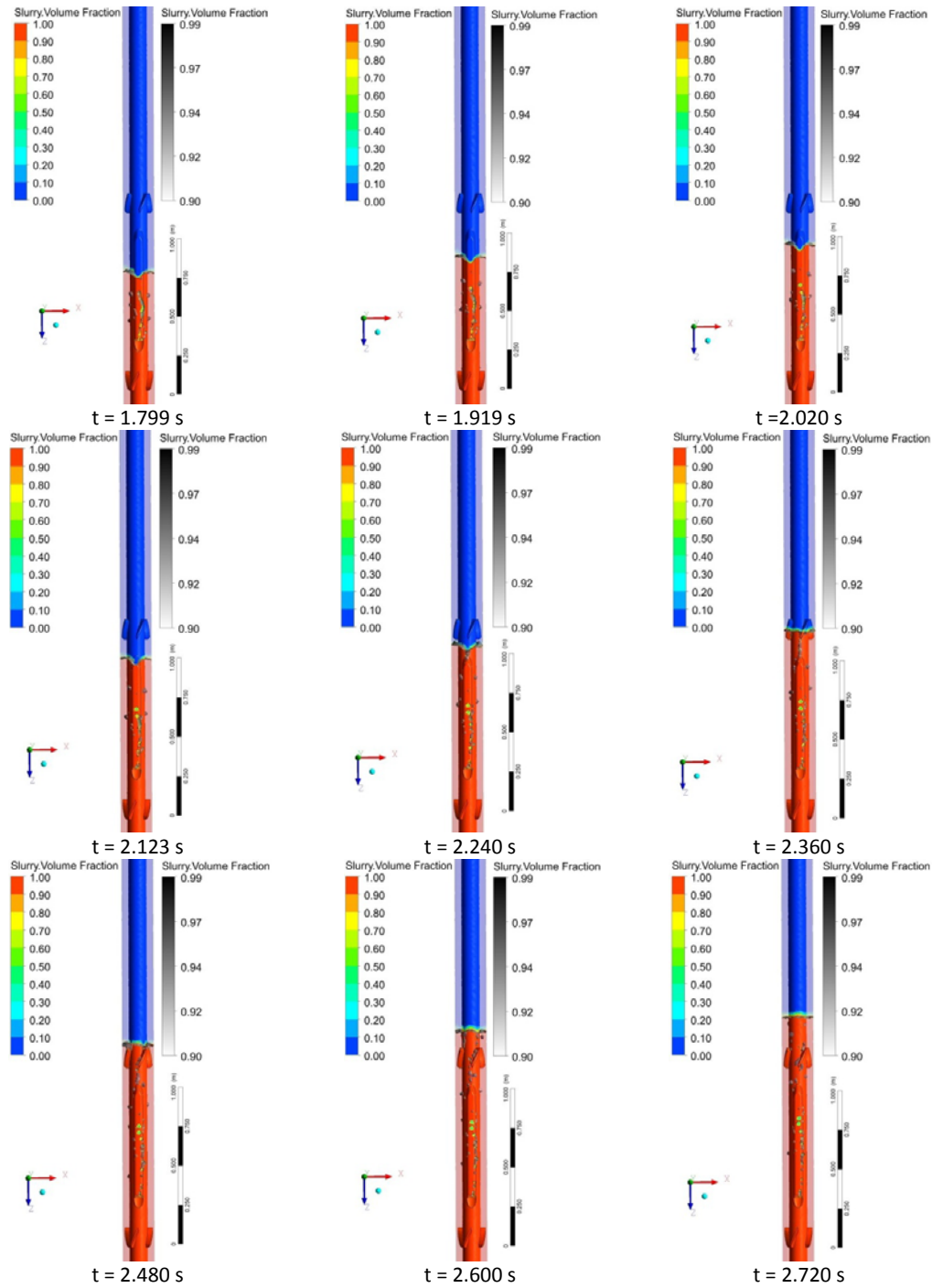


Figure D.2 VOF simulation results of 3D model of novel sensor housing and tubing conveyed with two sets of four flow deflector fins (Type-IV) each located at 127.0 mm down and up stream of the sensor housing within a borehole section of 5.00 m length. Output at time  $t = 1.799, 1.919, 2.020, 2.123, 2.240, 2.360, 2.480, 2.600$  and  $2.720$  s, while the cement slurry is displacing through the annulus. Each snapshot shows cement slurry volume fraction, ISVF from 0.90 to 0.99 (grey color map).

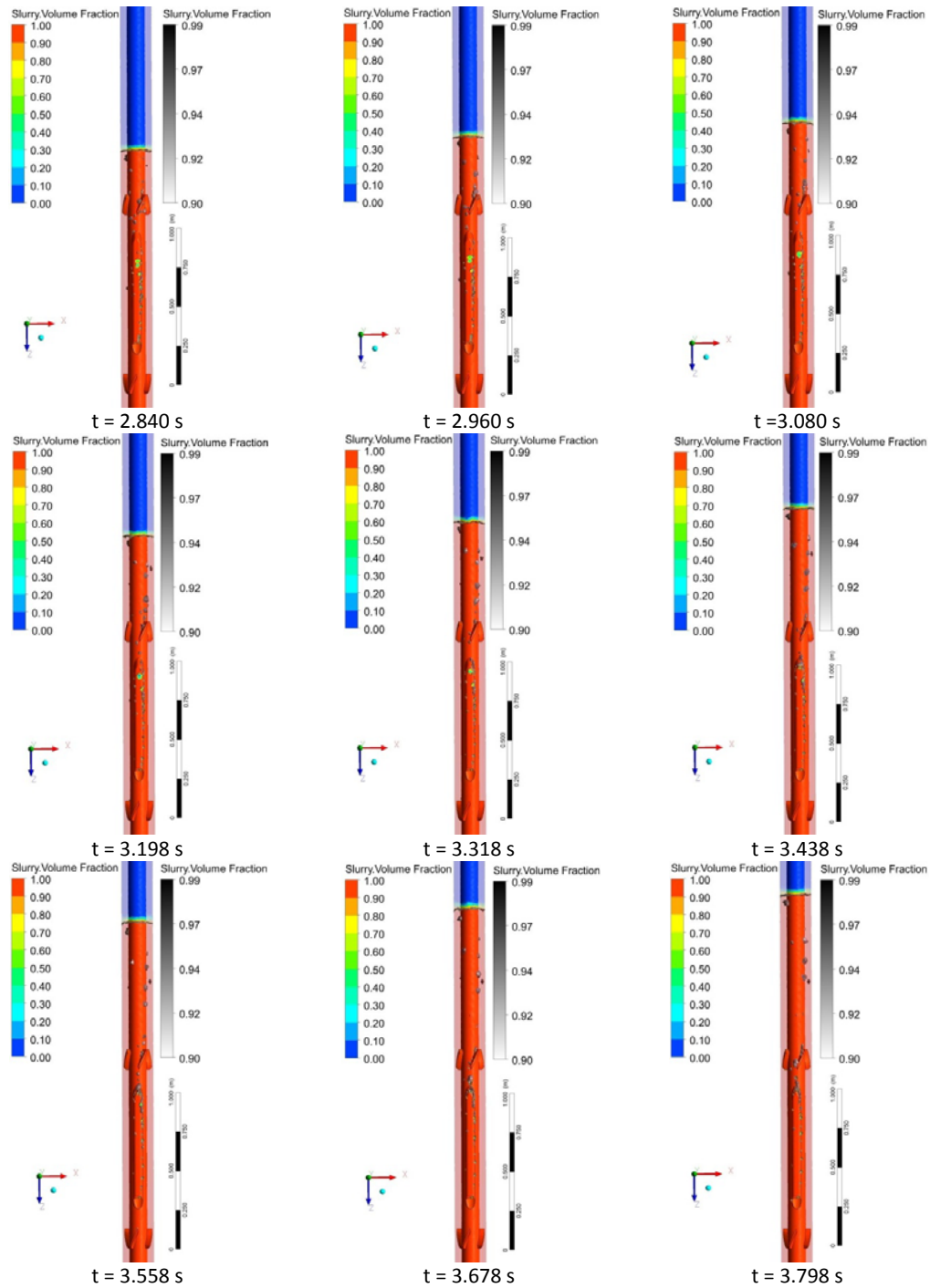


Figure D.3 VOF simulation results of 3D model of novel sensor housing and tubing conveyed with two sets of four flow deflector fins (Type-IV) each located at 127.0 mm down and up stream of the sensor housing within a borehole section of 5.00 m length. Output at time  $t = 2.840, 2.960, 3.080, 3.198, 3.318, 3.438, 3.558, 3.678$  and  $3.798$  s, while the cement slurry is displacing through the annulus. Each snapshot shows cement slurry volume fraction, ISVF from 0.90 to 0.99 (grey color map).

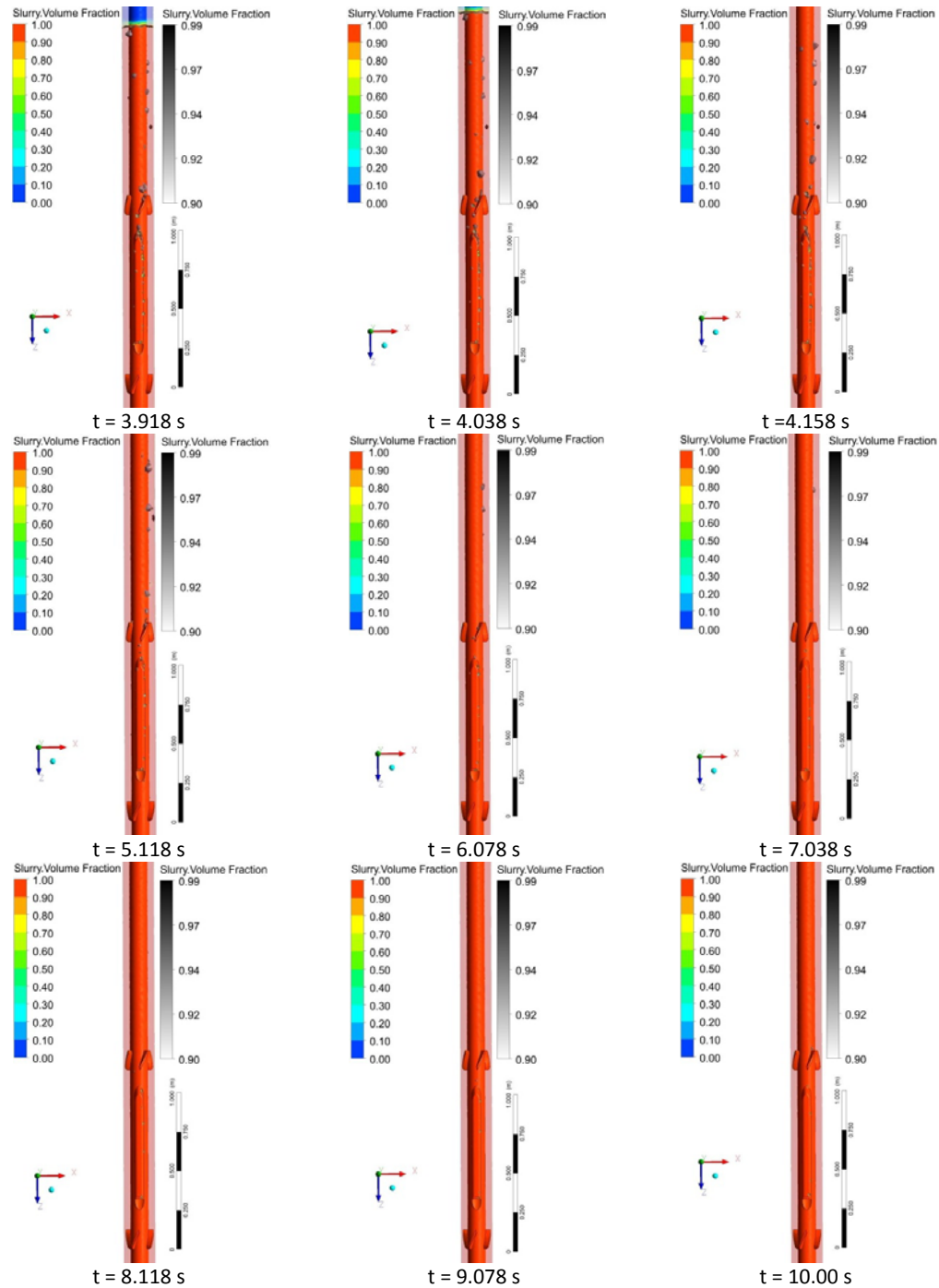


Figure D.4 VOF simulation results of 3D model of novel sensor housing and tubing conveyed with two sets of four flow deflector fins (Type-IV) each located at 127.0 mm down and up stream of the sensor housing within a borehole section of 5.00 m length. Output at time  $t = 3.918$ , 4.038, 4.158, 5.118, 6.078, 7.038, 8.118, 9.078 and 10.00 s, while the cement slurry is displacing through the annulus. Each snapshot shows cement slurry volume fraction, ISVF from 0.90 to 0.99 (grey color map).